# Modulating tissue mechanics to increase oxygen delivery to tumors

by

John Daniel Martin
B.S., University of Southern California (2007)



Submitted to the
Department of Chemical Engineering
in partial Fulfillment of the requirements for the degree of

Doctor of Philosophy in Chemical Engineering

at the

MASSACHUSETTS INSTITUTE OF TECHNOLOGY

February 2015



Signature of Author: Signature redacted
Department of Chemical Engineering
November 12, 2014

Certified by: Signature redacted
Rakesh K. Jain
Director, Edwin L. Steele Laboratory for Tumor Biology, Massachusetts General Hospital
Andrew Werk Cook Professor of Tumor Biology (Radiation Oncology), Harvard Medical School
Thesis Supervisor

Certified by: Signature redacted
Klavs F. Jensen
Department Head, Warren K. Lewis Professor of Chemical Engineering
Professor of Materials Science and Engineering
Thesis Supervisor

Accepted by: Signature redacted
Patrick S. Doyle
Robert T. Haslam (1911) Professor of Chemical Engineering
Chairman, Committee for Graduate Students

# Modulating tissue mechanics to increase oxygen delivery to tumors

by

John Daniel Martin

B.S., University of Southern California (2007)

Submitted to the

Department of Chemical Engineering

in partial Fulfillment of the requirements for the degree of

Doctor of Philosophy in Chemical Engineering

at the

MASSACHUSETTS INSTITUTE OF TECHNOLOGY

February 2015

# Modulating tissue mechanics to increase oxygen delivery to tumors

by

John Daniel Martin

Submitted to the Department of Chemical Engineering on
November 12, 2014, in partial fulfillment of the requirements for the
degree of Doctor of Philosophy in
Chemical Engineering

**Abstract**

Solid tumors have low oxygen tension – hypoxia – that fuels disease progression and treatment resistance. Thus, strategies for alleviating hypoxia are needed. Two factors affect tissue oxygen levels: oxygen supply via blood vessels and oxygen consumption by cells. I focused on improving supply to combat hypoxia. Two vessel abnormalities limit supply. Compression decreases the density of perfused vessels supplying tumors. Excessive leakiness slows blood flow partly by reducing the intravascular pressure drop. Strategies to repair leakiness towards decreasing hypoxia exist, so I developed approaches for overcoming compression.

In order to understand the origin of vessel compression, we developed the first *ex vivo* technique to estimate compressive solid stresses held in tumors. We made measurements of this residual solid stress in numerous tumor types from patients and mice to confirm that elevated stress is conserved across tumors. We then identified structural components within tumors that contribute to stress. Since cancer cells were known to compress vessels, we found that depleting them reduced stress, as did depleting fibroblasts, collagen, and hyaluronan. Depleting these components decompressed blood and lymphatic vessels.

After identifying targets to reduce stress, we sought to decrease stress therapeutically to improve treatment outcomes. First, we demonstrated that losartan, an FDA-approved therapy indicated for hypertension, decreases the activation of fibroblasts and the production and maintenance of collagen and hyaluronan. As a result, losartan decompressed vessels, restored perfusion, decreased hypoxia, and potentiated chemotherapy. These results provide a rationale for retrospective analyses

demonstrating losartan's benefit and for future clinical trials, one of which is currently underway (NCT01821729).

To understand how reversing compression modulates both individual vessels and the vascular network to improve oxygen delivery, we developed a technique using multi-photon phosphorescence quenching microscopy to map oxygenation to perfused blood vessels in live tissues. This technique allowed us to compare the effects of reversing compression to the effects of repairing leakiness on individual vessels and vascular network geometry. In comparing and contrasting these two strategies, we showed how each of these strategies could be improved to increase oxygen delivery. This work also has implications for optimally combining both treatment strategies to increase oxygen delivery to tumors.

Thesis Co-Supervisor: Rakesh K. Jain
Title: Director, Edwin L. Steele Laboratory for Tumor Biology, Massachusetts General Hospital
Andrew Werk Cook Professor of Tumor Biology (Radiation Oncology), Harvard Medical School

Thesis Co-Supervisor: Klavs F. Jensen
Title: Department Head, Warren K. Lewis Professor of Chemical Engineering
Professor of Materials Science and Engineering

**To Rosemary, John, and Margaret**

## Acknowledgments

I would like to express gratitude to those who have generously and selflessly supported me as I performed the research for this dissertation. My words here do not sufficiently express my thanks nor contain all of things for and people to which I owe gratitude. Nonetheless, first I would like to thank my thesis advisor, Professor Rakesh K. Jain for his enthusiastic mentorship. I am indebted to him for his encouragement and guidance in weekly (or more frequent) meetings over the last five and a half years. The example he sets through his dedication to both engineering and translational research will stay with me throughout my career.

I would also like to thank the members of my thesis committee, starting with my other thesis advisor, Professor Klavs F. Jensen. I had formal meetings with Dr. Jensen on three important occasions: interviewing at MIT, deciding on a lab, and pursuing a career after MIT. While these are three of the more moments during an MIT graduate student's path, he was ready with clear advice and friendly guidance.

Other members of my thesis committee include Professor Moungi G. Bawendi, who was a collaborator on the phosphorescence quenching microscopy research and on a number of projects that are not included in this dissertation. In particular, I am thankful for his presence at our labs' monthly collaborative meeting, as he has a knack for identifying holes in data and prescribing fixes for them. Professor William M. Deen provided many constructive comments. At all stages, he pushed me to improve my research. He also taught the transport phenomena course. I look back on that course with pride, as I am surprised at the wide range of problems we solved when I look back on the material. Professor Dai Fukumura mentored me in the phosphorescence quenching microscopy work and also in nanoparticle studies that do not appear in this dissertation. He always gives his full attention to provide thoughtful suggestions. He has a special talent for giving feedback on research that simultaneously makes you feel good about your research and guides you to improve your research. Professor Alan J. Grodzinsky is a collaborator that provided insight into experiments exploring the material properties of biological tissues. He has always been friendly and encouraging. He did not know me at the time, but his guest lecture in a course I was taking sparked an idea in me to try an experiment again in a different way.

I would like to acknowledge all members of the Steele Laboratory. I have received much guidance, friendship, and assistance from dozens of you. Unfortunately, I cannot thank all of you here and thus I am omitting a number of colleagues and friends that deserve

recognition. Nonetheless, I would like to specifically highlight Walid Kamoun, Yuhui Huang, Shom Goel, Dan Nguyen, Meenal Datta, and Delphine Lacorre for each providing all of the following: friendship, experimental and emotional support (often required simultaneously), and shared interest in sports. Ryan Lanning was my first mentor in the lab. Besides teaching me how to perform intravital microscopy, he was a kind friend and it was comforting to have a fellow Californian to complain to during my first winter in Boston. Triantafyllos Stylianopoulos involved me in his tissue mechanics projects. He has always looked out for my career. Additionally, we shared a lot of laughs: not all of his PowerPoint files include data. Giorgio Seano worked with me on a clinical trial involving angiogenesis and has started studying tissue mechanics himself. He was a supportive collaborator and friend. Vikash Chauhan was a mentor to me throughout my doctoral research. Many senior graduate students including Ryan Lanning left shortly after I joined the lab. Vikash remained to teach me what I might have otherwise learned from a number of senior graduate students. That suited Vikash fine, as he is a willing teacher. Vikash was a close collaborator and a closer friend.

I would like to thank family and friends who, in particular, supported me during my doctoral research. My parents, Rosemary and John, were always willing to help, usually by lending an ear, at a moment's notice. My sister Margaret spent three summers in Boston and worked with me for two. I appreciate her companionship and collaboration. A fellow MIT chemical engineer, Matthew Stuber was the first person I met in Boston, my first friend in Boston, and a great person to have lunch with every week. He was there for me to help me move to Boston and leave Boston. In between, we had many conversations over a wide range of topics. My friends from high school were a source of support from across the country. They now all know what solid stress is. I'm glad we stayed in touch. I relied on all of these people during my doctoral research, and thus they were instrumental in the completion of this dissertation.

# Table of Contents

**Chapter 0 Motivation** ..... **18**

**Chapter 1 Introduction** ..... **21**

*1.1. Abstract* ..... *22*

*1.2. Introduction* ..... *23*

*1.3. Solid mechanics of tumors* ..... *25*

Externally Applied Solid Stress ..... 25

Growth-Induced Solid Stress ..... 26

Desmoplasia and Solid Stress Accumulation ..... 27

Consequences of Solid Stresses for Cancer Progression and Treatment ..... 27

Mathematical Modeling of Solid Mechanics of Tumors ..... 28

*1.4. Fluid mechanics of tumors* ..... *30*

Vascular Fluid Mechanics ..... 30

Interstitial Fluid Mechanics ..... 32

Lymphatic Fluid Mechanics ..... 33

Consequences of Fluid Stresses for Cancer Progression and Treatment ..... 34

Mathematical Modeling of Fluid Mechanics of Tumors ..... 35

*1.5. Therapeutic strategies* ..... *38*

Stress-Alleviation Treatment ..... 38

Vascular Normalization Treatment ..... 39

Guidelines for the Optimal Use of Stress-Based Therapeutic Strategies ..... 40

*1.6. Concluding remarks* ..... *41*

*1.7. Figures* ..... *42*

*1.8. References* ..... *50*

**Chapter 2 Growth-induced solid stress in murine and human tumors: Causes, consequences an remedies** ..... **62**

*2.1. Abstract* ..... *63*

*2.2. Introduction* ..... *64*

*2.3. Results* ..... *67*

*2.4. Discussion* ..... *73*

*2.5. Figures* ..... *76*

*2.6. Methods* ..... *100*

*2.7. References* ..... *102*

*2.8. Supplement* ..... *106*

**Chapter 3 Angiotensin inhibition enhances drug delivery and potentiates chemotherapy by decompressing tumor blood vessels** ..... **114**

*3.1. Abstract* ..... *115*

*3.2. Introduction* ..... *116*

*3.3. Results* ..... *117*

*3.4. Discussion* ..... *123*

*3.5. Figures* ..... *126*

*3.6. Methods* ..... *157*

*3.7. References* ..... *164*

**Chapter 4 Multiphoton high-resolution measurement of partial pressure of oxygen in tumor tissue reveals differential effects of anti-angiogenic therapy** ..... **170**

*4.1.1. Abstract* ..... *171*

*4.1.2. Introduction* ..... *172*

*4.1.3. Results* ..... *174*

*4.1.4. Discussion* ..... *178*

*4.1.5. Figures* ..... *180*

*4.1.6. Methods* ..... *192*

*4.1.7. References* ..... *196*

**Chapter 5 Conclusion and future work** ..... **200**

## List of Figures

Figure 1-1 Schematic of the tumor mechanical microenvironment. ..... 43

Figure 1-2 Solid stress profile in tumors and evidence of vessel compression ..... 44

Figure 1-3 Externally applied and growth-induced solid stresses ..... 45

Figure 1-4 Abnormal fluid flow in tumors. ..... 46

Figure 1-5 Strategies to improve perfusion and drug delivery in solid tumors ..... 47

Figure 1-6 Stress-alleviation treatment. ..... 48

Figure 1-7 Vascular normalization treatment with the monoclonal antibody DC101. ..... 49

Figure 2-1 Model predictions for the total displacement of the tumor after releasing the growth-induced stress. ..... 77

Figure 2-2 Estimation of stress in transplanted and human tumors. ..... 78

Figure 2-3 Selective depletion of tumor constituents reduces growth-induced stress and decreases tumor opening. ..... 79

Figure 2-4 Saridegib increases tumor vessel diameter and reopens compressed vessels by reducing stress. ..... 80

Figure 2-5 Strategies to alleviate growth-induced solid stress in tumors. ..... 81

Figure 2-6 Supplementary Figure 1. Boundary conditions of the model. ..... 82

Figure 2-7 Supplementary Figure 2. Model predictions of the tumor shape after making a cut for four values of . ..... 83

Figure 2-8 Supplementary Figure 3. Schematic of the deformation of the tumor after making a cut along one of its axes. ..... 84

Figure 2-9 Supplementary Figure 4. Parametric analysis of the model predictions. ..... 85

Figure 2-10 Supplementary Figure 5. Compressive circumferential growth-induced stress at the interior of the tumor as a function of the relative growth, $\lambda_s$. ..... 86

Figure 2-11 Supplementary Figure 6. Compressive circumferential growth-induced stress at the tumor interior as a function of the relative stiffness between the tumor periphery and center. ..... 87

Figure 2-12 Supplementary Figure 7. Normalized tumor opening for five transplanted sub-cutaneous tumor models. ..... 88

Figure 2-13 Supplementary Figure 8. Tumor opening as a function of tumor volume and mass density for two orthotopic cancer cell lines. ..... 89

Figure 2-14 Supplementary Figure 9. Tumor opening of human pancreatic neuroendocrine tumors. ..... 90

Figure 2-15 Supplementary Figure 10. Interstitial fluid pressure measurements of B16F10, Mu89, E0771, and U87 tumors. ..... 91

Figure 2-16 Supplementary Figure 11. Solid stress of ectopic tumors after collagen or cancer cell depletion. ..... 92

Figure 2-17 Supplementary Figure 12. Staining of E0771 tumors for co-localization of vimentin and aSMA confirms human fibroblast levels were reduced by diphtheria toxin treatment. ..... 93

Figure 2-18 Supplementary Movie 1 - A freshly excised, orthotopically grown 4T1 breast tumor is cut. ..... 94

Figure 2-19 Supplementary Movie 2 - A freshly excised kidney from a female SCID mouse is cut following the same procedure as with tumors ..... 95

Figure 3-1 Collagen and hyaluronan interact to compress tumor blood vessels. ..... 127

Figure 3-2 Losartan decreases pro-fibrotic stromal activity in tumors. ..... 129

Figure 3-3 Losartan reduces matrix and stromal density in tumors. ..... 130

Figure 3-4 Stromal angiotensin signaling induces matrix production in tumors. ..... 131

Figure 3-5 Losartan targets solid stress in tumors. ..... 132

Figure 3-6 Losartan decompresses tumor vessels to increase drug and oxygen delivery. ..... 133

Figure 3-7 Losartan potentiates chemotherapy. ..... 135

Figure 3-8 Supplementary Figure S1. CAFs isolated from pancreatic tumors in mice. .. 136

Figure 3-9 Supplementary Figure S2. Compression of tumor blood vessels in human breast cancer. ..... 137

Figure 3-10 Supplementary Figure S3. AK4.4 pancreatic tumors recapitulate the desmoplasia and hypo-perfusion of genetically-engineered KPC mouse tumors and human pancreatic ductal adenocarcinoma. ..... 138

Figure 3-11 Supplementary Figure S4. Losartan improves the perfusion of tumor blood vessels in mouse breast and pancreatic tumors. ..... 139

Figure 3-12 Supplementary Figure S5. Losartan reduces the expression of active-TGF-β1 and CCN2 in mouse breast and pancreatic tumors. ..... 140

Figure 3-13 Supplementary Figure S6. Losartan reduces the expression of hyaluronan in mouse breast and pancreatic tumors. ..... 141

Figure 3-14 Supplementary Figure S7. Losartan decreases matrix staining intensity in tumors. ..... 142

Figure 3-15 Supplementary Figure S8. Losartan reduces αSMA+ CAF density in mouse breast and pancreatic tumors. ..... 143

Figure 3-16 Supplementary Figure S9. The ACE-I lisinopril decreases matrix levels less than losartan. ..... 144

Figure 3-17 Supplementary Figure S10. A panel of angiotensin receptor blockers reduces solid stress. ..... 145

Figure 3-18 Supplementary Figure S11. Losartan does not improve perfusion in well-perfused tumors. ..... 146

Figure 3-19 Supplementary Figure S12. Losartan does not decrease tumor VEGF levels. ..... 147

Figure 3-20 Supplementary Figure S13. Losartan slightly increases blood vessel diameter. ..... 148

Figure 3-21 Supplementary Figure S14. Losartan increases the effective permeability of all sizes of nanoparticles. ..... 149

Figure 3-22 Supplementary Figure S15. Losartan and lisinopril do not decrease blood pressure at 40 mg/kg dose. ..... 150

Figure 3-23 Supplementary Figure S16. Losartan does not affect individual blood vessel flow velocity at doses that do not reduce blood pressure. ..... 151

Figure 3-24 Supplementary Figure S17. Losartan results in a normalized network of perfused vessels. ..... 152

Figure 3-25 Supplementary Figure S18. Losartan reduces hypoxia. ..... 153

Figure 3-26 Supplementary Figure S19. Losartan reduces hypoxia in an additional tumor model. ..... 154

Figure 3-27 Supplementary Figure S20. Losartan potentiates chemotherapy against tumor growth. ..... 155

Figure 3-28 Supplementary Figure S21. Losartan enhances chemotherapy in immunocompetent and immunodeficient mice. ..... 156

Figure 4-1 Multiphoton Phosphorescence Quenching Microscopy. ..... 181

Figure 4-2 Measurement of $pO_2$ in various murine tissues. ..... 183

Figure 4-3 DC101 increases the maximum distance to a vessel by pruning small perfused vessels ..... 184

Figure 4-4 DC101 does not improve the delivery of oxygen from individual vessels .... 185

Figure 4-5 Losartan maintains oxygenation of tumors by improving vessel network geometry. ..... 187

Figure 4-6 Supplementary Figure S1. The distribution of perfused vessel diameters does not change after three days after control treatment with IgG in E0771 tumors. ..... 188

Figure 4-7 Supplementary Figure S2. The distribution of perfused vessel diameters does not change after three days of control treatment (PBS) in E0771 tumors ..... 189

Figure 4-8 Supplementary Figure S3. The maximum distance from a vessel decreases in losartan-treated E0771 tumors. ..... 190

Figure 4-9 Supplementary Figure S4. The maximum distance from a vessel did not change in control-treated (PBS) E0771 tumors. ..... 191

## List of Tables

Table 2-1 Supplementary Table 1. Mechanical material properties of the tumor types employed in the study. ..... 96

Table 2-2 Supplementary Table 2. Experimentally measured doubling time and model estimates of the growth stretch ratio and the growth-induced solid stress in the interior of the transplanted tumors employed in the study. ..... 97

Table 2-3 Supplementary Table 3. Comparison of IFP measured with the piezoelectric probe and wick-in-needle techniques. ..... 98

Table 2-4 Supplementary Table 4. Dimensions and model estimates of the growth-induced solid stress developed in the interior of surgically excised human tumors along the circumferential direction. ..... 99

# *Chapter 0 Motivation*

Oxygen levels are highly regulated in the tissues making up our bodies, because oxygen is critical for the function of our organs. Each organ, and each type of cell within an organ, requires a unique amount of oxygen to support its function. Thus, the observation that all tumors have lower average oxygen levels than the organ they grow in implies that tumors are organs that benefit from having low oxygen levels. This state of oxygen concentration lower than normal physiological oxygen concentration is called hypoxia. Indeed, patients that have less oxygen in their tumors live less and respond less to therapy. Thus, hypoxia is a negative prognostic and predictive biomarker.

There are a number of processes that hypoxia stimulates. These processes make tumors more deadly. First, hypoxia induces a cancer stem cell phenotype. Low oxygen might make these cells quiescent and not proliferative, allowing them to preserve their stemness and remain potent. Second, hypoxia promotes resistance to radiotherapy, chemotherapy, and immunotherapy. These treatment strategies, which comprise all non-surgical techniques to treat cancer, depend to varying degrees on a chemical reaction involving oxygen to produce the desired cytotoxic effects. Third, low oxygen levels promote genomic instability and affect the expression of growth factors, oncogenes, and tumor suppressor genes. As a result, low oxygen levels stimulate mutations and other conditions that make the cancer cell population more aggressive and able to withstand treatment and immune defenses. Fourth, hypoxia promotes epithelial to mesenchymal transition, invasion, and metastasis. These processes allow cancer cells to spread throughout the body. This makes the primary tumor more deadly. Fifth, hypoxia promotes a wound healing response that includes inflammation, immunosuppression, and fibrosis. Sixth, hypoxia promotes abnormal angiogenesis that can lead to deeper levels of hypoxia. Seventh, hypoxia induces resistance to hypoxia in cancer cells. Eighth, hypoxia promotes a switch to anaerobic metabolism. Through these eight mechanisms, hypoxia makes tumors more deadly.

Oxygen levels are reduced in tumors because there is decreased supply of oxygen without a simultaneous decrease in the consumption of oxygen by rapidly proliferating cancer cells. Thus, the balance that holds in normal organs is not maintained. There are two reasons why supply of oxygen is reduced. The first is that tumor vessels are leaky and the second is that tumor vessels are compressed. Tumor vessel leakiness has been extensively studied and various treatment strategies have been validated clinically. The

causes of tumor vessel compression are less clear and there are no clinically validated strategies to reduce it. Thus, the goal of my doctoral research was to answer the question, "why is vascular function impaired by vessel compression in tumors?" The answer to this question has been pursued for at least a half of a century, since cancer researchers first observed red blood cells in regions of tumors apparently disconnected from the body's circulation. As basic and clinical research reveal the insidious role of compression-induced vascular dysfunction in driving tumor progression and resistance to treatment, understanding and reversing vessel compression in tumors has become crucial. Developing new strategies to prevent tumor progression and overcome inherent resistance to existing therapies will improve treatment outcomes. In this dissertation, I define the causes of tumor vessel compression, develop a treatment strategy to overcome compression, and evaluate the effects of this strategy on the vasculature.

One of the limiting factors in addressing the question posed above was the lack of techniques to measure tissue-level solid stresses that were hypothesized to cause vessel compression. In this dissertation, I describe a technique we developed to estimate solid stress in tumor tissue. This technique enabled the discovery of the structural components of tumors that generate, store, and transmit solid stresses. This technique also allowed us to prove that solid stresses are uniquely responsible for compressing tumor vessels.

With the identification of structural components that contribute to solid stress and vessel compression, I then investigated whether there were existing therapies that could efficiently target these tumor components towards overcoming inherent resistance to systemic chemotherapy. FDA-approved anti-hypertensive agents that target angiotensin II signaling affects the activation, production, and maintenance of the components that contribute to solid stress. I demonstrated that this class of therapeutics, approved to relieve hypertension by blocking angiotensin II receptor I, also synergistically increases the delivery and efficacy of systemic chemotherapies in murine cancer models. While retrospective analyses of these anti-hypertensive agents combined with chemotherapy are promising, they need to be evaluated in prospective clinical trials, one of which we recently initiated.

Finally, after demonstrating that targeting solid stress can help overcome the physiological resistance of tumors to chemotherapy, I examined how various subsets of tumor vessels are affected by a reduction in solid stress. To address this, I monitored the spatial and temporal distribution and function of tumor vessels using real-time

measurements in murine cancer models. For this purpose, we adapted a technique to measure oxygenation – phosphorescence quenching microscopy – to a technique to image tumor vasculature – multi-photon microscopy. I used this technique to longitudinally monitor the effects of decompressing vessels on the function of subsets of vessels. Furthermore, I compared the strategy of decompressing vessels to other strategies known to increase oxygenation in certain tumors. This knowledge will guide optimal use of anti-solid stress therapies to increase oxygenation in tumors. Furthermore, it provides guidelines for combining multiple strategies to increase oxygenation in tumors in order to impair tumor progression and resistance to systemic chemotherapies.

# *Chapter 1 Introduction*

Some of the work, text and figures presented in this chapter are adapted from the following reference with permissions granted by Annual Reviews:

Jain RK, Martin JD, Stylianopoulos T. 2014. The role of mechanical forces in tumor growth and therapy. *Annu. Rev. Biomed. Eng.* 16:321–46

## 1.1. Abstract

Tumors generate physical forces during growth and progression. These physical forces are able to compress blood and lymphatic vessels, reducing perfusion rates and creating hypoxia. When exerted directly on cancer cells, they can increase cells' invasive and metastatic potential. Tumor vessels— while nourishing the tumor—are usually leaky and tortuous, which further decreases perfusion. Hypoperfusion and hypoxia contribute to immune evasion, promote malignant progression and metastasis, and reduce the efficacy of a number of therapies, including radiation. In parallel, vessel leakiness together with vessel compression causes a uniformly elevated interstitial fluid pressure that hinders delivery of blood-borne therapeutic agents, lowering the efficacy of chemo- and nanotherapies. In addition, shear stresses exerted by flowing blood and interstitial fluid modulate the behavior of cancer and a variety of host cells. Taming these physical forces can improve therapeutic outcomes in many cancers.

## 1.2. Introduction

A solid tumor is an aberrant tissue made of cancer cells and a variety of host cells—all embedded in an extracellular matrix—nourished by blood vessels and drained by lymphatic vessels (1). Solid tumors often stiffen as they grow in a host's normal tissue. Stiffening, which is perhaps the only mechanical aspect of a tumor that clinicians and patients can feel/sense, is caused by an increase in the structural components of the tumor, particularly in the amount of cancer cells, stromal cells, and the extracellular matrix constituents. As tumor tissue becomes stiffer than the surrounding tissue, the continued generation of forces by the tumor constituents displaces the surrounding normal tissue and allows the tumor to invade and grow in size. Thus, tumor growth involves the generation of mechanical forces both within the tumor and between the tumor and the host tissue. These mechanical forces, coupled with aberrant tumor blood vessels, induce abnormal solid and fluid stresses (i.e., force per unit area) that facilitate tumor progression and hinder response to various treatments (2).

Solid stress—the mechanical forces exerted by the nonfluid components of a tumor—is accumulated within tumors as the rapid proliferation of cancer cells strains the tumor microenvironment, which itself pushes against and deforms the surrounding normal tissue (**Figure 1**). The solid stress held solely within a tumor—that remains in the tissue after it is excised and external loads are removed—is referred to as growth-induced or residual stress (3–5). An additional, externally applied stress is generated as the growing tumor deforms the normal tissue, which, in turn, resists tumor expansion (5, 6). Solid stresses affect tumor pathophysiology in at least two ways: directly, by compressing cancer and stromal cells, and indirectly, by deforming blood and lymphatic vessels. Cell compression alters gene expression, cancer cell proliferation, apoptosis and invasiveness, stromal cell function, and extracellular matrix synthesis and organization (7–13). Blood and lymphatic vessel compression reduces the delivery of oxygen, nutrients, and drugs, creating a hypoxic and acidic microenvironment and compromising therapeutic outcomes (1, 5, 14–18).

Fluid stresses—the forces exerted by the fluid components of the tumor—include the microvascular and interstitial fluid pressures (MVP and IFP, respectively), as well as the shear stress exerted by blood and lymphatic flow on the vessel wall and by interstitial flow on cancer and stromal cells and extracellular matrix (19). Fluid stresses are determined in large part by the combined effect of the structure of tumor vessels and the

compression of blood and lymphatic vessels. Blood vessel compression reduces the effective flow cross section of the vessel and, thus, increases the resistance to blood flow, which can affect MVP, shear stress, and perfusion (20) (**Figure 1**). In addition, compression of lymphatic vessels hinders the drainage of excessive interstitial fluid (21, 22). This, in turn, results in accumulation of fluid in the interstitial space and formation of edema, which is often seen in patients. Furthermore, the hyperpermeability of the tumor vessels, formed during the process of angiogenesis, usually leads to increased fluid flux from the vascular to the interstitial space. This fluid leakage reduces tumor perfusion and, along with the loss of functional lymphatics through physical compression, elevates IFP (21). This is a vicious cycle, as elevated IFP also reduces perfusion without compressing leaky tumor vessels, because the upstream microvascular pressure is communicated to the extravascular space and then to downstream vessels, minimizing the pressure drop between upstream and downstream segments of vessels and leading to reduced flow (23, 24). Taken together, the effects of elevated IFP make it a major barrier to drug delivery (22, 25–28).

Here, we review the existing knowledge on solid and fluid mechanics of tumors and describe the mechanisms by which tumor mechanics affect cancer cell growth and metastasis and inhibit the delivery of drugs. We also propose therapeutic strategies that can alter the tumor mechanical microenvironment and improve the delivery of therapeutic agents and, thus, the efficacy of cancer treatment.

## 1.3.Solid mechanics of tumors

Externally applied and growth-induced stresses affect tumor progression and treatment either directly, by being exerted on cancer and stromal cells and extracellular matrix constituents, or indirectly, by deforming blood and lymphatic vessels. The two stresses compose the total solid stress, which begins to evolve from the early stages of carcinogenesis (29). Unlike fluid pressure, solid stress can be direction dependent. Thus, total solid stress is compressive in the interior of the tumor in all directions, whereas at the interface with the normal tissue, it is compressive in the radial and tensile in the circumferential directions as shown in **Figure 2*a*** (5, 6). We review separately the externally applied and growth-induced solid stresses.

### *Externally Applied Solid Stress*

The effect of solid stress applied externally by the surrounding tissue on solid tumors has been studied in vitro by growing avascular tumor spheroids within a polymer matrix (7, 11, 12, 30). We first grew cancer cells within an agarose gel of varying concentration to increase the compressive stress exerted on the cells and found that increasing compressive stress inhibits spheroid growth (7). The inhibitory effect of stress on growth is, however, reversible, and growth-inhibited spheroids resume normal growth once the stress is removed. Later, we repeated the experiment to investigate the underlying mechanisms and found that compressive stresses suppress cancer cell proliferation and induce apoptotic cell death via the mitochondrial pathway (11). More specifically, anisotropic (i.e., nonuniform) mechanical loads can induce apoptosis in regions of high compressive stress and allow proliferation in low-stress regions of the tumor spheroid (11). As a result, external forces can shape tumor morphology: Isotropic (i.e., uniform) loads lead to the growth of spherical cancer cell aggregates, whereas anisotropic loads force cancer cells to grow preferentially in the direction of least stress. Again, tumor spheroid growth patterns are reversible, and the aggregates can be remodeled by altering the stress field. Moreover, compressive stress can enhance the invasive phenotype of cancer cells (13) (**Figure 3*a***) and increase the expression of genes that remodel the extracellular matrix and tumor vessels (12, 31, 32). Estimates of the external stress levels in the spheroids are in the range of 28 to 120 mm Hg (3.7 to 16.0 kPa) depending on the concentration of the matrix (7, 11). Recently, with the use of mathematical modeling, we found, based on experimental data for murine tumors, that the externally applied stress at the tumor interior can exceed 150 mm Hg (20 kPa) (6).

These stresses are sufficient to compress fragile intratumoral blood and lymphatic vessels, whereas the tensile circumferential stress at the interface of the tumor with the normal tissue can deform peritumoral vessels to elliptical shapes (**Figure 2*b***).

### *Growth-Induced Solid Stress*

Growth-induced or residual solid stress is accumulated within tumors during progression as the growth of proliferating cancer cells strains the tumor microenvironment and stores strain energy (**Figure 1**) (5). This stress is evident when a tumor is excised, with no external loads applied, and a cut is made along its longest axis. The cut releases the stress and allows the tissue to relax, resulting in simultaneous swelling at the center and retraction at the boundary of the tumor. These relaxations lead to a significant opening at the location of the cut (**Figure 3*b***). The retraction of the tissue is indicative of tension at the tumor periphery. The swelling at the center indicates that the intratumoral region is in compression, which presumably balances the tension at the periphery. The tensile growth-induced stress at the periphery causes a smooth transition of the circumferential stress from compressive inside the tumor to tensile at the interface with the normal tissue (6).

Based on experimental data and with the use of mathematical models, the levels of compressive growth-induced stress at the intratumoral region were estimated to be in the range of 35 to 142 mm Hg (4.7 to 18.9 kPa) for human tumors, 2 to 60 mm Hg (0.3 to 8.0 kPa) for murine tumors, and 0 to 10 mm Hg (0 to 1.3 kPa) for avascular tumor spheroids (5, 33, 34). Interestingly, tumors with higher growth-induced stress levels exhibited lower growth rates, presumably owing to reduced cancer cell proliferation and increased apoptosis (5, 11). Finally, according to our calculations, growth-induced stress contributes less than 30% of the total solid stress of a tumor, which suggests that the contribution of the external stress from the host tissue is more significant (6).

Cancer cells, stromal cells, and the extracellular matrix participate in the accumulation of growth-induced stress (5). Cancer and stromal cells contribute to growth-induced stress by generating forces during proliferation and contraction. They both also contribute to the remodeling of matrix components. The extracellular matrix constituents, such as collagen and hyaluronic acid, store and transmit stress in a manner dependent on their mechanical properties. Collagen fibers, which are remarkably stiff in tension and provide tensile strength to tissues, can contribute to growth-induced stress by virtue of the fibers' ability to resist stretching when connected cells are forced apart. Collagen

fibers are also remodeled and pulled by fibroblasts. By contrast, hyaluronic acid provides compressive resistance because of its capacity to trap water molecules. Water is incompressible, and because water molecules cannot escape from the tumor, they resist the compressive stress developed in the tumor interior. Thus, collagen and hyaluronic acid collaborate in stress generation (35).

### *Desmoplasia and Solid Stress Accumulation*

It is notable that during tumor progression, extensive extracellular matrix synthesis and remodeling can take place. One pathway through which this occurs is the activation or overexpression of transforming growth factor-β (TGF-β). TGF-β can regulate the production of matrix-modifying enzymes [e.g., matrix metalloproteinases (MMPs) and lysyl oxidase (LOX)] in order to increase matrix protein synthesis and cross-linking and decrease matrix proteinase activity (36–38), thereby increasing matrix stiffness (36). Stiffening of the matrix and the resulting increase of the stress levels can, in turn, induce production of fibronectin, enhance focal adhesions, and increase cytoskeletal tension by Rho/ROCK signaling activation (39, 40). Matrix stiffening can also promote integrin clustering and enhance PI3 kinase activity, which regulates tumor invasion and other processes that promote tumor progression (41, 42).

In addition, mechanical stress and TGF-β activation can convert fibroblasts or other quiescent precursor cells into contractile myofibroblasts, also known as cancer-associated fibroblasts, which produce more extracellular matrix molecules (collagen-I, fibronectin, glycosaminoglycans) and remodel the extracellular matrix (8, 43, 44). Production of new extracellular matrix again increases tissue stiffness and solid stress, and myofibroblast contraction further activates latent TGF-β from the extracellular matrix (10, 43), creating a positive feedback loop. TGF-β may also play a role in both endothelial-to-mesenchymal transition (EndMT) and epithelial-to-mesenchymal transition (EMT), which are associated with loss of intercellular adhesion and acquisition of a motile phenotype that promotes cancer cell invasion and metastasis (45, 46).

### *Consequences of Solid Stresses for Cancer Progression and Treatment*

Blood vessel compression, caused by solid stresses, reduces tumor perfusion and, thus, the supply of oxygen and nutrients (14). Limited oxygen and nutrient supply results in the formation of necrotic tissue at the tumor interior. But because oxygen and nutrients

are essential for tumor progression, a question arises about why solid tumors compress their own vessels. One hypothesis is that vessel compression by solid stress protects cancer cells from the immune system of the host (1, 47). The cells of the immune system require an effective vascular network to continuously patrol the human body. Vessel compression prevents these cells from entering the tumor, whereas the resulting hypoxia compromises their killing potential (48). Hypoxia also produces growth factors [e.g., TGF-β and vascular endothelial growth factor (VEGF)] that suppress the activity of macrophages and have the potential to convert macrophages to protumorigenic (tumor-friendly) cells (49). Furthermore, a hypoxic microenvironment can select for cells that can survive in a harsh microenvironment, which enhances the invasive and metastatic potential of cancer cells and lowers the efficacy of radiation and immunotherapy (1, 49–51).

Vessel compression can also exclude large tumor regions from the systemic administration of therapeutic agents by reducing blood flow and creating vascular shunts (i.e., short, high-flow vascular pathways that bypass long, downstream pathways) (52–54). Therefore, drugs might not be able to reach certain regions of tumors in sufficient amounts. Furthermore, the collapse of intratumoral lymphatic vessels contributes to the uniform elevation of IFP, which can be equal to or locally exceed MVP transiently (21, 22, 26, 55, 56). As we discuss in detail below, IFP elevation eliminates pressure gradients across the tumor vasculature and in the interstitial space of tumors and, thus, inhibits convective transport of drugs.

### *Mathematical Modeling of Solid Mechanics of Tumors*

Several mathematical models have been developed to study the biomechanical response of solid tumors. Most of them make use of the multiplicative decomposition of the deformation gradient tensor, $\boldsymbol{F}$ (see Appendix in this chapter), to account for tumor growth, $\boldsymbol{F}_g$, evolution of growth-induced stress, $\boldsymbol{F}_r$, and the mechanical interactions with the surrounding normal tissue, $\boldsymbol{F}_e$ (5, 6, 57–60):

$$\boldsymbol{F} = \boldsymbol{F}_e\boldsymbol{F}_r\boldsymbol{F}_g. \quad (1)$$

The tensors $\boldsymbol{F}_r$ and $\boldsymbol{F}_g$ are usually assumed to be isotropic, and their values are taken either based on experimental observations, based on phenomenological expressions (e.g., Gompertz law for tumor growth), or by relating growth to the concentration of oxygen and nutrients. Methodologies also exist that involve the incorporation of a

growth strain factor to drive tumor expansion (33, 34).

Although the mathematical framework for tumor growth is well defined, little work has been done to date regarding constitutive modeling of solid tumors compared with other biological tissues, such as arteries, heart valve leaflets, and articular cartilage. Tumors are often modeled as isotropic, hyperelastic materials (e.g., neo-Hookean or Blatz–Ko) with strain energy density functions given as follows (5, 57, 59, 60):

neo-Hookean: $W = 0.5\mu(-3 + II_1) - 0.5\kappa(-1 + J_e)^2$, (2)

Blatz-Ko: $$W = -\frac{Gf}{2}\left(I_1 - 3 - \frac{2}{q}(I_3^{q/2} - 1) + \frac{G(1-f)}{2}\left(\frac{I_2}{I_3} - 3 - \frac{2}{q}(I_3^{-q/2} - 1)\right)\right), \quad (3)$$

where $\mu$ and $\kappa$ are the shear and bulk modulus of the material, respectively; $J_e$ is the determinant of the elastic deformation gradient tensor $\boldsymbol{F}$; and $II = I J^{-2/3}$. $G$ is the tumor shear modulus; $I_1$, $I_2$, and $I_3$ are the invariants of the strain tensor $\boldsymbol{F}^T\boldsymbol{F}$; and $f \in [0, 1]$ and $q < 0$ are nondimensional parameters. Additionally, tumors have been treated as isotropic poroelastic materials composed of a solid and a fluid phase (6, 61) or as a mixture of more than two components (58). These models work well and provide accurate qualitative predictions for the mechanical microenvironment of tumors and its effect on tumor growth, progression, and treatment. However, they are limited in that tumors are not isotropic and their structure is too complex to be described by continuum- level constitutive equations. A main reason for the uncertainty of the mechanical behavior of tumors is a lack of experimental studies. Indeed, most of the models developed to date lack experimental validation. Spatial and temporal heterogeneities in the structure of a tumor, as well as differences between the primary tumor and its metastases and among tumors of the same type or tumors of different types, render the derivation of a global constitutive equation a challenging task. To deal with the structural heterogeneity of tumors, development of structure-based models that incorporate directly tumors' heterogeneity by utilizing multiscale methodologies—similar to those developed for other soft tissues—is a promising approach (62, 63).

## 1.4. Fluid mechanics of tumors

Fluid mechanics of tumors involve flow along the tumor vasculature, across the vessel wall, and through the tumor interstitial space and drainage of excessive fluid by the lymphatic network. Abnormalities in the tumor microenvironment due to the formation of hyperpermeable tumor blood vessels and the accumulation of solid stress affect blood flow, MVP, IFP, and fluid shear stresses (19, 64). As a result, tumors are often hypoperfused: The arteriovenous MVP gradient drops, whereas IFP increases uniformly throughout the tumor interior. At the same time, fluid shear stresses cause remodeling of the vascular network, and lymphatic flow is limited only to the tumor periphery. Here, we review separately vascular, interstitial, and lymphatic flows and their effects on tumor progression and treatment.

### *Vascular Fluid Mechanics*

Blood flow rate, $Q$, in the vasculature of normal and tumor tissues is given by the microvascular pressure drop, $\Delta MVP$, divided by the flow resistance, $FR$: $Q = \Delta MVP/FR$. The resistance to fluid flow can be either due to vascular network geometry (e.g., vessel morphology, tortuosity) or due to changes in blood viscosity. In solid tumors, both geometric and viscous resistances are elevated (20, 65, 66).

Rapid tumor growth requires a sufficient vascular network to feed cancer cells with nutrients and oxygen. For that reason, proangiogenic factors [e.g., VEGF, platelet-derived growth factor (PDGF)], which induce angiogenesis, are upregulated in order to recruit endothelial cells to form new vessels (67, 68). Tumor vessels are usually immature and have an abnormal structure and function (1, 54, 69, 70). The endothelial lining that forms the vessel wall can have wide junctions, have large numbers of fenestrae and transendothelial channels, and be accompanied by a discontinuous or absent basement membrane and poor pericyte coverage. As a result, the openings in the tumor vessel wall can be as large as a few micrometers in size, much larger than the pores of normal vessels, which are less than 10 nm (71–73). The large pores of tumor vessels enhance leakage of blood plasma to the interstitial space, which, in turn, increases red blood cell concentration (hemoconcentration) and blood viscosity (66, 74, 75). In addition, tumor vessels can be dilated and tortuous (70) and create vascular shunts (52). Finally, as mentioned above, blood and lymphatic vessels can be compressed owing to solid stresses, which further increases geometric resistance to flow. As a result of all these abnormalities, blood velocity in tumors is highly heterogeneous

and is not correlated with vessel diameter. It can also be an order of magnitude lower than the velocity in normal vessels, ranging from 0.001 to 10 mm/s (53, 76) (**Figure 4*a***). In normal vessels, which have higher velocities, shear stress contributes to the regulation of an important step in metastasis. Shear stress controls whether circulating tumor cells (CTCs) adhere to normal blood vessel walls in distant organs. Increasing shear increases the amount of collisions of CTCs with vessel walls, but it also reduces their residence time of adhesion, which could impair extravasation (77).

Within intratumoral vessels, the lower shear stress applied to endothelial cells contributes to the regulation of angiogenesis and tumor vascular network abnormalities. Shear stress from blood flow on the endothelial lining is transmitted by the glycocalyx layer. This layer is a negatively charged fibrous structure of proteins and macromolecules and is connected to the cytoskeleton of endothelial cells (78). This connection allows the layer to mediate the transduction of fluid shear stress to the endothelial cell lining. Through this mechanism, high and low shear stresses regulate different steps of angiogenesis. A lack of shear stress, indicative of a static vessel, induces endothelial cells to sprout to seek new sources of blood flow. Nitric oxide (NO) production, however, with moderate levels of shear stress results in the attenuation of sprouting (79). Whereas low shear stress encourages endothelial cells to seek alternate sources of nutrients, higher shear stress induces vessel branching, which is termed intussusceptive angiogenesis (80). This process occurs as endothelial cells, protruding into the vessel lumen, connect to form a pillar within the vessel. The pillar's location is governed by shear stress because it forms where there was high velocity and, thus, low shear in the original vessel. As a result of the branching, there is a stress reduction in the individual endothelial cells, but the flow rate within the original, single vessel is maintained by the combination of the two vessels. Therefore, high and low shear stresses affect angiogenesis in single vessels in different ways.

The effect of shear stress on a single vessel can have a substantial impact on the blood flow through nearby regions of the vascular network. Functional shunts are an interesting example of this relationship. They occur in situations in which there is a short arteriovenous connection through which blood flow can bypass the downstream vascular network. The shear stress is often high in the short vessel serving as the functional shunt, which causes the shunt to dilate, allowing more blood to flow through the shunt (81). The feeding arteriole downstream of the shunt senses less flow and shear stress. As a consequence, it reduces in diameter, further discouraging flow throughout

the vascular network downstream of the branch point from the shunt (52). Abnormal shear stress in a single vessel can impair blood flow to downstream regions of tumors, contributing to the low perfusion found in multiple areas in most solid tumors.

### *Interstitial Fluid Mechanics*

The driving forces for interstitial flow are hydrostatic and osmotic pressure gradients between the vascular and interstitial space. The interstitial space of solid tumors is composed of a network of collagen fibers, along with other fibrillar and space-filling proteins and molecules, such as proteoglycans and glycosaminoglycans (e.g., hyaluronic acid) (82, 83). The compressive stress throughout a tumor compresses the matrix into a dense and tortuous network that hinders transport of fluid. We provided the first measurements of the interstitial fluid velocity and found that it is on the order of 0.2 to 0.8 $\mu m/s$ (84), resulting in very low Reynolds number (i.e., Stokes flow). Even with low flow velocity, shear stress can be high when there are small pores. Nonetheless, in tumors, the shear stress applied to cells remains low because the matrix shields the cells from stress, and local gradients in hydraulic conductivity divert flow from cells (85).

Despite the low velocity of the interstitial fluid, studies have shown that fluid shear stress— similarly to solid stress—can upregulate TGF-β, causing myofibroblast differentiation and contraction and extracellular matrix reorganization and stiffening (86, 87). Therefore, the role of fluid and solid stresses on TGF-β-dependent pathways appears to be synergistic. Furthermore, despite the fact that the interstitial shear stresses are up to two orders of magnitude lower than the intravascular shear stresses, when applied to cancer cells they can stimulate oncogenic signaling pathways (88). Stromal cells may increase their motility in response to interstitial flow as a result of a small shear gradient across the cell (89). Thus, interstitial shear stress influences cancer cell and stromal cell behavior. Shear stress generated by interstitial flow also affects angiogenesis. Interstitial flow increases the rate of vessel morphogenesis, which is the rearrangement of the vessel wall microanatomy before sprouting. After sprouting, invading endothelial cells preferentially protrude against the direction of interstitial flow (79). In this way, a vessel, which began sprouting because of low intravascular shear stress, sprouts in the direction of another leaky vessel—in other words, toward a higher pressure region.

Interstitial fluid flow is governed in large part by the hydraulic conductivity of the interstitial space, a measure of the resistance to fluid flow in porous and fibrous media.

The higher the conductivity, the more easily fluid will percolate through the extravascular space of the tissue. Importantly, interstitial hydraulic conductivity, together with vessel leakiness and lymphatic dysfunction, is a regulator of IFP, and the low conductivity values often found in tumors contribute to the elevation of IFP to values comparable to those of MVP (**Figure 4*b***). For fibrous media, which are our focus, hydraulic conductivity depends on the volume fraction, surface charge, and organization of the fibers (90, 91). Therefore, tumors rich in collagen might exhibit hydraulic conductivity an order of magnitude lower than that of tumors of low collagen content (92). As mentioned above, in many tumors an accumulation of fibrillar collagen types I and III occurs presumably owing to increased activity of tumorigenic factors, such as TGF-β, that might stiffen the extracellular matrix and induce fibrosis (38, 93). Therefore, this desmoplastic response of tumors further decreases hydraulic conductivity. The hydraulic conductivity of the interstitium is also influenced by the negatively charged proteoglycans and glycosaminoglycans. Increasing the glycosaminoglycan concentration leads to increased flow resistance owing to the capacity of these polysaccharides to trap water (90). Accordingly, depletion of glycosaminoglycans with MMP-1 and MMP-8 increases the hydraulic conductivity and, thus, the interstitial fluid velocity (94). Cancer and stromal cells form another barrier to interstitial fluid flow. High cellular density, which is common in many cancers, reduces the space available for flow and, thus, increases fluid resistance. Also, plasma proteins, soluble collagen, and the thin and elongated glycosaminoglycan chains that are contained in the interstitial fluid might significantly increase the viscosity of the interstitial space (95, 96).

### *Lymphatic Fluid Mechanics*

The lymphatic network drains excessive fluid from the interstitial space and returns it back to the blood circulation. By doing so, it regulates the fluid balance in tissues and prevents formation of edema. Tumor lymphatics have two phenotypes that are common in many cancers. They are not functional in the intratumoral region (97, 98), and they are hyperplastic and exhibit increased flow at the periphery (99, 100). The loss of functionality is attributed to compressive solid stress that is developed in tumors. This stress has been shown to collapse intratumoral lymphatic vessels and, thus, to eliminate lymph flow. Lymphangiogenesis in the tumor periphery is regulated by the expression of VEGF-C and VEGF-D. Overexpression of these growth factors in tumors might result in hyperplasia of the vessels, dilation of their lumen, and increased volumetric flow rate

(**Figure 4*c***) (100–102). The lymph fluid velocity in tumors is on the order of 5 μm/s, about an order of magnitude higher than the interstitial fluid velocity (103–106). The increase in lymph flow rate of the peritumor lymphatic vessels might lead to a 200-fold increase in the accumulation of cancer cells in lymph nodes and a 4-fold increase in metastasis, despite the absence of intratumoral lymphatics (98, 100). Therefore, lymph flow plays a crucial role in the dissemination of cancer cells.

Another regulator of lymphatic function is NO (1, 107, 108). NO is synthesized by NO synthase (NOS) and can be neuronal (nNOS), endothelial (eNOS), or inducible (iNOS). nNOS and eNOS are constitutively expressed by neuronal and endothelial cells, whereas iNOS is induced by inflammatory cytokines, endotoxin, hypoxia, and oxidative stress. We have shown that eNOS maintains strong lymphatic contractions and that its inhibition decreases lymphatic fluid velocity (106). We attribute this effect to the regulation of the deeper collecting lymphatics of eNOS, as the velocity of the superficial lymphatics did not change with eNOS inhibition. iNOS levels can maintain lymphatic pumping during inflammation and infection (109, 110). Lymphatic flow is also susceptible to changes in the interstitial flow. An increase in interstitial flow can stimulate lymphatic endothelial cell morphogenesis and increase lymphatic permeability (111, 112). Therefore, the composition of the interstitial space and particularly the hydraulic conductivity can regulate not only interstitial but also lymphatic flow (87).

### *Consequences of Fluid Stresses for Cancer Progression and Treatment*

Heterogeneous and compromised vascular flow results in heterogeneous distribution of therapeutic agents in the tumor, and thus it can reduce the efficacy of the treatment. In addition, because not all tumor vessels are leaky, the delivery of large therapeutic agents (e.g., nanotherapeutics), through the enhanced permeability and retention (EPR) effect, is not uniform (113). Furthermore, the excessive leakage of blood plasma from the abnormal vascular network, in conjunction with the lack of functional lymphatic vessels to maintain fluid balance as well as the increased resistance to interstitial fluid flow owing to low hydraulic conductivity, results in interstitial hypertension (22, 26, 56, 114–117). Young and coworkers (118) reported in 1950 the first measurements of elevated IFP, in tumors growing in rabbits, but the implications of this interstitial hypertension for tumor progression and treatment were not fully revealed until nearly four decades later. In 1988, we showed mathematically and confirmed later with experimental measurements that IFP is uniformly elevated throughout the bulk of a tumor (**Figure 4*b***) with a precipitous drop to normal values in the tumor margin creating a steep pressure

gradient (21). Elevated IFP can compromise the efficacy of therapeutics and facilitate metastasis in multiple ways. First, the uniform elevation of IFP can reach and locally exceed MVP transiently, which, as discussed above, eliminates transvascular and interstitial pressure gradients and, thus, the convective transport of drugs across the vessel wall and in the interior of the tumor (26, 28, 55, 56, 119). Second, the steep pressure gradients in the periphery cause fluid leaking from the blood vessels located in the tumor margin—but not from the vessels in the tumor interior—to ooze into the surrounding normal tissue (1, 27). This oozing fluid would facilitate transport of growth factors and cancer cells into the surrounding tissue, thereby fueling tumor growth, progression, and lymphatic metastasis. It also reduces the retention time of small drugs (<10 nm in diameter) and, thus, inhibits their homogeneous distribution inside the tumor.

### *Mathematical Modeling of Fluid Mechanics of Tumors*

Modeling blood flow in the highly irregular structure of the tumor vasculature is a challenging task. Direct solution of the equations of flow in a three-dimensional vascular network is computationally intensive. For that reason, most studies assume an idealized, one-dimensional blood flow (i.e., axial flow) that follows Poiseuille's equation (24, 28, 120),

$$Q = \frac{\pi R^4}{8\mu_{app}} \frac{\Delta P}{L}, \quad (4)$$

where $R$ is the vessel radius, $\Delta P$ is the pressure difference along a vessel of length $L$, and $\mu_{app}$ is an apparent viscosity that describes the rheological properties of both blood plasma and cells. Empirical equations have been derived that correlate $\mu_{app}$ with the hematocrit (red blood cell concentration) and vessel diameter (Fåhræus–Lindqvist effect) (121). Based on this approach, several methodologies have been developed to model tumor progression taking into account the concentration of oxygen and nutrients, shear forces, cell proliferation and apoptosis, the evolution and remodeling of the tumor vascular network, and other biochemical processes (122–124).

Coupled with Equation 1 is the equation that describes the fluid exchange rate, $Q_{trans}$, between the vascular and interstitial space. This equation is given by Starling's approximation as (22)

$$Q_{trans} = L_p S[P_v - P_i - \sigma(\pi_v - \pi_i)], \quad (5)$$

where $L_p$ is the hydraulic conductivity of the vessel wall; $S$ is the surface area of the vessel; $P_v$ and $P_i$ are the MVP and IFP, respectively; $\pi_v$ and $\pi_i$ are the osmotic pressure in the vascular and interstitial space, respectively; and $\sigma$ is the osmotic reflection coefficient for plasma proteins.

In addition, mathematical models have been developed to study blood rheology taking into account red blood cells and white blood cells, as well as their interactions (125–129). These models provide predictions not only for the fluid flow, but also for the viscosity of the blood and for the deformation and distribution of the cells in the vessel. In other models, remodeling of the vascular network is considered as a function of the shear stress exerted on the endothelial lining of the vessel wall, the vascular pressure, and the metabolic stimuli (e.g., partial oxygen pressure) (130). Vascular remodeling usually involves changes in the structure, diameter, and wall thickness of the vessel, and for low vascular pressures it might also include vessel collapse.

As in every fibrous medium subject to low-Reynolds-number flow, the interstitial fluid velocity, v, can be described by the well-known Darcy's equation as

$$v = -K\nabla P_i \quad (6)$$

or by the Brinkman's equation as

$$\mu\nabla^2 v - \frac{1}{K}v = \nabla P_i, \quad (7)$$

where $K$ is the hydraulic conductivity of the interstitial space, $P_i$ is the IFP, and $\mu$ is the viscosity.

Brinkman's equation can be seen as Darcy's equation with an additional term for viscous stresses in the fluid phase. Both hydraulic conductivity and IFP can severely affect fluid flow in the tumor interstitium.

Several mathematical expressions have been derived to predict the hydraulic conductivity of a fibrous medium. Many of them refer to two-dimensional solutions of low-Reynolds-number flows parallel and transverse to spatially periodic arrays of fibers (131). These expressions relate the hydraulic permeability (i.e., the hydraulic

conductivity multiplied by the viscosity) to the fiber volume fraction and might include more than one family of fibers (132). More recently, mathematical approaches to calculate hydraulic conductivity in three-dimensional fiber structures have been developed. These approaches, apart from the fiber volume fraction, might also account for fiber organization and/or surface charge (91, 133). Caution must be taken, however, when such methods are used to calculate the hydraulic conductivity of tumors. The complex structure of the tumor interstitial space involves heterogeneously distributed fibers with multiple orientations, sizes, and surface charges that cannot be represented directly by the idealized structures of these models. Alternatively, empirical equations that are based on experimental studies exist and provide the hydraulic conductivity of tumors as a function of collagen, proteoglycan, and glycosaminoglycan contents (90, 134).

Finally, the flow rate entering the lymphatic circulation from the interstitial space, $Q_l$, is given by Starling's approximation as (25)

$$Q_l = L_{pl} S_l (P_i - P_l), \quad (8)$$

where $L_{pl}$ is the hydraulic conductivity of the lymphatic wall, $S_l$ is the surface area of the lymphatic vessel, $P_i$ is the IFP, and $P_l$ is the pressure of the lymphatic vessel. As mentioned above, intratumoral lymphatics are dysfunctional, and thus it is common to consider lymphatic flow to be negligible. More detailed approaches for modeling lymphatic drainage and pumping utilizing homogenization or lattice Boltzmann methods exist (135, 136). For example, one group of investigators (136) modeled increases in shear stress to trigger NO emission by the endothelium, which, in turn, caused dilation of the vessel and increased lymph flow, suggesting a direct mechanism of fluid stress control of lymph flow.

## 1.5.Therapeutic strategies

Given the fact that solid and fluid mechanics in tumors are determined mainly by the accumulation of solid stress and the formation of abnormal vessels, we have proposed two types of therapeutic strategies to improve drug delivery and efficacy (1, 18). On one hand, stress-alleviation treatments have the ability to reopen compressed blood vessels and, thus, improve perfusion and drug delivery in hypoperfused tumors (5, 35). On the other hand, vascular normalization strategies aim to decrease the leakiness in hyperpermeable tumors, which is a different mechanism to improve perfusion and delivery of therapeutic agents (1) (**Figure 5**). Which of the two strategies is more beneficial depends on the microenvironment of the tumor and particularly on whether tumor vessels are hyperpermeable, compressed, both, or neither. Use of these two strategies alone or in combination could improve therapeutic outcomes.

### *Stress-Alleviation Treatment*

A stress-alleviation strategy is based on the following sequence of events: alleviate stress levels, re- open compressed tumor blood vessels, improve perfusion, and enhance drug delivery and efficacy, resulting in improved overall survival. Stress reduction also increases the diameter of intratumor lymphatic vessels, but their function is not restored—presumably owing to impaired lymphatic valves in the draining lymphatics (1, 16). Constituents of the tumor microenvironment—other than cancer cells—that contribute to the generation of solid stress include stromal cells and extracellular matrix components (5). Indeed, we have shown that pharmacological depletion of tumor stroma with saridegib, an inhibitor of the sonic hedgehog pathway, alleviates stress levels and increases blood vessel diameter and tumor perfusion without affecting vascular density (**Figure 6*b–e***) (5). In another study, use of saridegib improved chemotherapy in murine pancreatic cancers and the overall survival of the mice (137). In addition, enzymatic degradation of hyaluronan when combined with cytotoxic drugs has been shown to decompress blood vessels and improve tumor perfusion, drug delivery, and the overall survival of mice bearing pancreatic tumors (17, 138). Modification of the extracellular matrix can be also achieved by inhibiting signaling pathways that drive the activation of cancer-associated fibroblasts (139). We have been able to achieve this by inhibiting either the activity of angiotensin II with angiotensin-converting enzyme inhibitors or the signaling of angiotensin II with angiotensin receptor blockers (35). Many of these drugs are widely prescribed as antihypertensive therapies.

Specifically, the clinically approved antihypertensive drug losartan, an angiotensin receptor blocker, reduces collagen and hyaluronan levels in murine tumors (**Figure 6*a***) by decreasing stromal expression of TGF-β as well as other fibrosis- signaling molecules (35). This, in turn, alleviates solid stress levels and improves tumor perfusion as well as the delivery of both chemotherapeutic agents and nanomedicines, thereby increasing the overall survival of mice bearing tumors (35, 140). These findings have led to a clinical trial at Massachusetts General Hospital in patients with advanced pancreatic ductal adenocarcinoma—a uniformly fatal disease with very poor prognosis (see **http://ClinicalTrials.gov**, trial identifier number NCT01821729). Retrospective clinical studies have also shown that treatment with angiotensin receptor blockers and angiotensin-converting enzyme inhibitors may improve survival in patients with pancreatic, lung, and renal cancers (141–143).

### *Vascular Normalization Treatment*

Compromised blood flow rates in tumors are also due to the formation of leaky and tortuous vessels. Therefore, one goal of a therapeutic strategy is to change the phenotype of the abnormal tumor vasculature to a more functional phenotype that resembles the structure of normal vessels. We call this strategy vascular normalization and suggest the use of judicious doses of antiangiogenic therapy to realize this goal (1, 49, 68, 144).

Indeed, vascular normalization remodels the tumor vasculature by increasing pericyte coverage of blood vessels and, thus, decreasing vessel leakiness. As a result, tumor perfusion is increased (**Figure 7*a,b***), and IFP is decreased. Therefore, the pressure difference across the vessel wall is restored (**Figure 7*c***), which, in turn, enhances the extravasation of therapeutic agents (28, 145– 151). A decrease in the size and number of vessel wall openings, however, decreases the maximum size of particles that can pass through the vessel wall. Thus vascular normalization improves the delivery of nanoparticles less than 60 nm in diameter (28) (**Figure 7*d*** ). Furthermore, normalization is dose dependent, and high doses will prune the vessels and reduce perfusion (**Figure 7*a,b***) and drug delivery (1, 149). Also, vascular normalization has a transient effect: When anti-VEGF treatment is continued for a long time, excessive vessel pruning occurs, which again reduces perfusion and drug delivery. This dose and time dependence of vascular normalization results in a normalization window within which drug delivery is improved (1, 49, 68, 152). Clinical studies have verified in humans that antiangiogenic agents can normalize tumor vasculature and that the patients whose tumor blood perfusion increases survive longer (1). Agents that have been used include a monoclonal

antibody (bevacizumab) to block VEGF-A in patients with rectal cancer and an inhibitor of all three VEGF receptor tyrosine kinases (VEGF-1, -2, -3) (cediranib) in patients with recurrent or newly diagnosed glioblastoma (116, 117, 150–154).

### *Guidelines for the Optimal Use of Stress-Based Therapeutic Strategies*

With the use of mathematical modeling, we recently showed that stress-alleviation treatments to decompress vessels and improve perfusion could be effective in poorly or moderately permeable tumors, such as pancreatic and colon cancers, and various sarcomas (18). By contrast, vascular normalization treatment is more effective in hyperpermeable tumors with open vessels, such as a subset of glioblastomas, melanomas, and ovarian carcinomas. These tumors are expected to have low solid-stress levels, with perfusion determined mainly by the permeability of the tumor vasculature. In this case, normalization treatment will decrease permeability and improve perfusion and drug delivery. Finally, if a tumor is hyperpermeable with abundant compressed vessels, as are a subset of mammary carcinomas, the two treatments have to be combined so that stress alleviation will open up the vessels, and vascular normalization will make them less permeable. Identification of which tumors have vasculatures that are leaky, compressed, both, or neither is a challenging task. We can make some general statements, such as pancreatic cancers have compressed vessels, but there are many tumors, such as breast cancers, for which the levels of solid stress and the permeability are highly variable from one tumor to the next and potentially from the primary site to the metastatic site. Thus, it could be hard to choose an appropriate strategy until the state of an individual tumor is known. Existing and/or emerging imaging modalities may be able to help in this selection (150, 151).

## 1.6. Concluding remarks

Our hypothesis is that the abnormal mechanical microenvironment of tumors enables them to be protected from the immune system of the host body, resist anticancer therapies, and coordinate their progression. The tumor mechanical microenvironment is quite different from that of normal tissues and is characterized by accumulation of solid stress, low perfusion rates, and elevation of IFP. To improve treatment, we need to revert tumors from their abnormal path back toward a normal state. This can be achieved with the modification of the tumor microenvironment and modulation of mechanical stresses. We propose two complementary therapeutic strategies: the normalization of the tumor vasculature with judicious doses of anti-VEGF therapy and the normalization of the tumor extravascular space with stress-alleviation therapy. The fact that certain drugs that normalize the tumor microenvironment are already clinically approved and/or are being used in clinical practice for other diseases is encouraging. The scope of the scientific effort should now be to identify new, safe, and well-tolerated drugs that normalize the tumor microenvironment and can be used in a combinatorial treatment with immune, radiation, or chemotherapy (1). Specific guidelines for the optimal use of these therapeutic strategies are essential given the dynamic and highly heterogeneous nature of tumors and the differences between primary tumors and metastases. Importantly, these strategies have to be tailored to individual patients, and techniques, such as imaging methods, must be developed to enable this personalization.

## 1.7. Figures

**Figure 1-1 Schematic of the tumor mechanical microenvironment.**

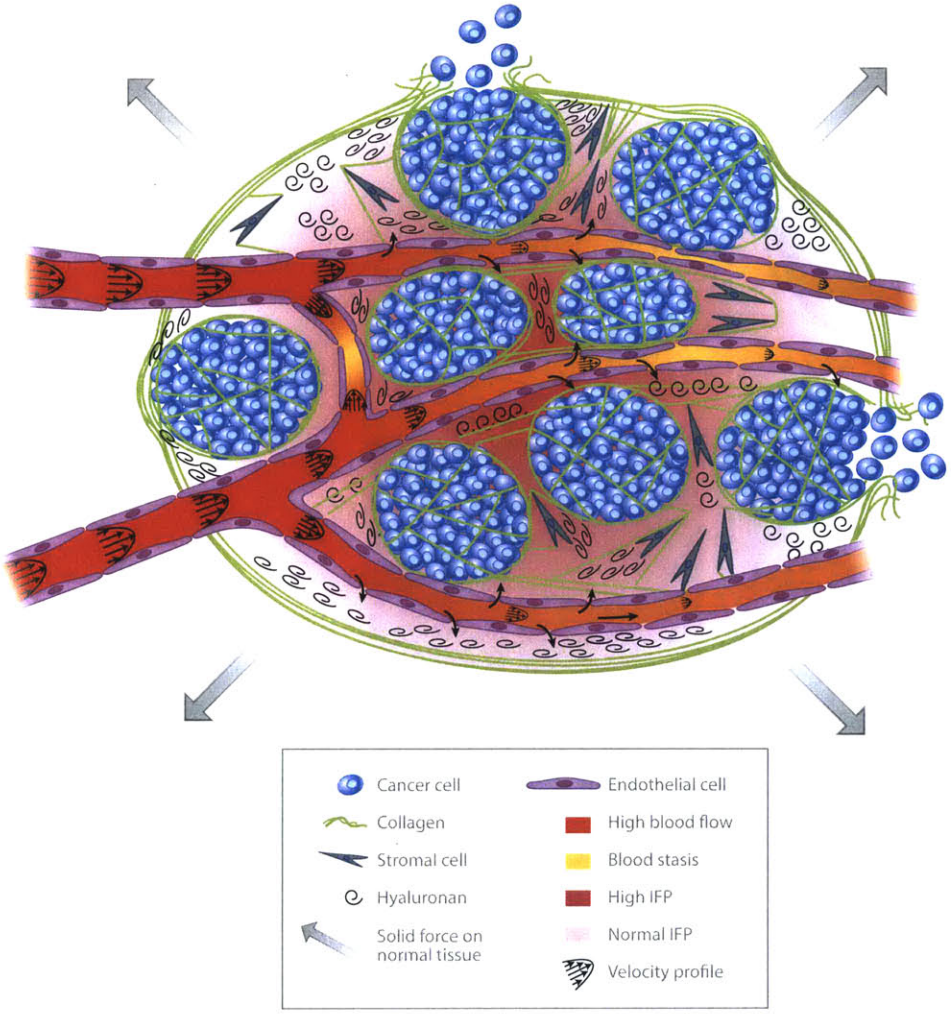


Schematic of the tumor mechanical microenvironment. Cancer cells along with myofibroblasts (stromal cells) stretch collagen fibers and compress hyaluronan, and this interaction stores growth-induced solid stress in all constituents. This stress can compress or even collapse intratumoral vessels, reducing blood flow. The remaining uncompressed vessels are often leaky, resulting in excessive fluid crossing the vessel wall and contributing to elevated interstitial fluid pressure. Vessel leakiness further reduces perfusion and, along with vessel compression, can cause blood stasis. At the macroscopic scale, the tumor pushes against the surrounding normal tissue, which, in turn, restricts tumor expansion. Abbreviation: IFP, interstitial fluid pressure.

**Figure 1-2 Solid stress profile in tumors and evidence of vessel compression.**

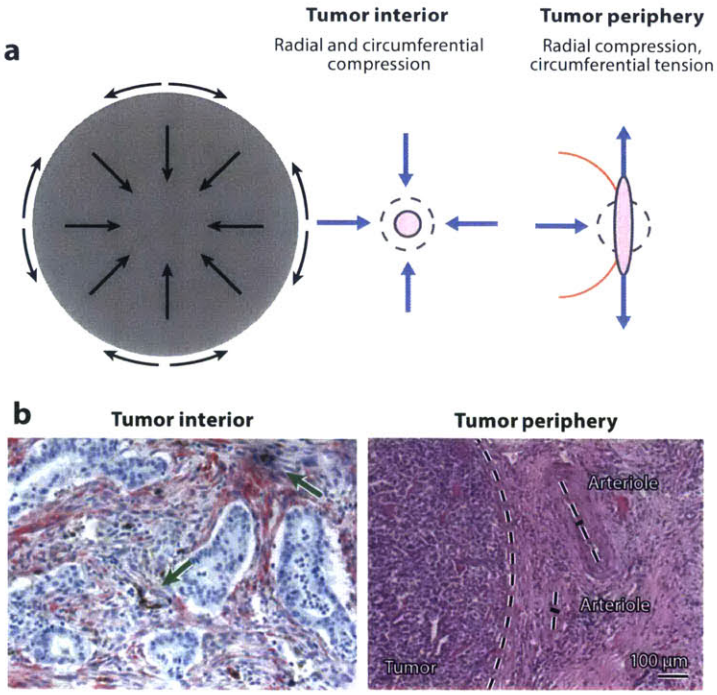


(*a*) Solid stresses are compressive in the interior of the tumor in both the radial and circumferential directions, whereas at the periphery, radial stresses are compressive, and circumferential stresses are tensile. (*b*) Histological sections of human pancreatic tumor. The solid stress profile can collapse intratumor vessels (*left*; *green arrows* show position of collapsed vessels), whereas peripheral vessels obtain elliptical shapes (*right*; *dashed black lines* show tumor margin and the two main axes of the arterioles). (Panels *a* and right-hand side of panel *b* adapted with permission from 6; left-hand side of panel *b* based on personal communication with Dr. Yves Boucher, Massachusetts General Hospital.)

**Figure 1-3 Externally applied and growth-induced solid stresses.**

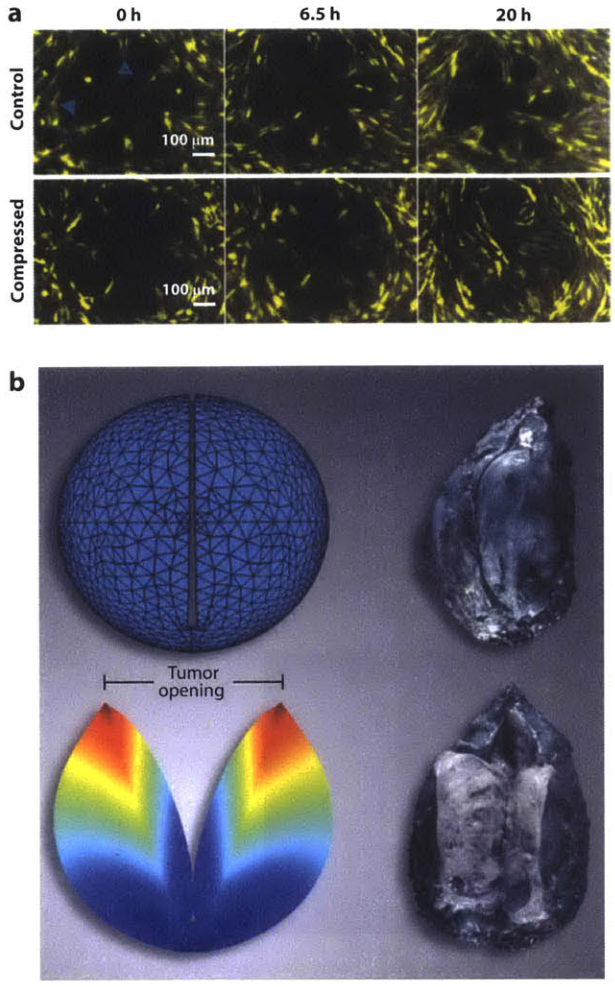


(*a*) Direct cancer cell compression enhances the invasive phenotype of 67NR cells. 67NR monolayers form a rosette shape, the control group is stress free, and the compressed group is subject to 773-Pa compressive stress. Under compressive stress, the 67NR cells move faster toward the center of the rosette, which suggests increased motility and invasiveness. (Panel reproduced with permission from 13.) (*b*) Evidence of growth-induced stress in a soft tissue sarcoma. Cutting an excised tumor along its longest axis (80% of its thickness) causes retraction of the surface and swelling of the interior of the tumor. These deformation modes are caused by relaxation of the growth-induced stress and result in a measurable tumor opening. Thus, even though no external loads are exerted on the excised tumor, the tumor still holds growth-induced, residual stress. Growth-induced stress is estimated with the use of mathematical modeling by simulating the cutting experiment. (Panel reproduced with permission from 5.)

**Figure 1-4 Abnormal fluid flow in tumors.**

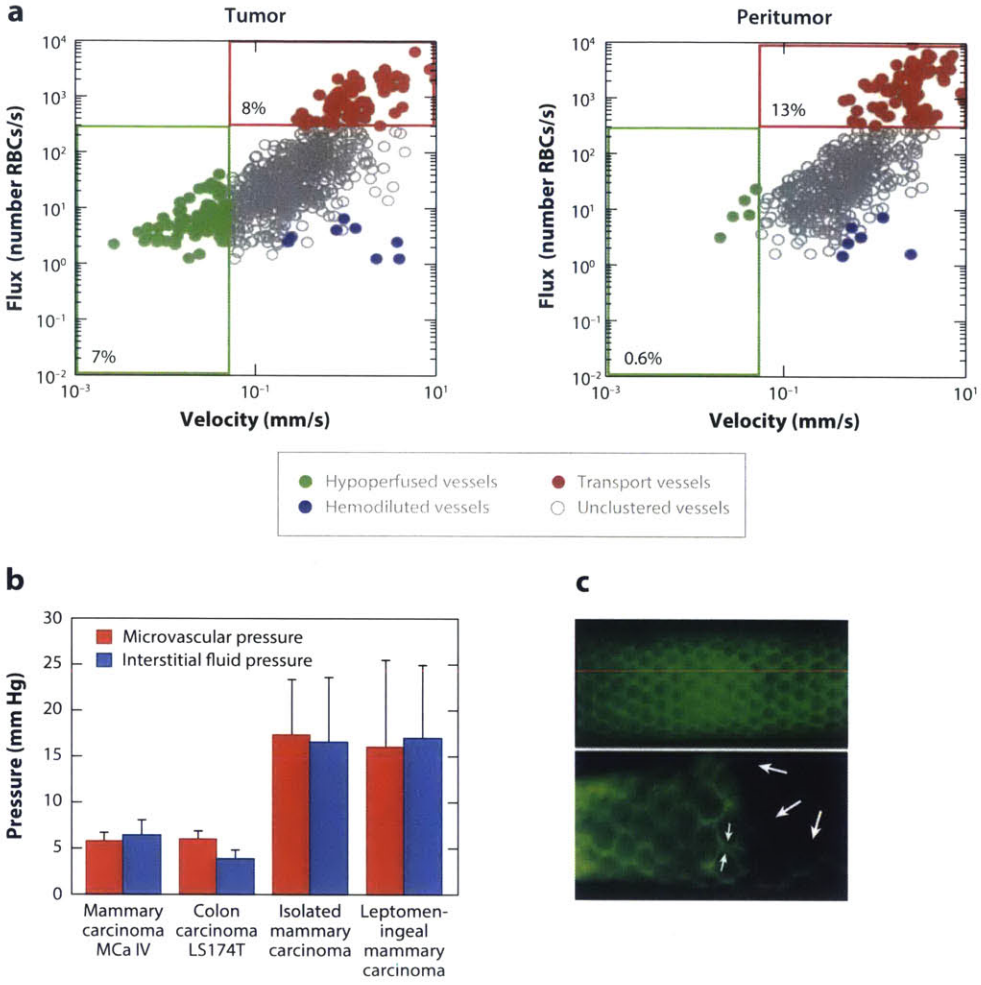


(*a*) Red blood cell (RBC) flux and blood velocity in interior and peripheral vessels of a glioma growing in a mouse brain. A significantly larger proportion of interior vessels are hypoperfused, with velocities of less than 0.1 mm/s, compared with peripheral vessels. (Panel reproduced with permission from 53.) (*b*) Interstitial fluid pressure in tumors is elevated and comparable to microvascular pressure. (Panel adapted with permission from 114). (*c*) Lymphatics are absent from the tumor interior and hyperplastic at the periphery. Fluorescence lymphangiography images of a normal (*top*) and a sarcoma-bearing (*bottom*) mouse tail. At the normal tissue, lymphatics form a functional network ( *green*). At the tumor interior (*right side of bottom panel* ) lymphatics are absent but have a larger diameter at the margin. Large arrows indicate attenuated vessels inside the tumor. Small arrows indicate the increased diameter of the lymphatic capillary at the margin. (Panel reproduced with permission from 97.)

**Figure 1-5 Strategies to improve perfusion and drug delivery in solid tumors.**

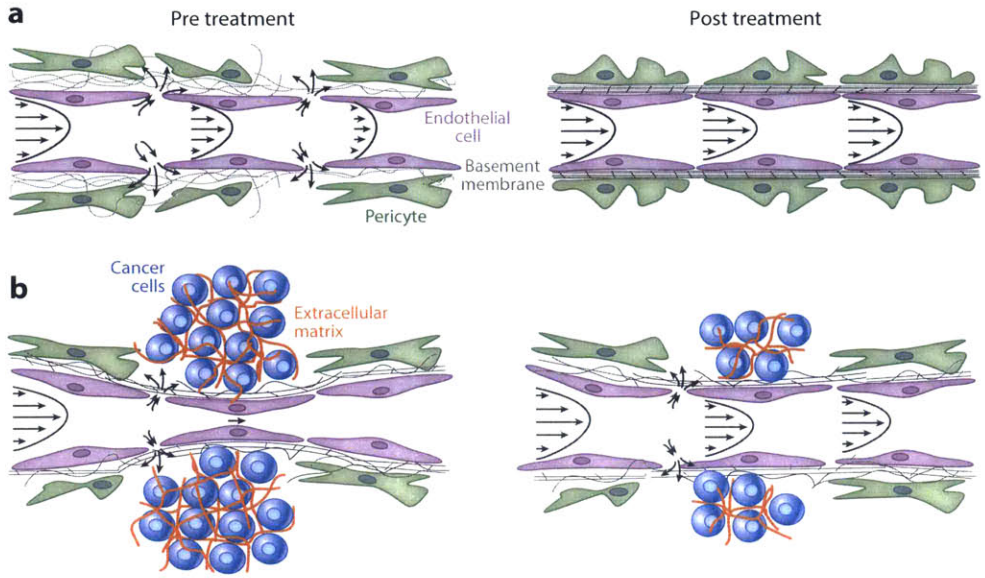


(*a*) Vascular normalization increases pericyte coverage, which decreases vessel permeability and improves perfusion. (*b*) Stress-alleviation treatment depletes structural components of the tumor microenvironment, which decompresses tumor blood vessels and improves perfusion. Improved perfusion rates increase the delivery of drugs. These strategies can be used either alone or in combination based on whether tumor blood vessels are leaky, compressed, both, or neither. (Figure adapted with permission from 18.)

**Figure 1-6 Stress-alleviation treatment.**

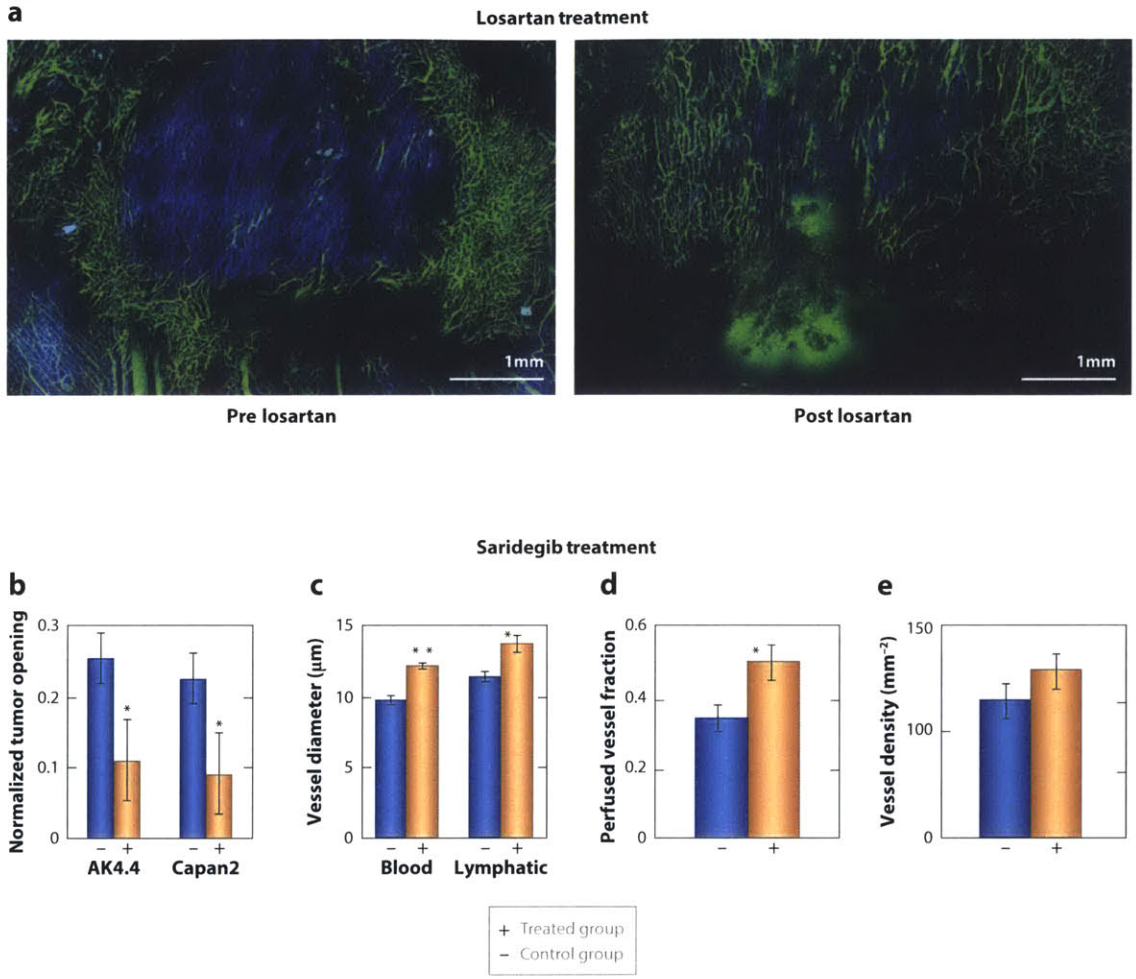


(a) Intravital multiphoton microscopy images show that treatment with the angiotensin receptor blocker losartan lowers collagen levels (blue) and increases the density of perfused vessels ( green) in an orthotopic mammary adenocarcinoma (E0771). (Panel reproduced with permission from 35.) Treatment with the sonic hedgehog inhibitor saridegib (b) reduces solid stress levels, measured as a function of tumor opening (see Figure 3b), in two pancreatic ductal adenocarcinomas (AK4.4 and Capan2) and (c) increases blood and lymphatic vessel diameter as well as (d ) the fraction of perfused vessels, (e) without affecting vascular density. Asterisks represent a statistically significant difference between the control group (−) and the saridegib-treated group (+) (∗$p < 0.05$, ∗∗$p < 0.01$). (Panels b–e reproduced with permission from 5.)

**Figure 1-7 Vascular normalization treatment with the monoclonal antibody DC101.**

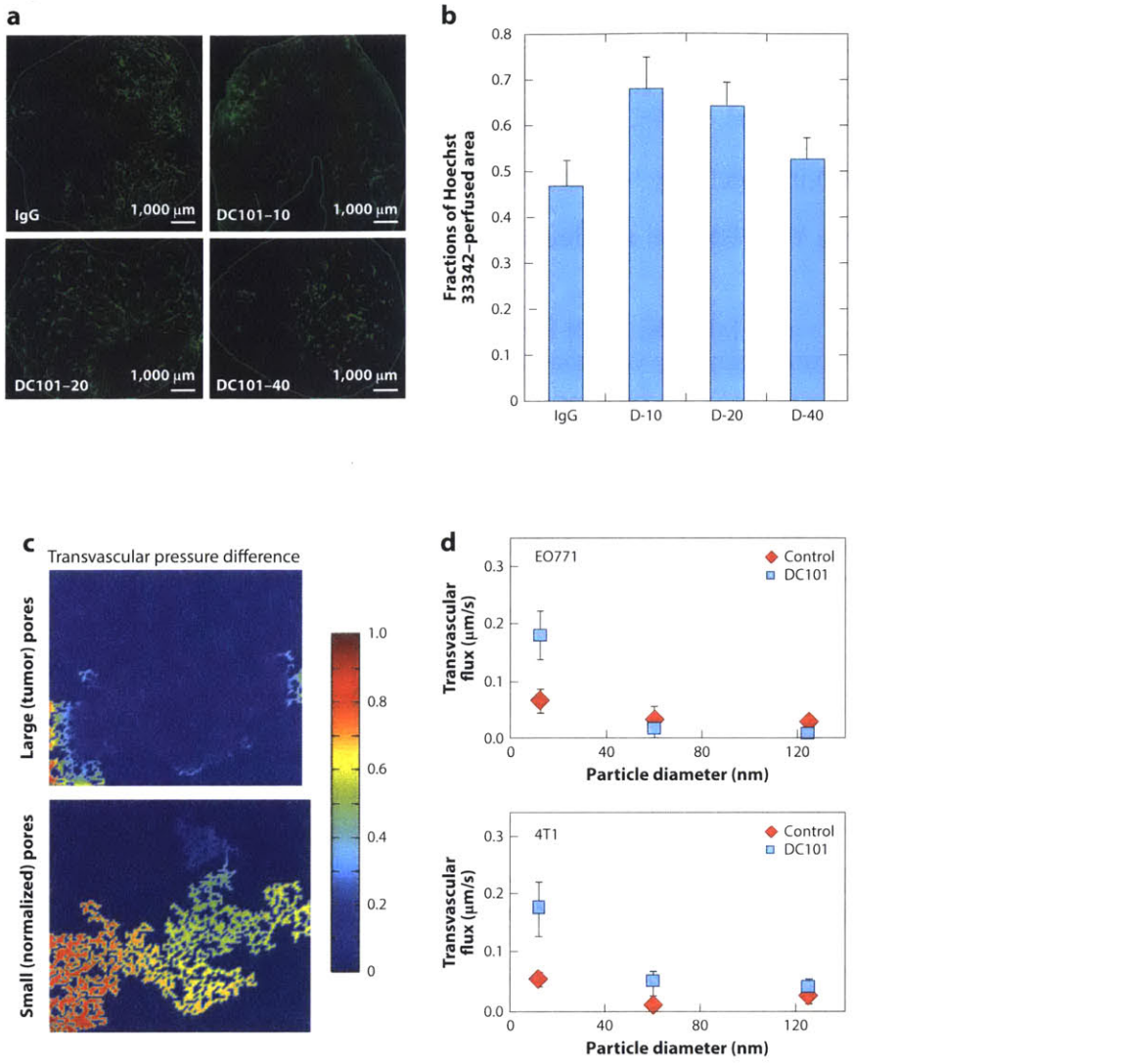


Normalization of tumor vessels improves tumor perfusion in a dose-dependent manner. (*a*) Perfusion images of whole-tumor tissue taken by multispectral confocal microscopy. Animals were treated with IgG (control) and 10, 20, or 40 mg of DC101 per kilogram of body weight ( *green*: Sytox staining). (*b*) Quantification of fractions of Hoechst 33342–positive area in the whole-tumor area presents perfused regions of the tumors shown in panel *a* for the control (IgG) and the three DC101 doses (D-10, D-20, and D-40). (*c*) Model predictions for the effect of vessel wall pore size on the pressure difference across the tumor vessel wall. Pressure is made dimensionless by division with the inlet vasculature pressure. A decrease in vessel wall pore size with vascular normalization restores a transvascular pressure difference. (*d* ) Normalization of tumor vasculature and the resulting increase in transvascular pressure difference improve flux of nanoparticles across the tumor vessel wall in a size-dependent manner in two orthotopic mammary adenocarcinomas (E0771 and 4T1). Abbreviation: IgG, immunoglobulin G. (Panel *a* adapted from and panel *b* reproduced with permission from 149; panels *c* and *d* reproduced with permission from 28.)

## 1.8. References


1. Jain RK. 2013. Normalizing tumor microenvironment to treat cancer: bench to bedside to biomarkers. *J. Clin. Oncol.* 31:2205–18

2. Jain RK. 2014. An indirect way to tame cancer. *Sci. Am.* 310:46–53

3. Chuong CJ, Fung YC. 1986. On residual stresses in arteries. *J. Biomech. Eng.* 108:189–92

4. Skalak R, Zargaryan S, Jain RK, Netti PA, Hoger A. 1996. Compatibility and the genesis of residual stress by volumetric growth. *J. Math. Biol.* 34:889–914

5. Stylianopoulos T, Martin JD, Chauhan VP, Jain SR, Diop-Frimpong B, et al. 2012. Causes, consequences, and remedies for growth-induced solid stress in murine and human tumors. *Proc. Natl. Acad. Sci. USA* 109:15101–8

6. Stylianopoulos T, Martin JD, Snuderl M, Mpekris F, Jain SR, Jain RK. 2013. Coevolution of solid stress and interstitial fluid pressure in tumors during progression: implications for vascular collapse. *Cancer Res.* 73:3833–41

7. Helmlinger G, Netti PA, Lichtenbeld HC, Melder RJ, Jain RK. 1997. Solid stress inhibits the growth of multicellular tumor spheroids. *Nat. Biotechnol.* 15:778–83

8. Tomasek JJ, Gabbiani G, Hinz B, Chaponnier C, Brown RA. 2002. Myofibroblasts and mechano- regulation of connective tissue remodelling. *Nat. Rev. Mol. Cell Biol.* 3:349–63

9. Paszek MJ, Weaver VM. 2004. The tension mounts: Mechanics meets morphogenesis and malignancy. *J. Mammary Gland Biol. Neoplasia* 9:325–42

10. Wipff PJ, Hinz B. 2009. Myofibroblasts work best under stress. *J. Bodyw. Mov. Ther.* 13:121–27

11. Cheng G, Tse J, Jain RK, Munn LL. 2009. Micro-environmental mechanical stress controls tumor spheroid size and morphology by suppressing proliferation and inducing apoptosis in cancer cells. *PLoS ONE* 4:e4632

12. DemouZN.2010.Geneexpressionprofilesin3Dtumoranalogsindicatecompressivest raindifferentially enhances metastatic potential. *Ann. Biomed. Eng.* 38:3509–20

13. Tse JM, Cheng G, Tyrrell JA, Wilcox-Adelman SA, Boucher Y, et al. 2012. Mechanical compression drives cancer cells toward invasive phenotype. *Proc. Natl. Acad. Sci. USA* 109:911–16

14. Helmlinger G, Yuan F, Dellian M, Jain RK. 1997. Interstitial pH and $pO_2$ gradients in solid tumors in vivo: High-resolution measurements reveal a lack of correlation. *Nat. Med.* 3:177–82

15. Griffon-Etienne G, Boucher Y, Brekken C, Suit HD, Jain RK. 1999. Taxane-induced apoptosis decompresses blood vessels and lowers interstitial fluid pressure in solid tumors: clinical implications. *Cancer Res.* 59:3776–82

16. Padera TP, Stoll BR, Tooredman JB, Capen D, di Tomaso E, Jain RK. 2004.

Pathology: Cancer cells compress intratumour vessels. *Nature* 427:695

17. Provenzano PP, Cuevas C, Chang AE, Goel VK, Von Hoff DD, Hingorani SR. 2012. Enzymatic targeting of the stroma ablates physical barriers to treatment of pancreatic ductal adenocarcinoma. *Cancer Cell* 21:418–29

18. Stylianopoulos T, Jain RK. 2013. Combining two strategies to improve perfusion and drug delivery in solid tumors. *Proc. Natl. Acad. Sci. USA* 110:18632–37

19. Koumoutsakos P, Pivkin I, Milde F. 2013. The fluid mechanics of cancer and its therapy. *Annu. Rev. Fluid Mech.* 45:325–55

20. Jain RK. 1988. Determinants of tumor blood flow: a review. *Cancer Res.* 48:2641–58

21. Jain RK, Baxter LT. 1988. Mechanisms of heterogeneous distribution of monoclonal antibodies and other macromolecules in tumors: significance of elevated interstitial pressure. *Cancer Res.* 48:7022–32

22. Baxter LT, Jain RK. 1989. Transport of fluid and macromolecules in tumors. I. Role of interstitial pressure and convection. *Microvasc. Res.* 37:77–104

23. Netti PA, Roberge S, Boucher Y, Baxter LT, Jain RK. 1996. Effect of transvascular fluid exchange on pressure–flow relationship in tumors: a proposed mechanism for tumor blood flow heterogeneity. *Microvasc. Res.* 52:27–46

24. Baish JW, Netti PA, Jain RK. 1997. Transmural coupling of fluid flow in microcirculatory network and interstitium in tumors. *Microvasc. Res.* 53:128–41

25. Baxter LT, Jain RK. 1990. Transport of fluid and macromolecules in tumors. II. Role of heterogeneous perfusion and lymphatics. *Microvasc. Res.* 40:246–63

26. Boucher Y, Baxter LT,Jain RK. 1990. Interstitial pressure gradients in tissue-isolated and subcutaneous tumors: implications for therapy. *Cancer Res.* 50:4478–84

27. Jain RK, Tong RT, Munn LL. 2007. Effect of vascular normalization by antiangiogenic therapy on interstitial hypertension, peritumor edema, and lymphatic metastasis: insights from a mathematical model. *Cancer Res.* 67:2729–35

28. Chauhan VP, Stylianopoulos T, Martin JD, Popovic Z, Chen O, et al. 2012. Normalization of tumour blood vessels improves the delivery of nanomedicines in a size-dependent manner. *Nat. Nanotechnol.* 7:383–88

29. Hagendoorn J, Tong R, Fukumura D, Lin Q, Lobo J, et al. 2006. Onset of abnormal blood and lymphatic vessel function and interstitial hypertension in early stages of carcinogenesis. *Cancer Res.* 66:3360–64

30. Kaufman LJ, Brangwynne CP, Kasza KE, Filippidi E, Gordon VD, et al. 2005. Glioma expansion in collagen I matrices: analyzing collagen concentration-dependent growth and motility patterns. *Biophys. J.* 89:635–50

31. Koike C, McKee TD, Pluen A, Ramanujan S, Burton K, et al. 2002. Solid stress facilitates spheroid formation: potential involvement of hyaluronan. *Br. J.*

*Cancer* 86:947–53

32. Rivron NC, Vrij EJ, Rouwkema J, Le Gac S, Van den Berg A, et al. 2012. Tissue deformation spatially modulates VEGF signaling and angiogenesis. *Proc. Natl. Acad. Sci. USA* 109:6886–91

33. Roose T, Netti PA, Munn LL, Boucher Y, Jain RK. 2003. Solid stress generated by spheroid growth estimated using a linear poroelasticity model. *Microvasc. Res.* 66:204–12

34. Sarntinoranont M, Rooney F, Ferrari M. 2003. Interstitial stress and fluid pressure within a growing tumor. *Ann. Biomed. Eng.* 31:327–35

35. Chauhan VP, Martin JD, Liu H, Lacorre DA, Jain SR, et al. 2013. Angiotensin inhibition enhances drug delivery and potentiates chemotherapy by decompressing tumor blood vessels. *Nat. Commun.* 4:2516

36. Branton MH, Kopp JB. 1999. TGF-β and fibrosis. *Microbes Infect.* 1:1349–65

37. Butcher DT, Alliston T, Weaver VM. 2009. A tense situation: forcing tumour progression. *Nat. Rev. Cancer* 9:108–22

38. Egeblad M, Rasch MG, Weaver VM. 2010. Dynamic interplay between the collagen scaffold and tumor evolution. *Curr. Opin. Cell Biol.* 22:697–706

39. Paszek MJ, Zahir N, Johnson KR, Lakins JN, Rozenberg GI, etal. 2005. Tensional homeostasis andthe malignant phenotype. *Cancer Cell* 8:241–54

40. Samuel MS, Lopez JI, McGhee EJ, Croft DR, Strachan D, et al. 2011. Actomyosin-mediated cellular tension drives increased tissue stiffness and beta-catenin activation to induce epidermal hyperplasia and tumor growth. *Cancer Cell* 19:776–91

41. Friedland JC, Lee MH, Boettiger D. 2009. Mechanically activated integrin switch controls $\alpha 5\beta 1$ function. *Science* 323:642–44

42. Levental KR, Yu H, Kass L, Lakins JN, Egeblad M, et al. 2009. Matrix crosslinking forces tumor progression by enhancing integrin signaling. *Cell* 139:891–906

43. Wipff PJ, Rifkin DB, Meister JJ, Hinz B. 2007. Myofibroblast contraction activates latent TGF-β1from the extracellular matrix. *J. Cell Biol.* 179:1311–23

44. Karagiannis GS, Poutahidis T, Erdman SE, Kirsch R, Riddell RH, Diamandis EP. 2012. Cancer- associated fibroblasts drive the progression of metastasis through both paracrine and mechanical pressure on cancer tissue. *Mol. Cancer Res.* 10:1403–18

45. Potenta S, Zeisberg E, Kalluri R. 2008. The role of endothelial-to-mesenchymal transition in cancer progression. *Br. J. Cancer* 99:1375–79

46. Kalluri R, Weinberg RA. 2009. The basics of epithelial-mesenchymal transition. *J. Clin. Investig.* 119:1420–28

47. Huang Y, Goel S, Duda DG, Fukumura D, Jain RK. 2013. Vascular normalization as an emerging strategy to enhance cancer immunotherapy. *Cancer Res.*

73:2943–48

48. Facciabene A, Peng X, Hagemann IS, Balint K, Barchetti A, et al. 2011. Tumour hypoxia promotes tolerance and angiogenesis via CCL28 and $T_{reg}$ cells. *Nature* 475:226–30

49. Goel S, Duda DG, Xu L, Munn LL, Boucher Y, et al. 2011. Normalization of the vasculature for treatment of cancer and other diseases. *Physiol. Rev.* 91:1071–121

50. Wilson WR, Hay MP. 2011. Targeting hypoxia in cancer therapy. *Nat. Rev. Cancer* 11:393–410

51. Carmeliet P, Jain RK. 2011. Molecular mechanisms and clinical applications of angiogenesis. *Nature* 473:298–307

52. Pries AR, Hopfner M, Le Noble F, Dewhirst MW, Secomb TW. 2010. The shunt problem: control of functional shunting in normal and tumour vasculature. *Nat. Rev. Cancer* 10:587–93

53. Kamoun WS, Chae SS, Lacorre DA, Tyrrell JA, Mitre M, et al. 2010. Simultaneous measurement of RBC velocity, flux, hematocrit and shear rate in vascular networks. *Nat. Methods* 7:655–60

54. Baish JW, Stylianopoulos T, Lanning RM, Kamoun WS, Fukumura D, et al. 2011. Scaling rules for diffusive drug delivery in tumor and normal tissues. *Proc. Natl. Acad. Sci. USA* 108:1799–803

55. Boucher Y, Kirkwood JM, Opacic D, Desantis M, Jain RK. 1991. Interstitial hypertension in superficial metastatic melanomas in humans. *Cancer Res.* 51:6691–94

56. Less JR, Posner MC, Boucher Y, Borochovitz D, Wolmark N, Jain RK. 1992. Interstitial hypertension in human breast and colorectal tumors. *Cancer Res.* 52:6371–74

57. Ambrosi D, Mollica F. 2002. On the mechanics of a growing tumor. *Int. J. Eng. Sci.* 40:1297–316

58. Ambrosi D, Preziosi L. 2009. Cell adhesion mechanisms and stress relaxation in the mechanics of tumours. *Biomech. Model. Mechanobiol.* 8:397–413

59. MacLaurin J, Chapman J, Jones GW, Roose T. 2012. The buckling of capillaries in solid tumours. *Proc. R. Soc. A* 468:4123–45

60. Ciarletta P. 2013. Buckling instability in growing tumor spheroids. *Phys. Rev. Lett.* 110:158102

61. Byrne H, Preziosi L. 2003. Modelling solid tumour growth using the theory of mixtures. *Math. Med. Biol.* 20:341–66

62. Stylianopoulos T, Barocas VH. 2007. Multiscale, structure-based modeling for the elastic mechanical behavior of arterial walls. *J. Biomech. Eng.* 129:611–18

63. Sander E, Stylianopoulos T, Tranquillo R, Barocas V. 2009. Image-based

biomechanics of collagen- based tissue equivalents. *IEEE Eng. Med. Biol. Mag.* 28:10–18

64. Chauhan VP, Stylianopoulos T, Boucher Y, Jain RK. 2011. Delivery of molecular and nanomedicine to tumors: transport barriers and strategies. *Annu. Rev. Chem. Biomol. Eng.* 2:281–98

65. Sevick EM, Jain RK. 1989. Geometric resistance to blood flow in solid tumors perfused ex vivo: effects of tumor size and perfusion pressure. *Cancer Res.* 49:3506–12

66. Sevick EM, Jain RK. 1989. Viscous resistance to blood flow in solid tumors: effect of hematocrit on intratumor blood viscosity. *Cancer Res.* 49:3513–19

67. Carmeliet P, Jain RK. 2000. Angiogenesis in cancer and other diseases. *Nature* 407:249–57

68. Jain RK. 2005. Normalization of tumor vasculature: an emerging concept in antiangiogenic therapy. *Science* 307:58–62

69. Leunig M, Yuan F, Menger MD, Boucher Y, Goetz AE, et al. 1992. Angiogenesis, microvascular architecture, microhemodynamics, and interstitial fluid pressure during early growth of human adenocarcinoma LS174T in SCID mice. *Cancer Res.* 52:6553–60

70. Vakoc BJ, Lanning RM, Tyrrell JA, Padera TP,Bartlett LA, et al. 2009.Three-dimensionalmicroscopy of the tumor microenvironment in vivo using optical frequency domain imaging. *Nat. Med.* 15:1219–23

71. Jain RK. 1987. Transport of molecules across tumor vasculature. *Cancer Metastasis Rev.* 6:559–93

72. Hobbs SK, Monsky WL, Yuan F, Roberts WG, Griffith L, et al. 1998. Regulation of transport pathways in tumor vessels: role of tumor type and microenvironment. *Proc. Natl. Acad. Sci. USA* 95:4607–12

73. Hashizume H, Baluk P, Morikawa S, McLean JW, Thurston G, et al. 2000. Openings between defective endothelial cells explain tumor vessel leakiness. *Am. J. Pathol.* 156:1363–80

74. Less JR, Posner MC, Skalak TC, Wolmark N, Jain RK. 1997. Geometric resistance and microvascular network architecture of human colorectal carcinoma. *Microcirculation* 4:25–33

75. Sun C, Jain RK, Munn LL. 2007. Non-uniform plasma leakage affects local hematocrit and blood flow: implications for inflammation and tumor perfusion. *Ann. Biomed. Eng.* 35:2121–29

76. Yuan F, Salehi HA, Boucher Y, Vasthare US, Tuma RF, Jain RK. 1994. Vascular permeability and microcirculation of gliomas and mammary carcinomas transplanted in rat and mouse cranial windows. *Cancer Res.* 54:4564–68

77. Wirtz D, Konstantopoulos K, Searson PC. 2011. The physics of cancer: the role of physical interactions and mechanical forces in metastasis. *Nat. Rev. Cancer* 11:512–22

78. Tarbell JM, Weinbaum S, Kamm RD. 2005. Cellular fluid mechanics and mechanotransduction. *Ann. Biomed. Eng.* 33:1719–23

79. Song JW, Munn LL. 2011. Fluid forces control endothelial sprouting. *Proc. Natl. Acad. Sci. USA* 108:15342–47

80. Djonov VG, Kurz H, Burri PH. 2002. Optimality in the developing vascular system: branching remodeling by means of intussusception as an efficient adaptation mechanism. *Dev. Dyn.* 224:391–402

81. Kamiya A, Ando J, Shibata M, Masuda H. 1988. Roles of fluid shear stress in physiological regulation of vascular structure and function. *Biorheology* 25:271–78

82. Nagy JA, Dvorak AM, Dvorak HF. 2012. Vascular hyperpermeability, angiogenesis, and stroma generation. *Cold Spring Harb. Perspect. Med.* 2:a006544

83. Kalluri R, Zeisberg M. 2006. Fibroblasts in cancer. *Nat. Rev. Cancer* 6:392–401

84. Chary SR, Jain RK. 1989. Direct measurement of interstitial convection and diffusion of albumin in normal and neoplastic tissues by fluorescence photobleaching. *Proc. Natl. Acad. Sci. USA* 86:5385–89

85. Pedersen JA, Lichter S, Swartz MA. 2010. Cells in 3D matrices under interstitial flow: effects of extracellular matrix alignment on cell shear stress and drag forces. *J. Biomech.* 43:900–5

86. Ng CP, Hinz B, Swartz MA. 2005. Interstitial fluid flow induces myofibroblast differentiation and collagen alignment in vitro. *J. Cell Sci.* 118:4731–39

87. Swartz MA, Lund AW. 2012. Lymphatic and interstitial flow in the tumour microenvironment: linking mechanobiology with immunity. *Nat. Rev. Cancer* 12:210–19

88. Avvisato CL, Yang X, Shah S, Hoxter B, Li W, et al. 2007. Mechanical force modulates global gene expression and β-catenin signaling in colon cancer cells. *J. Cell Sci.* 120:2672–82

89. Shieh AC. 2011. Biomechanical forces shape the tumor microenvironment. *Ann. Biomed. Eng.* 39:1379– 89

90. Levick JR. 1987. Flow through interstitium and other fibrous matrices. *Q. J. Exp. Physiol.* 72:409–37

91. Stylianopoulos T, Yeckel A, Derby JJ, Luo XJ, Shephard MS, et al. 2008. Permeability calculations in three-dimensional isotropic and oriented fiber networks. *Phys. Fluids* 20:123601

92. Netti PA, Berk DA, Swartz MA, Grodzinsky AJ, Jain RK. 2000. Role of extracellular matrix assembly in interstitial transport in solid tumors. *Cancer Res.* 60:2497–503

93. Huijbers IJ, Iravani M, Popov S, Robertson D, Al-Sarraj S, et al. 2010. A role for fibrillar collagen deposition and the collagen internalization receptor endo180 in glioma invasion. *PLoS ONE* 5:e9808

94. Mok W, Boucher Y, Jain RK. 2007. Matrix metalloproteinases-1 and -8 improve the distribution and efficacy of an oncolytic virus. *Cancer Res.* 67:10664–68

95. Clayes IL, Brady JF. 1993. Suspensions of prolate spheroids in Stokes flow. Part 2. Statistically homogeneous dispersions. *J. Fluid Mech.* 251:443–77

96. Stylianopoulos T, Diop-Frimpong B, Munn LL, Jain RK. 2010. Diffusion anisotropy in collagen gels and tumors: the effect of fiber network orientation. *Biophys. J.* 99:3119–28

97. Leu AJ, Berk DA, Lymboussaki A, Alitalo K, Jain RK. 2000. Absence of functional lymphatics within a murine sarcoma: a molecular and functional evaluation. *Cancer Res.* 60:4324–27

98. Padera TP, Kadambi A, diTomaso E, Carreira CM, Brown EB, et al. 2002. Lymphatic metastasis in the absence of functional intratumor lymphatics. *Science* 296:1883–86

99. Isaka N, Padera TP, Hagendoorn J, Fukumura D, Jain RK. 2004. Peritumor lymphatics induced by vascular endothelial growth factor-C exhibit abnormal function. *Cancer Res.* 64:4400–4

100. Hoshida T, Isaka N, Hagendoorn J, di Tomaso E, Chen YL, et al. 2006. Imaging steps of lymphatic metastasis reveals that vascular endothelial growth factor-C increases metastasis by increasing delivery of cancer cells to lymph nodes: therapeutic implications. *Cancer Res.* 66:8065–75

101. Jeltsch M, Kaipainen A, Joukov V, Meng X, Lakso M, et al. 1997. Hyperplasia of lymphatic vessels in VEGF-C transgenic mice. *Science* 276:1423–25

102. Alitalo K, Tammela T, Petrova TV. 2005. Lymphangiogenesis in development and human disease. *Nature* 438:946–53

103. Berk DA, Swartz MA, Leu AJ, Jain RK. 1996. Transport in lymphatic capillaries. II. Microscopicvelocity measurement with fluorescence photobleaching. *Am. J. Physiol.* 270:H330–37

104. Fischer M, Franzeck UK, Herrig I, Costanzo U, Wen S, et al. 1996. Flow velocity of single lymphatic capillaries in human skin. *Am. J. Physiol.* 270:H358–63

105. Swartz MA, Berk DA, Jain RK. 1996. Transport in lymphatic capillaries. I. Macroscopic measurements using residence time distribution theory. *Am. J. Physiol.* 270:H324–29

106. Hagendoorn J, Padera TP, Kashiwagi S, Isaka N, Noda F, et al. 2004. Endothelial nitric oxide synthase regulates microlymphatic flow via collecting lymphatics. *Circ. Res.* 95:204–9

107. Gasheva OY, Zawieja DC, Gashev AA. 2006. Contraction-initiated NO-dependent lymphatic relaxation: a self-regulatory mechanism in rat thoracic duct. *J. Physiol.* 575:821–32

108. Kajiya K, Huggenberger R, Drinnenberg I, Ma B, Detmar M. 2008. Nitric oxide mediates lymphatic vessel activation via soluble guanylate cyclase $\alpha 1\beta 1$-impact on inflammation. *FASEB J.* 22:530–37

109. Liao S, Cheng G, Conner DA, Huang Y, Kucherlapati RS, et al. 2011. Impaired lymphatic contraction associated with immunosuppression. *Proc. Natl. Acad. Sci. USA* 108:18784–89

110. Kesler CT, Liao S, Munn LL, Padera TP. 2013. Lymphatic vessels in health and disease.*WileyInterdiscip. Rev. Syst. Biol. Med.* 5:111–24

111. Ng CP, Helm CL, Swartz MA. 2004. Interstitial flow differentially stimulates blood and lymphatic endothelial cell morphogenesis in vitro. *Microvasc. Res.* 68:258–64

112. Miteva DO, Rutkowski JM, Dixon JB, Kilarski W, Shields JD, Swartz MA. 2010. Transmural flow modulates cell and fluid transport functions of lymphatic endothelium. *Circ. Res.* 106:920–31

113. Yuan F, Leunig M, Huang SK, Berk DA, Papahadjopoulos D, Jain RK. 1994. Microvascular permeability and interstitial penetration of sterically stabilized (stealth) liposomes in a human tumor xenograft. *Cancer Res.* 54:3352–56

114. Boucher Y, Jain RK. 1992. Microvascular pressure is the principal driving force for interstitial hypertension in solid tumors: implications for vascular collapse. *Cancer Res.* 52:5110–14

115. Nathanson SD, Nelson L. 1994. Interstitial fluid pressure in breast cancer, benign breast conditions, and breast parenchyma. *Ann. Surg. Oncol.* 1:333–38

116. Willett CG, Boucher Y, diTomaso E, Duda DG, Munn LL, et al. 2004. Direct evidence that the VEGF- specific antibody bevacizumab has antivascular effects in human rectal cancer. *Nat. Med.* 10:145–47

117. Willett CG, Duda DG, di Tomaso E, Boucher Y, Ancukiewicz M, et al. 2009. Efficacy, safety, and biomarkers of neoadjuvant bevacizumab, radiation therapy, and fluorouracil in rectal cancer: a multidisciplinary Phase II study. *J. Clin. Oncol.* 27:3020–26

118. Young JS, Lumsden CE, Stalker AL. 1950. The significance of the "tissue pressure" of normal testicular and of neoplastic (Brown-Pearce carcinoma) tissue in the rabbit. *J. Pathol. Bacteriol.* 62:313–33

119. Stylianopoulos T, Soteriou K, Fukumura D, Jain RK. 2013. Cationic nanoparticles have superior transvascular flux into solid tumors: insights from a mathematical model. *Ann. Biomed. Eng.* 41(1):68–77

120. Pozrikidis C, Farrow DA. 2003. A model of fluid flow in solid tumors. *Ann. Biomed. Eng.* 31:181–94

121. Pries AR, Secomb TW, Gaehtgens P, Gross JF. 1990. Blood flow in microvascular networks: experiments and simulation. *Circ. Res.* 67:826–34

122. Welter M, Bartha K, Rieger H. 2008. Emergent vascular network inhomogeneities and resulting blood flow patterns in a growing tumor. *J. Theor. Biol.* 250:257–80

123. Cai Y, Xu S, Wu J, Long Q. 2011. Coupled modelling of tumour angiogenesis, tumour growth and blood perfusion. *J. Theor. Biol.* 279:90–101

124. Wu M, Frieboes HB, McDougall SR, Chaplain MA, Cristini V, Lowengrub J. 2012. The effect of interstitial pressure on tumor growth: coupling with blood and lymphatic vascular systems. *J. Theor. Biol.* 320:131–51

125. Pozrikidis C. 2005. Axisymmetric motion of a file of red blood cells through capillaries. *Phys. Fluids* 17:1–14

126. Sun C, Munn LL. 2005. Particulate nature of blood determines macroscopic rheology: a 2-D lattice Boltzmann analysis. *Biophys. J.* 88:1635–45

127. Dupin MM, Halliday I, Care CM, Alboul L, Munn LL. 2007. Modeling the flow of dense suspensions of deformable particles in three dimensions. *Phys. Rev. E* 75:066707

128. Pivkin IV, Karniadakis GE. 2008. Accurate coarse-grained modeling of red blood cells. *Phys. Rev. Lett.* 101:118105

129. Li X, Vlahovska PM, Karniadakis GE. 2013. Continuum- and particle-based modeling of shapes and dynamics of red blood cells in health and disease. *Soft Matter* 9:28–37

130. Pries AR, Cornelissen AJ, Sloot AA, Hinkeldey M, Dreher MR, et al. 2009. Structural adaptation and heterogeneity of normal and tumor microvascular networks. *PLoS Comput. Biol.* 5:e1000394

131. Jackson GW, James DF. 1986. The permeability of fibrous porous media. *Can.J.Chem.Eng.*64:364–74

132. Ethier R. 1994. Flow through mixed fibrous porous materials. *AIChE J.* 37:1227–36

133. Mattern KJ, Nakornchai C, Deen WM. 2008. Darcy permeability of agarose-glycosaminoglycan gels analyzed using fiber-mixture and Donnan models. *Biophys. J.* 95:648–56

134. Jain RK. 1987. Transport of molecules in the tumor interstitium: a review. *Cancer Res.* 47:3039–51

135. Roose T, Swartz MA. 2012. Multiscale modeling of lymphatic drainage from tissues using homogenization theory. *J. Biomech.* 45:107–15

136. Kunert C, Padera TP, Munn LL. 2012. *Lattice Boltzmann simulations of lymphatic pumping*. Presented at Am. Phys. Soc. (APS), Mar. Meet., Feb. 27–Mar. 2 (Abstr. #D42.002)

137. Olive KP, Jacobetz MA, Davidson CJ, Gopinathan A, McIntyre D, et al. 2009. Inhibition of Hedgehog signaling enhances delivery of chemotherapy in a mouse model of pancreatic cancer. *Science* 324:1457–61

138. Jacobetz MA, Chan DS, Neesse A, Bapiro TE, Cook N, et al. 2012. Hyaluronan impairs vascular function and drug delivery in a mouse model of pancreatic cancer. *Gut* 62:112–20

139. Liu J, Liao S, Diop-Frimpong B, Chen W, Goel S, et al. 2012. TGF-βblockadeimprovesthedistribution and efficacy of therapeutics in breast carcinoma by normalizing the tumor stroma. *Proc. Natl. Acad. Sci. USA*

109:16618–23

140. Diop-Frimpong B, Chauhan VP, Krane S, Boucher Y, Jain RK. 2011. Losartan inhibits collagen I synthesis and improves the distribution and efficacy of nanotherapeutics in tumors. *Proc. Natl. Acad. Sci. USA* 108:2909–14

141. Nakai Y, Isayama H, Ijichi H, Sasaki T, Sasahira N, et al. 2010. Inhibition of renin-angiotensin system affects prognosis of advanced pancreatic cancer receiving gemcitabine. *Br. J. Cancer* 103:1644–48

142. Wilop S, Von Hobe S, Crysandt M, Esser A, Osieka R, Jost E. 2009. Impact of angiotensin I converting enzyme inhibitors and angiotensin II type 1 receptor blockers on survival in patients with advanced non- small-cell lung cancer undergoing first-line platinum-based chemotherapy. *J. Cancer Res. Clin. Oncol.* 135:1429–35

143. Keizman D, Huang P, Eisenberger MA, Pili R, Kim JJ, et al. 2011. Angiotensin system inhibitors and outcome of sunitinib treatment in patients with metastatic renal cell carcinoma: a retrospective examination. *Eur. J. Cancer* 47:1955–61

144. Jain RK. 2001. Normalizing tumor vasculature with anti-angiogenic therapy: a new paradigm for combination therapy. *Nat. Med.* 7:987–89

145. Lee CG, Heijn M, diTomaso E, Griffon-Etienne G, Ancukiewicz M, et al. 2000. Anti-vascular endothelial growth factor treatment augments tumor radiation response under normoxic or hypoxic conditions. *Cancer Res.* 60:5565–70

146. Izumi Y, Xu L, di Tomaso E, Fukumura D, Jain RK. 2002. Tumour biology: Herceptin acts as an anti-angiogenic cocktail. *Nature* 416:279–80

147. Wildiers H, Guetens G, De Boeck G, Verbeken E, Landuyt B, et al. 2003. Effect of antivascular endothelial growth factor treatment on the intratumoral uptake of CPT-11. *Br. J. Cancer* 88:1979–86

148. Tong RT, Boucher Y, Kozin SV, Winkler F, Hicklin DJ, Jain RK. 2004. Vascular normalization by vascular endothelial growth factor receptor 2 blockade induces a pressure gradient across the vasculature and improves drug penetration in tumors. *Cancer Res.* 64:3731–36

149. Huang Y, Yuan J, Righi E, Kamoun WS, Ancukiewicz M, et al. 2012. Vascular normalizing doses of antiangiogenic treatment reprogram the immunosuppressive tumor microenvironment and enhance immunotherapy. *Proc. Natl. Acad. Sci. USA* 109:17561–66

150. Emblem KE, Mouridsen K, Bjornerud A, Farrar C, Jennings D, et al. 2013. Vessel architectural imaging identifies cancer patient responders to anti-angiogenic therapy. *Nat. Med.* 19:1178–83

151. Batchelor TT, Gerstner ER, Emblem KE, Duda DG, Kalpathy-Cramer J, et al. 2013. Improved tumor oxygenation and survival in glioblastoma patients who show increased blood perfusion after cediranib and chemoradiation. *Proc. Natl. Acad. Sci. USA* 110:19059–64

152. Batchelor TT, Sorensen AG, diTomaso E, Zhang WT, Duda DG, et al. 2007.

AZD2171, a pan-VEGF receptor tyrosine kinase inhibitor, normalizes tumor vasculature and alleviates edema in glioblastoma patients. *Cancer Cell* 11:83–95

153. Sorensen AG, Batchelor TT, Zhang WT, Chen PJ, Yeo P, et al. 2009. A "vascular normalization index" as potential mechanistic biomarker to predict survival after a single dose of cediranib in recurrent glioblastoma patients. *Cancer Res.* 69:5296–300

154. Sorensen AG, Emblem KE, Polaskova P, Jennings D, Kim H, et al. 2012. Increased survival of glioblastoma patients who respond to anti-angiogenic therapy with elevated blood perfusion. *Cancer Res.* 72:402–7

# Appendix

### Deformation gradient tensor

The deformation gradient tensors maps from one tangent space to another. It indicates how a body is deforming locally going from one state to another. It is a second order tensor.

If X is the position of a given material element in a tumor and x is the position of the same element after the tumor tissue grows and deforms, then the motion of the body can be defined as

$$x = \aleph(X, t)$$

and the deformation gradient tensor is

$$F = \frac{\partial \aleph}{\partial X}$$

Note that in our model the tissue is fixed so there is no translation or velocity. Thus, the product of the deformation gradient tensors, $F$, can be interpreted as the total deformation gradient tensor. This tensor can undergo factorization of matrices into a product of matrices. In this way, we can account for deformations material elements of tumor tissue will undergo resulting from individual sources (i.e. growth of the tumor tissue, confinement by surrounding tissue, and evolution of growth-induced stress). Decomposition of deformation gradient tensors is commonly used to account for various parts of deformations (e.g. elastic versus plastic deformations within a single body).

We can experimentally measure $F$ and we can assume a growth contribution based on experimental observations, phenomenological expressions, or by relating growth to the availability of oxygen and nutrients. Thus, the practical purpose of this decomposition of deformation gradient tensors is to isolate the elastic deformation component. The elastic deformation component is necessary for the constitutive relationship that relates strain to stress. In our study, we assumed tumor tissue to behave as a hyperelastic neo-Hookean material.

$$W = 0.5(\mu(-3 + \mathrm{II}_1) + \kappa(-1 + J_e)^{-2})$$

Where $\mu$ and $\kappa$ are the shear and bulk modulus of the tumor tissue, respectively. $J_e$ is the determinant of the elastic deformation gradient $F_e$. $\mathrm{II}_1 = \mathrm{I}_1 J_e^{-2/3}$, where $\mathrm{I}_1$ is the first invariant of the right Cauchy-Green deformation tensor.

Knowing the elastic deformation component allows the Cauchy stress tensor to be calculated from this elastic strain.

$$\sigma = J_e^{-1} F_e \frac{\partial W}{\partial F_e^T}$$

# *Chapter 2 Growth-induced solid stress in murine and human tumors: Causes, consequences an remedies*

Some of the work, text and figures presented in this chapter are adapted from reference under the permissions of the journal:

Stylianopoulos T*, Martin JD*, Chauhan VP, Jain SR, Diop-Frimpong B, et al. 2012. Causes, consequences, and remedies for growth-induced solid stress in murine and human tumors. *Proc. Natl. Acad. Sci. USA* 109:15101–8

[1]These authors contributed equally to this work.

## 2.1. Abstract

The presence of growth-induced solid stresses in tumors has been suspected for some time, but these stresses were largely estimated using mathematical models. Solid stresses can deform the surrounding tissues and compress intratumoral lymphatic and blood vessels. Compression of lymphatic vessels elevates interstitial fluid pressure, while compression of blood vessels reduces blood flow. Reduced blood flow, in turn, leads to hypoxia, which promotes tumor progression, immunosuppression, inflammation, invasion and metastasis, and lowers the efficacy of chemo-, radio- and immunotherapies. Thus, strategies designed to alleviate solid stress have the potential to improve cancer treatment. However, a lack of methods for measuring solid stress has hindered the development of solid stress-alleviating drugs. Here we present a simple technique to estimate the growth-induced solid stress accumulated within animal and human tumors, and demonstrate that this stress can be reduced by depleting cancer cells, fibroblasts, collagen, and/or hyaluronan resulting in improved tumor perfusion. Furthermore, we show that therapeutic depletion of carcinoma-associated fibroblasts with an inhibitor of the sonic hedgehog pathway reduces solid stress, decompresses blood and lymphatic vessels and increases perfusion. In addition to providing new insights into the mechanopathology of tumors, our approach can serve as a rapid *in vivo* screen for stress-reducing and perfusion-enhancing drugs.

## 2.2. Introduction

Elevated interstitial fluid pressure (IFP) and solid stress are hallmarks of the mechanical microenvironment of solid tumors (1). IFP is the isotropic stress (i.e., applied equally in all directions) exerted by the fluid, while solid stress is exerted by the non-fluid components. In 1950, Young and co-workers provided the first measurements of IFP in tumors growing in rabbits and found it to be elevated compared to IFP in normal testicular tissue (2). However, the implications of this interstitial hypertension for tumor progression and treatment were not fully revealed for nearly four decades. In 1988, we developed a mathematical model that showed IFP is uniformly elevated throughout the bulk of a tumor and precipitously drops to normal values in the tumor margin causing a steep pressure gradient (3, 4). Based on the model's results, we predicted that diffusion rather than convection would be the dominant mode of transport within tumors, because of nearly uniform pressure within the tumor. Furthermore, we predicted that the steep pressure gradients in the periphery would cause fluid leaking from the blood vessels located in the tumor margin – but not from the vessels in the tumor interior - to "ooze" into the surrounding normal tissue. This oozing fluid would facilitate transport of growth factors and cancer cells into the surrounding tissue – fueling tumor growth, progression and lymphatic metastasis. In subsequent years, we confirmed these predictions about IFP experimentally both in animal models and human tumors (5-15). Moreover, we revealed the key mechanisms leading to the elevated IFP – high vascular permeability coupled with mechanical compression of downstream blood vessels and draining lymphatic vessels (16-18). We also posited that the high vascular permeability would cause flow stasis in tumor vessels further compromising drug delivery (19, 20).

Realizing the adverse consequences of abnormal function of tumor vessels, we proposed that the judicious application of antiangiogenic agents would normalize tumor vessels and improve their function. Specifically, the decreased vascular permeability would decrease IFP and increase blood flow in previously static blood vessels, thereby increasing drug delivery and treatment efficacy of a number of therapies (1, 21, 22). We and others have provided compelling evidence in support of this therapeutic strategy in both animal and human tumors (14, 22-27). More crucially, we have shown that the extent of vascular normalization and the resulting increase in tumor blood perfusion correlate with increased survival of brain tumor patients receiving antiangiogenic therapy (28, 29). Understanding the causes and consequences of vessel leakiness and elevated IFP enabled us to find a clinically translatable strategy to improve the treatment

outcome (22). However, vascular normalization by antiangiogenic agents can only improve the function of vessels that have an open lumen and are not compressed by solid stress. Thus, a better understanding of the solid stress present in tumors is needed to develop new therapies and the further improve treatment outcome.

In contrast to the elevated IFP, much less is known about the causes, consequences and remedies for solid stresses in tumors. It is assumed that solid stress is accumulated within tumors as the proliferating cancer cells strain nearby structural elements of tumor and normal tissues. Some of the stress within the tumor is contributed by reciprocal forces from the surrounding normal tissue; the rest is stored within cells and matrix components of the tumor, and thus persists after the tumor is excised and external loads are removed. This stored stress is referred to as "growth-induced solid" or "residual" stress (30). By compressing blood and lymphatic vessels and creating hypoxia and interstitial hypertension, these solid stresses contribute to tumor progression and resistance to various treatments (1).

Because there were no simple techniques available to measure solid stresses in tumors *in vivo*, initially, we relied on *in vitro* studies and mathematical models. In 1997, we provided the first estimates of the magnitude of solid stresses in tumor spheroids, which represent an avascular phase of a tumor (31). We found that an external stress applied to a tumor spheroid inhibits tumor growth by decreasing proliferation and increasing apoptosis. In addition, the external stress field determines the shape of the spheroid. Using material properties of tumor tissue measured independently, we estimated the maximum magnitude of the solid stress to be in the range of 45 to 120 mmHg (6 to 16 kPa). In 2009, we provided a more accurate measurement of the growth-induced stress and found it to be 28 mmHg (3.7 kPa) (32). More recently, we have shown that the mechanical stress can also directly increase cancer cell invasion, aiding tumor progression (33).

Given the importance of solid stresses in tumor progression and treatment and lack of any *in vivo* data, we developed a mathematical model for solid stress based on our previous model for IFP. The model predicted a uniform compressive circumferential stress at the center of the tumor and tensile circumferential stress at the periphery (34). Moreover, the magnitude of the calculated compressive stress - comparable to that measured in spheroids (31, 32) - was large enough to compress vessels and nearby organs, obstruct large blood vessels with life threatening consequences, or induce pain by pressing on nerves (18). By performing *in vivo* experiments, we confirmed that cancer

cells could compress and collapse their own blood and lymphatic vessels, and destroying cancer cells around vessels could indeed reopen them (17, 18). However, whether other components of solid tumors contribute to the compressive stresses and how these can be alleviated was not understood.

To this end, we develop here a new technique to measure growth-induced solid stress in freshly excised human and animal tumors, and investigate the effects of this stress on blood and lymphatic vessels. This technique involves measuring the extent of tissue relaxation after removing all external stresses and using these data to calculate the growth-induced solid stress by employing a mathematical model. We use this simple technique to demonstrate that solid stress is elevated in a range of murine and human tumors. Then, we employ our technique to identify key components of tumors – cancer cells, stromal cells, collagen and hyaluronan – that contribute to the generation and accumulation of growth-induced solid stress in tumors. Finally, we demonstrate that therapeutic depletion of carcinoma-associated fibroblasts (CAFs) with an inhibitor of the sonic hedgehog pathway reduces solid stress, decompresses vessels and increases perfusion.

## 2.3. Results

### Mathematical modeling guides development of our experimental technique

Growth-induced solid stress is extensively characterized in arterial, cardiac and brain tissues (35-37). These tissues can be excised in such a way to retain growth-induced stress; a subsequent cut of the excised tissue then releases the stress, and the tissue deforms in a measurable way. Using the material properties characterizing tissue stiffness, mathematical models can be used to calculate the stress from the measured deformations. We hypothesized that tumor-growth must strain solid components within the tumor, storing growth-induced stress. This stress is distinct from the solid stress that might be exerted on the tumor by the confining normal tissue's resistance to the tumor's expansion.

Acknowledging that tumors might be more fragile than these normal tissues, we set out to find the best way to make similar cuts to measure deformation and estimate growth-induced stresses in excised tumors. Using a computational model (details in Supplement) we explored various modes of cutting and predicted the resulting deformations (Figure 1). Cutting spheroids into hemispheres resulted in perpendicular swelling that was too small to measure in a clinical setting (Figure 1A). Making a cut through an excised slab of tumor tissue produced measurable deformations (Figure 1B). However, this proved inconsistent in practice, as the process of excising the slab often released the growth-induced stress before the final cut could be made. In another simulation the model predicted that a partial cut through the center of the tumor (80% of the diameter) would result in a measurable deformation (Figure 1C). The mode of deformation involves simultaneous swelling at the center and retraction at the boundary. These deformations arise from the model's assumption of compressive radial and circumferential stress in the center balanced by tensile circumferential stress at the boundary (34, 38) (Figure 1D & E). The release of this stress results in a significant gap, or an "opening," at the location of the cut. Rigorous sensitivity analysis of the model (Supplementary Figures 1-6) confirmed that this approach was robust.

### Estimation of growth-induced stress in transplanted and human tumors

To demonstrate that elevated growth-induced stress is a hallmark of solid tumors, we estimated growth-induced stress levels in tumors formed from nine different cancer cell lines implanted orthotopically in mice. We cut the tumors and measured the stress

relaxation as the extent of "tumor opening" normalized to the diameter of the tumor (Figure 2A-C, Supplementary Figure 7, and Supplementary Movie 1). Further cuts of the relaxed halves did not result in appreciable shape changes. The experimental deformations confirmed the main assumption of the model – stress in the tumor interior is compressive and it is balanced by tensile circumferential stress at the periphery (Figure 1E).

Calculation of growth-induced stress requires not only on the extent of relaxation (normalized opening), but also the material properties of the tissue that characterize its stiffness. Thus, quantitative assessment of growth-induced stress requires material properties of each tumor analyzed. To calculate growth-induced stress, the experimentally measured tumor openings (Figure 2C), were combined with previously-measured or estimated material properties of tumor tissue (Supplementary Table 1) and our mathematical model (details in the Supplement). From the material properties presented in Supplementary Table 1, the stiffness is related to the shear modulus, $\mu$. Note that even though the U87 tumor exhibits similar extent of relaxation to the other tumor types, it has much higher stress because it is considerably stiffer than the other three tumors whose stiffness we measured previously (Supplementary Table 1). It is possible that other tumors may be stiffer than these tumors. Model predictions established that the compressive growth-induced stress in the interior of murine tumors ranged from 2.8 to 60.1 mmHg (0.37 - 8.01 kPa) (Supplementary Table 2). This is consistent with previous estimates of compressive stress in multi-cellular tumor spheroids *in vitro,* which fall in the range 28 - 120 mmHg (3.7 - 16.0 kPa) (31, 32).

Interestingly, the tumors with the highest stress exhibit the slowest growth rate (Supplementary Table 2). Additionally, the extent of relaxation increased linearly with tumor volume before reaching a plateau, but did not correlate with tumor density (mass per unit volume), which remained constant as volume increased (Supplementary Figure 8). These results demonstrate that growth-induced stress accumulates with growth and this stress is independent of tumor density. Using the same procedure, we confirmed that the kidneys (Supplementary Movie 2) of mice did not open measurably. These results support our hypothesis that growth-induced stress is elevated in tumors compared to normal, non-contractile organs.

After validating the existence of growth-induced solid stress in murine tumors, we tested whether growth-induced stress was similarly elevated in human specimens. We performed tumor relaxation measurements in ten malignant, freshly excised human

tumors. All deformed similarly to the transplanted murine tumors (Figure 2B & D, Supplementary Figure 9). Assuming a conservative estimate for the material properties of the human tumors (i.e., to provide upper bounds for the stresses), the calculated stresses ranged from 16.4 to 142.4 mmHg (2.2 - 19.0 kPa, Supplementary Table 4). Therefore, human tumors accumulate growth-induced stress similar to those in our mouse models. After confirming that growth-induced solid stress is a general feature of solid tumors, we sought to identify tumor components that contribute to the generation and accumulation of stress.

**Solid stress is not affected by interstitial fluid pressure**

Collapsed lymphatic and blood vessels are known to contribute to elevated interstitial fluid pressure (IFP) in tumors and not the other way around (9, 17, 18, 31). Therefore, we hypothesized that solid stress would not be affected by IFP. To this end, we developed a methodology that measures solid stress, independent of fluid pressure. Other techniques, such as piezoelectric probes (39), measure a combination of solid stress and fluid pressure, making interpretation of results difficult. Indeed, measurements in the normal pancreas *in situ* using a piezoelectric probe were significantly higher that those obtained by the wick-in-needle technique - an established technique to measure interstitial fluid pressure (Supplementary Table 3). Furthermore, the piezoelectric probe reported higher values in the pancreas *in situ* versus exteriorized pancreas, suggesting that stress from the surrounding organs in the abdomen contributes to these measurements. Using the wick-in-needle technique we further confirmed that growth-induced solid stress, which is solely contained within – and transmitted by – solid structural components, is not affected by the IFP (Supplementary Figure 10).

**Cancer and stromal cells generate growth-induced solid stress**

Because cancer cells are known to compress vessels (17, 18), we hypothesized that they contribute to the accumulation of growth-induced stress. Proliferating cancer cells exert force on other cells and surrounding structures; the force on nearby components causes them to deform, resulting in accumulation of solid stress.

Since depletion of cancer cells likely changes the material properties in addition to stresses, determination of growth induced stress levels before and after depletion requires knowledge of the corresponding material properties. However, our original goal was to develop an easy-to-implement and simple method to determine whether

stress levels change after a stress-alleviating intervention. We recognized that, if two tumors shared the same stress level, a stiffer tumor would have less relaxation than a compliant one. Thus, if after depletion of cancer cells, compliant (i.e. treated) tumors open less than the more stiff control tumors, then we can conclude that cancer cell depletion reduces stress. The same principle applies to any other intervention that results in a reduction of stiffness.

To test this hypothesis, we depleted cancer cells and measured relaxation. In mice with orthotopic (human melanoma Mu89) or ectopic (human glioma U87) tumors (Figure 3A and Supplementary Figure 11) we injected diphtheria toxin i.v. 24 hrs before tumor excision. We have shown previously that this treatment kills only human cells (18). Depletion of cancer cells in Mu89 and U87 tumors reduced the tumor opening by 40% and 30%, respectively ($p=0.001$ for Mu89, $p=0.026$ for U87; Student's t-test). These results demonstrate that cancer cells contribute to the generation of growth-induced stress.

Stromal cells, as they proliferate and contract to remodel the extracellular matrix (40), also apply forces on other tumor components. We therefore hypothesized that depleting fibroblasts would reduce growth-induced solid stress. To test this, we co-implanted human breast CAFs with murine mammary adenocarcinoma cells in the mammary fat pad of female SCID mice, using a method developed previously (41). To kill the human CAFs we injected mice with diphtheria toxin. Tumors in which the CAFs were depleted had reduced relaxation and less human vimentin staining – a marker used to identify human CAFs (Figure 3A & B and Supplementary Figure 12). Since CAFs contribute to accumulation of growth-induced stress like cancer cells, we hypothesized that they compress vessels, as cancer cells do (17, 18). Indeed, we found that CAF-depleted tumors had larger mean vessel diameters (Figure 3C), suggesting that depleting CAFs can improve perfusion in desmoplastic tumors.

**Extracellular matrix contributes to growth-induced solid stress**

Another prime candidate for accumulation of growth-induced stress is the extracellular matrix, which is composed of collagen, proteoglycans and glycosaminoglycans (42-44). We hypothesized that collagen fibers contribute to growth-induced stress by virtue of the ability of these fibers to resist stretching, thereby confining the proliferating cells. Collagen fibers are also remodeled and pulled by fibroblasts (40, 45). Collagen resists tensile stress, because it becomes stiffer as it is stretched. This is true for both capsular (if present) and interstitial collagen, as the extracellular matrix in tumors is extensively

cross-linked. Since our model and experiments have shown that tumors are in tension in the periphery and compression in the interior, we expect that peripheral collagen stores more stress than interior collagen. To assess the role of collagen in stress accumulation, we incubated the excised tumors in collagenase or serum (control arm) long enough for the enzymes to radially diffuse one-sixth of the tumors' radii and measured stress levels. We found that the tumor opening decreased with collagenase incubation in three orthotopic models (Mu89, E0771 and 4T1) and one ectopic model (U87) (Figures 3D & E and Supplementary Figure 11).

In contrast to collagen, hyaluronan resists compression. Its negatively charged chains repel due to electrostatic repulsion and trap water forming a poorly-compressible matrix. Consequently, we reasoned that, for storing growth-induced stress, hyaluronan in the compressed tumor interior would be more important than hyaluronan in the tumor periphery, which is under tension. To test this, we first incubated tumors in hyaluronidase as we did with collagenase. Digesting peripheral hyaluronan had no effect on relaxation. However, when we administered hyaluronidase systemically, we found the tumor relaxation to be reduced in two orthotopic models (Figure 3F). Indeed, hyaluronidase treatment has recently been shown to decompress intratumor vessels (39). Therefore, collagen and hyaluronan store growth-induced stress through their ability to resist tensile and compressive stresses, respectively.

**Therapeutic depletion of CAFs reduces solid stress and increases tumor perfusion**

CAFs contribute to the production of collagen and both of these tumor components contribute to the accumulation of solid stress. Thus, we hypothesized that therapeutic agents that deplete CAFs would alleviate solid stress and decompress vessels. The sonic hedgehog (SHH) pathway is involved in the generation of the desmoplastic response in pancreatic and other tumors (46). Moreover, depletion of desmoplasia by targeting this pathway in pancreatic tumors combined with gemcitabine has been shown to enhance survival in mice (47). To this end, we inhibited the proliferation of CAFs in highly desmoplastic, hypo-vascular pancreatic tumors with saridegib (IPI-926), which targets and blocks the Smoothened receptor and SHH signaling (Figure 4). Indeed, saridegib treatment reduced growth-induced stress (Figure 4C) and opened compressed vessels (Figures 4A, and B). Specifically, saridegib treatment led to a 10% increase in diameter of both blood and lymphatic vessels (Figure 4D) and a 47% increase in the fraction of perfused blood vessels (Figure 4E). One reason that a small change in vessel diameter can lead to a large change in perfused vessel fraction is that decompressing one vessel

can re-perfuse several downstream vessels. Since the vessel density did not increase significantly (Figure 4F), our work suggests that increased angiogenesis is not required to increase perfusion in hypo-perfused tumors. Instead, reducing solid stress can increase the number of *functional* vessels and this increase in *functional* vascular density can lead to increased perfusion, which could enhance drug delivery (48). This mechanism can also explain in part the connection between drug delivery and collagen content reported previously by our lab (49-52).

## 2.4. Discussion

The presence of growth-induced solid stress in tumors had been suspected, but these stresses had to be estimated using theoretical or computational models (30, 34). Here we presented a simple technique to determine the growth-induced solid stress accumulated within a freshly excised tumor and demonstrated that this stress could be reduced by depleting cancer cells, fibroblasts, collagen, and/or hyaluronan (Figure 5). Based on our results, solid stress likely develops in two ways in tumors. First, cells generate force during proliferation and contraction. This force is stored as deformations within other cells and the extracellular matrix. The matrix is cross-linked to itself in a microstructure and links to cells directly through cell-matrix and indirectly through cell-cell interactions. Second, as cells within tumors proliferate and create new solid material – cells and matrix fibers – the accumulated material pushes against the surrounding tumor microenvironment. The expansion of the tumor microenvironment is resisted by the surrounding macroenvironment of the normal organ. Since cancer cells proliferate uncontrollably, ignoring contact inhibition signals to stop replicating, their expansion imposes elastic strain on the surrounding tumor microenvironment, storing stress through the deformation of compliant structures and collapsing more fragile structures such as blood and lymphatic vessels. This solid stress is accumulated within the tumor, and is maintained even after the tumor is excised. It is this growth-induced or "residual" solid stress, rather than the stress caused by mechanical interactions with the surrounding macroenvironment of the normal organ, that our technique estimates.

Using this technique, we demonstrated that growth-induced solid stress mediates vessel compression. Compression of vessels by the tumor itself raises an interesting paradox: since tumors need functional blood vessels to supply oxygen and nutrients why do tumors compress their own vessels? Our hypothesis is that the vessel compression – a hallmark of all solid tumors – could be a mechanism that cancer cells exploit to evade the host's immune response. Immune cells circulate in our body via blood vessels and thus, vessel compression may reduce their access. Although many immune cells still infiltrate the tumor, hypoxia and acidity – resulting from impaired perfusion – can attenuate their killing potential (53). Hypoxia also has the potential to convert resident macrophages into pro-tumorigenic cells. In addition, growth factors produced in response to hypoxia (e.g., TGFb, VEGF) suppress the activity of macrophages and lymphocytes, block the maturation of dendritic cells that process tumor antigens and present to the immune cells (22). Furthermore, a harsh hypoxic and acidic

microenvironment imposes a survival advantage for more malignant cancer cells, harbors the so called "cancer initiating cells", confers resistance to cell death by apoptosis and autophagy, and enhances the invasive and metastatic potential of cancer cells (54). Finally, hypoxia lowers the efficacy of radiation, chemotherapy and immunotherapy (22, 55).

The compression of vessels also creates two potential barriers to drug delivery. First, the collapse of blood vessels hinders access of systemically administered drugs (56). This might explain, in part, the fact that tumors with more extracellular matrix might be more resistant to treatment. For instance, pancreatic ductal adenocarcinomas, chondrosarcomas and chordomas are rich in extracellular matrix and refractory to chemotherapy (39, 47, 57). Second, the lack of lymphatic vessel function reduces drainage leading to uniformly elevated IFP (3, 4). As a result, the transport of large therapeutics like antibodies and nanoparticles is reduced, because the dominant mechanism of transport becomes diffusion, which is a very slow process for large particles and macromolecules (58).

It is possible that depleting the extracellular matrix in order to alleviate solid stress and decompress vessels could make it easier for the cancer cells to metastasize by either invading the surrounding tissue or escaping through the blood vessels. Similarly, digesting the matrix to open intratumoral vessels and improve blood flow might promote tumor growth by delivering more nutrients to cancer cells. These concerns need further study, but several observations suggest that therapies able to ease solid stress and improve perfusion and delivery of drugs counteract any pro-tumor effects (29, 39, 47).

The deformation induced by solid stress is inversely proportional to the tissue stiffness. Indeed, increased tumor tissue stiffness has been linked to tumor incidence and progression (59, 60). Furthermore, the stiffness of the ECM has been shown to direct stem cell differentiation, cell-cell and cell-matrix adhesion, hyaluronan synthesis, and the expression of genes that play important roles in invasion and metastasis (60-64). Our technique can be used to determine whether an intervention reduces growth-induced solid stress without measuring the stiffness, as long as the experimental group known to be less stiff has a smaller normalized tumor opening. However, to more precisely determine the magnitudes of growth-induced solid stress, measurements of tissue stiffness and growth patterns are necessary.

In conclusion, by developing a simple technique, we demonstrated that it is possible to increase perfusion by alleviating solid stress and thereby decompressing vessels. It is likely that reducing solid stress would reduce IFP by lowering the venous resistance (9). However, despite this potential to lower IFP, the "anti-solid stress" strategy is distinct from the "vessel normalization" strategy, which employs direct or indirect antiangiogenic agents to prune immature vessels and fortify those remaining (1, 21). Vessel normalization, in contrast, requires the blood vessels to be open and perfused. This fact explains why antiangiogenic agents have failed thus far in desmoplastic tumors – such as pancreatic ductal carcinoma, which have abundant compressed vessels and are hypo-perfused. On the other hand, the antiangiogenic agents might work if combined judiciously with "anti-solid stress" agents that decompress vessels and improve tumor perfusion. Anti-solid stress approaches could also be combined with tumor-targeting ligands (65) and matrix modifying agents (52) to improve drug delivery and efficacy. The easy-to-implement, simple technique presented here can rapidly test whether certain tumor components contribute to the accumulation of growth-induced solid stress, without the need for measurements of material properties in some cases. Additionally, it can serve as a rapid in vivo screen for stress-reducing and perfusion-enhancing drugs.

## 2.5. Figures

**Figure 2-1 Model predictions for the total displacement of the tumor after releasing the growth-induced stress.**

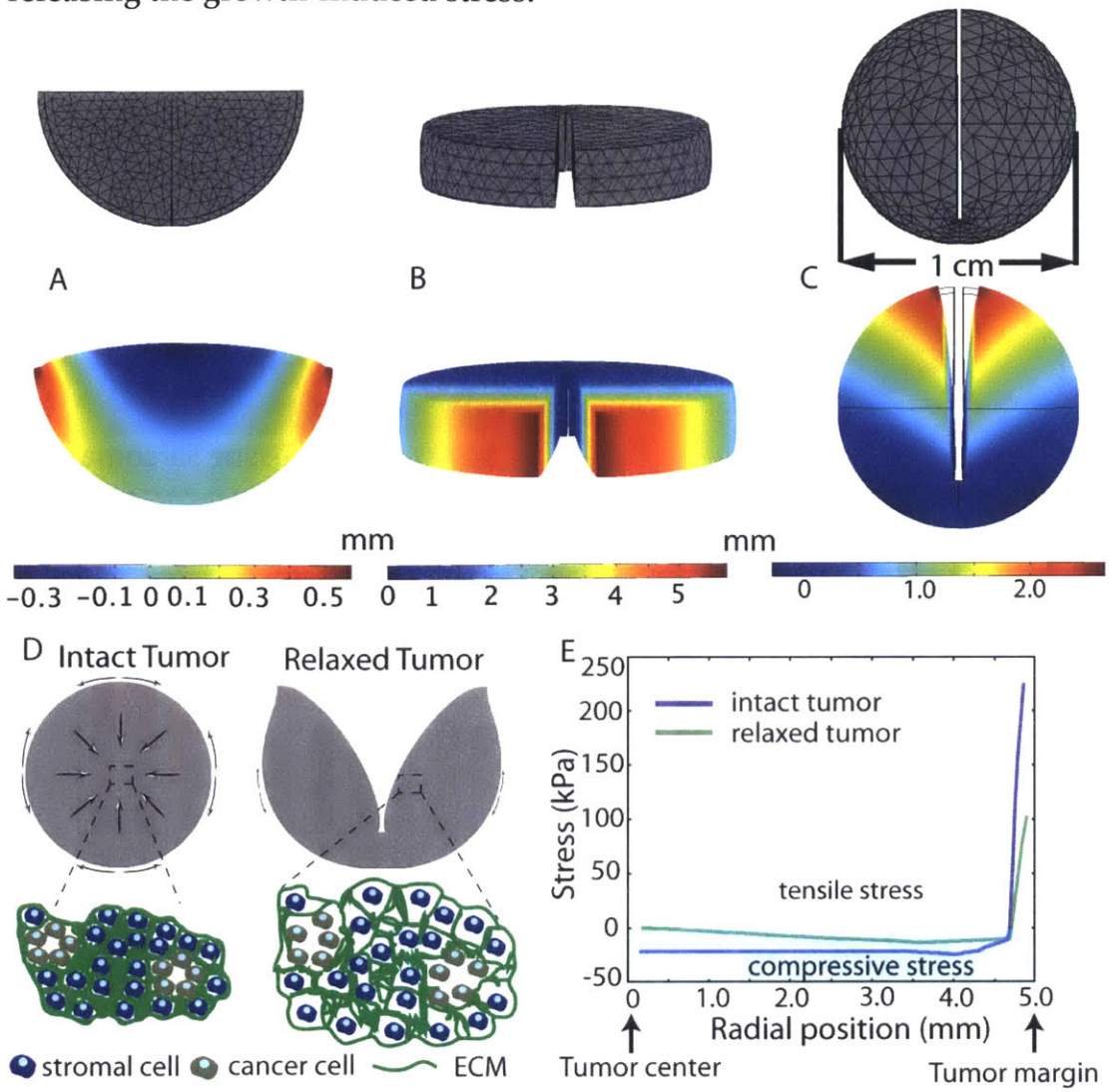


Model predictions for the total displacement of the tumor after releasing the growth-induced stress by (A) cutting the tumor in half, (B) cutting a slice of the tumor, and (C) cutting the whole tumor. The tumor has a diameter of 1 cm, and the depth of the cut (in B and C) is 0.8 cm. Notice the different displacement scales on the legends. Negative total displacements denote swelling (compressive stress) and positive total displacements opening (tensile stress) of the tissue. (D) Schematic of growth-induced stresses in tumors. In the tumor center circumferential and radial stresses are compressive, while in the periphery radial stress is compressive and circumferential stress is tensile (direction indicated with arrows). A partial cut through the center of the tumor (80% through the diameter) releases the stresses and the tumor deforms in a measurable way. Compressive stresses in the tumor interior squeeze tumor components. After the tumor is cut and the stresses are released, the tumor interior decompresses (swells). E. Spatial distribution of the circumferential growth-induced stress in an intact tumor and after making a cut. Compressive circumferential stresses at the tumor interior diminish, while tensile circumferential stresses at the periphery are also alleviated considerably.

**Figure 2-2 Estimation of stress in transplanted and human tumors.**

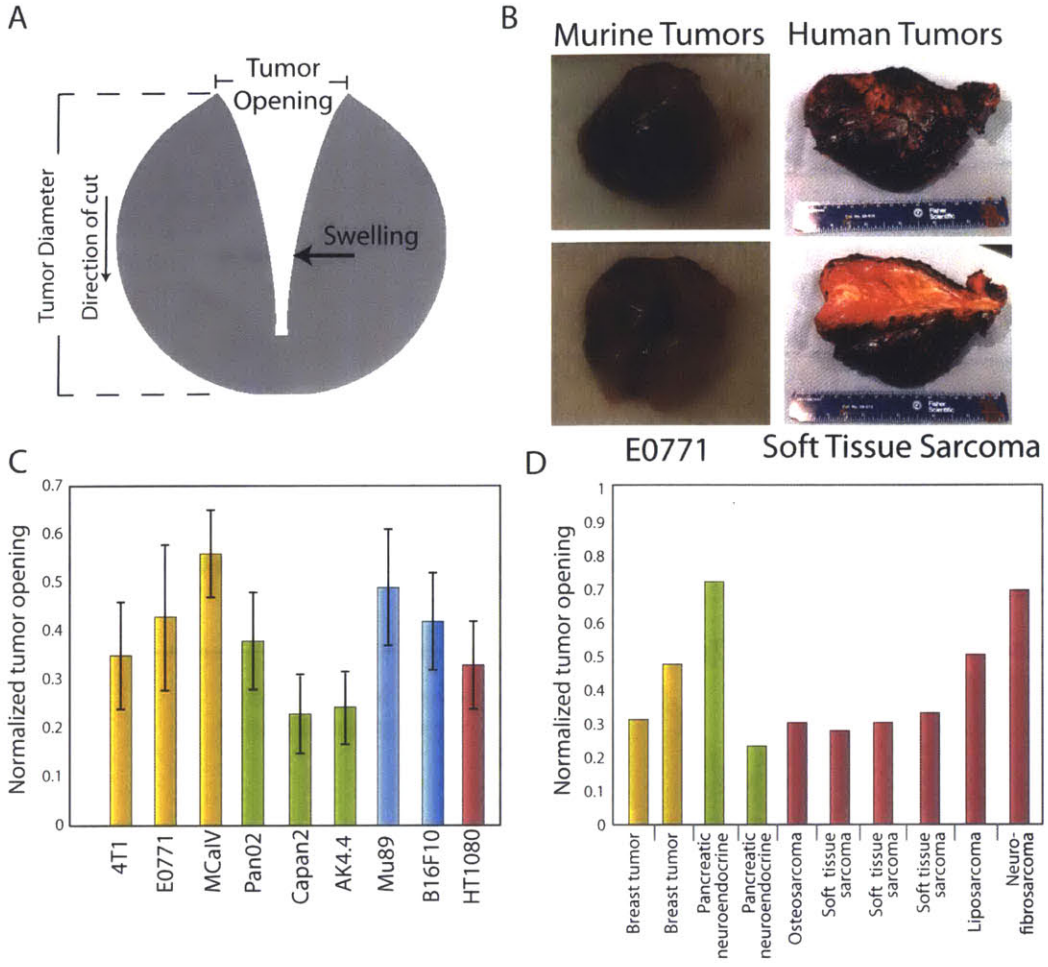


Estimation of stress in transplanted and human tumors: (A) Schematic of tumor deformation after making a cut and releasing growth-induced stress. The retraction of the tumor at the surface is indicative of circumferential tension at the tumor margin while, the swelling of the inner surface at the point of cut is indicative of compression in the intratumoral region, which presumably balances the tension at the margin. Measuring the displacement (tumor opening) accounts for both retraction and swelling. (B) Photographs of the initial and final shape of tumors after making a cut. (C, D) Tumor openings were measured in transplanted orthotopic tumors surgically excised from mice and human tumors surgically excised from patients. The diameters of the mouse tumors (C) are ~1 cm and the dimensions of the human tumors (D) are given in Supplementary Table 4. Normalized tumor opening is the tumor opening as a fraction of the initial tumor diameter. For non-spherical tumors an equivalent diameter was used for a sphere that has the same volume as the volume of the tumors. Yellow columns represent breast tumors, green columns pancreatic tumors, blue columns melanomas and maroon columns sarcomas.

**Figure 2-3 Selective depletion of tumor constituents reduces growth-induced stress and decreases tumor opening.**

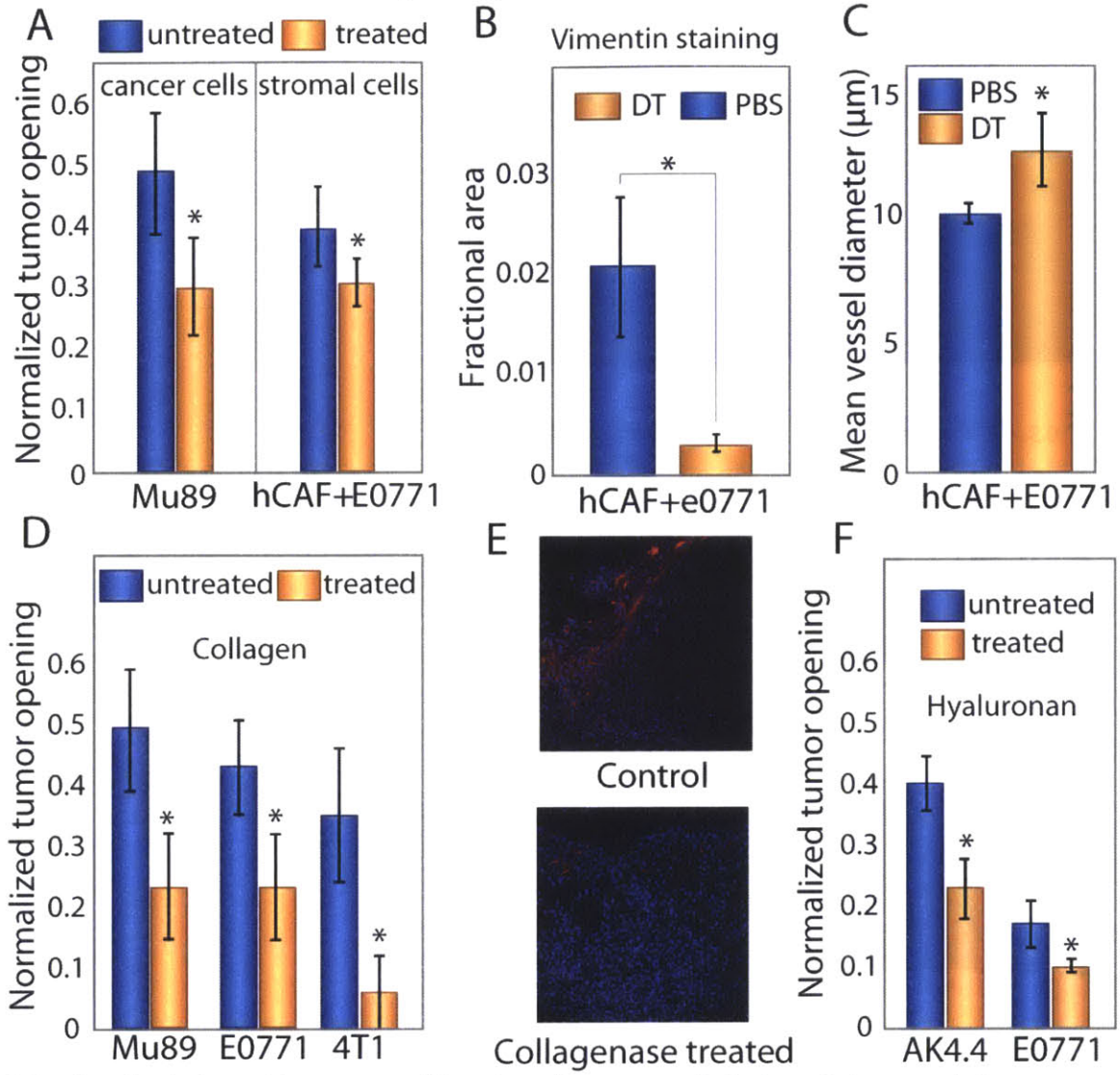


Selective depletion of tumor constituents reduces growth-induced stress and decreases tumor opening. (A) Depletion with diphtheria toxin of human cancer cells in human Mu89 tumors or human stromal cells in E0771 tumors co-implanted with human CAFs decreased tumor opening ($p=0.001$ and $p=0.023$, respectively; Student's t-test). (B) Staining of E0771 tumors for co-localization of vimentin confirms human fibroblast levels were reduced by diphtheria toxin treatment. The decrease in vimentin stained area is significant ($p=0.03$; Student's t-test). (C) Depletion of stromal cells also increased mean blood vessel diameter ($p=0.05$; Student's t-test). (D) Treatment with bacterial collagenase decreased significantly the tumor opening and thus, the growth-induced stress for all tumors ($p=0.003$ for Mu89, $p=0.025$ for E0771 and $p=4x10\text{-}6$ for 4T1; Student's t-test). (E) Staining of Mu89 tumors for cell nuclei (blue) and collagen (red) shows reduction of collagen after treatment with collagenase. (F) Treatment with hyaluronidase also significantly decreased the tumor opening in AK4.4 and E0771 tumors ($p=0.022$ and $p=0.027$, respectively; Student's t-test). All tumor models are orthotopic.

**Figure 2-4 Saridegib increases tumor vessel diameter and reopens compressed vessels by reducing stress.**

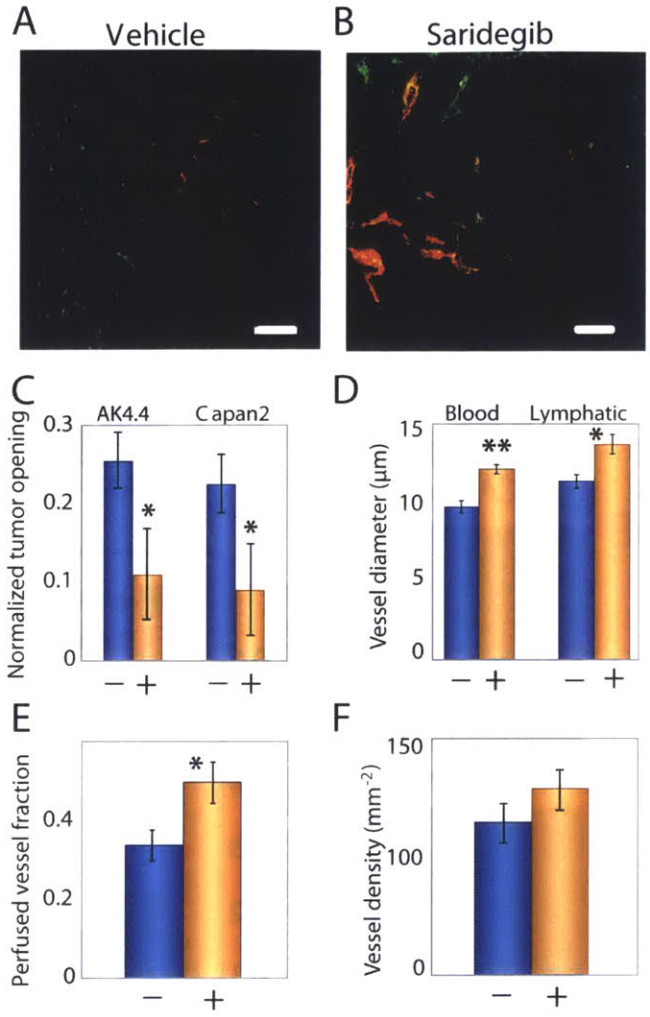


Saridegib increases tumor vessel diameter and reopens compressed vessels by reducing stress. (A) Orthotopically transplanted AK4.4 pancreatic tumors are hypovascular with compressed vessel structures stained with CD31 (green). These tumors also have reduced perfusion, as detected by lectin (red). (B) Treatment with saridegib increased the number of lectin-perfused vessels. (C, D, E, F) Treatment with saridegib, reduced stress (Panel C, p=0.046 for AK4.4 and p=0.022 for Capan2; Student's t-test) in tumors leading to increased vessel diameter (Panel D, Blood vessels: CD31 staining p=0.003, Lymphatic vessels: LYVE-1 staining, p=0.004; Student's t-test) and fraction of perfused vessels (Panel E, p=0.049; Student's t-test) without increasing vessel density (Panel F, p=NS) in AK4.4. Scale bar is 100 μm. +, saridegib; -, vehicle.

**Figure 2-5 Strategies to alleviate growth-induced solid stress in tumors.**

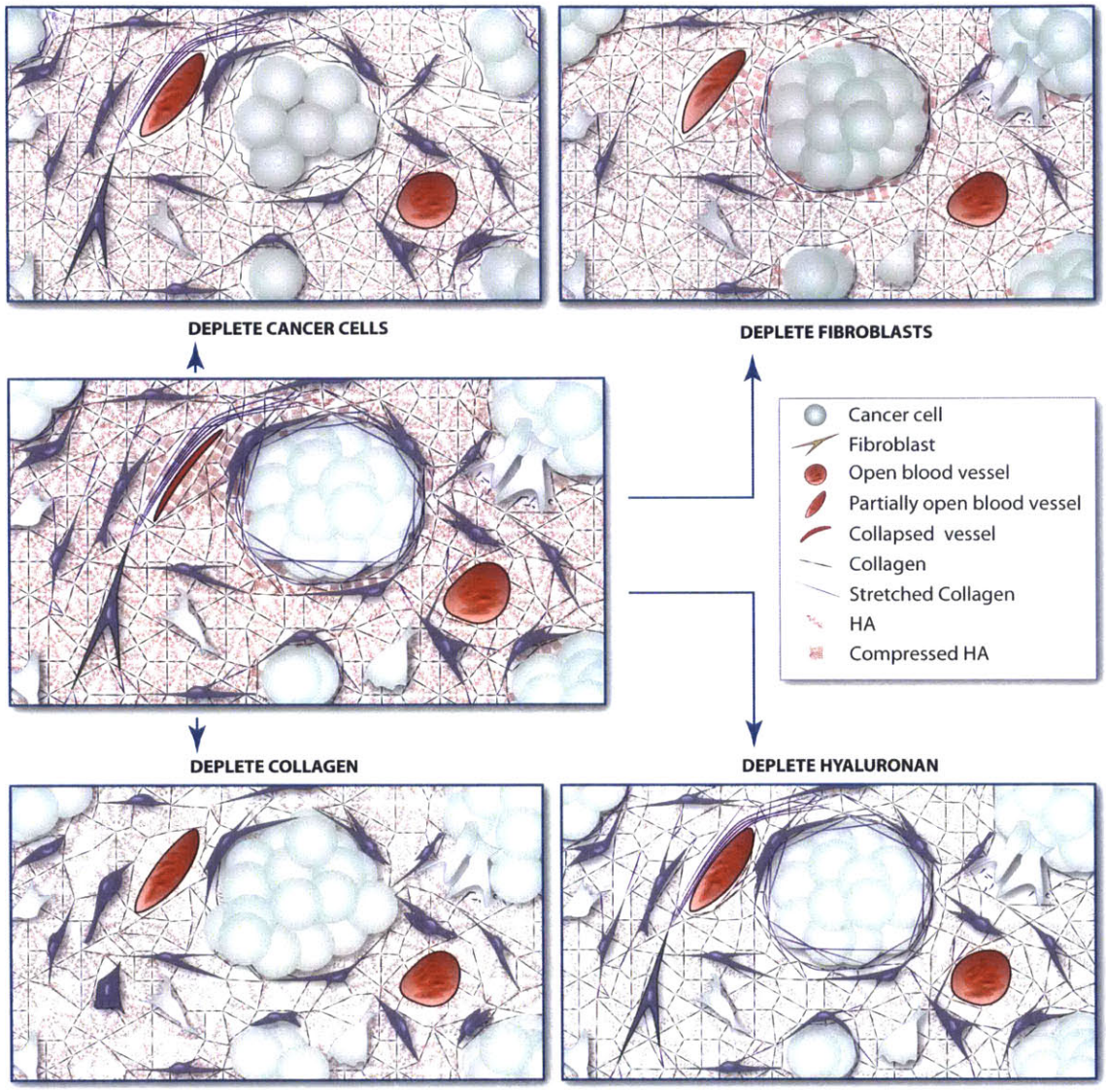


Strategies to alleviate growth-induced solid stress in tumors. Center Panel: In an untreated tumor, proliferating cancer cells and activated fibroblasts deform the extracellular matrix resulting in stretched collagen fibers, compressed hyaluronan (HA) and deformed cells – all storing solid stress. This stress compresses intratumor blood and lymphatic vessels. Potential strategies to alleviate solid stress and decompress vessels involve depleting these components. Depleting cancer cells (Top Left Panel) or fibroblasts (Top Right Panel) relaxes collagen fibers, hyaluronan and the remaining cells, alleviating solid stress. Depleting collagen (Bottom Left Panel) alleviates the stress that was held within these fibers as well as relaxes stretched / activated fibroblasts and compressed cancer cells within nodules. Finally, depleting hyaluronan (Bottom Right Panel) alleviates the stored compressive stress, allowing nearby components to decompress. (Note that other stromal cells, such as, pericytes, macrophages, and various immune cells that might also control production of collagen or hyaluronan are not shown. Lymphatic vessels are also not shown.)

**Figure 2-6 Supplementary Figure 1. Boundary conditions of the model.**

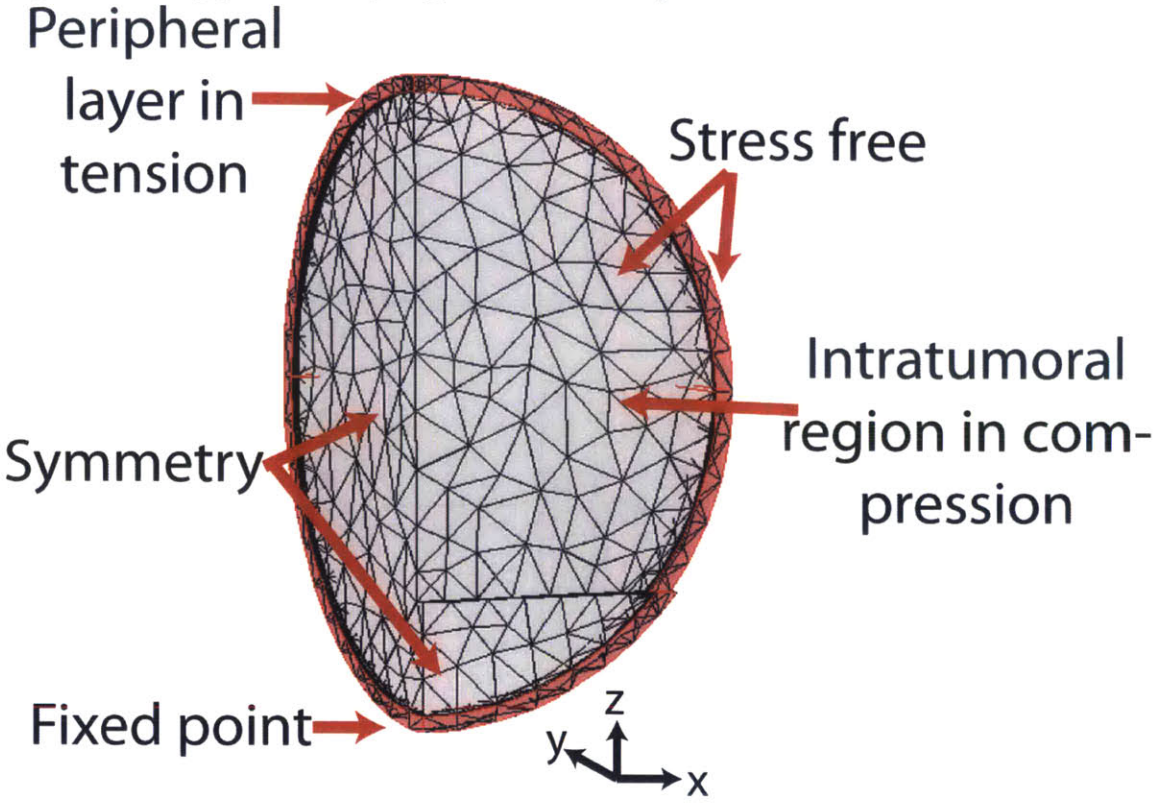


**Supplementary Figure 1.** Boundary conditions of the model. Because of symmetry we solved for the one quarter of the domain and applied symmetry boundary conditions at the planes of symmetry and stress-free boundary conditions at the free surfaces.

**Figure 2-7 Supplementary Figure 2. Model predictions of the tumor shape after making a cut for four values of $\mu^*$.**

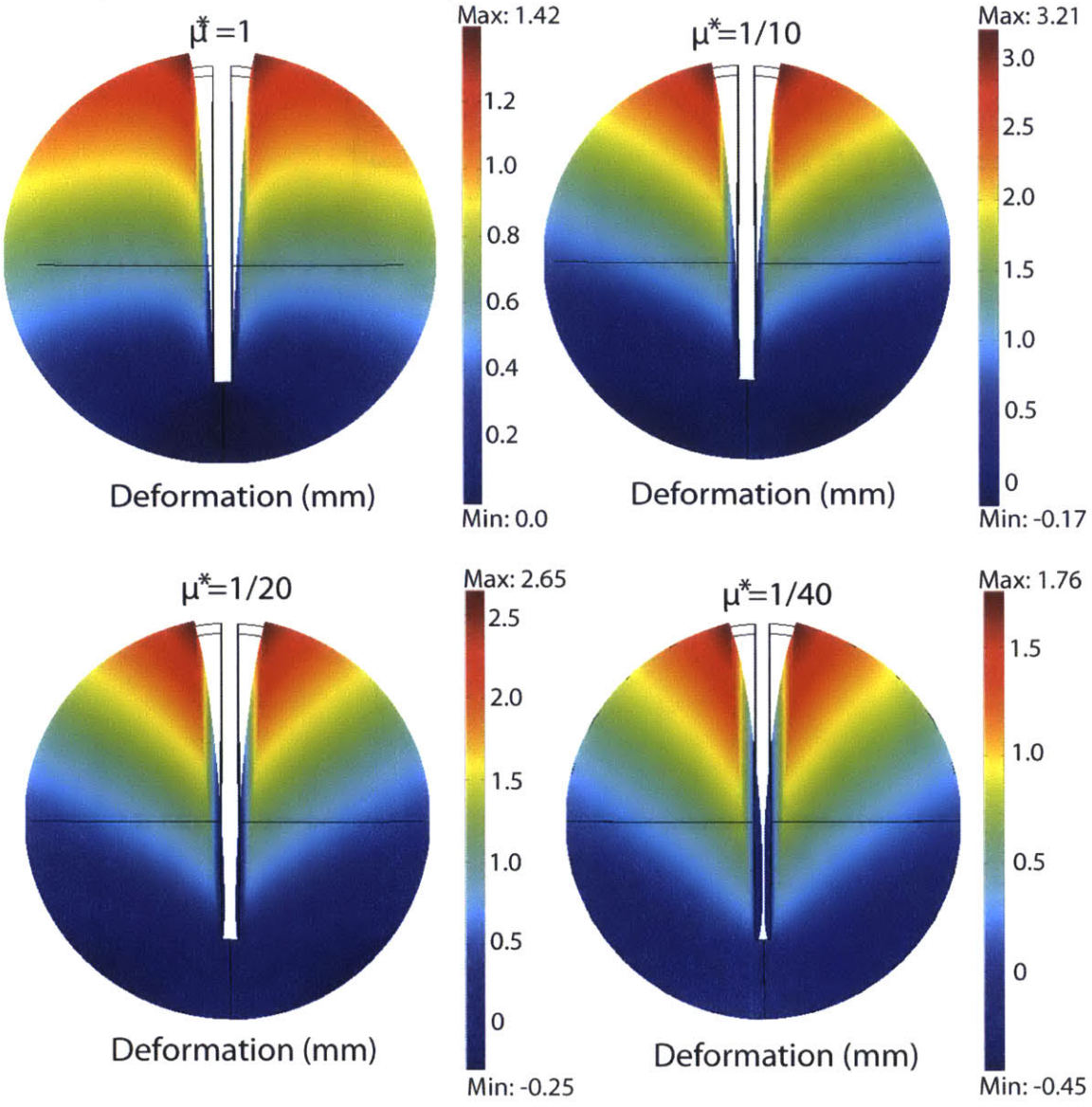


**Supplementary Figure 2.** Model predictions of the tumor shape after making a cut for four values of $\mu^*$. The value of $\lambda_g^*$ was 1.2, the peripheral layer occupied the 5% of the thickness, and the depth of the cut was 0.8 cm.

**Figure 2-8 Supplementary Figure 3. Schematic of the deformation of the tumor after making a cut along one of its axes.**

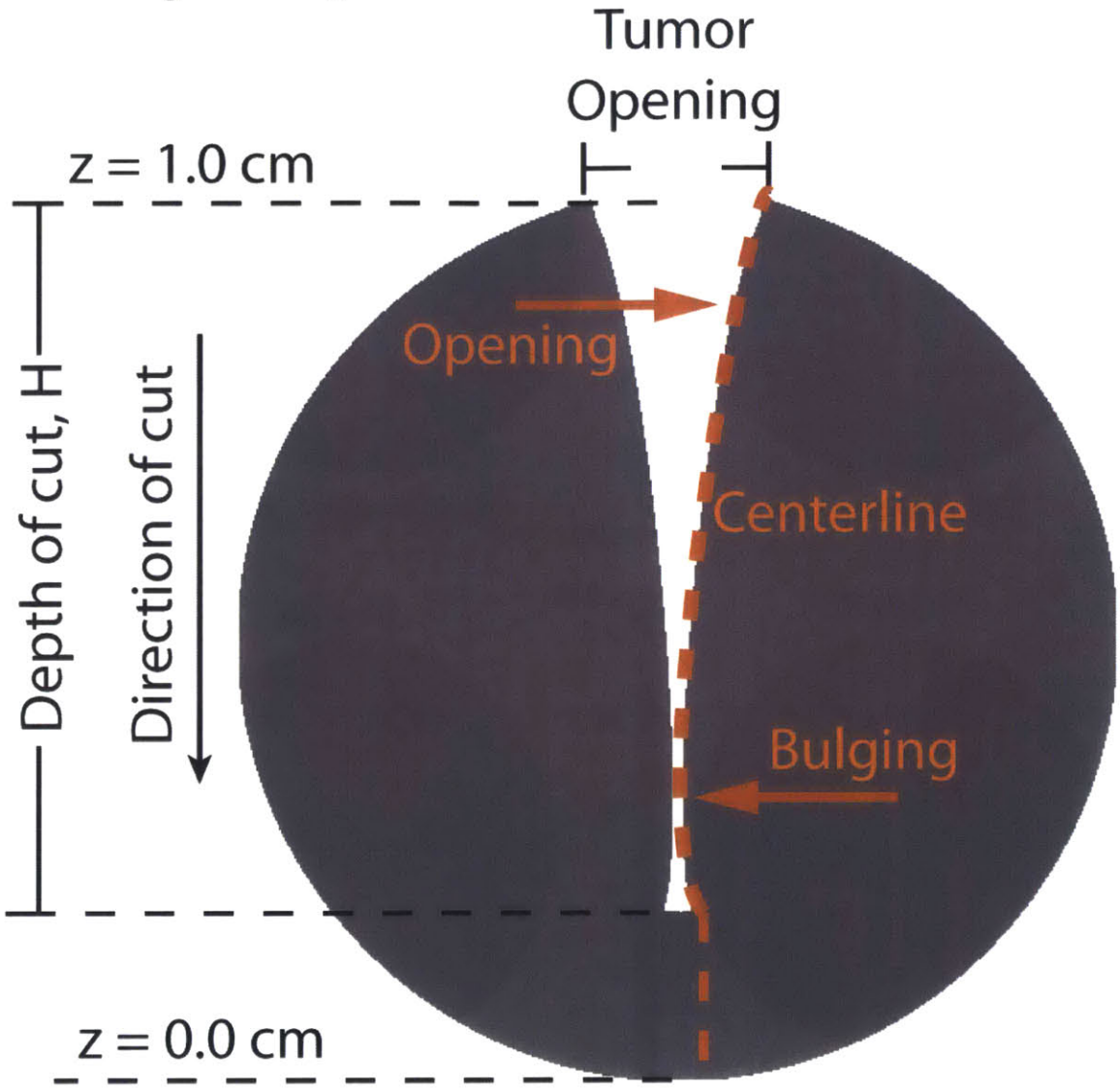


**Supplementary Figure 3.** Schematic of the deformation of the tumor after making a cut along one of its axes. The figure shows the centerline of the inner surface of the tumor that is presented in Supplementary Figure 4, and the tumor opening that was measured experimentally in Figs. 2, 3 and 4 in the main text.

**Figure 2-9 Supplementary Figure 4. Parametric analysis of the model predictions.**

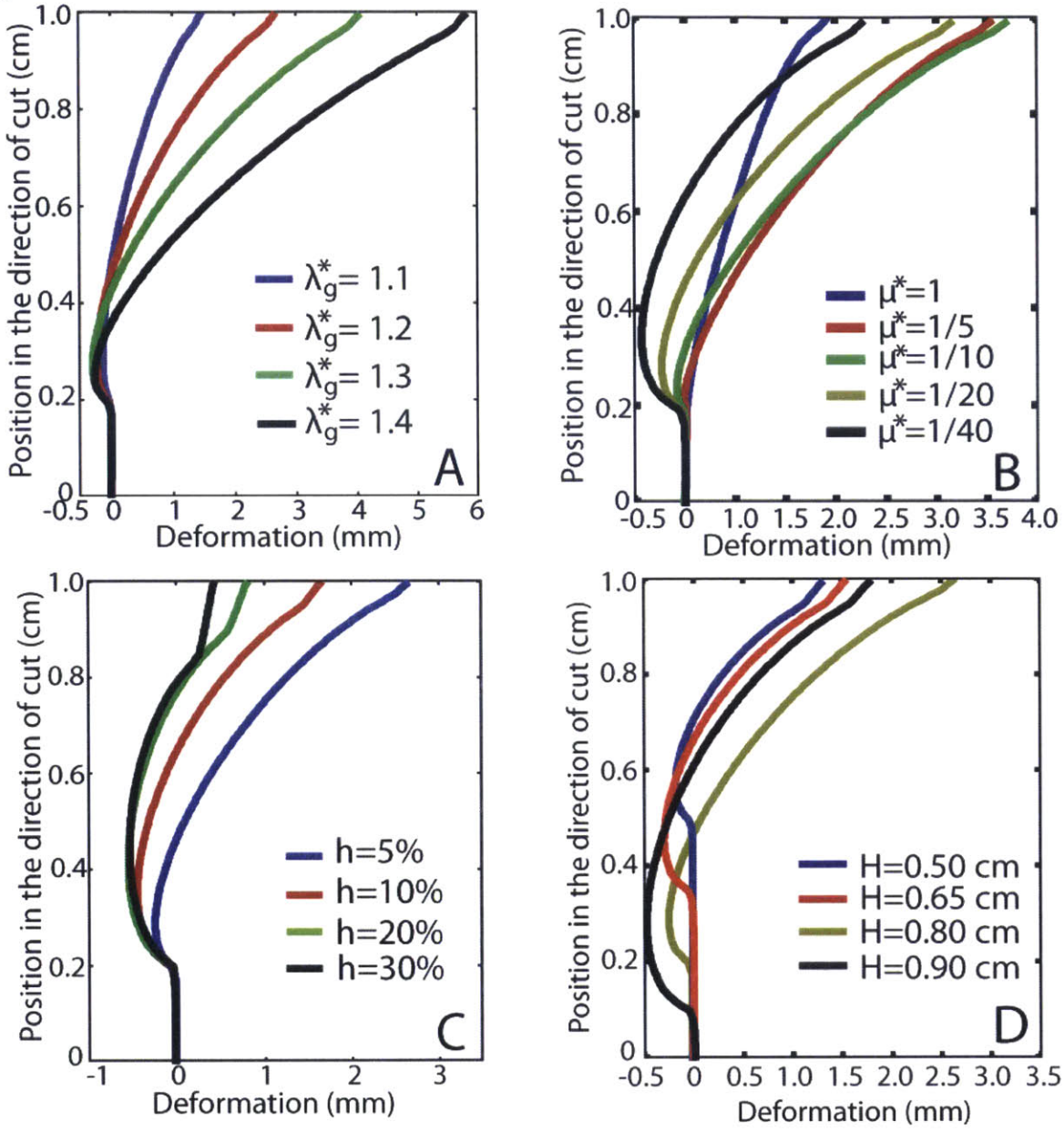


**Supplementary Figure 4.** Parametric analysis of the model predictions. The plots depict the deformation of the centerline of the inner surface of the tumor as shown in Figure 3. Panel **A**: $\mu^*$=1/20, h=5%, H=0.8 cm. Panel **B**: $\lambda_g^*$=1.2, h=5%, H=0.8 cm. Panel **C**: $\lambda_g^*$=1.2, $\mu^*$=1/20, H=0.8 cm. Panel **D**: $\lambda_g^*$=1.2, $\mu^*$=1/20, h=5%.

**Figure 2-10 Supplementary Figure 5. Compressive circumferential growth-induced stress at the interior of the tumor as a function of the relative growth, $\lambda_g^*$.**

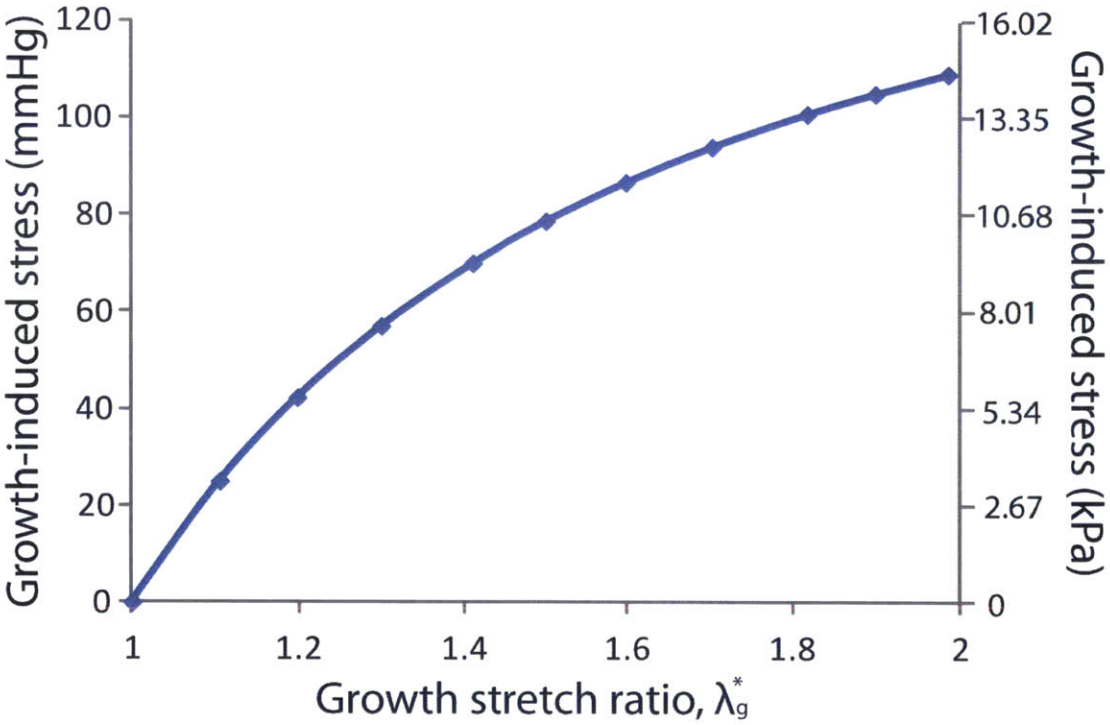


**Supplementary Figure 5**. Compressive circumferential growth-induced stress at the interior of the tumor as a function of the relative growth, $\lambda_g^*$. The shear modulus, $\mu$, of the interior was set constant to 150 mmHg and that of the periphery to 3000 mmHg.

**Figure 2-11 Supplementary Figure 6. Compressive circumferential growth-induced stress at the tumor interior as a function of the relative stiffness between the tumor periphery and center.**

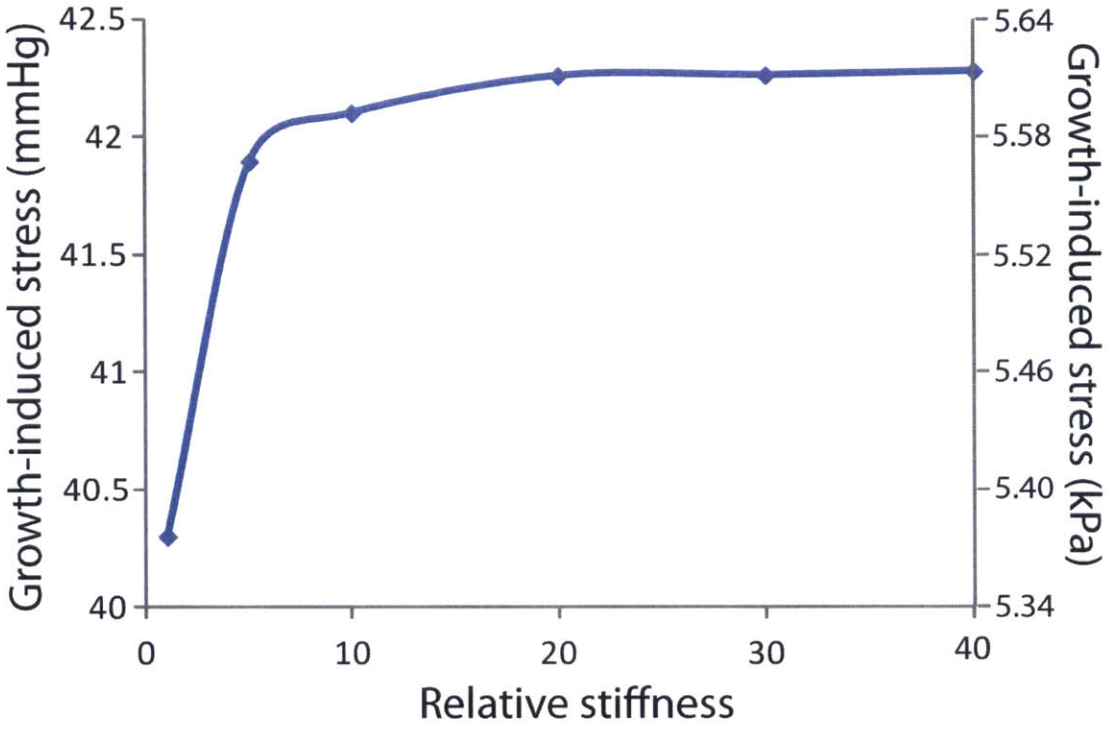


**Supplementary Figure 6**. Compressive circumferential growth-induced stress at the tumor interior as a function of the relative stiffness between the tumor periphery and center. The stiffness (shear modulus) at the center was kept constant at 150 mmHg and the stiffness at the periphery was increased from 150 - 6000 mmHg. $\lambda$ was set constant to 1.2.

**Figure 2-12 Supplementary Figure 7. Normalized tumor opening for five transplanted sub-cutaneous tumor models.**

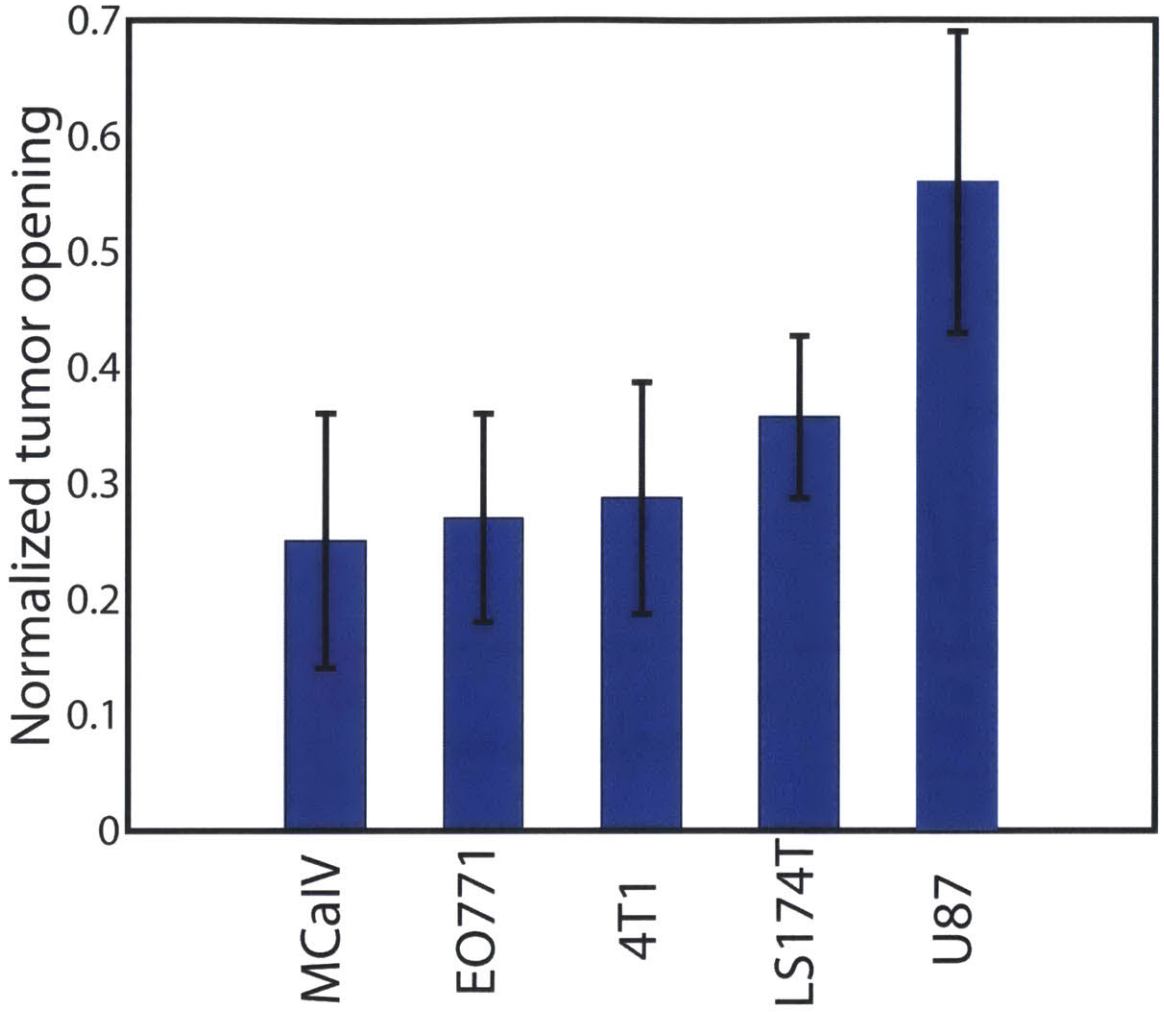


**Supplementary Figure 7.** Normalized tumor opening for five transplanted sub-cutaneous tumor models. The tumors grew on the flank of SCID mice. MCaIV, E0771, and 4T1 are murine mammary adenocarcinomas (breast tumors), LS174T is a human colon adenocarcinoma (colon tumor), and U87 is a human glioblastoma (brain tumor).

**Figure 2-13 Supplementary Figure 8. Tumor opening as a function of tumor volume and mass density for two orthotopic cancer cell lines.**

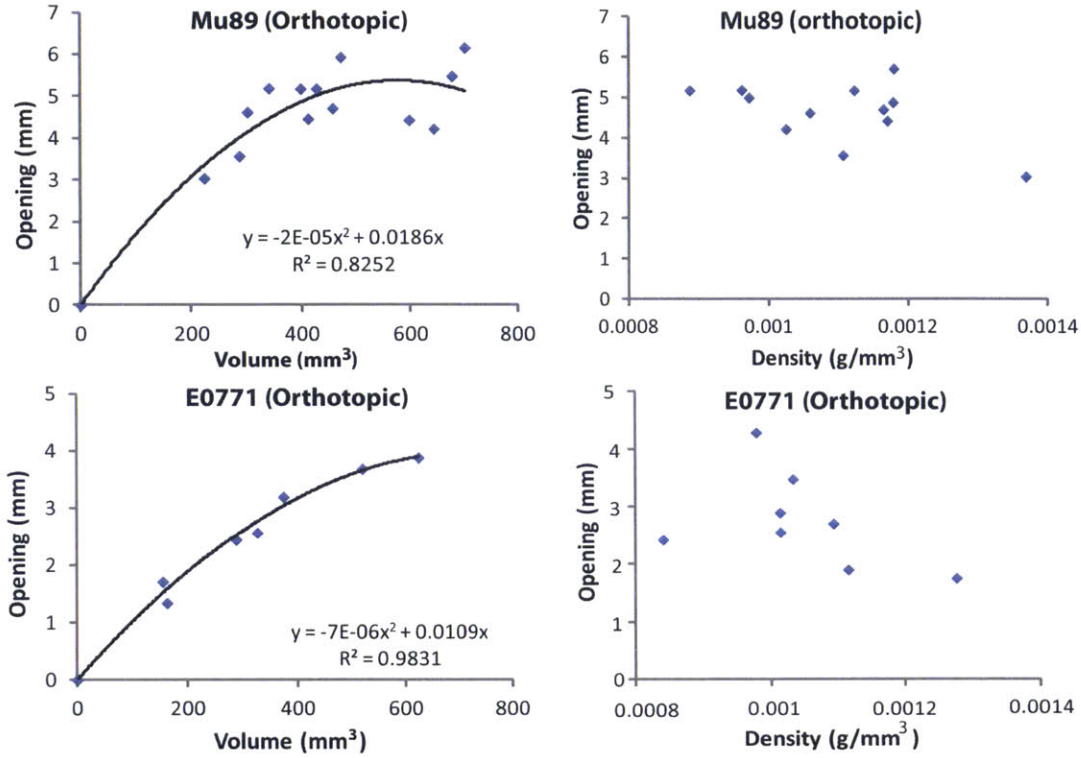


**Supplementary Figure 8.** Tumor opening as a function of tumor volume and mass density for two orthotopic cancer cell lines: Mu89 melanomas and E0771 mammary adenocarcinomas. Tumor opening increases linearly with volume before reaching a plateau. Higher volumes are usually correlated with increased necrosis, which is likely to reduce the interior swelling and thus reduces opening. No dependence of tumor opening on density was observed.

**Figure 2-14 Supplementary Figure 9. Tumor opening of human pancreatic neuroendocrine tumors.**

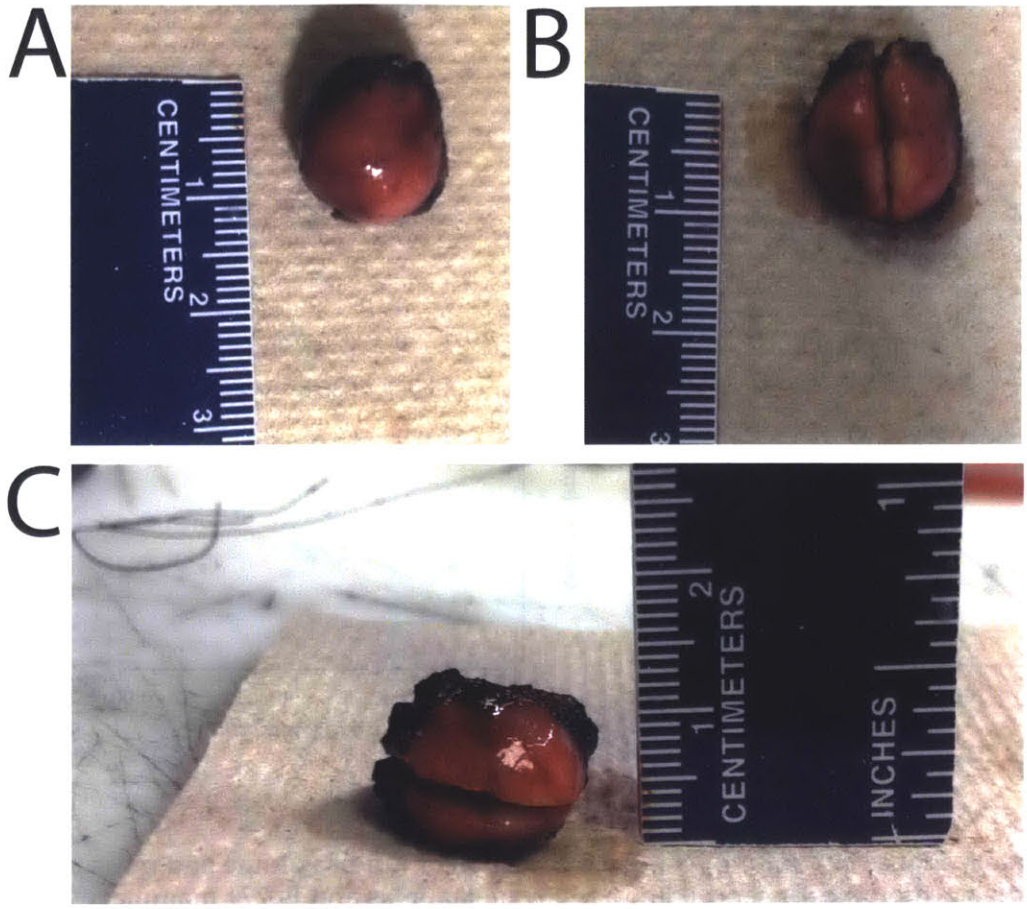


**Supplementary Figure 9.** Tumor opening of human pancreatic neuroendocrine tumors. A human pancreatic neuroendocrine tumor after it is excised from a patient before processing for histology (A) opens after a partial cut (B). The tumor opening is not affected after the tumor is placed on its side (C) or the tumor is closed manually.

**Figure 2-15 Supplementary Figure 10. Interstitial fluid pressure measurements of B16F10, Mu89, E0771, and U87 tumors.**

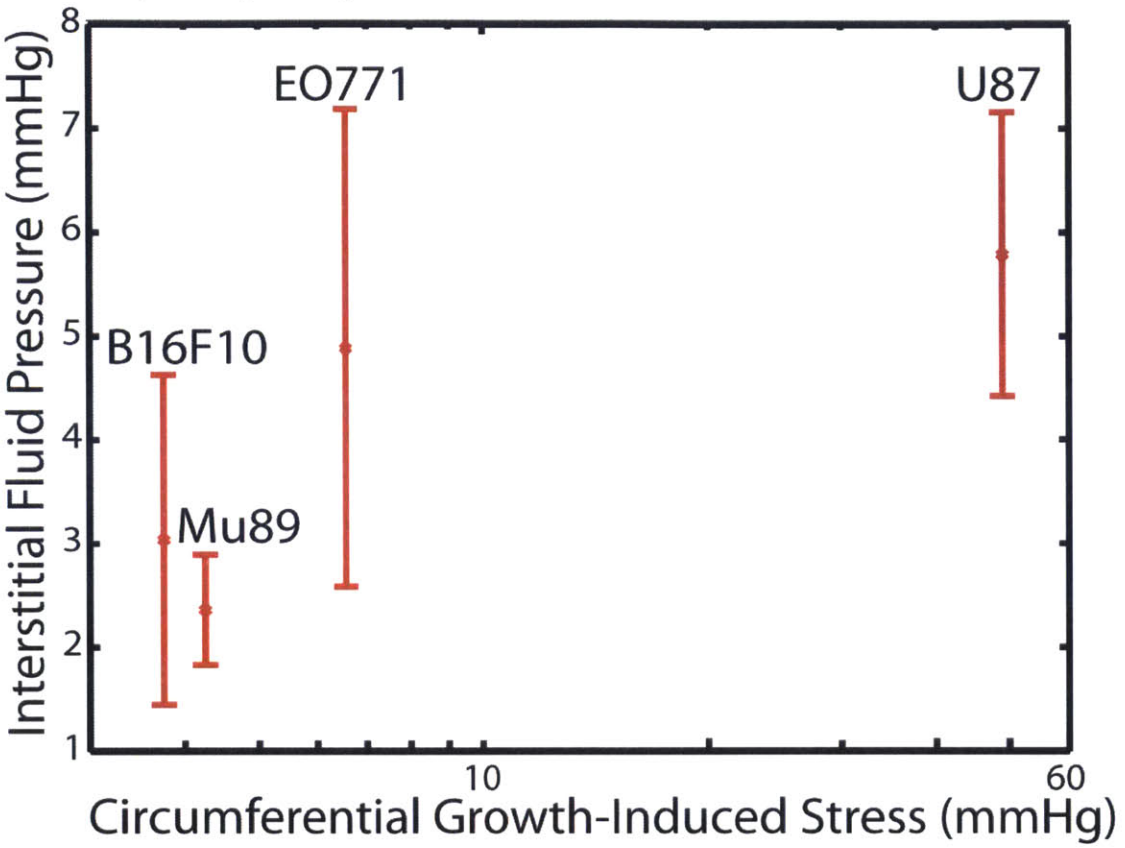


**Supplementary Figure 10.** Interstitial fluid pressure measurements of B16F10, Mu89, E0771, and U87 tumors. Even though E0771 breast tumors exhibit less growth-induced stress than U87 gliomas, there is no statistically significant difference in their interstitial fluid pressure ($p=0.345$).

**Figure 2-16 Supplementary Figure 11. Solid stress of ectopic tumors after collagen or cancer cell depletion.**

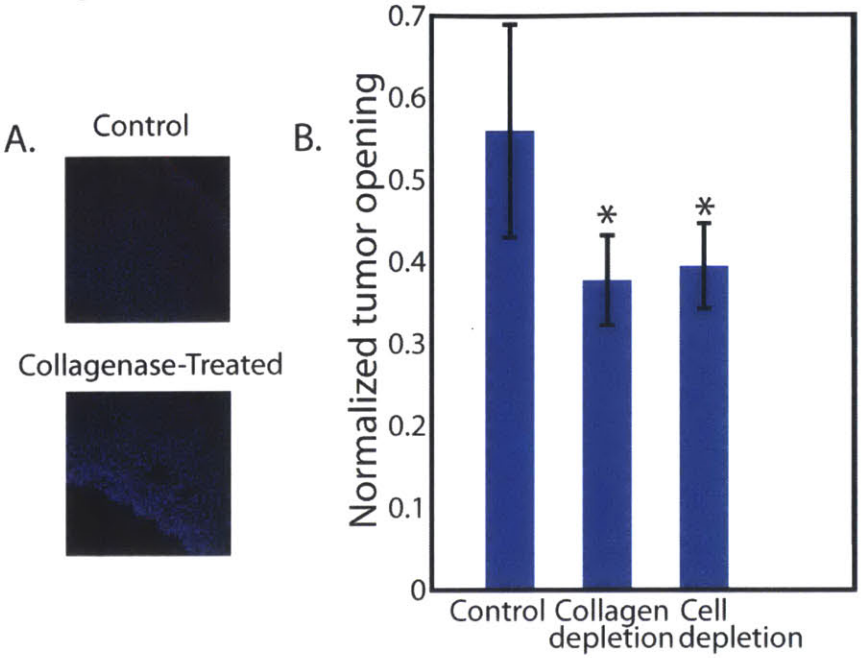


**Supplementary Figure 11.** A) Treatment of U87 tumors with bacterial collagenase altered the collagen structure. Blue and red colors represent the nuclei and collagen, respectively. B) Tumor opening of U87 glioblastoma implanted on the flank of SCID mice. Treatment with bacterial collagenase decreased significantly the tumor opening and thus, the growth-induced stress ($p=0.013$). In addition, depletion of cancer cells with diphtheria toxin decreased the tumor opening significantly ($p=0.026$).

**Figure 2-17 Supplementary Figure 12. Staining of E0771 tumors for co-localization of vimentin and aSMA confirms human fibroblast levels were reduced by diphtheria toxin treatment.**

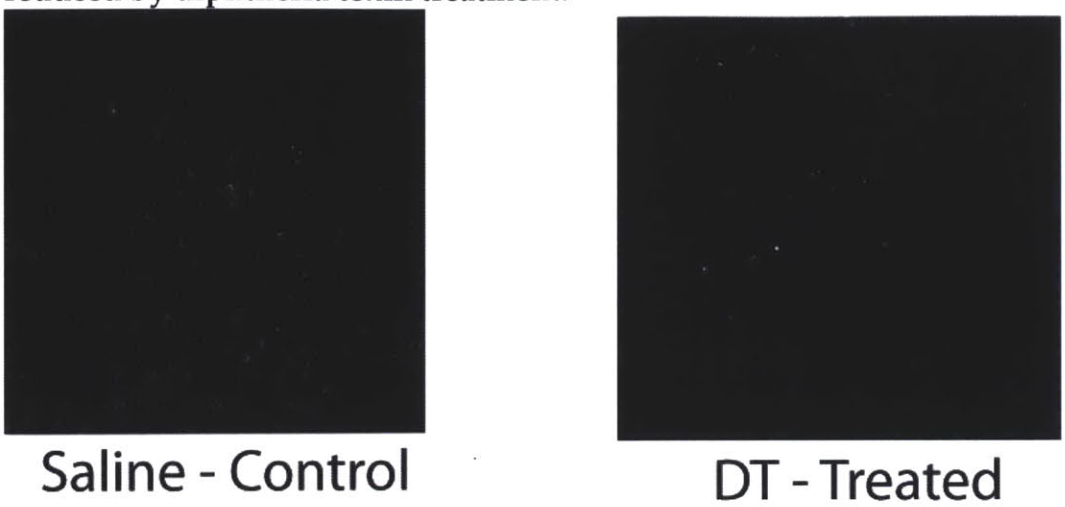


**Supplementary Figure 12.** Staining of E0771 tumors for co-localization of vimentin and aSMA confirms human fibroblast levels were reduced by diphtheria toxin treatment. Representative images show more human cells are intact in control compared to diphtheria toxin treated tumors.

**Figure 2-18 Supplementary Movie 1 - A freshly excised, orthotopically grown 4T1 breast tumor is cut.**

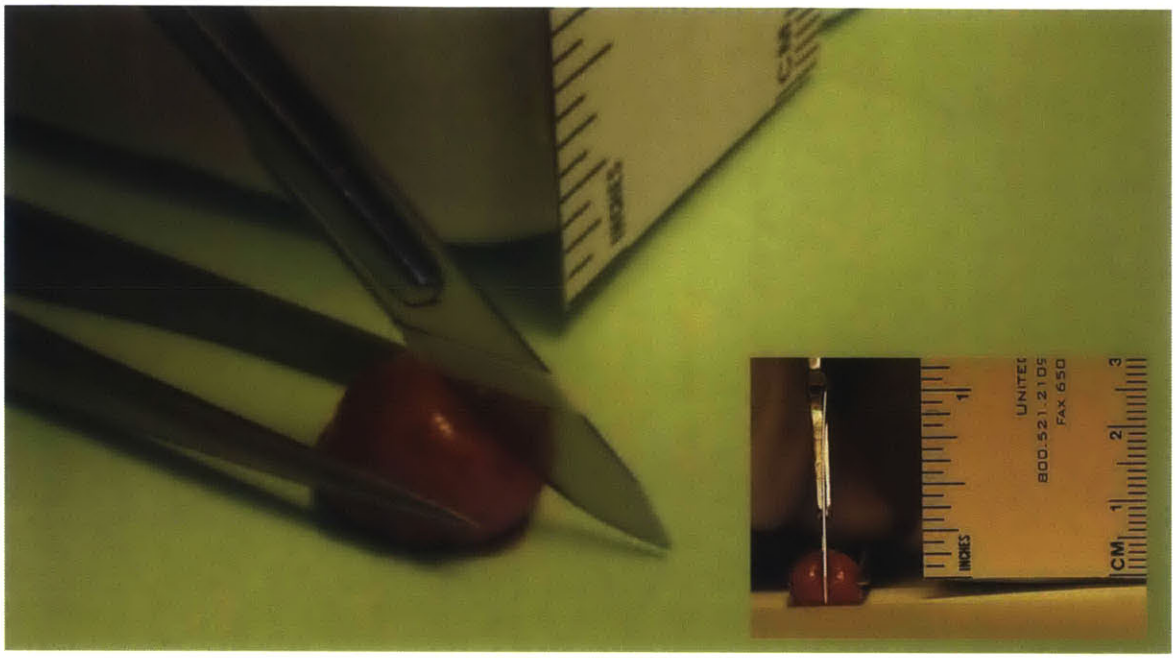


**Supplementary Movie 1 -** A freshly excised, orthotopically grown 4T1 breast tumor is cut. After the cutting is completed, the tumor is allowed to relax for 10 minutes. The real-time is displayed on the left. Note the white tape of the scalpel. This tape was placed on the scalpel to indicate the depth of the tumor to cut. This assures the tumor was cut 80% of its depth.

**Figure 2-19 Supplementary Movie 2 - A freshly excised kidney from a female SCID mouse is cut following the same procedure as with tumors.**

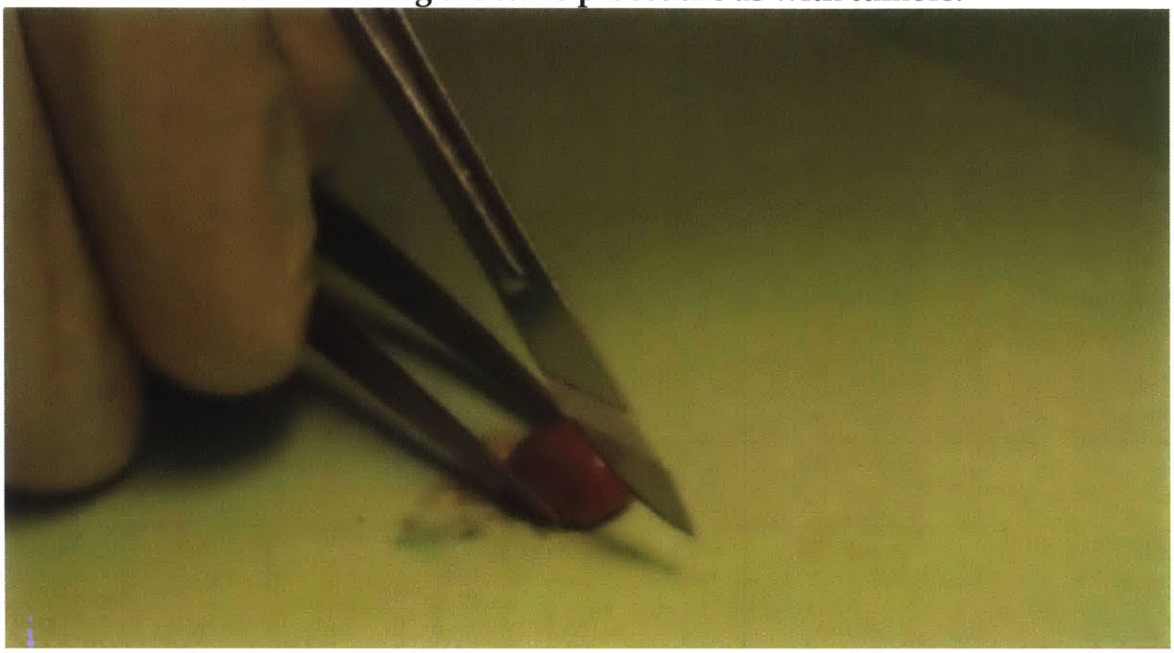

**Supplementary Movie 2 -** A freshly excised kidney from a female SCID mouse is cut following the same procedure as with tumors. The kidney does not deform measurably.

**Table 2-1 Supplementary Table 1. Mechanical material properties of the tumor types employed in the study.**

| Tumor origin | Tumor type | Cancer cell line | Bulk Modulus κ, | | Shear Modulus μ, | |
|---|---|---|---|---|---|---|
| | | | mmHg | kPa | mmHg | kPa |
| Epithelial | Breast | MCaIV, 4T1, E0771 | 50 | 6.7 | 37.5 | 5.0 |
| | Colon | LS174T | 30 | 4.0 | 22.5 | 3.0 |
| | Pancreatic | Pan02, Capan-2, AK4.4 | Not available | | Not available | |
| Mesenchymal | Sarcoma | HT1080 | Not available | | Not available | |
| | Melanoma | Mu89, B16F10 | 19 | 2.5 | 14.25 | 1.9 |
| | Glioma | U87 | 200 | 26.7 | 150 | 20.0 |

**Supplementary Table 1.** Mechanical material properties of the tumor types employed in the study. The shear modulus, μ, is a measure of the stiffness of the tumor. The higher the value of the shear modulus the stiffer the tumor is. The values of μ and κ shown here were measured experimentally in our previous work (5,6).

**Table 2-2 Supplementary Table 2. Experimentally measured doubling time and model estimates of the growth stretch ratio and the growth-induced solid stress in the interior of the transplanted tumors employed in the study.**

| Cancer cell line | Doubling time (days) | Growth stretch ratio, $\lambda_g^*(\mu^*=1/10\text{-}1/40)$ | Compressive circumferential stress ($\mu^*=1/10\text{-}1/40$) | |
|---|---|---|---|---|
| | | | mmHg | kPa |
| U87 (ectopic) | 5.18 | 1.17 - 1.32 | 38.0 - 60.1 | 5.07 - 8.01 |
| Mu89 | 2.13 | 1.15 - 1.29 | 3.2 - 5.3 | 0.43 - 0.71 |
| B16F10 | 0.94 | 1.13 - 1.25 | 2.8 - 4.7 | 0.37 - 0.63 |
| LS174T | 1.88 | 1.11 - 1.20 | 5.0 - 8.4 | 0.67 - 1.12 |
| E0771 (ectopic) | 2.21 | 1.08 - 1.14 | 4.9 - 8.2 | 0.65 - 1.09 |
| E0771 (orthotopic) | - | 1.13 - 1.25 | 7.4 - 12.4 | 0.99 - 1.65 |
| MCaIV (ectopic) | 2.50 | 1.07 - 1.13 | 4.5 - 7.4 | 0.60 - 0.99 |
| MCaIV (orthotopic) | - | 1.19 - 1.34 | 8.4 - 14.5 | 0.67 - 1.99 |
| 4T1 (ectopic) | 2.25 | 1.09 - 1.16 | 5.3 - 8.8 | 0.71 - 1.17 |
| 4T1 (orthotopic) | - | 1.11 - 1.20 | 6.3 - 10.5 | 0.84 - 1.40 |

**Supplementary Table 2.** Experimentally measured doubling time and model estimates of the growth stretch ratio and the growth-induced solid stress in the interior of the transplanted tumors employed in the study. Doubling time is a measure of tumor growth rate. High doubling times correspond to slow growing tumors. The growth-induced solid stress in the tumor interior is compressive. The table shows the estimates of the growth-induced solid stress in the circumferential direction of the tumor. Material properties of pancreatic tumors and HT1080 soft tissue sarcoma are not available and analysis was not performed.

**Table 2-3 Supplementary Table 3. Comparison of IFP measured with the piezoelectric probe and wick-in-needle techniques.**

| Method | Normal pancreas |
|---|---|
| Piezoelectric probe (N=4) | 9.8 (8.5 -11.3) |
| Wick-in-needle (N=8) | -0.3 (-1.3 - 0.7) |

**Supplementary Table 3.** Comparison of IFP measured with the piezoelectric probe and wick-in-needle techniques. The gold standard wick-in-needle technique measures IFP only while the piezoelectric probe measures IFP along with a component of solid stress. Values are given as mean (range) in mmHg.

**Table 2-4 Supplementary Table 4. Dimensions and model estimates of the growth-induced solid stress developed in the interior of surgically excised human tumors along the circumferential direction.**

| Tumor type | Tumor dimensions (cm) | Compressive circumferential stress | |
|---|---|---|---|
| | | mmHg | kPa |
| Breast tumor | 2.2x2.5x2.0 | 75.1 - 97.2 | 10.0 - 12.9 |
| Breast tumor | 2.6x2.7x1.6 | 99.5 - 142.4 | 13.3 - 19.0 |
| Pancreatic neuroendocrine tumor | 1.4x1.6x1.2 | 54.9 - 81.2 | 7.3 - 10.8 |
| Pancreatic neuroendocrine tumor | 1.3x1.8x0.9 | 16.4 - 31.2 | 2.2 - 4.2 |
| Osteosarcoma | 13.0x15.7x9.8 | 35.3 - 48.3 | 4.7 - 6.4 |
| Soft tissue sarcoma | 5.0x5.9x3.1 | 73.7 - 107.6 | 9.8 - 14.3 |
| Soft tissue sarcoma | 6.5x10.5x4.0 | 42.9 - 57.2 | 5.7 - 7.6 |
| Soft tissue sarcoma | 12.0x15.0x6.0 | 50.8 - 58.5 | 6.7 - 7.8 |
| Liposarcoma | 6.2x6.9x6.8 | 41.8 - 58.7 | 5.6 - 7.8 |
| Neurofibrosarcoma | 8.5x12.0x8.0 | 45.6 - 62.3 | 6.1 - 8.3 |

**Supplementary Table 4.** Dimensions and model estimates of the growth-induced solid stress developed in the interior of surgically excised human tumors along the circumferential direction. The growth-induced solid stress in the tumor interior is compressive. The table shows the estimates of the growth-induced solid stress in the circumferential direction of the tumor*.

* We used the mechanical properties of U87 tumors, the stiffest tumor in Supplementary Table 1.

## 2.6. Methods

**Animal and tumor models.** Tumors were prepared by implanting a small piece ($1mm^3$) of viable tumor tissue from a source tumor animal into the orthotopic site of a male FVB mouse (AK4.4) or a severe combined immunodeficient (SCID) mouse (other cell lines). The orthotopic sites included the mammary fat pad (mfp), the pancreas and the flank. Specifically, we used the following eleven cell lines: human melanoma Mu89 (orthotopic-flank), human glioblastoma U87 (ectopic-flank), human fibrosarcoma HT1080 (orthotopic-flank), human colon adenocarcinoma LS174T (ectopic-flank), murine melanoma B16F10 (orthotopic-flank), murine mammary tumor 4T1 (orthotopic-mfp and ectopic-flank), murine mammary adenocarcinoma MCaIV (orthotopic-mfp and ectopic-flank), murine mammary adenocarcinoma E0771 (orthotopic-mfp and ectopic-flank), murine pancreatic adenocarcinoma Pan02 (orthotopic-pancreas), pancreatic adenocarcinoma Capan-2 (orthotopic-pancreas), and murine pancreatic adenocarcinoma AK4.4 (orthotopic-pancreas). AK4.4 cells were isolated from spontaneous pancreatic tumors arising in $Kras^{G12}$ - $p53^{-/-}$ mice (66).

To grow mouse tumors bearing human cancer-associated fibroblasts (CAFs), we adopted our previously used procedure (41). Female SCID mice were co-implanted s.c. in the mfp with $5 \times 10^6$ E0771 tumor cells and $5 \times 10^6$ human CAFs in 0.1 ml of PBS (i.e., 1:10 ratio). All animal experiments were done with the approval of the Institutional Animal Care and Use Committee. For each tumor type 4-12 specimens were used.

**Growth-induced solid stress measurements.** When the tumor diameters reached ~1 cm, the animals were anaesthetized by injecting 0.2 *ml* of ketamine-xylazine solution (100/10 mg/kg body weight) i.m. Subsequently, each tumor was excised, washed with Hanks' Balanced Salt Solution (HBSS) and its three dimensions and weight were measured. To measure the opening, we cut the tumor along its longest axis, ~80% of its thickness. Then, the tumor was allowed to relax for 10 min in order to diminish any transient, poro-elastic response. Afterwards, we measured the opening at the surface of the tumor, in the center and close to the two edges of the cut. Performing preliminary measurements of the tumor opening we found that after 5 min the opening did not change. Thus, we considered 10 min to be sufficient time for stress relaxation. We report the maximum opening at the center of the tumor. We chose the tumor size to be 1 *cm*; tumors of smaller size ($< 0.5$ *cm*) often did not exhibit a measurable opening, while larger tumors had large necrotic areas, which affected the measurement. Supplementary

movies 1 and 2 demonstrate the technique performed on a tumor and normal mouse kidney, respectively. Stress was calculated from the measured opening using the mathematical model given in Supplement

A description of the IFP measurements, the piezoelectric probe measurements, the treatments to deplete collagen, hyalouronan and CAFs, the immunostaining methods and statistical analysis can be found in the Supplementary Information.

## 2.7. References


1. Jain RK (2005) Normalization of tumor vasculature: An emerging concept in antiangiogenic therapy. *Science* 307: 58-62.

2. Young JS, Lumsden CE & Stalker AL (1950) The significance of the 'tissue pressure' of normal testicular and of neoplastic (brown-pearce carcinoma) tissue in the rabbit. *J Path Bact* 62: 313-333.

3. Jain RK & Baxter LT (1988) Mechanisms of heterogeneous distribution of monoclonal antibodies and other macromolecules in tumors: Significance of elevated interstitial pressure. *Cancer Res* 48: 7022-32.

4. Baxter LT & Jain RK (1989) Transport of fluid and macromolecules in tumors. I. role of interstitial pressure and convection. *Microvasc Res* 37: 77-104.

5. Boucher Y, Baxter LT & Jain RK (1990) Interstitial pressure gradients in tissue-isolated and subcutaneous tumors: Implications for therapy. *Cancer Res* 50: 4478-84.

6. Boucher Y, Kirkwood JM, Opacic D, Desantis M & Jain RK (1991) Interstitial hypertension in superficial metastatic melanomas in humans. *Cancer Res* 51: 6691-4.

7. Roh HD, *et al* (1991) Interstitial hypertension in carcinoma of uterine cervix in patients: Possible correlation with tumor oxygenation and radiation response. *Cancer Res* 51: 6695-8.

8. Less JR, *et al* (1992) Interstitial hypertension in human breast and colorectal tumors. *Cancer Res* 52: 6371-4.

9. Boucher Y & Jain RK (1992) Microvascular pressure is the principal driving force for interstitial hypertension in solid tumors: Implications for vascular collapse. *Cancer Res* 52: 5110-4.

10. Gutmann R, *et al* (1992) Interstitial hypertension in head and neck tumors in patients: Correlation with tumor size. *Cancer Res* 52: 1993-5.

11. Boucher Y, Lee I & Jain RK (1995) Lack of general correlation between interstitial fluid pressure and oxygen partial pressure in solid tumors. *Microvasc Res* 50: 175-82.

12. Boucher Y, Leunig M & Jain RK (1996) Tumor angiogenesis and interstitial hypertension. *Cancer Res* 56: 4264-6.

13. Padera TP, *et al* (2002) Lymphatic metastasis in the absence of functional intratumor lymphatics. *Science* 296: 1883-6.

14. Tong RT, *et al* (2004) Vascular normalization by vascular endothelial growth factor receptor 2 blockade induces a pressure gradient across the vasculature and improves drug penetration in tumors. *Cancer Res* 64: 3731-6.

15. Jain RK, Tong RT & Munn LL (2007) Effect of vascular normalization by antiangiogenic therapy on interstitial hypertension, peritumor edema, and lymphatic metastasis: Insights from a mathematical model. *Cancer Res* 67: 2729-35.

16. Hobbs SK, *et al* (1998) Regulation of transport pathways in tumor vessels: Role of tumor type and microenvironment. *Proc Natl Acad Sci U S A* 95: 4607-12.

17. Griffon-Etienne G, Boucher Y, Brekken C, Suit HD & Jain RK (1999) Taxane-induced apoptosis decompresses blood vessels and lowers interstitial fluid pressure in solid tumors: Clinical implications. *Cancer Res* 59: 3776-82.

18. Padera TP, *et al* (2004) Pathology: Cancer cells compress intratumour vessels. *Nature* 427: 695.

19. Netti PA, Roberge S, Boucher Y, Baxter LT & Jain RK (1996) Effect of transvascular fluid exchange on pressure-flow relationship in tumors: A proposed mechanism for tumor blood flow heterogeneity. *Microvasc Res* 52: 27-46.

20. Baish JW, Netti PA & Jain RK (1997) Transmural coupling of fluid flow in microcirculatory network and interstitium in tumors. *Microvasc Res* 53: 128-41.

21. Jain RK (2001) Normalizing tumor vasculature with anti-angiogenic therapy: A new paradigm for combination therapy. *Nat Med* 7: 987-9.

22. Goel S, *et al* (2011) Normalization of the vasculature for treatment of cancer and other diseases. *Physiol Rev* 91: 1071-121.

23. Winkler F, *et al* (2004) Kinetics of vascular normalization by VEGFR2 blockade governs brain tumor response to radiation: Role of oxygenation, angiopoietin-1, and matrix metalloproteinases. *Cancer Cell* 6: 553-63.

24. Batchelor TT, *et al* (2007) AZD2171, a pan-VEGF receptor tyrosine kinase inhibitor, normalizes tumor vasculature and alleviates edema in glioblastoma patients. *Cancer Cell* 11: 83-95.

25. Willett CG, *et al* (2009) Efficacy, safety, and biomarkers of neoadjuvant bevacizumab, radiation therapy, and fluorouracil in rectal cancer: A multidisciplinary phase II study. *J Clin Oncol* 27: 3020-6.

26. Carmeliet P & Jain RK (2011) Principles and mechanisms of vessel normalization for cancer and other angiogenic diseases. *Nat Rev Drug Discov* 10: 417-27.

27. Chauhan VP, *et al* (2012) Normalization of tumour blood vessels improves the delivery of nanomedicines in a size-dependent manner. *Nat Nanotechnol* 7: 383-388.

28. Sorensen AG, *et al* (2009) A "vascular normalization index" as potential mechanistic biomarker to predict survival after a single dose of cediranib in recurrent glioblastoma patients. *Cancer Res* 69: 5296-5300.

29. Sorensen AG, *et al* (2012) Increased survival of glioblastoma patients who respond to anti-angiogenic therapy with elevated blood perfusion. *Cancer Res* 72: 402-407.

30. Skalak R, Zargaryan S, Jain RK, Netti PA & Hoger A (1996) Compatibility and the genesis of residual stress by volumetric growth. *J Math Biol* 34: 889-914.

31. Helmlinger G, Netti PA, Lichtenbeld HC, Melder RJ & Jain RK (1997) Solid stress inhibits the growth of multicellular tumor spheroids. *Nat Biotechnol* 15: 778-83.

32. Cheng G, Tse J, Jain RK & Munn LL (2009) Micro-environmental mechanical stress controls tumor spheroid size and morphology by suppressing proliferation and inducing apoptosis in cancer cells. *PLoS One* 4: e4632.

33. Tse JM, *et al* (2012) Mechanical compression drives cancer cells toward invasive phenotype. *PNAS* 109: 911-916.

34. Roose T, Netti PA, Munn LL, Boucher Y & Jain RK (2003) Solid stress generated by spheroid growth estimated using a linear poroelasticity model. *Microvasc Res* 66: 204-12.

35. Chuong CJ & Fung YC (1986) On residual stresses in arteries. *J Biomech Eng* 108: 189-92.

36. Omens JH, Vaplon SM, Fazeli B & McCulloch AD (1998) Left ventricular geometric remodeling and residual stress in the rat heart. *J Biomech Eng* 120: 715-9.

37. Xu G, Bayly PV & Taber LA (2009) Residual stress in the adult mouse brain. *Biomech Model Mechanobiol* 8: 253-62.

38. Sarntinoranont M, Rooney F & Ferrari M (2003) Interstitial stress and fluid pressure within a growing tumor. *Ann Biomed Eng* 31: 327-35.

39. Provenzano PP, *et al* (2012) Enzymatic targeting of the stroma ablates physical barriers to treatment of pancreatic ductal adenocarcinoma. *Cancer Cell* 21: 418-429.

40. Perentes JY, *et al* (2009) In vivo imaging of extracellular matrix remodeling by tumor-associated fibroblasts. *Nat Methods* 6: 143-5.

41. Duda DG, *et al* (2010) Malignant cells facilitate lung metastasis by bringing their own soil. *Proc Natl Acad Sci U S A* 107: 21677-82.

42. Nagy JA, *et al* (1989) Pathogenesis of tumor stroma generation: A critical role for leaky blood vessels and fibrin deposition. *Biochim Biophys Acta* 948: 305-326.

43. Dvorak HF (2003) Rous-whipple award lecture. how tumors make bad blood vessels and stroma. *Am J Pathol* 162: 1747-1757.

44. Kalluri R & Zeisberg M (2006) Fibroblasts in cancer. *Nat Rev Cancer* 6: 392-401.

45. Sander E, Stylianopoulos T, Tranquillo R & Barocas V (2009) Image-based biomechanics of collagen-based tissue equivalents. *IEEE Eng Med Biol Mag* 28: 10-8.

46. Bailey JM, *et al* (2008) Sonic hedgehog promotes desmoplasia in pancreatic cancer. *Clin Cancer Res* 14: 5995-6004.

47. Olive KP, *et al* (2009) Inhibition of hedgehog signaling enhances delivery of chemotherapy in a mouse model of pancreatic cancer. *Science* 324: 1457-61.

48. Baish JW, *et al* (2011) Scaling rules for diffusive drug delivery in tumor and normal tissues. *Proc Natl Acad Sci U S A* 108: 1799-803.

49. Netti PA, Berk DA, Swartz MA, Grodzinsky AJ & Jain RK (2000) Role of extracellular matrix assembly in interstitial transport in solid tumors. *Cancer Res* 60: 2497-503.

50. Brown E, *et al* (2003) Dynamic imaging of collagen and its modulation in tumors in vivo using second-harmonic generation. *Nat Med* 9: 796-800.

51. McKee TD, *et al* (2006) Degradation of fibrillar collagen in a human melanoma xenograft improves the efficacy of an oncolytic herpes simplex virus vector. *Cancer Res* 66: 2509-13.

52. Diop-Frimpong B, Chauhan VP, Krane S, Boucher Y & Jain RK (2011) Losartan inhibits collagen I synthesis and improves the distribution and efficacy of nanotherapeutics in tumors. *Proc Natl Acad Sci U S A* 108: 2909-2914.

53. Facciabene A, *et al* (2011) Tumour hypoxia promotes tolerance and angiogenesis via CCL28 and T(reg) cells. *Nature* 475: 226-230.

54. Wilson WR & Hay MP (2011) Targeting hypoxia in cancer therapy. *Nat Rev Cancer* 11: 393-410.

55. Carmeliet P & Jain RK (2011) Molecular mechanisms and clinical applications of angiogenesis. *Nature* 473: 298-307.

56. Jain RK (1988) Determinants of tumor blood flow: A review. *Cancer Res* 48: 2641-58.

57. D'Adamo DR (2011) Appraising the current role of chemotherapy for the treatment of sarcoma. *Semin Oncol* 38 Suppl 3: S19-29.

58. Jain RK & Stylianopoulos T (2010) Delivering nanomedicine to solid tumors. *Nat Rev Clin Oncol* 7: 653-64.

59. Levental KR, *et al* (2009) Matrix crosslinking forces tumor progression by enhancing integrin signaling. *Cell* 139: 891-906.

60. Goetz JG, *et al* (2011) Biomechanical remodeling of the microenvironment by stromal caveolin-1 favors tumor invasion and metastasis. *Cell* 146: 148-63.

61. Koike C, *et al* (2002) Solid stress facilitates spheroid formation: Potential involvement of hyaluronan. *Br J Cancer* 86: 947-53.

62. Engler AJ, Sen S, Sweeney HL & Discher DE (2006) Matrix elasticity directs stem cell lineage specification. *Cell* 126: 677-89.

63. Demou ZN (2010) Gene expression profiles in 3D tumor analogs indicate compressive strain differentially enhances metastatic potential. *Ann Biomed Eng* 38: 3509-20.

64. Reinhart-King CA (2011) How matrix properties control the self-assembly and maintenance of tissues. *Ann Biomed Eng* 39: 1849-56.

65. Sugahara KN, *et al* (2010) Coadministration of a tumor-penetrating peptide enhances the efficacy of cancer drugs. *Science* 328: 1031-35.

66. Hingorani SR, *et al* (2005) Trp53R172H and KrasG12D cooperate to promote chromosomal instability and widely metastatic pancreatic ductal adenocarcinoma in mice. *Cancer Cell* 7: 469-483.

## 2.8.Supplement

Description of the Mathematical Model

To gain insight into the shape of tumors after releasing the stress and to estimate the growth-induced stress, we constructed a three-dimensional finite element model of an entire tumor in COMSOL (Comsol Inc., Burlington, MA) and implemented an existing theory of tissue growth that has been applied successfully in arteries and brain tissue (1-3).

The tissue grows according to a specified growth deformation gradient tensor, $F_g$, so that the complete deformation gradient tensor F consists of two components: the growth component $F_g$, and the elastic component, $F_e$, i.e., $F= F_eF_g$. As a first approximation, we assumed a volumetric and isotropic growth of the tumor with $F_g=\lambda_g I$, where $\lambda_g$ is the growth "stretch ratio" (3). We also made the assumption that the tumor behaves as a hyper-elastic compressible neo-Hookean material with strain energy density function, $W$, given by:

$$W = 0.5\left(\mu\left(-3+\mathrm{II}_1\right)+\kappa\left(-1+J_e\right)^{-2}\right) \qquad (1)$$

where $\mu$ and $\kappa$ are the shear and bulk modulus of the material respectively, and $J_e$ is the determinant of the elastic deformation gradient tensor $F_e$. $II_1 = I_1 J_e^{-2/3}$, where $I_1$ is the first invariant of the right Cauchy-Green deformation tensor. This equation does not account for any transient, poroelastic behavior. Finally, the Cauchy stress tensor is given by the equation:

$$\boldsymbol{\sigma} = J_e^{-1}\mathbf{F}_e\frac{\partial W}{\partial \mathbf{F}_e^T} \qquad (2)$$

More details about the implementation of the model can be found in Refs (2, 4).

In the present study we used values of the parameters $\mu$ and $\kappa$ for several tumor types measured previously and presented in Table 1 (5, 6).

Previous studies have shown a uniform compressive stress in the intratumoral region that turns to tensile at the margin (6, 7). Therefore, we assumed that a thin layer at the tumor periphery is in tension, while the intratumoral region in compression. Furthermore, the growth, and thus, the distribution of the stress are taken to be uniform throughout the intratumoral region and the periphery, but the growth stretch ratio $\lambda$ between these two regions is different.

The deformation of the tumor after a cut depends on the relative growth and stiffness between the intratumoral region and the peripheral layer, i.e., $\lambda_g^* = \lambda_{gt} / \lambda_{gc}$ and $\mu^* = \mu_t / \mu_c$, where the subscripts $t$ and $c$ denote intratumoral region and peripheral layer, respectively. We did a parametric analysis of the simulation depicted in Figure 1C in the main text, which simulates the cutting mode that we employed in our experimental procedure. We varied $\lambda_g^*$, $\mu^*$, the thickness of the peripheral layer, $h$, and the depth of the cut $H$. Because of symmetry we performed our analysis on one-quarter of the domain. We applied a stress-free boundary condition to the outer and the inner free surfaces, a symmetry boundary condition to the inner symmetry planes, and fixed the bottom edge of the tumor to keep it in place (Supplementary Figure 1).

Supplementary Figure 2 shows the deformation of the tumor for constant $\lambda_g^*$, $h$ and $H$ and for four values of $\mu^*$. In the plots, a positive deformation indicates opening of the tumor, while a negative deformation indicates bulging of the inner surface. As the peripheral layer becomes stiffer (i.e., $\mu^*$ decreases), the bulging of the inner surface increases and the opening initially increases and then drops. Notice that bulging is observed only when the peripheral tumor layer is stiffer than the intratumoral region.

The deformation of the centerline of the tumor is the dashed line in Supplementary Figure 3. We separately varied the parameters $\lambda_g^*$, $h$, $H$ or $\mu^*$ while keeping the other three constant. Supplementary Figure 4 depicts the predictions of the mathematical model. Increase in the growth stretch ratio $\lambda_g^*$ increases the opening of the tumor but does not affect the bulging of the inner surface (Supplementary Figure 4A). In contrast, changes in the stiffness of the peripheral layer can significantly affect both bulging and opening (Supplementary Figure 4B). Importantly, there is a maximum in tumor opening as $\mu^*$ decreases (peripheral layer stiffens). This intriguing finding is the result of two

competing effects, the tension at the margin and the compression at the interior of the tumor. Hence, increase in the thickness of the peripheral layer would decrease opening and increase bulging (Supplementary Figure 4C). Finally, the depth of the cut affects both bulging and opening (Supplementary Figure 4D).

The parameter $\lambda_s$ describes the relative cell proliferation between the tumor periphery and interior. Measurements of the spatial distribution of cancer cell proliferation (8,9) have shown that the proliferation rate is higher at the periphery of the tumor, where there are more blood vessels. The proliferation rate at the periphery can be twice as much as the rate at the center. In Supplementary Figure 5 we plot the circumferential, compressive growth-induced stress at the interior of the tumor as a function of the relative growth, $\lambda_s$. As the relative growth increases, growth-induced stress increases as well.

In addition, we performed simulations keeping $\lambda_s$ constant and varying the relative stiffness, $\mu$ between the interior and the periphery of the tumor (Supplementary Figure 6). The figure shows that stiffening of the tumor periphery has little effect on the intratumoral compressive growth-induced stress.

Model limitations

Our mathematical approach to quantify stress in tumors is subject to several assumptions and limitations. The magnitude of the stress given by the model depends on the specified material properties and growth. The material properties that we used were based on previous measurements in our lab (6, 7), which are in the same range as in other published studies (10, 11). But when depleting tumor constituents the material properties change. Thus, as discussed in the main text, in many cases we compared normalized tumor openings rather than stress magnitudes because of the uncertainty of the material properties. In addition we assumed an isotropic and uniform growth of the tumor and peripheral layer, which might not be true given its heterogeneous structure. This is an approximation that we had to make because of the lack of any experimental findings of growth patterns in our tumor models. Also, we used the neo-Hookean constitutive equation to describe the mechanical behavior of tumors. Tumors as most biological tissues are complex, heterogeneous, and poro-elastic structures and an isotropic, continuum-level constitutive equation might not be sufficient to describe their mechanical response. Nonetheless, the model predictions were consistent with our cutting experiments, which suggests that our assumptions are reasonable. As more data

become available, they can be easily incorporated into our current framework. Finally, another limitation of the model is that many different growth fields or combinations of growth patterns and material properties can give rise to similar residual stress distributions. Added to this the fact that the cutting experiment only eliminates most of the stress, not all, making it difficult to come up with a unique growth pattern. Hence, the current results provide an estimate of the growth-induced stress in tumors.

Quantification of Growth-induced Stress Using the Mathematical Model

To quantify the growth-induced stress from the opening measurements, we employed the mathematical model, which was implemented in COMSOL using the finite element method. The tumors were represented as ellipsoids. The length of the three axes of the tumors, which we incorporated into the model, were measured after the tumors were excised and before performing the cutting experiment. We simulated the experiment using the material properties shown in Table 1. Even though bulging of the inner surface was evident in all types of tumors, it was not possible to perform accurate measurements of it. To estimate the compressive stress of the intratumoral region, we varied $\mu$ from 1/10, where bulging is first observed (Supplementary Figure 2), to 1/40, where the two inner surfaces are almost in contact and calculated the value of $\lambda_g^*$ that matched the experimentally measured tumor opening. Subsequently, knowing the growth stretch ratio, $\lambda_g^*$, we used our model to convert this stretch to growth-induced stress. The thickness, $h$, of the peripheral layer was set to 5% based on previous studies and the depth of our cuts was approximately 80% of tissue thickness. We followed the same methodology to quantify the compressive, growth-induced stress of the human tumors presented in Table 3. Human tumors were modeled as ellipsoids based on the dimensions in the three coordinate directions, and we used the material properties of the stiffest tumor shown in Supplementary Table 1.

Supplementary Materials and Methods

Interstitial fluid pressure measurement. Interstitial fluid pressure (IFP) was measured with the wick-in-needle technique (12) prior to tumor excision. For each tumor, IFP was measured in at least two different tumor locations.

Piezoelectric probe measurement. We measured the combination of IFP and some component of solid stress using a piezoelectric probe (13). Briefly, we connected a Millar

Mikro-Tip pressure catheter transducer (SPR-1000, 0.33 mm diameter) to a PCU-2000 Pressure Control Unit and an ADInstruments PowerLab data acquisition system. After calibration, we placed the catheter using a 25-gauge needle to create a space in the tissue to insert the probe after needle withdrawal.

Tumor growth rate measurement. Tumor planar dimensions (x, y) were measured with a digital caliper every 2 days. The volume of the tumor was estimated by the expression: $V = \frac{\pi}{6}(xy)^{3/2}$. Tumor doubling time, T, was calculated by fitting the equation: $V = V_0 2^{t/T}$ to the experimental data.

Collagenase, hyaluronidase and diphtheria toxin treatment. Bacterial collagenase from Clostridium histolyticum (Sigma-Aldrich, C0773) was prepared by dissolving 1 *mg* collagenase in 10 *ml* of 50mM TES buffer containing 0.36*mM* calcium chloride (TESCA), pH 7.4 at 37C. After excision, the tumor was placed in the collagenase solution remaining at 37C for 2hrs prior to measurement. Hyaluronidase (Sigma-Aldrich, H3506) was administered I.P. 24 hrs and 1 hr before tumor excision, each time in a volume of 0.1 ml/20 g body weight to provide an enzyme activity of 100,000 IU/kg (14).

Human cells are 1,000 times more sensitive to diphtheria toxin than murine cells and thus can be depleted by diphtheria toxin *in vivo* in mice (15, 16). Mice were injected once intraperitoneally with 1 $\mu g$ of diphtheria toxin in 0.3 *ml* of PBS (15). After 24 hrs the tumor was excised to perform the measurement.

Saridegib treatment. Male FVB and male SCID mice bearing orthotopic, human pancreatic adenocarcinomas AK4.4 and Capan-2 were treated as described previously (19). Saridegib was dissolved in a 5% aqueous solution of hydroxypropil-β-cyclodextran (HPBCD). Accounting for potency of the batch received, the resulting solution was 5 mg/ml. After sonication and vortexing, the solution was sterile filtered. 40 mg/kg of the resulting drug was administered daily by gavage for 8 days or 10 days in mice bearing AK4.4 and Capan-2, respectively.

Immunofluorescence staining, imaging and analysis. For frozen sections, staining was performed according to a previously described protocol (17, 18). Human vimentin staining was done only on frozen tissues, according to a previously described protocol (16). After retro-orbital injection of biotinylated-lectin five minutes prior to tumor removal (100 $\mu$L, Vector Labs) tissues were excised, fixed for two to three hrs in 4%

formaldehyde in PBS, incubated in 30% sucrose in PBS overnight at 4°C, and frozen in optimal cutting temperature compound (Tissue-Tek). Transverse tumor sections, 40 μm thick, were immunostained with antibodies to endothelial marker CD31, and counterstained by mounting with DAPI-containing medium (Vectashield, Vector Labs). Collagen I staining was done on both frozen and paraffin embedded tissues. In both cases, collagen I was detected using the LF-67 antibody provided by Dr. Larry Fisher (National Institute of Dental Research, Bethesda, MD). For paraffin sections, slides were treated with 3% hydrogen peroxide prior to antigen retrieval with Target Retrieval Solution, pH 9 (DAKO, Carpinteria, CA). The slides were further treated with 0.05% trypsin before the primary antibody was applied.

Eight random images (four interior, four periphery) at 20x magnification at a resolution of 1.3 pixels to microns were taken from each slide. Images of collagen and vimentin stained sections were analyzed by thresholding based on the average image intensity. The fraction of pixels above threshold was used as a measure of the content in each tumor. Non-viable tissue area was excluded from the analysis. For vascular analysis, vessels were segmented using a custom, semi-automated tracing program developed in MATLAB (MathWorks, Natick, MA) allowing the removal of structures under thirty pixels and regions of auto-fluorescence.

Statistical Analysis. The data are presented as means with standard errors. Groups were compared using a Student's t-test.

References

1. Rodriguez EK, Hoger A & McCulloch AD (1994) Stress-dependent finite growth in soft elastic tissues. *J Biomech* 27: 455-67.

2. Taber LA (2008) Theoretical study of beloussov's hyper-restoration hypothesis for mechanical regulation of morphogenesis. *Biomech Model Mechanobiol* 7: 427-41.

3. Xu G, Bayly PV & Taber LA (2009) Residual stress in the adult mouse brain. *Biomech Model Mechanobiol* 8: 253-62.

4. Alford PW, Humphrey JD & Taber LA (2008) Growth and remodeling in a thick-walled artery model: Effects of spatial variations in wall constituents. *Biomech Model Mechanobiol* 7: 245-62.

5. Netti PA, Berk DA, Swartz MA, Grodzinsky AJ & Jain RK (2000) Role of extracellular matrix assembly in interstitial transport in solid tumors. *Cancer Res* 60: 2497-503.

6. Roose T, Netti PA, Munn LL, Boucher Y & Jain RK (2003) Solid stress generated by spheroid growth estimated using a linear poroelasticity model. *Microvasc Res* 66: 204-12.

7. Sarntinoranont M, Rooney F & Ferrari M (2003) Interstitial stress and fluid pressure within a growing tumor. *Ann Biomed Eng* 31: 327-35.

8. Hermens AF & Barendsen GW (1967) Cellular proliferation patterns in an experimental rhabdomyosarcoma in the rat. *Europ. J. Cancer* 3: 361-369.

9. Brammer I, Zywietz F & Jung H (1979) Changes of histological and proliferative indices in the walker carcinoma with tumour size and distance from blood vessel. *Europ. J. Cancer* 13: 1329-1336.

10. Samuel MS, *et al* (2011) Actomyosin-mediated cellular tension drives increased tissue stiffness and beta-catenin activation to induce epidermal hyperplasia and tumor growth. *Cancer Cell* 19: 776-91.

11. Levental I, *et al* (2010) A simple indentation device for measuring micrometer-scale tissue stiffness. *J Phys Condens Matter* 22: 194120.

12. Boucher Y, Baxter LT & Jain RK (1990) Interstitial pressure gradients in tissue-isolated and subcutaneous tumors: Implications for therapy. *Cancer Res* 50: 4478-84.

13. Provenzano PP, *et al* (2012) Enzymatic targeting of the stroma ablates physical barriers to treatment of pancreatic ductal adenocarcinoma. *Cancer Cell* 21: 418-429.

14. Muckenschnabel I, Bernhardt G, Spruss T & Buschauer A Pharmacokinetics and tissue distribution of bovine testicular hyaluronidase and vinblastine in mice: An attempt to optimize the mode of adjuvant hyaluronidase administration in cancer chemotherapy. *Cancer Letters 1998 Sep 11;131(1):71-84.*

15. Padera TP, *et al* (2004) Pathology: Cancer cells compress intratumour vessels. *Nature* 427: 695.

16. Duda DG, *et al* (2010) Malignant cells facilitate lung metastasis by bringing their own soil. *Proc Natl Acad Sci U S A* 107: 21677-82.

17. Pluen A, Netti PA, Jain RK & Berk DA (1999) Diffusion of macromolecules in agarose gels: Comparison of linear and globular configurations. *Biophys J* 77: 542-52.

18. Znati CA, *et al* (2003) Irradiation reduces interstitial fluid transport and increases the collagen content in tumors. *Clin Cancer Res* 9: 5508-13.

19. Olive KP, *et al* (2009) Inhibition of hedgehog signaling enhances delivery of chemotherapy in a mouse model of pancreatic cancer. *Science* 324: 1457-61.

# *Chapter 3 Angiotensin inhibition enhances drug delivery and potentiates chemotherapy by decompressing tumor blood vessels*

Some of the work, text and figures presented in this chapter are adapted from reference under perfmissions from Nature Communications and Creative Commons license:

Chauhan VP*, Martin JD*, Liu H, Lacorre DA, Jain SR, et al. 2013. Angiotensin inhibition enhances drug delivery and potentiates chemotherapy by decompressing tumor blood vessels. *Nat. Commun.* 4:2516

** these authors contributed equally to this work*

## 3.1. Abstract

**Cancer and stromal cells actively exert physical forces (solid stress) to compress tumor blood vessels, thus reducing vascular perfusion. Tumor interstitial matrix also contributes to solid stress, with hyaluronan implicated as the primary matrix molecule responsible for vessel compression due to its swelling behavior. Here we show, unexpectedly, that hyaluronan compresses vessels only in collagen-rich tumors – suggesting that collagen and hyaluronan together are critical targets for decompressing tumor vessels. We demonstrate that the angiotensin inhibitor losartan reduces stromal collagen and hyaluronan production, associated with decreased expression of pro-fibrotic signals TGF-β1, CCN2, and ET-1, downstream of angiotensin-II-receptor-1 inhibition. Consequently, losartan reduces solid stress in tumors resulting in increased vascular perfusion. Through this physical mechanism, losartan improves drug and oxygen delivery to tumors, thereby potentiating chemotherapy and reducing hypoxia in breast and pancreatic cancer models. Thus angiotensin inhibitors – inexpensive drugs with decades of safe use – could be rapidly repurposed as cancer therapeutics.**

## 3.2. Introduction

Drug and oxygen delivery in tumors is dependent on the organization and efficiency of perfused vessels[1-3]. Solid stress (pressure from solid tissue components) accumulates in tumors as cancer and stromal cells proliferate in a confined microenvironment created by cross-linked matrix molecules[4-6]. The matrix stores and transmits this stress throughout the tumor[7], collapsing blood vessels to limit perfusion[8,9]. Meanwhile, patients with low tumor perfusion – presumably with extensive hypoxia and impaired drug delivery – show poorer chemotherapy responses and shorter survival versus patients with high perfusion[10,11]. Thus there is an urgent need for drugs that can target solid stress to improve blood perfusion and drug delivery in tumors.

Stromal cells and matrix contribute to solid stress, but the mechanisms through which these components interact to compress tumor vessels remain unclear. Uncovering these mechanisms could lead to novel paradigms for enhancing tumor perfusion. In this study, we show that different tumor matrix components produced by cancer-associated fibroblasts (CAFs) collaborate to compress vessels. We demonstrate that angiotensin signaling blockade inactivates CAFs to reduce their production of these matrix components while also reducing CAF density. Through this mechanism, we find that angiotensin receptor blockers (ARBs) reduce solid stress, decompress tumor vessels, increase drug and oxygen delivery, and improve chemotherapy outcomes. Thus, solid stress can be targeted by decreasing CAF activity and agents that do so can improve tumor perfusion and enhance chemotherapy.

## 3.3. Results

*Hyaluronan and collagen collaborate to compress tumor blood vessels*

Hyaluronan has been proposed to be the primary matrix molecule responsible for vessel compression[12], but its exact mechanism remains unclear. Hyaluronan interacts with collagen in a complex manner[13], and both contribute to the accumulation of solid stress through these interactions[5]. Thus, we examined whether collagen may also affect vessel compression (Fig. 1a,b). We therefore measured vessel perfusion (patency) in multiple orthotopic tumors and compared it with hyaluronan and collagen levels. Interestingly, we found that both hyaluronan and collagen area fraction were inversely associated with perfused vessel fractions (Fig. 1c). The mean of these matrix area fractions had an even stronger inverse-correlation with perfusion, indicating a complex non-linear relationship between the two matrix molecules and perfusion. Surprisingly, we found that vessel perfusion did not correlate with hyaluronan area fractions in tumors with low collagen levels (Fig. 1d); rather, hyaluronan and perfusion were inversely correlated only in collagen-rich tumors. In contrast, perfusion inversely correlated with collagen area fraction in both hyaluronan-rich and hyaluronan-poor tumors (Fig 1e). These findings indicate that collagen is needed for hyaluronan to exert compression on blood vessels, suggesting that both are potential targets for vessel decompression in desmoplastic tumors.

*Angiotensin inhibition reduces stromal fibrosis signaling*

We therefore sought a translatable therapy that targets both collagen and hyaluronan. We recently found that the ARB losartan can reduce collagen I production in CAFs by downstream inhibition of TGF-β1 activation[14, 15] through TSP-1 inhibition[16-18]. Since hyaluronan synthesis is similarly TGF-β1-dependent, we expected that losartan would also decrease hyaluronan production. We generated transgenic FVB mice expressing the fluorescent protein dsRed driven by the promoter for alpha smooth-muscle actin (αSMA)[19], a marker for activated CAFs. In these mice (*αSMA-dsRed/FVB*), we orthotopically implanted AK4.4 pancreatic tumor cells, treated these mice with losartan or saline (control), then isolated the CAFs (activated pancreatic stellate cells) from their tumors using fluorescence-activated cell sorting (Supplementary Fig. S1). We confirmed that CAF expression of TGF-β1 and collagen I was reduced by losartan (Fig. 2a,b). We then measured expression of hyaluronan synthases (HAS) 1-3 in these CAFs and found

that HAS1-3 were also greatly decreased by losartan (Fig. 2a,b). Thus losartan is a dual-inhibitor of stromal collagen and hyaluronan production.

Losartan rapidly reduces established tumor matrix levels[13], which implies that it degrades or destabilizes matrix through an uncharacterized mechanism in addition to preventing matrix production through TGF-β1. CCN2 (CTGF), a matricellular protein, stabilizes the transient fibrosis produced by TGF-β1 activity[20, 21] and is downstream of angiotensin signaling through TGF-β1 in other fibrosis diseases[22, 23], suggesting that losartan could be destabilizing the matrix by inhibiting CCN2 expression. By comparing CAFs isolated from losartan- versus saline-treated mice, we found that losartan reduced expression of CCN2 (Fig. 2a,b). We next used immunohistochemistry to assess how losartan affects CCN2, active TGF-β1, and matrix levels in orthotopic E0771 and AK4.4 models, which recapitulate the desmoplasia observed in human mammary adenocarcinoma and in human pancreatic ductal adenocarcinoma, respectively (Supplementary Figs. 2, 3, 4). Losartan reduced both CCN2 and active TGF-β1 in E0771 breast and AK4.4 pancreatic tumors (Fig. 2c-f and Supplementary Fig. S5). Furthermore, losartan decreased collagen I and hyaluronan in both of these tumors (Fig. 3a-d and Supplementary Figs. S4, S6, S7). Thus, losartan decreases stromal matrix production through TGF-β1 while potentially destabilizing the existing matrix through CCN2. Collectively these effects lead to a reduction in collagen and hyaluronan levels in desmoplastic tumors.

*Angiotensin inhibition decreases CAF density in tumors*

Since the effects of losartan on matrix expression in tumors were pronounced, and since angiotensin signaling has been previously shown to activate fibroblasts in other fibrosis diseases[24, 25], we next tested whether losartan could also reduce CAF density. We found that losartan lowered the density of αSMA+ cells in E0771 and AK4.4 tumors (Fig. 3e,f and Supplementary Fig. S8), indicating a decrease in activated CAFs. In other fibrotic diseases, fibroblast activation occurs through endothelin-1 (ET-1) expression[26] downstream of TGF-β1[27] and angiotensin signaling[28]. Thus, we expected that losartan may reduce ET-1 expression by CAFs. Indeed, in the CAFs isolated from losartan- or saline-treated mice, we found that losartan decreased the expression of ET-1 (Fig. 2a,b). Therefore, losartan appears to reduce activation of fibroblasts or stellate cells to αSMA+ CAF phenotype, leading to a reduction in CAF density.

*AT1 and AT2 signaling opposingly affect tumor fibrosis*

To investigate how best to target angiotensin signaling, we next investigated the role of angiotensin receptor signaling in tumor desmoplasia. We first studied the effects of the angiotensin converting enzyme inhibitor (ACE-I) lisinopril on the matrix, because ACE-Is block both angiotensin-II-receptor-2 (AT1) and angiotensin-II-receptor-2 (AT2) signaling. Intriguingly, lisinopril reduced collagen I and hyaluronan in AK4.4 tumors to a lesser extent than losartan (Supplementary Fig. S9). This suggests that AT2 inhibition leads to increased collagen levels in tumors, in opposition to AT1 inhibition. We confirmed this by implanting E0771 in knockout mouse models of AT1 (*Agtr1a*$^{-/-}$) and AT2 (*Agtr2*$^{-/-}$). We found that tumors in the AT1 knockout mice had lower levels of collagen I and hyaluronan than tumors in wild-type mice (Fig. 4a,b), whereas the tumors in AT2 knockout mice had higher collagen I and hyaluronan levels than tumors in wild-type mice (Fig. 4c,d), indicating that stromal AT2 signaling inhibits tumor desmosplasia while AT1 signaling promotes it. Importantly, this result fits with the known effects of angiotensin signaling on fibrosis in other diseases[30,31]. To confirm the relevance of stromal AT1 and AT2 inhibition, we measured the expression of these receptors in CAFs and cancer cells from wild-type mice. We found that CAFs isolated from AK4.4 tumors express far more AT1 and AT2 than AK4.4 or E0771 cancer cells (Fig. 4e). We confirmed this result with immunohistochemistry in E0771 tumors, where we found that a moderate fraction of CAFs in these tumors express AT1 at high levels while most other cells express AT1 at low levels, whereas most CAFs express high levels of AT2 while a small fraction of other cells express similar AT2 levels (Fig. 4f,g). These results indicated that the cellular targets of angiotensin blockers relating to matrix production are CAFs rather than cancer cells. Thus, the anti-desmoplasia benefits of ARBs are due to specific AT1 inhibition in tumor stroma, and ACE-Is may not provide the same benefits due to combined AT1 and AT2 inhibition.

*Angiotensin inhibition lowers solid stress in tumors*

We next investigated the effects of losartan on solid stress in tumors. We measured solid stress in these tumors using our recently established technique[5]. Losartan reduced solid stress in both E0771 and AK4.4 tumors (Fig. 5a), as well as in 4T1 breast and Pan-02 pancreatic tumors (Fig. 5b). We additionally tested a panel of ARBs and found that they all reduced solid stress (Supplementary Fig. S10), further suggesting that the mechanism of action is via AT1 inhibition rather than an off-target effect of losartan. These data indicate that angiotensin blockers may be capable of decompressing vessels in desmoplastic tumors by reducing solid stress through their anti-matrix effects.

*Angiotensin inhibition decompresses tumor blood vessels*

We hypothesized that the reduction in solid stress by losartan would increase vascular perfusion in our desmoplastic tumor models. We found these tumors to be severely hypo-perfused (Supplementary Fig. S4): only 23% of vessels in E0771 breast tumors and 21% in AK4.4 pancreatic tumors were perfused with blood (Fig. 6a,b). Of note, collagen-rich areas seemed to co-localize with low-perfusion areas (Fig. 3a). Losartan significantly improved the perfused vessel fraction to 43% in E0771 and 45% in AK4.4 (Fig. 6a,b). Losartan treatment also increased the fraction of vessels with open lumen in E0771 and AK4.4 (Fig. 6c), further indicating vascular decompression as the mechanism of action[9]. Interestingly, the open lumen fraction was higher than the perfused vessel fraction in both models – perhaps due to collapse or occlusion in feeding vessels or flow cessation and clot formation[9]. Importantly, losartan did not significantly improve perfusion in the well-perfused L3.6pl tumor model, which has low collagen and 68% vessel perfusion at baseline (Supplementary Fig. S11), confirming the findings of our previous study[14]. Thus, losartan can increase blood perfusion in tumors by opening existing collapsed blood vessels.

Despite the previous classification of angiotensin inhibitors as antiangiogenics[32], we found that losartan did not reduce VEGF levels (Supplementary Fig. S12), affect the CD31+ vessel density in these tumors (Fig. 6d,e), or decrease vessel diameter (Supplementary Fig. S13). Furthermore, losartan increased the effective permeability of the blood vessels for all sizes of nanoparticles (Supplementary Fig. S14), which is inconsistent with the 'vascular normalization' effect that results from antiangiogenic therapy[33]. Moreover, this dose did not decrease blood pressure in a separate group of tumor-bearing mice with advanced disease (Supplementary Fig. S15)[34], and correspondingly did not affect flow rates in individual blood vessels (Supplementary Fig. S16). As such, we confirmed that losartan does not improve perfusion by reducing vessel leakiness or increasing blood flow – as seen after vascular normalization[33,35], but rather does so through 'microenvironmental normalization' (Fig. 6f).

*Angiotensin inhibitors enhance drug and oxygen delivery*

Since drug and oxygen delivery to tissues is governed by vascular perfusion, we tested the effects of losartan on delivery to tumors. We first engaged a mathematical approach to analyze the efficiency of the vascular network for drug and oxygen delivery. Using multiphoton microscopy, we imaged the perfused vessel networks of E0771 tumors (Fig.

6a). Based on metrics of intervascular spaces[34], we found that losartan reduces the distance drugs and oxygen must travel to reach tumor cells (Supplementary Fig. S17). We then measured the total tissue accumulation of the small-molecule chemotherapeutic fluorouracil (5-FU). Losartan improved 5-FU delivery to AK4.4 tumors, while not affecting delivery to normal organs (Fig. 6g). These data imply that this strategy for enhancing delivery selectively affects tumors, which is expected since solid stress does not accumulate in most normal organs[5]. We then studied oxygenation using phosphorescence quenching microscopy[35]. We found that losartan treatment maintained tumor oxygen levels in E0771 tumors, while control-treated tumors showed a typical growth-dependent drop in oxygenation (Fig. 6h,i). We confirmed this decrease in tumor hypoxia by using pimonidazole staining in E0771 and 4T1 (Fig. 6j and Supplementary Figs. S18, S19). Thus, reducing solid stress through 'microenvironmental normalization' with angiotensin inhibitors increases the delivery of drugs and oxygen to tumors.

*Angiotensin inhibition potentiates chemotherapy*

Given these effects on delivery, we tested losartan in combination with doxorubicin in E0771 and 4T1 tumors, or with 5-FU in AK4.4 tumors. We found that the combination of losartan with chemotherapy significantly delayed E0771, 4T1, and AK4.4 tumor growth, while monotherapy had no effect (Fig. 7a,b,c and Supplementary Fig. S20). Moreover, the combination of losartan and chemotherapy increased median survival (time to death or excessive tumor burden) for mice bearing E0771 and 4T1 tumors compared with monotherapy (Fig. 7d,e). Similarly, the combination increased median survival (time to death) for mice bearing AK4.4 tumors, whereas monotherapy did not extend survival (Fig. 7f). Importantly, losartan alone – despite increasing blood perfusion – did not shorten survival in any model. The results of the combination for survival were somewhat better than for primary tumor growth delay, indicating a possible effect on metastases. Correspondingly, losartan slightly decreased metastasis in E0771 (Supplementary Fig. S21), consistent with previous studies[36] and likely due to the role of angiotensin signaling in promoting the metastatic cascade[37,38]. Of note, we found that losartan combined with doxorubicin delayed tumor growth in both immunodeficient and immunocompetent models of breast cancer (Fig. 7a,b and Supplementary Fig. S21), though the effects appeared less pronounced in immunocompetent mice even at high doses of doxorubicin. This might be due to differential effects on bone-marrow derived cells and proliferating endothelial cells, or resistance induced by the immune microenvironment[39]. Together, these data demonstrate that angiotensin inhibitors can

improve the effectiveness of small-molecule chemotherapeutics through anti-matrix effects.

## 3.4. Discussion

This study highlights the complex role of the tumor matrix as a drug delivery barrier. While the distribution of larger drugs such as nanomedicines is hindered by steric interactions with collagen, the matrix does not directly limit the distribution of smaller, conventional chemotherapeutics[39]. Rather, the matrix indirectly limits the delivery of conventional chemotherapy through vascular compression. Both hyaluronan and collagen fibers contribute to solid stress in tumors: hyaluronan does so by resisting compression, while collagen does so by resisting tension and confining the local microenvironment[5]. Our results lead to a new model for how hyaluronan and collagen affect vessel compression. As cancer and stromal cells proliferate, they attempt to expand their local tumor microenvironment, exerting tensile stress. This tensile stress stretches collagen fibers in the microenvironment, which store tensile elastic 'strain' energy and stiffen, thereby resisting this expansion. The effect is to confine these cells, such that the force they generate while proliferating becomes a compressive stress. These cells cannot transmit compressive stress perpendicularly to the fibers of this stiffened collagen, so this compressive stress is instead exerted largely on hyaluronan in the local tumor microenvironment. Hyaluronan, whose internal charges repel each other electrostatically and trap water molecules, resists this compression, only storing compressive 'strain' energy until maximally compressed. Beyond this maximal compression, the excess compressive stress is transmitted by hyaluronan to tumor vessels. These tumors vessels, which lack the complete coverage by pericytes and basement membrane that fortifies mature vessels, are structurally weak and cannot resist compression. If collagen levels are low in a tumor, the microenvironment is more easily expanded by proliferating cells and thus compressive stress is not produced to as high a level. As a result, hyaluronan does not contribute to vessel compression in collagen-poor tumors. If hyaluronan levels are low, the compressive stress is not transmitted to vessels to as great a degree. Thus, hyaluronan appears responsible for transmitting compressive stress to vessels in all cases when there is not direct cell contact, while collagen enables compressive stress to be applied to hyaluronan by cells.

Analyses of retrospective clinical data suggest that the use of angiotensin-II receptor type-1 blockers (ARBs) and angiotensin converting enzyme inhibitors (ACE-Is) to manage hypertension in cancer patients receiving standard therapies is correlated with longer survival in pancreatic and other cancers[40-43] as well as a reduced risk of recurrence in breast cancer[44]. However, a causal relationship between the use of ARBs/ACE-Is and

its clinical benefit – as well as the mechanism behind this potential effect – has not been revealed. AT1 signaling has been shown to increase VEGF expression by CAFs[45], and both ACE-Is and ARBs can decrease VEGF expression and angiogenesis[46, 47]. It has therefore been assumed that their indirect antiangiogenic properties, through downstream VEGF inhibition, benefit survival additively. Our current findings, in line with our previous report[14], do not support this antiangiogenic mechanism. Furthermore, we detected no growth delay or survival benefit with losartan monotherapy in our study. This is in contrast to the ability of angiotensin signaling through AT1 to promote tumor growth and metastasis[32, 37, 38, 48, 49], with signaling through AT2 hindering growth[50]. This is perhaps because these growth inhibitory effects are primarily seen at much higher doses of ARBs[38, 48, 51] or with long-term treatment[52]; indeed, when used at low doses, ARBs have been shown by others to not cause a growth delay[47]. It is also possible that this VEGF inhibition is due to direct effects of angiotensin inhibitors on cancer cells, and that our models do not respond similarly because the cancer cells used do not express high levels of AT1 or AT2. These inconsistent data notwithstanding, it should be noted that antiangiogenic therapy with bevacizumab has failed to prolong survival in desmoplastic tumors such as breast and pancreatic cancer[9], casting doubt on a possible antiangiogenic mechanism for the benefits observed with angiotensin inhibitors.

Here we have found that angiotensin inhibitors actually increase vessel perfusion through vascular decompression, doing so by reducing stromal activity and production of matrix components responsible for compression. Notably, these drugs are the first to target all stromal components (CAFs, hyaluronan, and collagen) known to contribute to solid stress[8]. Our findings also suggest that AT2 agonists or inhibitors of downstream signaling through TGF-β1, CCN2, or ET-1, may similarly reduce solid stress to enhance chemotherapy – though such agents have not been tested in this way. Similarly, angiotensin(1-7), a MAS agonist that can reduce CAF matrix production, may be useful for targeting solid stress[53]. Meanwhile, there are challenges to address for translation. Deleterious effects on blood pressure may contraindicate angiotensin inhibitors for some patients[54, 55]. Furthermore, we expect that angiotensin inhibitor distribution into tumors may be the most important factor controlling efficacy: drugs displaying a lack of tissue penetration (i.e. candesartan) would therefore be poor candidates relative to those with high penetration (i.e. losartan, telmisartan)[56]. Indeed, the inadequate tumor penetration of candesartan may explain why it only improved chemotherapy outcomes modestly, when comparing high versus low candesartan doses, in a recent pancreatic cancer study[54]. These factors are why losartan was selected over other angiotensin inhibitors for

a recently-initiated clinical trial in pancreatic cancer (NCT01821729) at Massachusetts General Hospital. Regardless, the safety and low cost of ARBs and ACE-Is – along with their potentiation of conventional chemotherapy – makes a strong case for repurposing angiotensin inhibitors as adjuncts for cancer therapies.

## 3.5. Figures

**Figure 3-1 Collagen and hyaluronan interact to compress tumor blood vessels.**

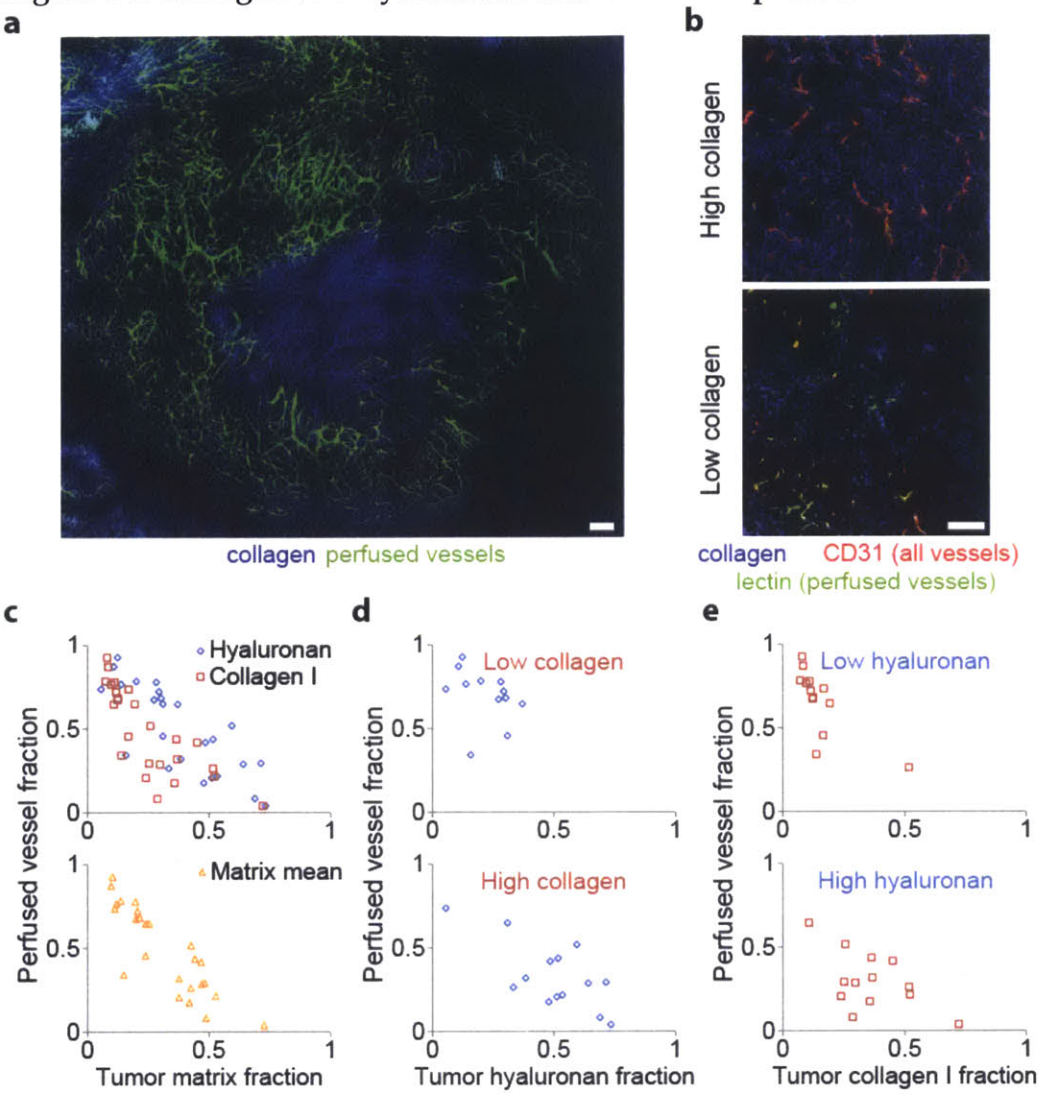


a, Representative image from intravital multiphoton microscopy of perfused tumor vessels (green) and collagen (blue), showing that high collagen levels colocalize with low perfusion in an E0771 breast tumor. Scale bar, 200$\mu$m. b, Histology images of vascular perfusion in orthotopic AK4.4 pancreatic tumors with high versus low collagen levels. High local collagen I levels (blue) appear to colocalize with collapsed vessels (red, collapsed; green/yellow, perfused) *in vivo*. Scale bar, 100μm. c, Correlation of perfused vessel fraction versus tumor matrix area fractions in multiple orthotopic pancreatic tumor models (AK4.4 and L3.6pl) in mice. Following lectin injection and animal sacrifice, perfusion was quantified as the fraction of vessels that are both lectin- and CD31-positive out of all CD31-positive vessels. Perfusion inversely correlates with both hyaluronan ($R$=-0.79, $P$<0.001, Pearson correlation) and collagen I ($R$=-0.78, $P$<0.001, Pearson correlation), but has a stronger inverse correlation ($R$=-0.86, $P$<0.001, Pearson correlation) with the average matrix area fraction. d, Grouping these tumors into those with either low (<17%) or high (≥17%) collagen reveals that perfusion does not correlate ($R$=-0.33, Pearson correlation) with hyaluronan in collagen-poor tumors but does inversely correlate ($R$=-0.71, $P$=0.004, Pearson correlation) in collagen-rich tumors. e, In

contrast, grouping the tumors into those with either low (<33%) or high (≥33%) hyaluronan shows that perfusion inversely correlates with collagen I in both hyaluronan-poor ($R$=-0.73, $P$=0.003, Pearson correlation) and hyaluronan-rich ($R$=-0.57, $P$=0.040, Pearson correlation) tumors.

**Figure 3-2 Losartan decreases pro-fibrotic stromal activity in tumors.**

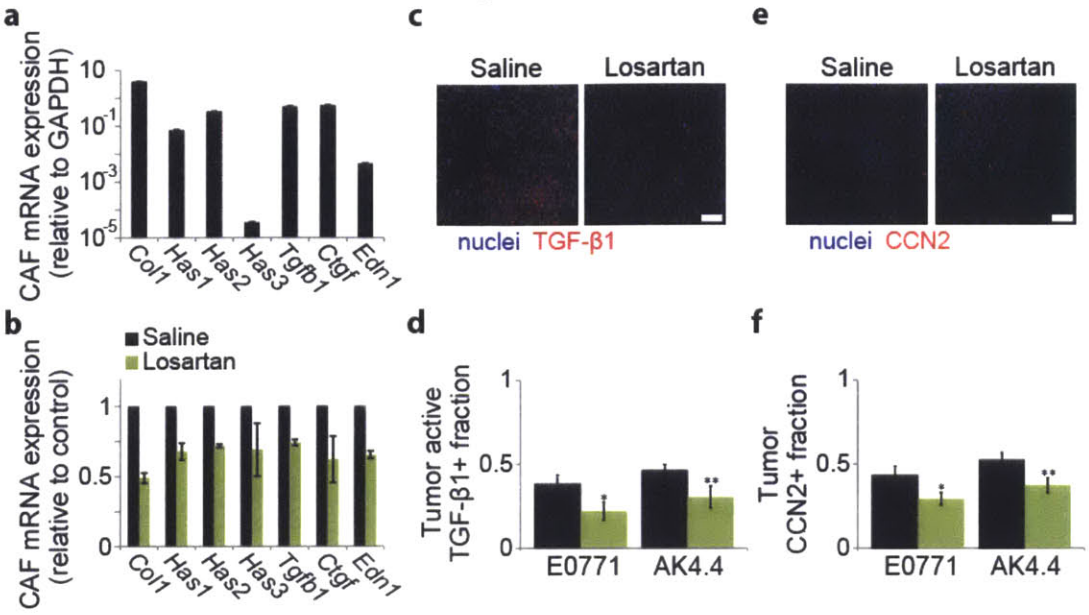


a, Expression levels of fibrosis-related genes in murine cancer-associated fibroblasts (CAFs) isolated from orthotopic AK4.4 pancreatic tumors. AK4.4 tumors were orthotopically implanted in *αSMA-dsRed/FVB* mice, resulting in αSMA+ CAFs that express dsRed. These mice were treated with losartan or saline (control), then the CAFs from their tumors were isolated using fluorescence-activated cell sorting for dsRed. The isolated control CAFs express high mRNA levels of collagen I (*Col1*), hyaluronan synthases 1-2 (*Has1*, *Has2*), TGF-β1 (*Tgfb1*), and CCN2 (*Ctgf*), with low levels of hyaluronan synthase 3 and moderate levels of ET-1 (*Edn1*). Levels normalized to GAPDH expression. b, Comparison of expression levels of fibrosis-related genes in the CAFs isolated from losartan- or saline-treated (control) mice. Losartan reduces the mRNA expression of each of these pro-fibrotic genes in CAFs ($P<0.05$, Student's t-test). Levels normalized to saline control. c, Histology images showing the effect of losartan on tumor TGF-β1 expression. Scale bar, 100μm. d, Immunohistochemical analysis of TGF-β1 expression with losartan treatment. Losartan reduces the expression of TGF-β1 in E0771 ($P=0.048$, Student's t-test) and AK4.4 tumors ($P=0.044$, Student's t-test). e, Histology images showing the effect of losartan on tumor CCN2 expression. Scale bar, 100μm. f, Immunohistochemical analysis of CCN2 expression with losartan treatment. Losartan reduces the expression of CCN2 in E0771 ($P=0.044$, Student's t-test) and AK4.4 ($P=0.046$, Student's t-test) tumors. Scale bar, 100μm. Animal numbers $n=4$ (CAF expression), $n=7$-8 (E0771 TGF-β1, CCN2), $n=4$-6 (AK4.4 TGF-β1, CCN2). Error bars indicate standard error of the mean.

**Figure 3-3 Losartan reduces matrix and stromal density in tumors.**

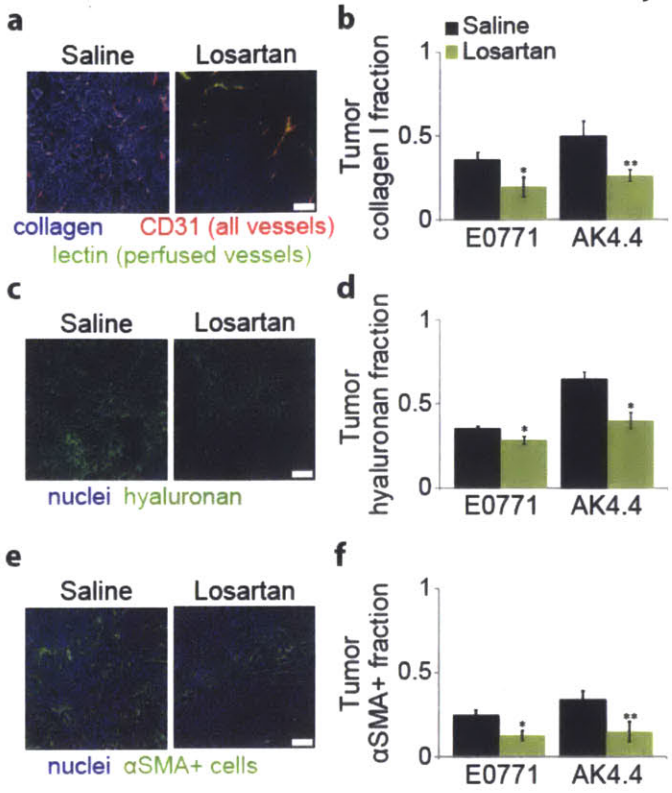


a, Histology images showing the effect of losartan on tumor collagen levels and perfusion. Scale bar, 100μm. b, Immunohistochemical analysis of tumor collagen levels following losartan treatment. Losartan decreases the collagen I positive area fraction in E0771 ($P$=0.040, Student's t-test) and AK4.4 ($P$=0.022, Student's t-test) tumors. c, Histology images showing the effect of losartan on tumor hyaluronan levels. Scale bar, 100μm. d, Immunohistochemical analysis of tumor hyaluronan levels following losartan treatment. Losartan also reduces the hyaluronan positive area fraction in E0771 ($P$=0.048, Student's t-test) and AK4.4 ($P$=0.019, Student's t-test) tumors, as assessed using a hyaluronan binding protein probe. e, Histology images showing the effect of losartan on tumor αSMA+ CAF levels. Scale bar, 100μm. f, Immunohistochemical analysis of αSMA+ CAF density with losartan treatment. Losartan reduces the CAF density in E0771 ($P$=0.019, Student's t-test) and AK4.4 ($P$=0.040, Student's t-test) tumors. Animal numbers $n$=5-7 (E0771 collagen), $n$=4-6 (AK4.4 collagen), $n$=4-5 (E0771 hyaluronan), $n$=4 (AK4.4 hyaluronan), $n$=5 (E0771 αSMA), $n$=5-6 (AK4.4 αSMA). Error bars indicate standard error of the mean.

**Figure 3-4 Stromal angiotensin signaling induces matrix production in tumors.**

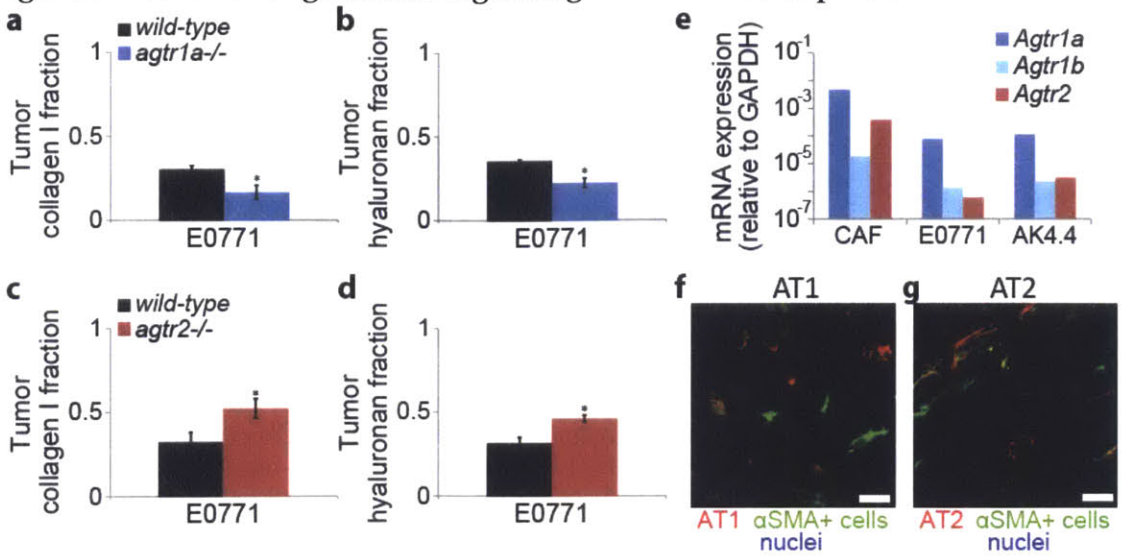


a, Tumor collagen and b, hyaluronan levels in angiotensin-II-receptor-1 (AT1) knockout mice. Orthotopic E0771 breast tumors implanted in AT1 knockout mice (*Agtr1a*$^{-/-}$) have (a) a lower collagen I area fraction ($P$=0.026, Student's t-test) and (b) a lower hyaluronan area fraction ($P$=0.011, Student's t-test) than E0771 tumors implanted in wild-type C57BL/6 mice. c, Tumor collagen and d, hyaluronan levels in angiotensin-II-receptor-2 (AT2) knockout mice. Orthotopic E0771 breast tumors implanted in AT2 knockout mice (*Agtr2*$^{-/-}$) have (c) a higher collagen I area fraction ($P$=0.047, Student's t-test) and (d) a higher hyaluronan area fraction ($P$=0.012, Student's t-test) than E0771 tumors implanted in wild-type C57BL/6 mice. Tumors were time- and size-matched at ~200mm$^3$. e, Expression of AT1 (*Agtr1a* and *Agtr1b* genes) and AT2 (*Agtr2* gene) mRNA in murine cancer-associated fibroblasts (CAFs) and cancer cells. CAFs isolated from AK4.4 tumors express over one order of magnitude more AT1 than either E0771 or AK4.4 cancer cells. Similarly, the CAFs express over two orders of magnitude more AT2 than either E0771 or AK4.4 cells. f, Expression of AT1 (red) in αSMA+ CAFs (green) and cancer cells in tumors. We imaged CAFs based on αSMA+ expression in E0771 tumors. We found that some CAFs in these tumors express AT1 at high levels while other cells express AT1 at low levels. Colocalization is shown in yellow. Scale bar, 25$\mu$m. g, Expression of AT2 (red) in αSMA+ CAFs (green) and cancer cells in tumors. Most CAFs express high levels of AT2 while some other cells express similar AT2 levels. Colocalization is shown in yellow. Scale bar, 25$\mu$m. Animal numbers $n$=4-5. Error bars indicate standard error of the mean.

**Figure 3-5 Losartan targets solid stress in tumors.**

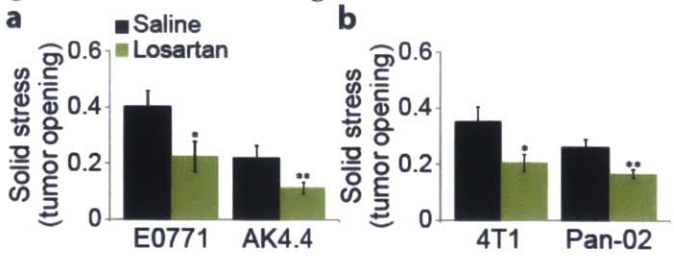


a, Solid stress levels in tumors after angiotensin inhibition using losartan. Solid stress was assessed using an ex vivo technique involving the measurement of the extent of tumor tissue relaxation (tumor opening relative to tumor diameter) following a stress-releasing incision, with larger openings indicating higher stress[5]. Through its anti-matrix effects, losartan reduces solid stress in E0771 ($P$=0.049, Student's t-test) and AK4.4 ($P$=0.043, Student's t-test). b, Losartan reduces solid stress in additional models, including 4T1 breast tumors ($P$=0.036, Student's t-test) and Pan-02 pancreatic tumors ($P$=0.0092, Student's t-test). Animal numbers $n$=5 (E0771), $n$=8-9 (AK4.4), $n$=10-11 (4T1), $n$=4-8 (Pan-02). Error bars indicate standard error of the mean.

**Figure 3-6 Losartan decompresses tumor vessels to increase drug and oxygen delivery.**

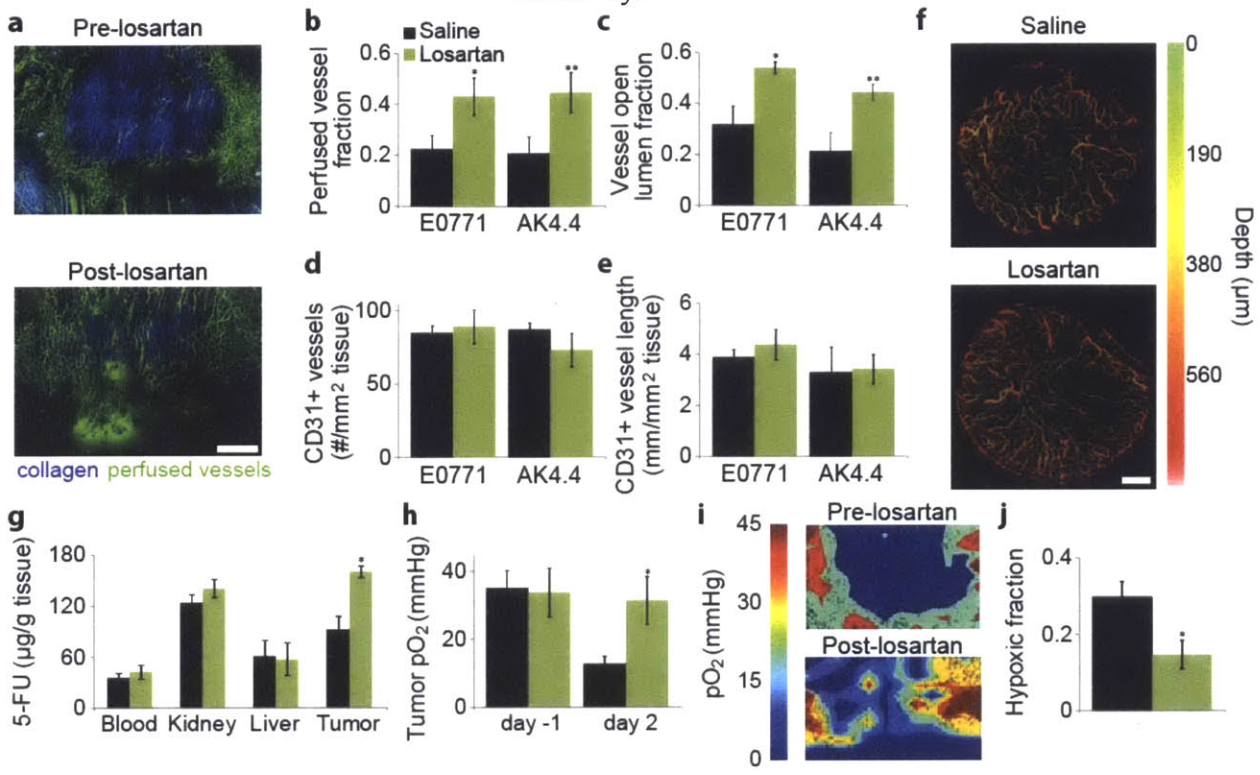


a, Representative images from intravital multiphoton microscopy of perfused tumor vessels (green) and collagen (blue), showing losartan increases the density of perfused vessels in an E0771 breast tumor. Scale bar, 1mm. b, Perfused vessel fractions after angiotensin inhibition using losartan. Losartan increases the fraction of vessels that are perfused in orthotopic E0771 breast ($P$=0.038, Student's t-test) and AK4.4 pancreatic ($P$=0.039, Student's t-test) tumors. c, Losartan also increases the fraction of vessels with open lumen in E0771 ($P$=0.040, Student's t-test) and AK4.4 ($P$=0.015, Student's t-test) tumors, indicating decompression as the mechanism. d, Vessel density and e, vessel length following angiotensin inhibition using losartan. Losartan does not affect vessel density, as quantified by the vessel number density (d) and the total vessel length (e), indicating no antiangiogenic effect at this 40mg/kg dose. f, Representative images from intravital optical frequency domain imaging of perfused vessels with losartan treatment. E0771 tumors in control mice have a low density and poor distribution of perfused vessels in three dimensions, whereas losartan-treated mice showed a more even distribution and higher density of perfused vessels. Scale bar, 1mm. g, Small-molecule drug delivery to tumors and various organs after angiotensin inhibition with losartan. Losartan increases the accumulation of the small-molecule chemotherapeutic 5-FU in AK4.4 pancreatic tumors by 74% ($P$=0.0063, Student's t-test) while not affecting accumulation in the normal organs. h, Oxygen delivery to tumors measured by phosphorescence quenching microscopy during angiotensin inhibition using losartan, with i, representative images. Losartan maintains the level of oxygenation (h) in the tissue, versus control tumors that become progressively more hypoxic with time ($P$=0.030, Student's t-test) as the tumors grow from 3mm to 5mm in diameter. Losartan increases oxygenation in some tumors (i), whereas all control tumors decrease in oxygen levels. Losartan also appears to result in a more homogenous distribution of well-oxygenated tumor tissue. Scale bar, 100μm. j, Hypoxic fraction in tumors measured by

pimonidazole injection and staining following angiotensin inhibition with losartan. Losartan decreases the hypoxic fraction in E0771 tumors ($P$=0.019, Student's t-test) due to the increase in oxygen delivery. Animal numbers $n$=7-9 (vessels), $n$=4-5 (vessel lumen), $n$=4 (drug delivery), $n$=6 (oxygen delivery), $n$=6-7 (hypoxia). Error bars indicate standard error of the mean.

**Figure 3-7 Losartan potentiates chemotherapy.**

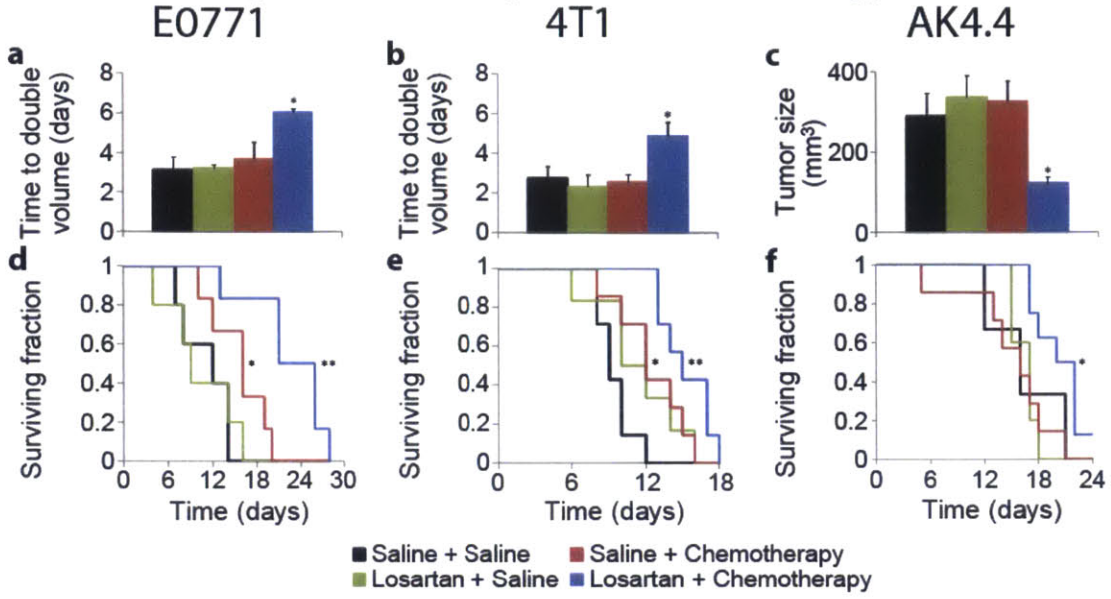


a, Quantification of tumor growth rates, based on the time to reach double the initial volume, for orthotopic E0771 breast tumors in response to treatment with losartan or saline control (40mg/kg daily from day 0 on) in combination with either the small-molecule chemotherapeutic doxorubicin or saline control (2mg/kg every 3 days from day 1 on). Doxorubicin and losartan monotherapy induce no significant growth delay versus the control treatment in these aggressive tumors. In contrast, their combination greatly limits tumor growth ($P$=0.040, Student's t-test). b, Quantification of tumor growth rates, based on the time to reach double the initial volume, for orthotopic 4T1 breast tumors using the same treatments as with E0771. Doxorubicin and losartan monotherapy induce no significant growth delay versus the control treatment. In contrast, their combination greatly limits tumor growth ($P$=0.024, Student's t-test). c, Volumes of orthotopic AK4.4 pancreatic tumors on day 7 in response to treatment with losartan or saline control (40mg/kg daily from day 0-7) in combination with either the small-molecule chemotherapeutic 5-FU or saline control (60mg/kg on days 2 and 6). 5-FU and losartan monotherapy induce no significant growth delay versus the control treatment, whereas their combination greatly inhibited tumor growth ($P$=0.0085, Student's t-test). d, Animal survival for E0771-bearing mice following the initiation of treatment. Doxorubicin monotherapy improves survival versus the control ($P$=0.048, log-rank test), while the combination of doxorubicin and losartan enhances this survival increase versus doxorubicin monotherapy ($P$=0.014, log-rank test). e, Animal survival for 4T1-bearing mice following the initiation of treatment. Doxorubicin monotherapy improves survival versus the control ($P$=0.045, log-rank test), while the combination of doxorubicin and losartan enhances this survival increase versus doxorubicin monotherapy ($P$=0.050, log-rank test). f, Animal survival for AK4.4-bearing mice following the initiation of treatment. The combination of 5-FU and losartan enhances survival versus 5-FU ($P$=0.019, log-rank test) or losartan monotherapy ($P$=0.027, log-rank test). Animal numbers $n$=5-6 (E0771, AK4.4 growth), $n$=3-8 (AK4.4 survival), $n$=6-7 (4T1). Error bars indicate standard error of the mean. Statistical tests were corrected for multiple comparisons using the Holm-Bonferroni method.

**Figure 3-8 Supplementary Figure S1. CAFs isolated from pancreatic tumors in mice.**

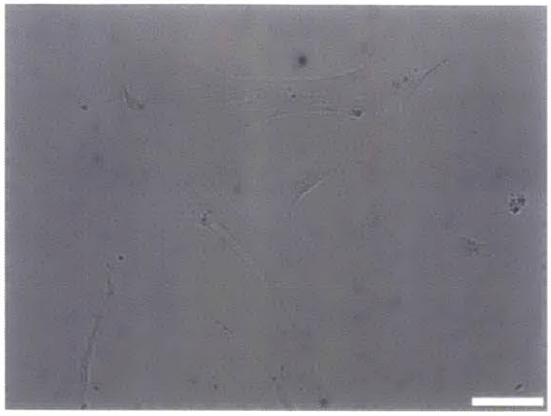

**Supplementary Figure S1. CAFs isolated from pancreatic tumors in mice.** We generated *αSMA*$^{P}$*-dsRed/Tie2*$^{P}$*-GFP*/FVB double-transgenic mice by crossing *Tie2*$^{P}$*-GFP*/FVB mice with *αSMA*$^{P}$*-dsRed* mice. Once established, this line was backcrossed to FVB mice for at least 10 generations. Cancer-associated fibroblasts (CAFs) were isolated from AK4.4 tumors implanted in these mice. These cells were cultured, and maintain typical fibroblast morphology. Scale bar, 20μm.

**Figure 3-9 Supplementary Figure S2. Compression of tumor blood vessels in human breast cancer.**

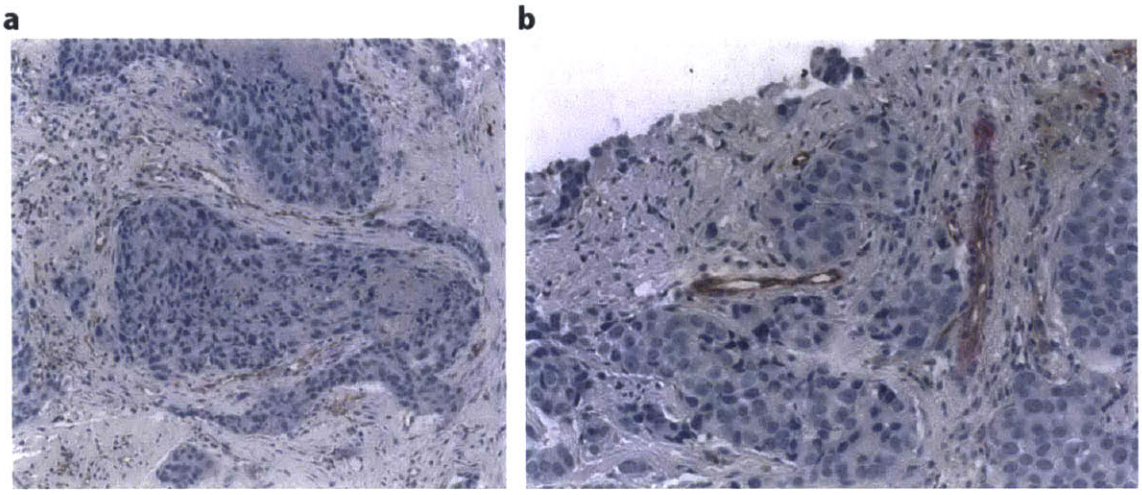


**Supplementary Figure S2. Compression of tumor blood vessels in human breast cancer. a,b**, Biopsies from patients with breast ductal adenocarcinomas, stained for CD31-positive vessels (brown). Unbridled cell proliferation of these tumor and stromal cells in a confined microenvironment results in vessel compression in the stroma (**a**) and within tumor nodes (**b**). All vessels appear to be compressed to some degree, with many completely collapsed. Left image is a 10x field, right image is a 20x field.

**Figure 3-10** Supplementary Figure S3. AK4.4 pancreatic tumors recapitulate the desmoplasia and hypo-perfusion of genetically-engineered KPC mouse tumors and human pancreatic ductal adenocarcinoma.

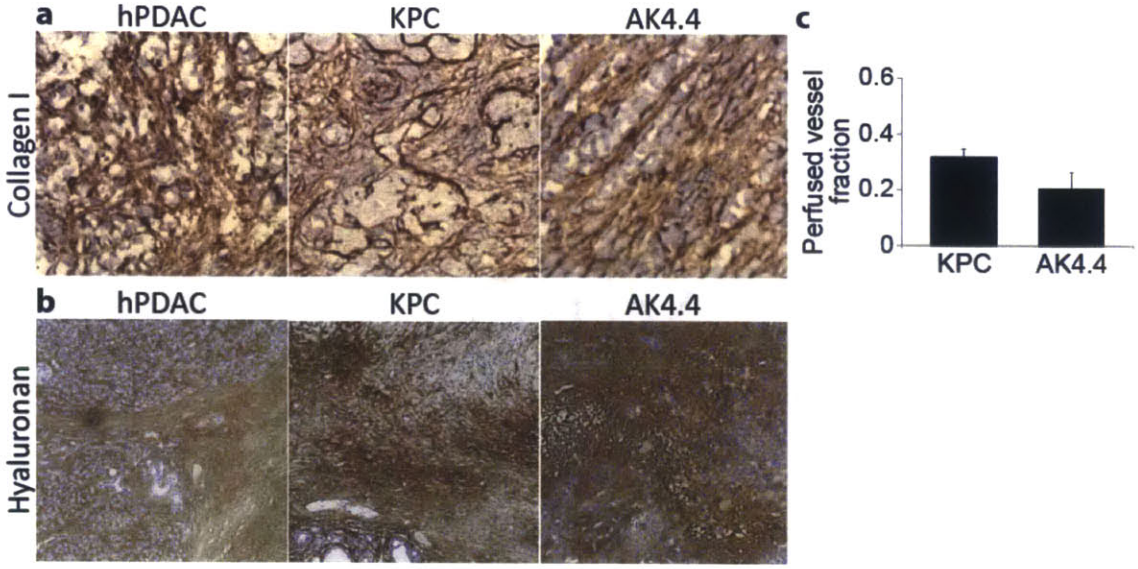


**Supplementary Figure S3. AK4.4 pancreatic tumors recapitulate the desmoplasia and hypo-perfusion of genetically-engineered KPC mouse tumors and human pancreatic ductal adenocarcinoma.** a,b, Histology comparing desmoplasia in human pancreatic ductal adenocarcinoma (hPDAC) tumors, KPC mouse tumors, and AK4.4 tumors in mice. AK4.4 has a similar composition to KPC and human PDAC, including high levels of (a) collagen I (brown) and (b) hyaluronan (brown). Collagen images are 20x fields, hyaluronan are 10x fields. c, Perfused vessel fractions, measured by histology with lectin and CD31 co-staining, in AK4.4 and KPC tumors. Both tumors show similarly low levels of vascular perfusion, a hallmark of PDAC. KPC perfusion data taken from the literature[4]. Animal numbers $n$=3 (KPC vessels), $n$=7 (AK4.4 vessels). Error bars indicate standard error of the mean.

**Figure 3-11 Supplementary Figure S4. Losartan improves the perfusion of tumor blood vessels in mouse breast and pancreatic tumors.**

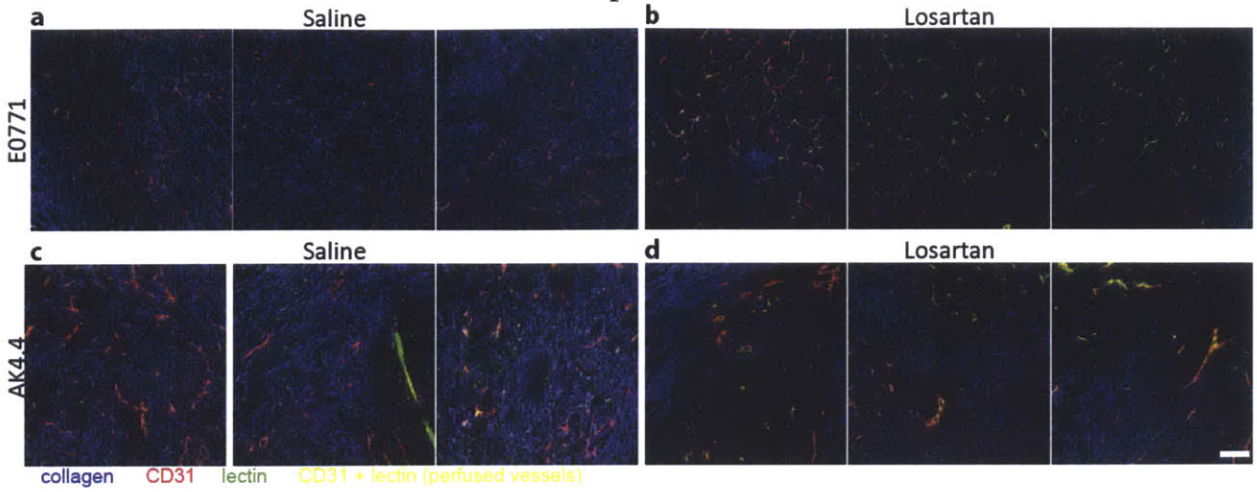


**Supplementary Figure S4. Losartan improves the perfusion of tumor blood vessels in mouse breast and pancreatic tumors. a,b,c,d**, Histology of mouse tumors showing collagen I (blue), CD31-positive vascular endothelium (red), and lectin-positive vessels (green), with CD31-lectin co-staining (yellow) denoting perfused vessels. Control E0771 breast tumors (**a**) are dense with collagen I and vessels, yet only a small fraction of these vessels are perfused. Control AK4.4 pancreatic tumors (**c**) have higher collagen I levels and a lower vessel density than E0771, with vessels that are also poorly perfused. Losartan improves perfusion in E0771 (**b**) and AK4.4 (**d**) without anti-angiogenic effects. Scale bar, 100μm.

**Figure 3-12 Supplementary Figure S5. Losartan reduces the expression of active-TGF-β1 and CCN2 in mouse breast and pancreatic tumors.**

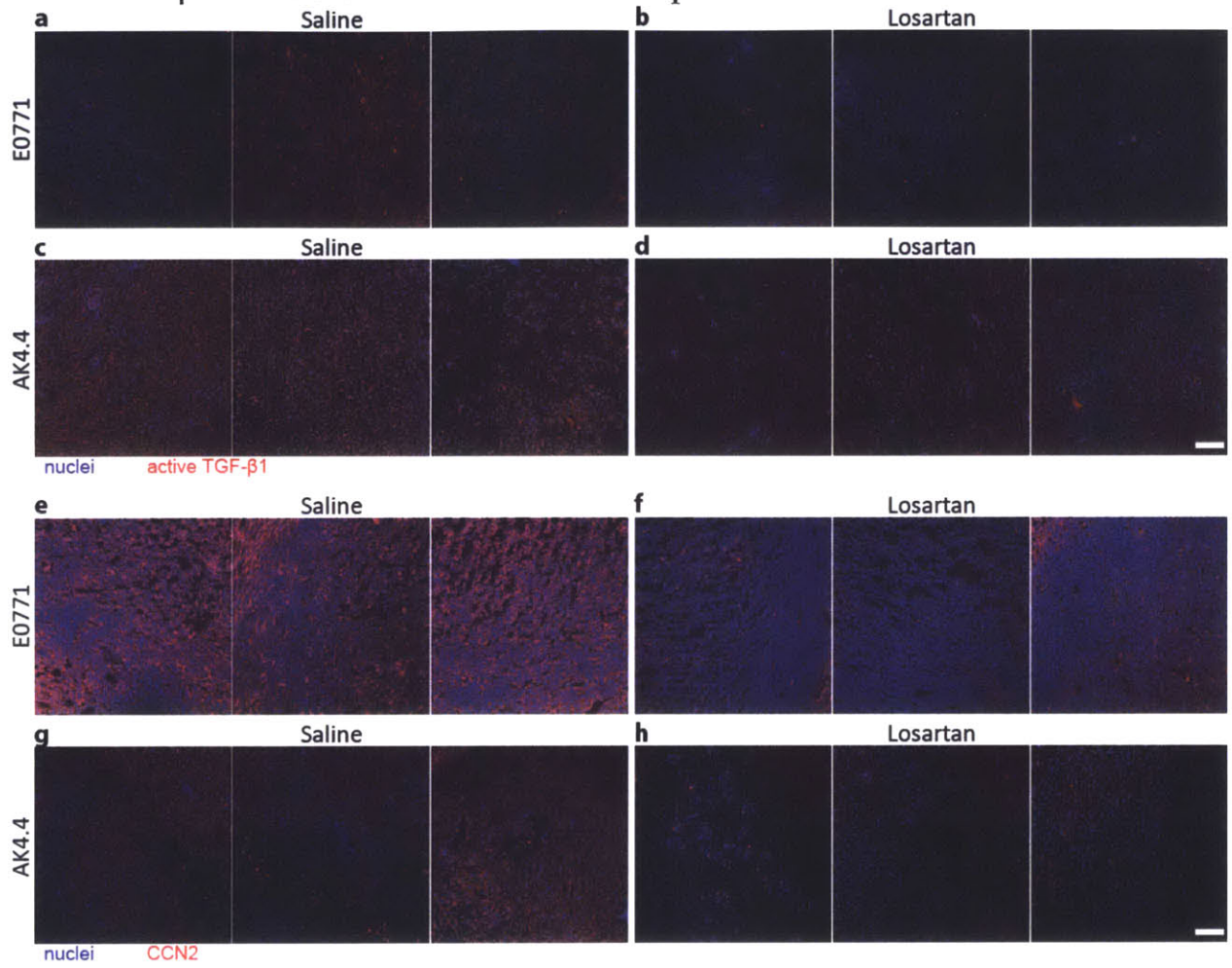


**Supplementary Figure S5. Losartan reduces the expression of active-TGF-β1 and CCN2 in mouse breast and pancreatic tumors. a,b,c,d**, Histology of mouse tumors showing active-TGF-β1 (red) and cell nuclei (blue). Control E0771 breast tumors (**a**) and AK4.4 pancreatic tumors (**c**) have high active-TGF-β1 levels. Losartan reduces active-TGF-β1 expression in E0771 (**b**) and AK4.4 (**d**). Scale bar, 100μm. **e,f,g,h**, Histology of mouse tumors showing CCN2 (red) and cell nuclei (blue). Control E0771 breast tumors (**e**) and AK4.4 pancreatic tumors (**g**) have high CCN2 levels. Losartan reduces CCN2 expression in E0771 (**f**) and AK4.4 (**h**). Scale bar, 100μm.

**Figure 3-13 Supplementary Figure S6. Losartan reduces the expression of hyaluronan in mouse breast and pancreatic tumors.**

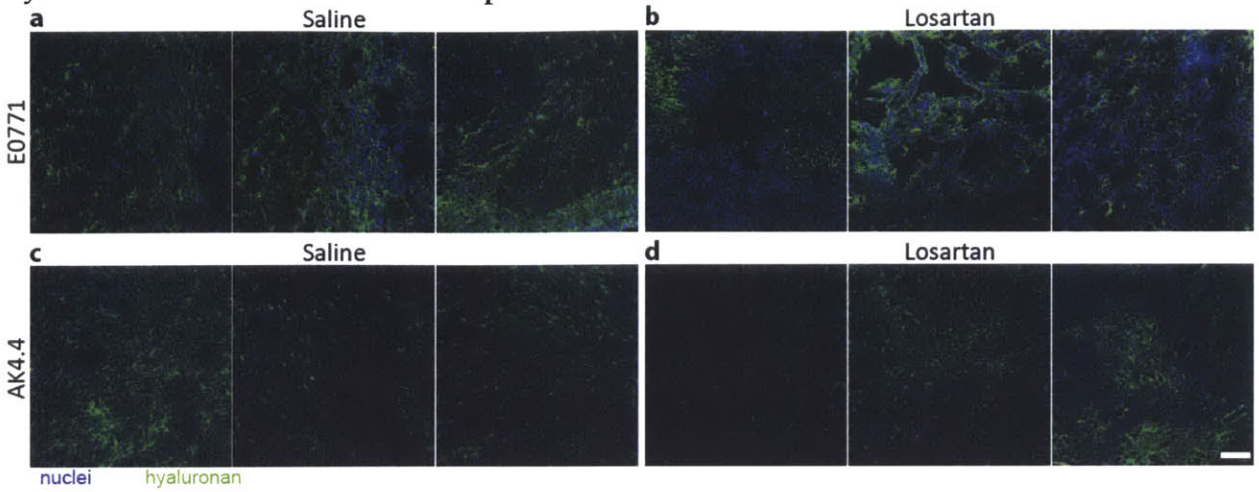


**Supplementary Figure S6. Losartan reduces the expression of hyaluronan in mouse breast and pancreatic tumors. a,b,c,d,** Histology of mouse tumors showing hyaluronan (green) and cell nuclei (blue). Control E0771 breast tumors (**a**) and AK4.4 pancreatic tumors (**c**) have high hyaluronan levels. Losartan reduces hyaluronan expression in E0771 (**b**) and AK4.4 (**d**). Scale bar, 100μm.

**Figure 3-14 Supplementary Figure S7. Losartan decreases matrix staining intensity in tumors.**

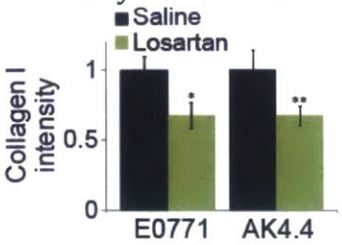


**Supplementary Figure S7. Losartan decreases matrix staining intensity in tumors.** Tumor matrix levels following angiotensin inhibition with losartan, measured by relative collagen I staining intensity. Losartan reduces the intensity, or concentration, of collagen I-positive staining in E0771 ($P$=0.048, Student's t-test) and AK4.4 ($P$=0.050, Student's t-test). Animal numbers $n$=5-7 (E0771), $n$=4-6 (AK4.4). Error bars indicate standard error of the mean.

**Figure 3-15 Supplementary Figure S8. Losartan reduces αSMA+ CAF density in mouse breast and pancreatic tumors.**

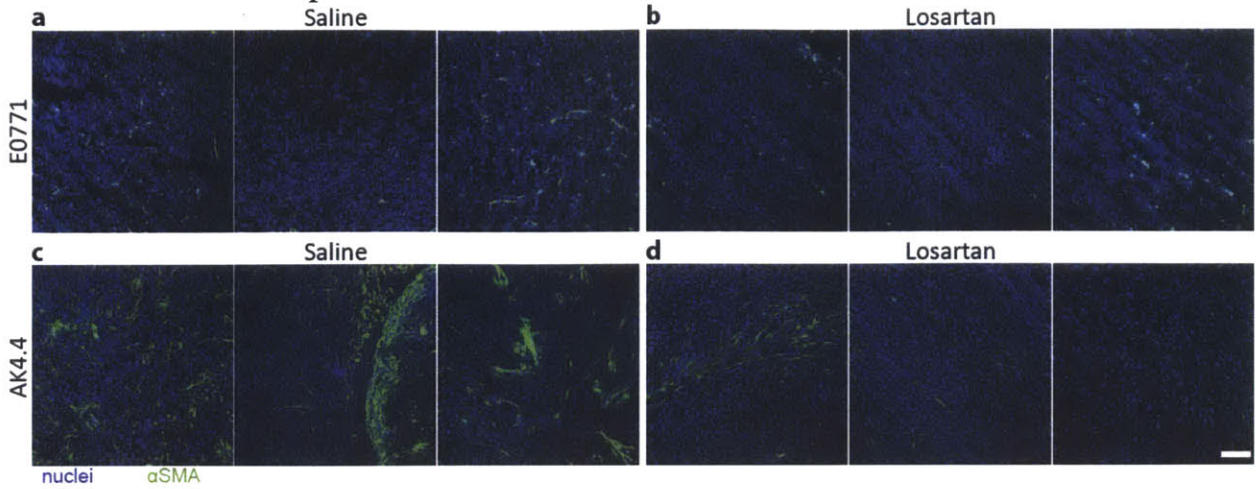


**Supplementary Figure S8. Losartan reduces αSMA+ CAF density in mouse breast and pancreatic tumors. a,b,c,d,** Histology of mouse tumors showing αSMA+ CAF cells (green) and cell nuclei (blue). Control E0771 breast tumors (**a**) are dense with CAFs, though control AK4.4 pancreatic tumors (**c**) have higher CAF density. Losartan reduces CAF density in E0771 (**b**) and AK4.4 (**d**). Scale bar, 100μm.

**Figure 3-16 Supplementary Figure S9. The ACE-I lisinopril decreases matrix levels less than losartan.**

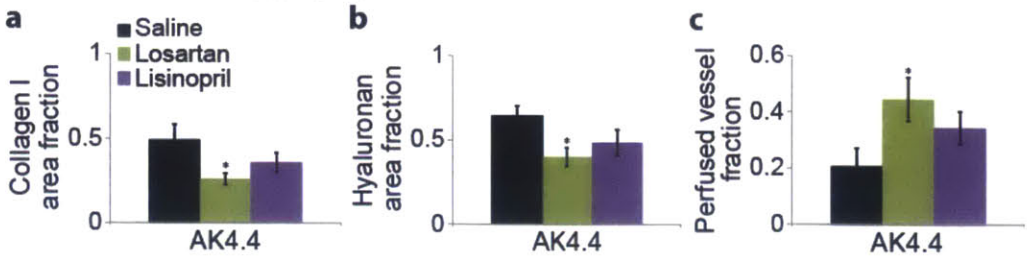


**Supplementary Figure S9. The ACE-I lisinopril decreases matrix levels less than losartan. a,b** Tumor matrix levels following angiotensin inhibition with lisinopril or losartan. Doses were chosen based on their relative doses in patients for hypertension indications (40mg/kg losartan, 40mg/kg lisinopril). Lisinopril decreases the (**a**) collagen I area fraction and (**b**) hyaluronan area fraction in orthotopic AK4.4 pancreatic tumors to a lesser degree than losartan. **c**, Perfused vessel fraction in tumors after angiotensin inhibition using lisinopril. Due to its lesser anti-matrix effects, lisinopril increases perfusion to a lesser degree than losartan. Losartan data are the same as in Figs. 3, 6. Animal numbers $n$=4-9 for all groups. Error bars indicate standard error of the mean.

**Figure 3-17 Supplementary Figure S10. A panel of angiotensin receptor blockers reduces solid stress.**

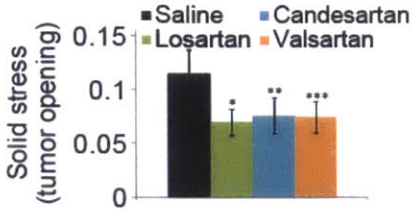


**Supplementary Figure S10. A panel of angiotensin receptor blockers reduces solid stress.** Solid stress levels in orthotopic E0771 breast tumors after angiotensin inhibition using the ARBs losartan, candesartan, and valsartan. Doses were chosen based on their relative doses in patients for hypertension indications (40mg/kg losartan, 3.2mg/kg candesartan, 32mg/kg valsartan). Losartan ($P$=0.0069, Student's t-test) candesartan ($P$=0.0091, Student's t-test), and valsartan ($P$=0.0091, Student's t-test) all reduce solid stress to a similar degree. Animal number $n$=6-7. Error bars indicate standard error of the mean. Statistical tests were corrected for multiple comparisons using the Holm-Bonferroni method.

**Figure 3-18 Supplementary Figure S11. Losartan does not improve perfusion in well-perfused tumors.**

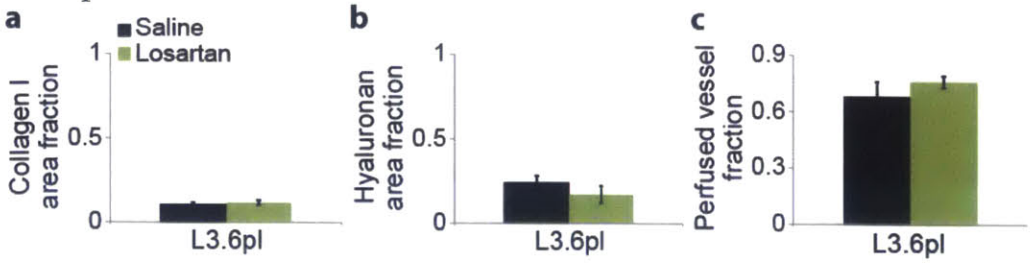


**Supplementary Figure S11. Losartan does not improve perfusion in well-perfused tumors. a,b**, Tumor matrix levels following angiotensin inhibition with losartan. The level of collagen I (**a**) is very low at baseline, thus losartan (20mg/kg) does not decrease the collagen I area fraction in orthotopic L3.6pl pancreatic tumors. Similarly, this low dose of losartan does not significantly reduce the hyaluronan area fraction (**b**) in these tumors. **c**, Perfused vessel fractions after angiotensin inhibition with losartan. Likely due to the low collagen I levels in this model, the tumors are highly perfused at baseline. Losartan does not improve perfusion in this model, likely because vessels are not compressed as a result of low baseline matrix levels. Animal numbers $n$=5-6 for all groups. Error bars indicate standard error of the mean.

**Figure 3-19** Supplementary Figure S12. Losartan does not decrease tumor VEGF levels.

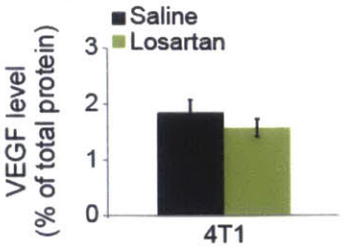


**Supplementary Figure S12. Losartan does not decrease tumor VEGF levels.** Tumor VEGF concentration after treatment with losartan. The VEGF concentration in orthotopic 4T1 breast tumors is not affected by losartan at this 40mg/kg dose, as measured by ELISA. Levels normalized to control. Animal numbers $n$=6-7. Error bars indicate standard error of the mean.

**Figure 3-20** Supplementary Figure S13. Losartan slightly increases blood vessel diameter.

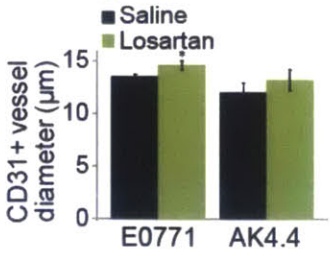


**Supplementary Figure S13. Losartan slightly increases blood vessel diameter.** Histology of tumor blood vessels, stained for CD31, after losartan treatment. Losartan increases vessel diameter in E0771 tumors ($P$=0.047, Student's t-test), but does not significantly increase vessel diameter in AK4.4 tumors. Animal numbers $n$=7-9. Error bars indicate standard error of the mean.

**Figure 3-21** Supplementary Figure S14. Losartan increases the effective permeability of all sizes of nanoparticles.

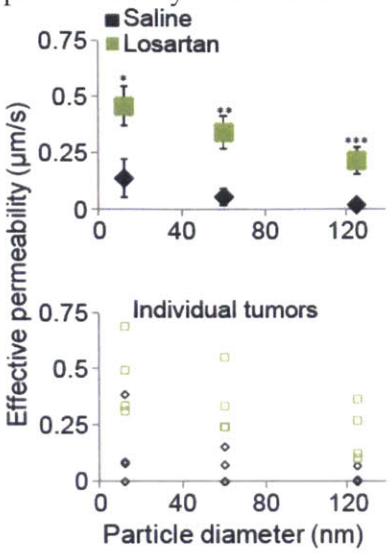


**Supplementary Figure S14. Losartan increases the effective permeability of all sizes of nanoparticles.** Transvascular penetration rates for nanoparticles after angiotensin inhibition with losartan. Penetration rates are quantified as effective permeability, which is the transvascular mass flux per unit vascular surface area and transvascular concentration difference. Closed symbols (top) denote averages by mouse, while open symbols (bottom) are individual tumors. Losartan enhances the effective permeability in a largely size-independent manner, improving the penetration of 12nm ($P$=0.039, Student's t-test), 60nm ($P$=0.013, Student's t-test), and 125nm ($P$=0.022, Student's t-test) nanoparticles. Animal numbers $n$=4. Error bars indicate standard error of the mean.

**Figure 3-22** Supplementary Figure S15. Losartan and lisinopril do not decrease blood pressure at 40 mg/kg dose.

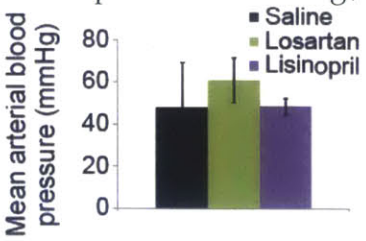


**Supplementary Figure S15. Losartan and lisinopril do not decrease blood pressure at 40 mg/kg dose.** Mean arterial pressure measured by coronary artery cannulation in mice bearing AK4.4 pancreatic tumors. Losartan and lisinopril treatment at a 40mg/kg dose does not lower blood pressure in these tumor-bearing mice[11]. Overall, blood pressure in these mice with advanced disease is lower than in healthy FVB mice (~90mmHg). Animal numbers $n$=3-4. Error bars indicate standard error of the mean.

**Figure 3-23** Supplementary Figure S16. Losartan does not affect individual blood vessel flow velocity at doses that do not reduce blood pressure.

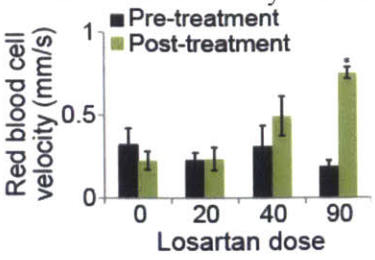


**Supplementary Figure S16. Losartan does not affect individual blood vessel flow velocity at doses that do not reduce blood pressure.** Mean measurements of blood flow rates in individual perfused blood vessels with losartan treatment. Flow rates were measured as mean red blood cell velocities using intravital microscopy. Losartan does not affect individual vessel blood flow in perfused blood vessels at the 40mg/kg dose used in this study. Losartan does increase individual vessel blood flow rates at a higher, 90mg/kg dose ($P<0.001$, Student's t-test). These data suggest that the effects of losartan on drug delivery and effectiveness are due to vessel decompression rather than modulation of blood flow rates in individual vessels. Animal numbers $n=6$. Error bars indicate standard error of the mean.

**Figure 3-24 Supplementary Figure S17. Losartan results in a normalized network of perfused vessels.**

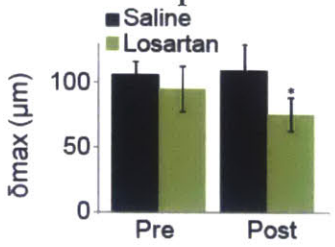


**Supplementary Figure S17. Losartan results in a normalized network of perfused vessels.** Mathematical analysis of perfused vessel network efficiency for delivery. Perfused vessel networks of E0771 tumors were imaged in three dimensions using multiphoton microscopy pre- and post-treatment (days 2-5). Analysis of the distance from each point in the tumor to the nearest perfused vessel[4] indicates that losartan decreases the distance drugs and oxygen must travel to reach tumor cells ($P$=0.029, Student's t-test). These data suggest that increasing perfusion with angiotensin inhibitors leads to a more normal vascular network structure. Animal numbers $n$=4. Error bars indicate standard error of the mean.

**Figure 3-25 Supplementary Figure S18. Losartan reduces hypoxia.**

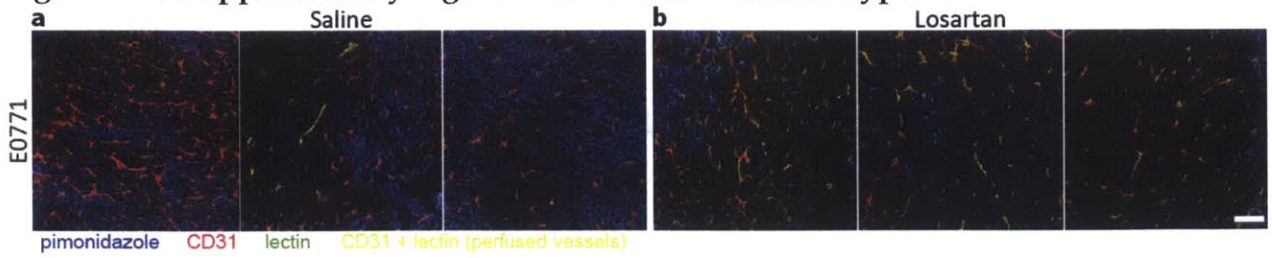


**Supplementary Figure S18. Losartan reduces hypoxia. a,b**, Histology of mouse tumors showing pimonidazole hypoxia staining (blue), CD31-positive vessels (red), and lectin-positive vessels (green), with CD31-lectin co-staining (yellow) denoting perfused vessels. Control E0771 breast tumors (**a**) show pronounced hypoxia away from the few vessels that are perfused. Losartan improves perfusion, reducing hypoxia (**b**). Scale bar, 100μm.

**Figure 3-26 Supplementary Figure S19. Losartan reduces hypoxia in an additional tumor model.**

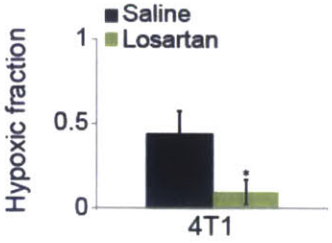


**Supplementary Figure S19. Losartan reduces hypoxia in an additional tumor model.** Hypoxic fraction in tumors measured by pimonidazole injection and staining following angiotensin inhibition with losartan. Losartan decreases the hypoxic fraction in 4T1 tumors ($P$=0.033, Student's t-test). Animal number $n$=5-7. Error bars indicate standard error of the mean.

**Figure 3-27 Supplementary Figure S20. Losartan potentiates chemotherapy against tumor growth.**

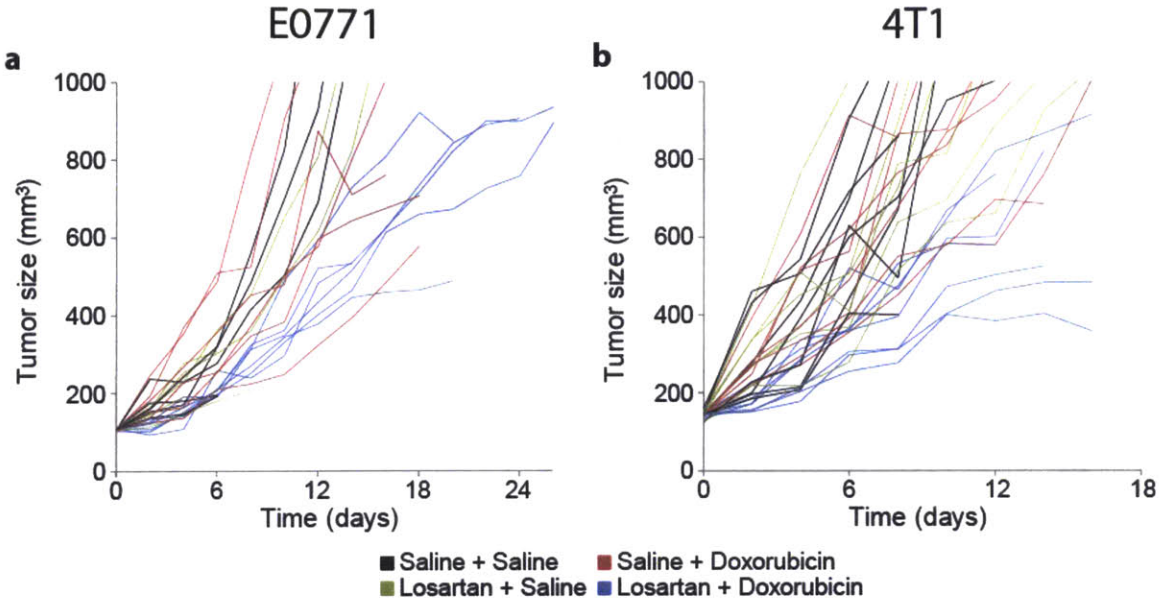


**Supplementary Figure S20. Losartan potentiates chemotherapy against tumor growth.** **a**,**b**, Volumes of orthotopic E0771 (**a**) and 4T1 (**b**) breast tumors in response to treatment with losartan or saline control (40mg/kg daily from day 0 on) in combination with either the small-molecule chemotherapeutic doxorubicin or saline control (2mg/kg every 3 days from day 1 on). Analysis presented in Fig. 7. Animal number n=5-7 for all groups.

**Figure 3-28 Supplementary Figure S21. Losartan enhances chemotherapy in immunocompetent and immunodeficient mice.**

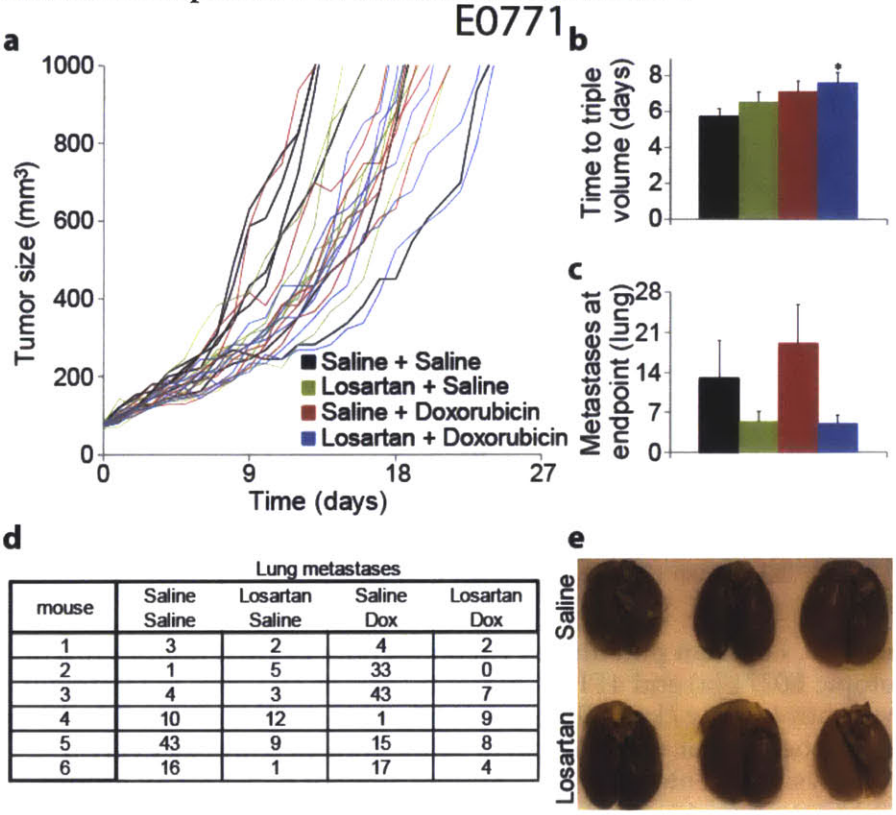


Lung metastases

| mouse | Saline Saline | Losartan Saline | Saline Dox | Losartan Dox |
|---|---|---|---|---|
| 1 | 3 | 2 | 4 | 2 |
| 2 | 1 | 5 | 33 | 0 |
| 3 | 4 | 3 | 43 | 7 |
| 4 | 10 | 12 | 1 | 9 |
| 5 | 43 | 9 | 15 | 8 |
| 6 | 16 | 1 | 17 | 4 |

**Supplementary Figure S21. Losartan enhances chemotherapy in immunocompetent and immunodeficient mice. a**, Volumes of orthotopic E0771 breast tumors in C57BL/6 mice in response to treatment with losartan or saline control (40mg/kg daily from day 0 on) in combination with either the small-molecule chemotherapeutic doxorubicin or saline control (5mg/kg every 3 days from day 1 on). **b**, Quantification of tumor growth rates, based on the time to reach triple the initial volume. Doxorubicin and losartan monotherapy induce no significant growth delay versus the control treatment in these aggressive tumors. In contrast, their combination greatly limits tumor growth versus the control ($P$=0.042, Student's t-test). **c,d**, Lung macrometastases at sacrifice. The median size of metastases was <0.5mm. Pooling both losartan-treated versus both saline-treated groups suggests that losartan decreases metastases in E0771-bearing mice ($P$=0.049, Student's t-test). **e**, Representative images of lung metastases (white nodules) from E0771 tumors in SCID mice treated with losartan. The metastases were larger in SCID mice. Animal number n=6 for all groups. Error bars indicate standard error of the mean. Statistical tests were corrected for multiple comparisons using the Holm-Bonferroni method.

## 3.6. Methods

Drug preparation: Angiotensin inhibitors (losartan, lisinopril, valsartan, and candesartan) were obtained as pills, crushed, and dissolved in phosphate buffered saline (PBS; for losartan and lisinopril) or PBS with 5% ethanol (for valsartan, candesartan) over 24 hours. The solutions were then sterile filtered for injection. Doxorubicin and 5-FU were obtained as solutions for injection. All drugs were purchased from the pharmacy at Massachusetts General Hospital.

Tumor models: AK4.4 cells (*Kras* and *p53*) were kindly provided by Dr. Nabeel Bardeesy, and were isolated from mice generating spontaneous pancreatic tumors (*Ptf1-Cre/LSL-Kras/p53*). Orthotopic pancreatic tumors were generated by implanting a small piece ($1mm^3$) of viable tumor tissue (from a source tumor in a separate animal) into the pancreas of a 6-8 week-old male FVB mouse (AK4.4 model) or C57BL/6 (Pan-02 model) mouse. Orthotopic breast tumors were similarly generated by implanting a chunk of viable tumor tissue into the mammary fat pad of a 6-8 week-old female severe combined immunodeficient (SCID) mouse (E0771 and 4T1 models) or C57BL/6 mouse (E0771 syngeneic model). For AT1 and AT2 knockout studies, E0771 cells were implanted by injection into the mammary fat pad of 6-8 week-old female C57BL/6, *agtr1a* (), or *agtr2* () mice. All animal procedures were carried out following the Public Health Service Policy on Humane Care of Laboratory Animals and approved by the Institutional Animal Care and Use Committee of Massachusetts General Hospital.

Vessel perfusion, matrix level, and hypoxia histology: For breast tumors, mice bearing orthotopic E0771 were split into time- and size-matched (~$100mm^3$) treatment groups. For pancreatic tumors, mice bearing orthotopic AK4.4 were split into treatment groups 6 days post-implantation. The mice were then treated with 40mg/kg losartan or an equal volume of PBS intraperitoneally each day for 6 (E0771) or 7 (AK4.4) days. On the day of the last treatment, mice were slowly (~2min) injected with 100$\mu$L of 1mg/mL biotinylated lectin (Vector Labs), administered via the retro-orbital sinus 5min prior to tumor removal. For hypoxia studies, the mice were also injected with 60mg/kg of pimonidazole at 10mg/mL 1hr prior to tumor removal. The tumors were then excised, fixed in 4% formaldehyde in PBS (30min/mm diameter of tissue), incubated in 30% sucrose in PBS overnight at 4°C, and frozen in optimal cutting temperature compound (Tissue-Tek). Transverse tumors sections, 40μm thick, were immunostained with antibodies to endothelial marker CD31 (MEC13.3 antibody, BD, 1:100 dilution), and

counterstained with DAPI (Vector Labs). Collagen I and hyaluronan were respectively detected using the LF-68 antibody (1:50 dilution) provided by Dr. Larry Fisher (NIDCR) and a biotinylated hyaluronan proteoglycan fragment (385911, Calbiochem) as previously described[40]. Staining for αSMA (C6198 antibody, Sigma, 1:100 dilution), active-TGF-β1 (G122A antibody, Promega, 1:15 dilution), CCN2 (TP-243 antibody, Torrey Pines, 1:100 dilution), AT1 (ab18801 antibody, Abcam, 1:100 dilution), and AT2 (AAR-012 antibody, Alomone, 1:200 dilution) were carried out in 10μm sections. For the detection of collagen I in AK4.4, KPC, and human pancreatic ductal adenocarcinoma, the paraffin-embedded sections were treated with a pH 9.0 antigen retrieval solution and counterstained with hematoxylin.

Histological image analysis: Eight random fields (four interior, four periphery) at 20x magnification were taken from each slide using a confocal microscope (Olympus). For vascular analysis, vessels were skeletonized and segmented using a custom, semi-automated tracing program developed in MATLAB (The MathWorks) allowing the removal of structures under thirty pixels and regions of autofluorescence. For perfusion fraction, the number of vessels counted by this program with colocalization of lectin and CD31 staining was divided by the number of vessels counted with CD31 staining. For vessel metrics, including diameter and density, the program determined the average size of all counted vessels and their length, as well as the count per area. For open versus closed lumen quantification, vessels were analyzed by eye and a vessel was counted as open if it had a clearly visible lumen throughout its length. Images of collagen I, hyaluronan, pimonidazole (hypoxia) αSMA, active-TGF-β1, and CCN2 stained sections were analyzed based on the area fraction of positive staining. Identical analysis settings and thresholds were used for all tumors.

Cancer-associated fibroblast studies: We generated *αSMA$^{P}$-dsRed/Tie2$^{P}$-GFP*/FVB double-transgenic mice by crossing *Tie2$^{P}$-GFP*/FVB mice[39] with *αSMA$^{P}$-dsRed* mice[38]. Once established, this line was backcrossed to FVB mice for at least 10 generations. Cancer-associated fibroblasts (CAFs) were isolated from AK4.4 tumors implanted in these mice. The mice were treated with 40mg/kg losartan or PBS for 7 days, then the tumors were collected and αSMA+ cells were isolated based on dsRed fluorescence using fluorescence-activated cell sorting (BD Biosciences). These cells were analyzed with qRT-PCR for mRNA of *Col1a1* (F GCTCCTCTTAGGGGCCACT, R CCACGTCTCACCATTGGGG), *Has1* (F, GGCGAGCACTCACGATCATC, R AGGAGTCCATAGCGATCTGAAG), *Has2* (F TGTGAGAGGTTTCTATGTGTCCT,

R ACC GTA CAG TCC AAA TGA GAA GT), *Has3* (F CCTGGAGCACCGTCGAATG, R CCTTGAGGTTTGGAAAGGCAA), *Tgfb1* (F GCAGTGGCTGAACCAAGGA, R AGCAGTGAGCGCTGAATCG), *Ctgf* (F CAAAGCAGCTGCAAATACCA, R GTCTGGGCCAAATGTGTCTT), and *Edn1* (F GCACCGGAGCTGAGAATGG, R GTGGCAGAAGTAGACACACTC). We also analyzed these cells, as well as AK4.4 and E0771 cells, for *Agtr1a* (F AACAGCTTGGTGGTGATCGTC, R CATAGCGGTATAGACAGCCCA), *Agtr1b* (F TGGCTTGGCTAGTTTGCCG, R ACCCAGTCCAATGGGGAGT), and *Agtr2* (F AACTGGCACCAATGAGTCCG, R CCAAAAGGAGTAAGTCAGCCAAG). Expression levels were normalized to the control (GAPDH), and losartan-treated levels were normalized to the PBS controls.

Solid stress: Solid stress was measured using the tumor opening technique[5]. When the tumors reached a size of ~1cm in diameter, the mice were anesthetized. Subsequently, each tumor was excised, washed with Hanks' Balanced Salt Solution (HBSS) and its three dimensions were measured. Each tumor was cut along its longest axis, to a depth of 80% of its shortest dimension, using a scalpel. The tumors were allowed to relax for 10 minutes in HBSS to diminish any transient, poro-elastic responses. Afterwards, the opening resulting from the cut was measured at the middle of the cut at the surface of the tumor. Solid stress is proportional to the size of the opening relative to the size of the dimension perpendicular to the cut.

Drug delivery: Mice bearing orthotopic AK4.4 were split into treatment groups 6 days after implantation. The mice were then treated with 40mg/kg losartan or an equal volume of PBS intraperitoneally each day for 7 days. On the day of the last treatment, mice were injected with 100mg/kg 5-FU, administered retro-orbitally 30min prior to tumor and organ removal. The tissue was dabbed of excess blood then snap-frozen in liquid nitrogen for analysis. 5-FU was isolated from the tissues and measured using liquid-liquid extraction followed by reverse-phase high-performance liquid chromatography with tandem mass-spectrometry.

In vivo imaging: For imaging studies, E0771 tumors were implanted in mice bearing mammary fat pad chambers[33] and allowed to grow to ~3mm in diameter. Multiphoton imaging was carried out on a custom-built multiphoton laser-scanning microscope using a confocal laser-scanning microscope body (Olympus 300, Optical Analysis) and a broadband femtosecond laser source (High Performance MaiTai, Spectra-Physics)[30]. Images were taken at ~60mW at sample surface. Mosaic images were taken in raster

pattern using a motorized stage (H101, Prior Scientific, Inc.) and customized automation software (LabView, National Instruments). Imaging studies were performed with a 20X magnification, 0.95NA water immersion objective (Olympus XLUMPlanFl, 1-UB965, Optical Analysis). Optical frequency-domain imaging was carried out after 7 days of treatments using a custom-built microscope[91].

Tissue oxygenation: We measured pO2 in the tumors using phosphorescence quenching microscopy[35], which was adapted to multiphoton microscopy. An oxygen-sensitive porphyrin, Oxyphor R2 (Oxygen Enterprises) was injected retro-orbitally 12hrs prior to imaging, and was reinjected immediately prior to imaging along with 2MDa FITC-dextran (Sigma-Aldrich) for functional vascular tracing. A mosaic image of the tumor was collected, and oxygen was then measured in an evenly spaced 12x12 grid at four depths (60, 120, 180, and 240μm) in the tumor. At each point in the grid, the phosphorescence lifetime of the probe was measured after each of several repeated brief intense pulses of 1020nm laser light, and these lifetime measurements were combined. A two-component model was used to calculate the oxygen tension from each lifetime measurement, accounting for binding and quenching of the probe by both oxygen and proteins. The grid was then overlaid on the mosaic to make an oxygen map.

Effective permeability: Effective permeability (transvascular flux) studies were carried out using a mixture of nanoparticles with diameters of 12nm (476nm emission), 60nm (540nm emission), and 125nm (625nm emission)[33]. Concentrations were adjusted with in vitro calibration to result in roughly equal photoluminescence intensity for all three nanoparticle samples under 800nm multiphoton excitation. Following retro-orbital injection of 200$\mu$L with these concentrations, multiphoton imaging was carried out as described above at depths from 0 - 201μm, with 2.76μm steps and 2.76x2.76μm pixels. Images were taken every 3min at each region of interest for a duration of 1hr. Images were analyzed using custom analysis software developed in Matlab (The Mathworks)[33, 92]. The analysis approach involved 3D vessel tracing to create vessel metrics and a 3D map of voxel intensity versus distance to the nearest vessel over time. Images were also corrected for sample movement over time with 3D image registration. The effective permeability (normalized transvascular flux) was calculated using $\frac{J_t}{S_v(C_v-C)} = P_{eff} = \lim_{t\to 0} \frac{\partial}{\partial t} \frac{\int_{r=R}^{\infty} C(r) r \partial r}{(C_v-C)R}$, where $J_t$ is the transvascular flux, $S_v$ is the vessel surface area, $C_v$ is the concentration of the probe in the vessel, C is the concentration of the probe immediately extravascular, $P_{eff}$ is the effective permeability, t is time after the initial image, r is the

distance from the vessel central axis, and R is the vessel radius at that point along the vessel. Fluorescence intensities were used as these concentrations. The calculation was made as an average over the entire imaged volume for each tumor.

Individual tumor vessel blood flow: Red blood cell (RBC) velocity was measured using intravital microscopy with the residence time line scanning technique in mice bearing orthotopic E0771 or 4T1 mammary tumors[93]. RBCs from a donor mouse were labeled *ex vivo* with 1,1-dioctadecyl-3,3,3,3-tetramethylindodicarbocyanine perchlorate (DID). These labeled RBCs were administered to mice bearing orthotopic E0771 or 4T1 mammary tumors via retro-orbital injection at a ratio of 3–5 labeled RBCs per 100 RBCs. Multiphoton imaging was carried out, applying laser scanning along a single line that intersects each vessel of interest. Repeated scanning along this line generated fluorescence intensity data along the line over time (x–t), in which 'images' of the fluorescent RBCs are compressed or elongated depending on the residence time of the cells in the scan. Velocities were extracted using $v_{rbc} = \frac{L_{rbc} \cdot f}{n_{scans} \cdot \sin(\alpha)}$, where $v_{rbc}$ is the RBC velocity, $L_{rbc}$ is the RBC length (7 μm), t is the residence time, f is line scan frequency (scans/s), nscans is the number of consecutive scan lines that detected the RBC, and $\alpha$ is the angle between vessel and line scan.

Breast tumor growth and survival studies: Mice bearing orthotopic E0771 or 4T1 breast tumors were split into treatment groups, time-matched for time after implantation and size-matched for tumor volume at this time (105mm$^3$ in E0771, 141mm$^3$ in 4T1). The mice were then treated with 40mg/kg losartan or an equal volume of PBS intraperitoneally on day 0 and each subsequent day. The mice were then treated with either 2mg/kg (SCID) or 5mg/kg (C57BL/6) doxorubicin, or an equal volume of saline, by intraperitonteal injection every three days beginning on day 1 (after 2 losartan or PBS treatments). Doxorubucin or control treatments were carried out four hours after losartan or control treatments. The primary tumors were then measured every 1-2 days, beginning on day 0, using calipers. Tumor growth was quantified using the time for each to reach double (SCID) or triple (C57BL/6) its initial volume. Animal survival was quantified based on time of death after initiation of treatment or time to reach excessive tumor burden (1000mm$^3$). For metastasis studies, mouse lungs were collected at sacrifice and were fixed in Bouin's solution. Macrometastases were counted using a stereomicroscope.

Pancreatic tumor growth and survival studies: Mice bearing orthotopic AK4.4 pancreatic tumors were split into treatment groups, size-matched for tumor volume ($22mm^3$) by surgical exposure, 6 days after implantation. The mice were treated with 40mg/kg losartan or an equal volume of PBS intraperitoneally on day 7 after implantation and each subsequent day. The mice were then treated with either 60mg/kg 5-FU or an equal volume of saline by intravenous injection on days 9 and 13 after implantation. Tumors were extracted on day 14 for measurement using calipers. Tumor growth was quantified using the size at day 14. For survival studies, mice were treated daily with losartan or PBS starting on day 3 after implantation until day 13, then with 5-FU or saline on days 5, 9, and 13.

Mean arterial pressure: Mice bearing orthotopic AK4.4 pancreatic tumors were used for blood pressure measurements. Mean arterial pressure was measured by cannulation of the left carotid artery after a longitudinal skin incision above the trachea[14]. After removal of the submandibular gland, the paratracheal muscles was split and the left carotid artery was isolated. The cranial end of the artery was ligated with a 6-0 silk suture and another suture was tied loosely around the central part of the artery. A metal clamp was then positioned caudally to stop blood flow during the cannulation. A polyethylene catheter (PE-10, Becton-Dickinson) filled with heparinised saline was then inserted through a hole cut proximally to the cranial ligature, and the other suture was tied tightly around the tubing and artery. The clamp was then removed and the end of the tubing was connected to a pressure transducer for the measurement of blood pressure.

Mathematical analysis and modeling: The analysis was carried out on mosaic images of whole tumors taken with multiphoton microscopy after injection of 2MDa FITC-dextran as a perfused vessel tracer. Details of the models and corresponding equations are described in Baish et al[14].

Statistical analysis: The data are presented as means with standard errors. Groups were compared using a Student's t-test, paired or unpaired, except for animal survival studies where a log-rank test was used. In pairwise comparisons within studies where multiple comparisons were made, *P* values were adjusted using Holm's method.

## 3.7. References


1. Chauhan, V.P., Stylianopoulos, T., Boucher, Y. & Jain, R.K. Delivery of Molecular and Nanoscale Medicine to Tumors: Transport Barriers and Strategies. *Annual Review of Chemical and Biomolecular Engineering* **2**, 281-298 (2011).

2. Tsai, A.G., Johnson, P.C. & Intaglietta, M. Oxygen gradients in the microcirculation. *Physiological Reviews* **83**, 933-963 (2003).

3. Jain, R.K. Normalizing Tumor Microenvironment to Treat Cancer: Bench to Bedside to Biomarkers. *Journal of Clinical Oncology* **31**, 2205-2218 (2013).

4. Helmlinger, G., Netti, P.A., Lichtenbeld, H.C., Melder, R.J. & Jain, R.K. Solid stress inhibits the growth of multicellular tumor spheroids. *Nature Biotechnology* **15**, 778-783 (1997).

5. Stylianopoulos, T. et al. Causes, consequences, and remedies for growth-induced solid stress in murine and human tumors. *Proceedings of the National Academy of Sciences of the United States of America* **109**, 15101-15108 (2012).

6. Stylianopoulos, T. et al. Co-evolution of solid stress and interstitial fluid pressure in tumors during progression: Implications for vascular collapse. *Cancer research* **73**, 3833-3841 (2013).

7. Janmey, P.A. & McCulloch, C.A. Cell mechanics: Integrating cell responses to mechanical stimuli. *Annual Review of Biomedical Engineering* **9**, 1-34 (2007).

8. Griffon-Etienne, G., Boucher, Y., Brekken, C., Suit, H.D. & Jain, R.K. Taxane-induced apoptosis decompresses blood vessels and lowers interstitial fluid pressure in solid tumors: clinical implications. *Cancer research* **59**, 3776-3782 (1999).

9. Padera, T.P. et al. Pathology: cancer cells compress intratumour vessels. *Nature* **427**, 695 (2004).

10. Park, M.S. et al. Perfusion CT: Noninvasive Surrogate Marker for Stratification of Pancreatic Cancer Response to Concurrent Chemo- and Radiation Therapy. *Radiology* **250**, 110-117 (2009).

11. Sorensen, A.G. et al. Increased Survival of Glioblastoma Patients Who Respond to Antiangiogenic Therapy with Elevated Blood Perfusion. *Cancer research* **72**, 402-407 (2012).

12. Provenzano, Paolo P. et al. Enzymatic Targeting of the Stroma Ablates Physical Barriers to Treatment of Pancreatic Ductal Adenocarcinoma. *Cancer Cell* **21**, 418-429 (2012).

13. Alexandrakis, G. et al. Two-photon fluorescence correlation microscopy reveals the two-phase nature of transport in tumors. *Nature medicine* **10**, 203-207 (2004).

14. Diop-Frimpong, B., Chauhan, V.P., Krane, S., Boucher, Y. & Jain, R.K. Losartan inhibits collagen I synthesis and improves the distribution and efficacy of

nanotherapeutics in tumors. *Proceedings of the National Academy of Sciences of the United States of America* **108**, 2909-2914 (2011).

15. Liu, J. et al. TGF-β blockade improves the distribution and efficacy of therapeutics in breast carcinoma by normalizing the tumor stroma. *Proceedings of the National Academy of Sciences* **109**, 16618-16623 (2012).

16. Naito, T. et al. Angiotensin II induces thrombospondin-1 production in human mesangial cells via p38 MAPK and JNK: a mechanism for activation of latent TGF-β1. *American Journal of Physiology - Renal Physiology* **286**, F278-F287 (2004).

17. Habashi, J.P. et al. Losartan, an AT1 antagonist, prevents aortic aneurysm in a mouse model of Marfan syndrome. *Science* **312**, 117-121 (2006).

18. Sweetwyne, M.T. & Murphy-Ullrich, J.E. Thrombospondin1 in tissue repair and fibrosis: TGF-beta-dependent and independent mechanisms. *Matrix Biology* **31**, 178-186 (2012).

19. Liao, S. et al. Impaired lymphatic contraction associated with immunosuppression. *Proceedings of the National Academy of Sciences of the United States of America* **108**, 18784-18789 (2011).

20. Mori, T. et al. Role and interaction of connective tissue growth factor with transforming growth factor-beta in persistent fibrosis: A mouse fibrosis model. *Journal of Cellular Physiology* **181**, 153-159 (1999).

21. Duncan, M.R. et al. Connective tissue growth factor mediates transforming growth factor beta-induced collagen synthesis: downregulation by cAMP. *FASEB Journal* **13**, 1774-1786 (1999).

22. Rodriguez-Vita, J. et al. Angiotensin II activates the Smad pathway in vascular smooth muscle cells by a transforming growth factor-beta-independent mechanism. *Circulation* **111**, 2509-2517 (2005).

23. Yang, F., Chung, A.C., Huang, X.R. & Lan, H.Y. Angiotensin II induces connective tissue growth factor and collagen I expression via transforming growth factor-beta-dependent and -independent Smad pathways: the role of Smad3. *Hypertension* **54**, 877-884 (2009).

24. Hama, K. et al. Angiotensin II stimulates DNA synthesis of rat pancreatic stellate cells by activating ERK through EGF receptor transactivation. *Biochemical and Biophysical Research Communications* **315**, 905-911 (2004).

25. Liu, W.B., Wang, X.P., Wu, K. & Zhang, R.L. Effects of angiotensin II receptor antagonist, Losartan on the apoptosis, proliferation and migration of the human pancreatic stellate cells. *World Journal of Gastroenterology* **11**, 6489-6494 (2005).

26. Leask, A. Targeting the TGF beta, endothelin-1 and CCN2 axis to combat fibrosis in scleroderma. *Cellular Signalling* **20**, 1409-1414 (2008).

27. Shi-Wen, X. et al. Constitutive ALK5-independent c-Jun N-terminal kinase activation contributes to endothelin-1 overexpression in pulmonary fibrosis: evidence of

an autocrine endothelin loop operating through the endothelin A and B receptors. *Molecular and Cellular Biology* **26**, 5518-5527 (2006).

28. Cheng, T.H. et al. Involvement of reactive oxygen species in angiotensin II-induced endothelin-1 gene expression in rat cardiac fibroblasts. *Journal of the American College of Cardiology* **42**, 1845-1854 (2003).

29. Habashi, J.P.H.J.P. et al. Angiotensin II Type 2 Receptor Signaling Attenuates Aortic Aneurysm in Mice Through ERK Antagonism. *Science* **332**, 361-365 (2011).

30. Ulmasov, B., Xu, Z., Tetri, L.H., Inagami, T. & Neuschwander-Tetri, B.A. Protective role of angiotensin II type 2 receptor signaling in a mouse model of pancreatic fibrosis. *Am. J. Physiol.-Gastroint. Liver Physiol.* **296**, G284-G294 (2009).

31. Nabeshima, Y. et al. Anti-fibrogenic function of angiotensin II type 2 receptor in CCl4-induced liver fibrosis. *Biochemical and Biophysical Research Communications* **346**, 658-664 (2006).

32. George, A.J., Thomas, W.G. & Hannan, R.D. The renin-angiotensin system and cancer: old dog, new tricks. *Nat. Rev. Cancer* **10**, 745-759 (2010).

33. Chauhan, V.P. et al. Normalization of tumour blood vessels improves the delivery of nanomedicines in a size-dependent manner. *Nature Nanotechnology* **7**, 383-388 (2012).

34. Baish, J.W. et al. Scaling rules for diffusive drug delivery in tumor and normal tissues. *Proceedings of the National Academy of Sciences of the United States of America* **108**, 1799-1803 (2011).

35. Helmlinger, G., Yuan, F., Dellian, M. & Jain, R.K. Interstitial pH and pO2 gradients in solid tumors in vivo: high-resolution measurements reveal a lack of correlation. *Nature medicine* **3**, 177-182 (1997).

36. Arnold, S.A. et al. Losartan Slows Pancreatic Tumor Progression and Extends Survival of SPARC-Null Mice by Abrogating Aberrant TGFβ Activation. *PLoS One* **7**, e31384 (2012).

37. Rodrigues-Ferreira, S. et al. Angiotensin II Facilitates Breast Cancer Cell Migration and Metastasis. *PLoS One* **7** (2012).

38. Amano, H. et al. Angiotensin II Type 1A Receptor Signaling Facilitates Tumor Metastasis Formation through P-Selectin-Mediated Interaction of Tumor Cells with Platelets and Endothelial Cells. *American Journal of Pathology* **182**, 553-564 (2013).

39. DeNardo, D.G. et al. Leukocyte Complexity Predicts Breast Cancer Survival and Functionally Regulates Response to Chemotherapy. *Cancer Discovery* **1**, 54-67 (2011).

40. Pluen, A. et al. Role of tumor-host interactions in interstitial diffusion of macromolecules: cranial vs. subcutaneous tumors. *Proceedings of the National Academy of Sciences of the United States of America* **98**, 4628-4633 (2001).

41. Keizman, D. et al. Angiotensin system inhibitors and outcome of sunitinib treatment in patients with metastatic renal cell carcinoma: A retrospective examination. *Eur. J. Cancer* **47**, 1955-1961 (2011).

42. Nakai, Y. et al. Inhibition of renin-angiotensin system affects prognosis of advanced pancreatic cancer receiving gemcitabine. *British Journal of Cancer* **103**, 1644-1648 (2010).

43. Wilop, S. et al. Impact of angiotensin I converting enzyme inhibitors and angiotensin II type 1 receptor blockers on survival in patients with advanced non-small-cell lung cancer undergoing first-line platinum-based chemotherapy. *Journal of Cancer Research and Clinical Oncology* **135**, 1429-1435 (2009).

44. Chae, Y.K. et al. Reduced Risk of Breast Cancer Recurrence in Patients Using ACE Inhibitors, ARBs, and/or Statins. *Cancer Investigation* **29**, 585-593 (2011).

45. Fujita, M. et al. Angiotensin type 1a receptor signaling-dependent induction of vascular endothelial growth factor in stroma is relevant to tumor-associated angiogenesis and tumor growth. *Carcinogenesis* **26**, 271-279 (2005).

46. Suganuma, T. et al. Functional expression of the angiotensin II type 1 receptor in human ovarian carcinoma cells and its blockade therapy resulting in suppression of tumor invasion, angiogenesis, and peritoneal dissemination. *Clinical Cancer Research* **11**, 2686-2694 (2005).

47. Yoshiji, H. et al. The angiotensin-I-converting enzyme inhibitor perindopril suppresses tumor growth and angiogenesis: Possible role of the vascular endothelial growth factor. *Clinical Cancer Research* **7**, 1073-1078 (2001).

48. Greco, S. et al. Angiotensin II activates extracellular signal regulated kinases via protein kinase C and epidermal growth factor receptor in breast cancer cells. *Journal of Cellular Physiology* **196**, 370-377 (2003).

49. Egami, K. et al. Role of host angiotensin II type 1 receptor in tumor angiogenesis and growth. *Journal of Clinical Investigation* **112**, 67-75 (2003).

50. Doi, C. et al. Angiotensin II type 2 receptor signaling significantly attenuates growth of murine pancreatic carcinoma grafts in syngeneic mice. *BMC Cancer* **10**, 67 (2010).

51. Rhodes, D.R. et al. AGTR1 overexpression defines a subset of breast cancer and confers sensitivity to losartan, an AGTR1 antagonist. *Proceedings of the National Academy of Sciences of the United States of America* **106**, 10284-10289 (2009).

52. Noguchi, R. et al. Synergistic inhibitory effect of gemcitabine and angiotensin type-1 receptor blocker, losartan, on murine pancreatic tumor growth via anti-angiogenic activities. *Oncology Reports* **22**, 355-360 (2009).

53. Cook, K.L., Metheny-Barlow, L.J., Tallant, E.A. & Gallagher, P.E. Angiotensin-(1-7) Reduces Fibrosis in Orthotopic Breast Tumors. *Cancer research* **70**, 8319-8328 (2010).

54. Nakai, Y. et al. A multicenter phase II trial of gemcitabine and candesartan combination therapy in patients with advanced pancreatic cancer: GECA2. *Invest New Drugs*, 1-6 (2013).

55. Michel, M.C., Foster, C., Brunner, H.R. & Liu, L. A systematic comparison of the properties of clinically used angiotensin II type 1 receptor antagonists. *Pharmacological Reviews* **65**, 809-848 (2013).

56. Bardeesy, N. et al. Both p16(Ink4a) and the p19(Arf)-p53 pathway constrain progression of pancreatic adenocarcinoma in the mouse. *Proceedings of the National Academy of Sciences of the United States of America* **103**, 5947-5952 (2006).

57. Sugaya, T. et al. Angiotensin II type 1a receptor-deficient mice with hypotension and hyperreninemia. *Journal of Biological Chemistry* **270**, 18719-18722 (1995).

58. Ichiki, T. et al. Effects on blood pressure and exploratory behaviour of mice lacking angiotensin II type-2 receptor. *Nature* **377**, 748-750 (1995).

59. Motoike, T. et al. Universal GFP reporter for the study of vascular development. *Genesis* **28**, 75-81 (2000).

60. Brown, E.B. et al. In vivo measurement of gene expression, angiogenesis and physiological function in tumors using multiphoton laser scanning microscopy. *Nature medicine* **7**, 864-868 (2001).

61. Vakoc, B.J. et al. Three-dimensional microscopy of the tumor microenvironment in vivo using optical frequency domain imaging. *Nature medicine* **15**, 1219-1223 (2009).

62. Chauhan, V.P. et al. Fluorescent Nanorods and Nanospheres for Real-Time In Vivo Probing of Nanoparticle Shape-Dependent Tumor Penetration. *Angewandte Chemie International Edition* **50**, 11417-11420 (2011).

63. Kamoun, W.S. et al. Simultaneous measurement of RBC velocity, flux, hematocrit and shear rate in vascular networks. *Nature Methods* **7**, 655-660 (2010).

# *Chapter 4 Multiphoton high-resolution measurement of partial pressure of oxygen in tumor tissue reveals differential effects of anti-angiogenic therapy*

Lanning RL*, Martin JD*, Chauhan VP, Niemeyer E, Kamoun WS, Han HS, Martin MR, Mousa AS, Stylianopoulos T, Brown EB, Bawendi M, Padera TP, Fukumura D, and Jain RK.

*These authors contributed equally

Manuscript in preparation

### 4.1.1. Abstract

Hypoxia drives resistance to standard therapies and is a major target for cancer drug development. Approaches for increasing oxygen supply by normalizing tumor vasculature can improve therapeutic outcomes, yet the connection between changes in vascular structure and function and modulation of hypoxia is still unknown. Here we developed a technique to longitudinally and simultaneously measure extravascular tissue oxygen tension and vascular metrics with sub-micron three-dimensional resolution in murine tumors. This method utilizes a low molecular weight palladium porphyrin, which can distribute evenly throughout tissues, to perform phosphorescence quenching microscopy with a multiphoton microscope. We applied this technique to assess the effects of vascular normalization with either an anti-VEGF-R2 antibody, DC101, or an angiotensin receptor blocker, losartan, on single vessel function and vessel network geometry. We found that a high dose of DC101 modestly improves single vessel function while also detrimentally pruning vessels from the network, whereas lower doses improve single vessel function without impairing vessel network geometry. Meanwhile losartan, which acts by decompressing collapsed vessels, improves the function of single vessels and improves vessel network geometry. Resultantly, losartan has a greater effect on tumor oxygenation than DC101. Thus, this technique can provide valuable insights into how different approaches to modulating tumor vasculature can affect hypoxia.

## 4.1.2. Introduction

Hypoxia (low oxygen level) is a hallmark of solid tumors and negatively impacts the outcome of cancer therapy in patients (*1, 2*). This paucity of oxygen is a consequence of blood vessel dysfunction that leads to impaired blood perfusion in tumors (*3-5*). Two types of vascular abnormalities in tumors affect oxygen supply in tumors by limiting blood flow: hyperpermeability and collapse. Tumor blood vessels bathe in a milieu of pro-angiogenic factors, contributing to an excessive leakiness to fluid that makes single vessel function inefficient for blood flow (*6*). The majority of blood vessels in a tumor may also be collapsed by compressive solid stress (a physical pressure), leading to a vessel network geometry that is inadequate to supply oxygen to all regions of a tumor (*7-10*).

Therapeutic strategies for repairing these two abnormalities to combat hypoxia involve either anti-angiogenic therapy to reduce vessel permeability or anti-solid stress therapy to decompress vessels (*4*). Low doses of anti-angiogenic therapies, such as the anti-VEGF-R2 antibody DC101, are sufficient to improve the function of single vessels in breast tumors, as assessed by vascular permeability (*11*). Furthermore, low dose DC101 can homogenize the distribution of perfused vessels and decrease hypoxia throughout breast tumors (*12*). Anti-solid stress therapy, as with the angiotensin receptor blocker losartan, can increase blood flow in individual vessels by decompressing them (*8*). Furthermore, losartan can increase the density of perfused vessels by re-opening collapsed vessels and resultantly reverses hypoxia (*8*). Understanding how these normalization strategies reduce hypoxia could help identify which tumors will respond to each approach, and could lead to new therapies that increase tumor oxygenation.

While vascular normalization is known to reduce hypoxia, it is unclear how the associated changes in tumor vessels directly affect oxygen delivery at either the single vessel or vessel network level. This opacity is largely due to a lack of techniques for following changes in blood vessel structure and function simultaneously with tissue oxygenation, though there are techniques for studying each separately. Multiphoton microscopy (MPM) allows rapid and longitudinal assessment of vessel structure and perfusion throughout murine tumor models with sub-micron resolution (*13*). Phosphorescence quenching microscopy (PQM) allows direct measurement of oxygenation in tissue based on the interaction of molecular oxygen with the excited

triplet state of a phosphorescent reporter molecule (16). Intravital PQM has been used extensively with single photon excitation and confocal methods to study oxygen, but this approach has very limited three-dimensional resolution, lacks the ability for measurements at the sub-micron level, and risks tissue photodamage. Recently, PQM has been adapted to MPM (MP-PQM) to provide measurements of oxygen in spatial relation to blood vessels, though this approach used a high molecular weight probe that is largely confined to the vasculature. Here, we describe a novel technique to achieve high-resolution oxygenation and vascular measurements by combining MP-PQM using a low molecular weight probe with MPM fluorescence angiography. We apply MP-PQM to demonstrate the differential effects of anti-angiogenic therapy on single vessel function and vascular network geometry. Further, we show that anti-solid stress therapy improves both single vessel function and vascular network geometry with respect to microscopic oxygen tension measurements

## 4.1.3. Results

***Oxygen Probe and system characterization***

We constructed a custom multiphoton phosphorescence quenching microscopy (MP-PQM) system for quantification of oxygen tension ($pO_2$) *in vitro* and *in vivo* (Figure 1A). To maximize signal to noise *in vivo*, measurement of phosphoresce lifetime was performed in the time-domain [18] utilizing an electro-optic modulator to gate pulses of the femtosecond excitation laser and stationary phase instead of scanning for measurments. The two-photon absorption cross-section of similar molecules to the Pd-porphyrin we employed is known to be low [19]. We measured the single- and two-photon action cross-sections in order to determine the ideal excitation wavelength, which also did not overlap with the single photon excitation or phosphorescence emission (Figure 1B). We elected the non-linear excitation at 1020nm rather than 800nm to take advantage of the optical window and limit cellular damage, reduce tissue scattering allowing for deeper measurements, and no overlap with the phosphorescence emission, which extends to 780nm. Non-linear, two-photon excitation of the Pd-porphyrin probe was confirmed at the selected excitation wavelength of 1020nm and was independent of oxygen tension (Figure 1C). This relationship held *in vivo*, confirming that excitation of Oxyphor R2 at 1020nm is a two-photon process (Figure 1D). Finally, we calibrated the Pd-porphyrin probe at various levels of $pO_2$ in solutions with differing concentrations of bovine serum albumin using a customized calibration system (Figure 1E). Given two states of the probe (free in solution or bound to protein), the best fit was to a two-component Stern-Volmer model (20) (Figure 1F).

***In vivo* validation**

Prior to quantifying changes in $pO_2$ due to targeted therapy in murine models of solid tumors, we performed intravital MP-PQM in a variety of normal and malignant tissues. We measured perturbations of the *in vivo* oxygen tension profiles in normal murine skin within the dorsal skinfold chamber model under normoxic (21% $FiO_2$) and hyperoxic (100% $FiO_2$) and correlated them to the vascular networks (Figure 2A). There was a dramatic shift in the oxygen tension probability distributions with the mean peak increasing from 32 to 52mmHg as well as a statistical difference in the mean $pO_2$ of all measurements (not shown). Notably, some regions of the murine skin capillary networks did not demonstrate increased $pO_2$ in response to hyperoxia, which has previously been demonstrated in skin musculature of mammals secondary to

vasoconstriction (21). To examine differences in $pO_2$ with respect to the vascular networks, we compared the normal murine mammary fat pad (MFP) to an orthotopic murine mammary carcinoma (E0771) model using the chamber window model. The normal MFP demonstrated no correlation of $pO_2$ with distance to nearest vessel (Pearson's correlation coefficient = 0.07), while the E0771 tumor measurements revealed a negative correlation (Pearson's = -0.27, $P < 0.05$; Figure 2B). Conversely, the normal MFP demonstrated a positive correlation of $pO_2$ with vessel diameter (Pearson's = 0.13), while there was no correlation in the orthotopic tumor model (Pearson's = -0.003). These results were consistent with previously reported studies (21).

Finally, we performed *in vivo* measurements in a variety of solid tumors. These included the orthotopic murine mammary carcinomas E0771 and MCaIV, the orthotopic xenograft human breast cancer cell line MDA-MB-361HK, and ectopically implanted MCaIV. We found that the mean oxygen tension ranged from 13.4 mmHg – 41.1 mmHg in these murine tumor models during tumor growth over 10 days. Only the orthotopic E0771 developed statistically lower mean $pO_2$ during local tumor progression (32.7 – 13.4mmHg, $p = 0.007$). The E0771 as well as the ectopic MCaIV tumors demonstrated statistically increasing hypoxic fractions (<10mmHg) during tumor growth (E0771: 13.5 – 59.8%, P=0.011; MCaIV: 8.7 – 38.3%, $P = 0.009$). Both tumor types had large avascular regions seen on intravital angiography by MPM. We correlated vascular metrics (vessel diameter, vascular volume fraction, and distance to nearest vessel from hypoxic regions) with $pO_2$. Across all tumor types, there was no correlation of vessel diameter with $pO_2$ in contrast to non-neoplastic tissues as seen above. In the E0771, the VVf had a statistically significant positive correlation with $pO_2$ which means that as the VVf decreased during tumor growth, the $pO_2$ decreased as well indicating a hypoperfused tumor. In all the tumors, the mean distance from hypoxic regions to the nearest vessel did not correlate with $pO_2$ suggesting the tortuous vascular network is inefficient at delivering nutrients, such as oxygen to the tumor.

***High dose anti-angiogenic therapy is detrimental to vascular network geometry***

We sought to use MP-PQM to unravel the effects of anti-angiogenic therapy (AAT) on oxygen delivery in an orthotopic murine breast tumor model by simultaneously characterizing single vessel function and vascular network geometry of the desmoplastic, hypo-perfused murine breast tumor model E0771 (Figure 3A). AATs prune immature tumor vasculature and fortify remaining vessels (*14*). Indeed, we found that high dose DC101 (40mg/kg) significantly reduced the density of perfused vessels

(Figure 3B). DC101-treated tumors had fewer small perfused vessels (Figures 3C and D) than controls (Supplementary Figure 1). As expected, DC101 pruned the smaller, immature vessels. This led to an increase in the maximum tissue distance from a vessel (Figure 3E). A common hypothesis of the effects of AAT is that it selectively prunes redundant vessels in order to divert flow to where it is most needed. Instead, by increasing the maximum distance to a vessel, DC101 prunes the vasculature in these desmoplastic breast tumors such that oxygen delivery is diminished (*15*).

***High dose anti-angiogenic therapy affects single vessel function of smaller vessels***

The other mechanism through which AAT improves oxygen delivery is by improving the function of individual vessels by fortifying their structure. Indeed, low doses of DC101 are sufficient to increase the transvascular flux of certain nanoparticles in a size-dependent manner in desmoplastic breast tumors (*11*). High dose DC101 did not change the interstitial oxygenation, indicating that individual vessels in treated tumors were no more efficient than vessels in control tumors (Figure 4A). Between the detrimental effects on network geometry and lack of effect on single vessel oxygen delivery, high dose DC101 did not increase nor maintain the mean oxygen tension throughout the tumor (Figure 4B).

In normal tissues, red blood cell velocity is linearly related to vessel diameter and oxygenation, but this relationship does not hold in tumors (*16*). We hypothesized that normal dose DC101 would normalize this relationship. Instead, we found that DC101 imposed an inverse relationship on vessel diameter and oxygen tension 50 microns from a vessel (Figure 4C). DC101 selectively prunes small vessels (Figures 3C and D) and maintains the oxygenation of small vessels (Figure 4D) even while oxygenation is falling throughout the tumor (Figure 4B). This indicates the DC101 imposes an inverse correlation between vessel diameter and interstitial oxygenation by pruning small vessels and fortifying the existing ones. Nonetheless, DC101 does not increase tumor oxygenation in this desmoplastic breast tumor model.

***Losartan improves both single vessel function and vessel network sufficiency***

After determining the effects of VEGF-blockade on oxygen delivery, we explored an alternative method to modify the tumor microenvironment in desmoplastic breast tumors. Losartan decreases the production and maintenance of desmoplasia in tumors (*17*) by reducing solid stress and decompressing vessels, thereby increasing the fraction

of perfused vessels (*8*). As a result, losartan reduces the maximum distance from a vessel, leading to an average higher oxygenation with a smaller fraction of hypoxic area (*8*). However, how losartan affects the distribution of size and the function of individual vessels remains unclear.

In contrast to high dose DC101, which reduces the amount of perfused small vessels, losartan maintained them at a higher number (Figure 5A) compared to controls (Supplementary Figure 2). This provides an explanation for reduced maximum distance from a vessel (Supplementary Figure 3) compared to controls (Supplementary Figure 4). While losartan reduces the maximum distance from a vessel (*8*), it does not change the convexity and fractal dimension of the vessel network (Supplementary Figure 3). In further contrast to DC101's effects, the losartan-induced change in perfused vessel size distribution led to a direct correlation between vessel diameter and interstitial oxygenation (Figure 5B). This suggests that the small vessels as a result of losartan treatment are poor suppliers of oxygen. These might be the same immature vessels DC101 prunes. Further, losartan increased the oxygen delivery from vessels with diameters larger than 40 microns (Figure 5C). Thus, losartan improves the distribution of tumor vessels by increasing the amount of small, inefficient perfused vessels. While these vessels are not efficient, they make the vascular network more capable of delivery oxygen (Figure 5D) compared to controls (Supplementary Figure 5).

### 4.1.4. Discussion

With our method, we demonstrated some important differences between normal vessels and tumor vessel regarding oxygen delivery. In normal skin, there is no correlation between oxygen tension and distance from the nearest vessel. This indicates that all regions of this tissue are well supplied with oxygen. In contrast, tumors exhibit a correlation between distance to the nearest vessel and oxygen tension. This indicates that there are decaying profiles of oxygen farther from a vessel. Cells near vessels are consuming oxygen, leaving regions farther from vessels with less oxygenation. Furthermore, in normal tissues there is a correlation between vessel diameter and interstitial oxygenation. All other features constant, a normal functioning vessel will have a higher velocity of red blood cells the larger its diameter. This will allow more oxygen to be delivery to tissues. Additionally, larger vessels branch into smaller vessels in an ordered fashion. This is not the case in tumors, as vessel diameter and interstitial oxygenation do not correlate. Indeed, methods to increase blood flow to increase tumor tissue oxygenation and drug delivery have failed, perhaps because there is no relationship between vessel diameter and interstitial oxygenation as in normal tissues. In other words, there are vessels with high blood flow that are hypoxic.

Both DC101 and losartan have been shown to reduce hypoxia, but in this study we demonstrate that they affect tumor vessels differently. DC101 prunes immature vessels and fortifies remaining ones. Interestingly, this lead to a reduction in the amount of small, perfused vessels, leading to an overall reduction in microvessel density. The remaining small vessels were fortified though, as they produced enhanced oxygen delivery compared to time- and size-matched controls. DC101 did not affect larger vessels. Losartan increased the amount of small, perfused vessels. This resulted in a more sufficient network geometry that distributed oxygen better throughout the tumor. The smaller vessels had worse function, as many immature and poorly perfused vessels were delivering oxygen after treatment. Interestingly, larger vessels exhibited better oxygen delivery. This is likely because losartan reduces the resistance to flow in tumors, leading to increased blood flow through tumors. This would be benefit larger vessels the most, as they are upstream of the smaller vessels.

The results of this study suggest that DC101 and losartan might be combinable. Retrospective studies have shown that similar combinations lead to a survival benefit. Our study indicates that losartan should be started shortly before DC101, as high dose DC101 quickly prunes small vessels, leading to an insufficient vascular network. Administering DC101 ahead of losartan would reduce losartan's effectiveness, as it would not be able to distribute throughout the tumor.

### 4.1.5. Figures

**Figure 4-1 Multiphoton Phosphorescence Quenching Microscopy.**

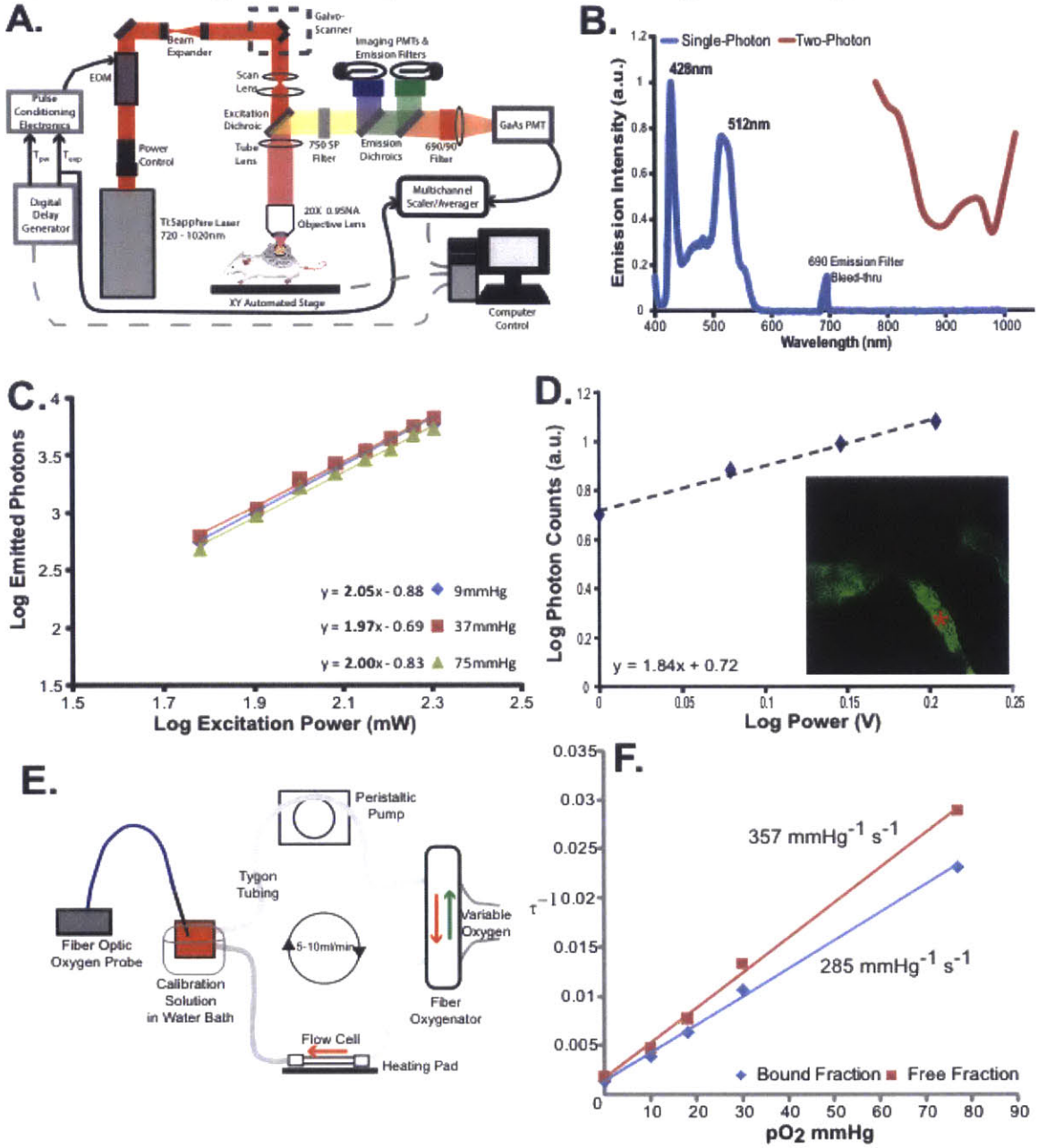


**Figure 1 – Multiphoton Phosphorescence Quenching Microscopy.** (**a**) Schematic of the experimental setup. EOM, electro-optic multiplier; PMTs, photomultiplier tubes; GaAs, Gallium arsenide; $T_{pw}$, temporal duration of the excitation pulse width; $T_{exp}$, duration of the experimental triggering time. Arrows indicate direction of communication. Dashed grey lines indicate two-way communication. (**b**) Single- and two-photon action cross-sections for Pd-porphyrin soluble oxygen sensor. The single-photon excitation spectrum

(blue line) does not show absorption or emission in the wavelength range of two-photon (red line). The lone peak at 690nm is due to excitation light at the same wavelength as the emission band-pass filter in the spectrophotometer. (**c**) Two-photon excitation at 1020nm of Pd-porphyrin phosphorescent oxygen sensor relating the emitted photons to the excitation power on a log-log scale. The experiment was repeated at oxygen tensions of 9 mmHg, 37 mmHg, and 75 mmHg (blue, red, and green lines, respectively). (**d**) *In vivo* two-photon excitation of Pd-porphyrin oxygen sensor. A series of time domain lifetime measurements performed in tumor vasculature (inset) shows the non-linear excitation of Pd porphyrin sensor. (**e**) Diagram of the recirculating, sealed calibration system employing a fiber oxygenator indicating the direction of fluid and gas flow. An independent $pO_2$ measurement is made with an optical fiber ruthenium-based probe. (**f**) Two-photon calibration of the free (green line), albumin-bound (blue line), and single-component fits (red line) of each phosphor species. The Stern-Volmer constant is given for each fit.

**Figure 4-2 Measurement of $pO_2$ in various murine tissues.**

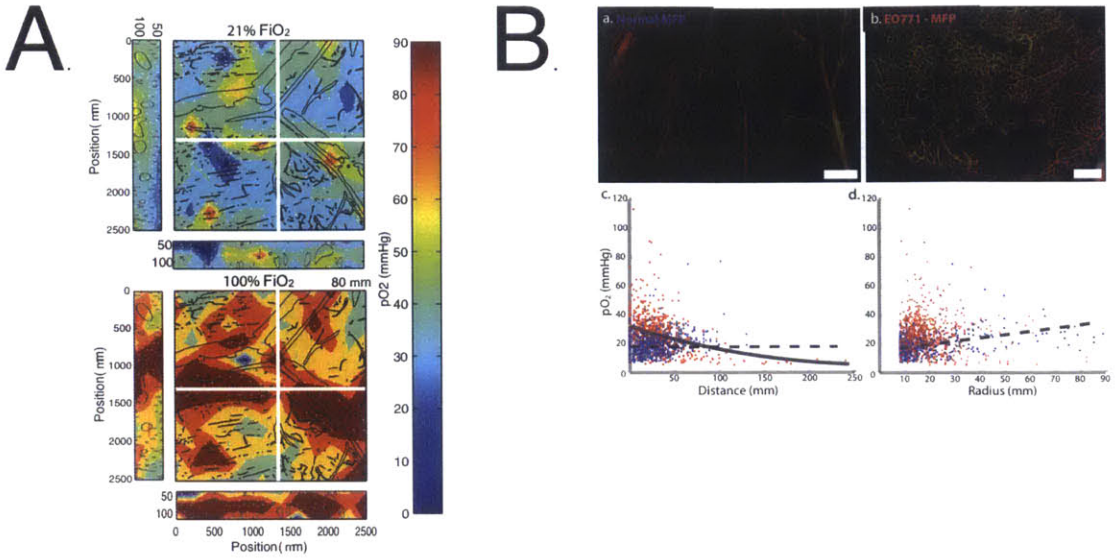


**Figure 2 – Measurement of $pO_2$ in various murine tissues.** (**a**) Oxygen tension map in normal murine skin at 21% and 100% inspired oxygen with depth projection of vasculature overlaid (**b**) Correlation of vascular metrics to $pO_2$ in both a normal mammary fat pad and orthotopic murine mammary carcinoma model (EO771). Left: Normal MFP has no correlation of $pO_2$ with distance from the nearest blood vessel (dashed line), while the mammary carcinoma demonstrates a significant negative correlation (solid line). Conversely, normal MFP $pO_2$ measurements have a positive correlation with vessel radius (dashed line), while the orthotopic tumor has no correlation. Blue – normal MFP. Red – mammary carcinoma.

**Figure 4-3 DC101 increases the maximum distance to a vessel by pruning small perfused vessels**

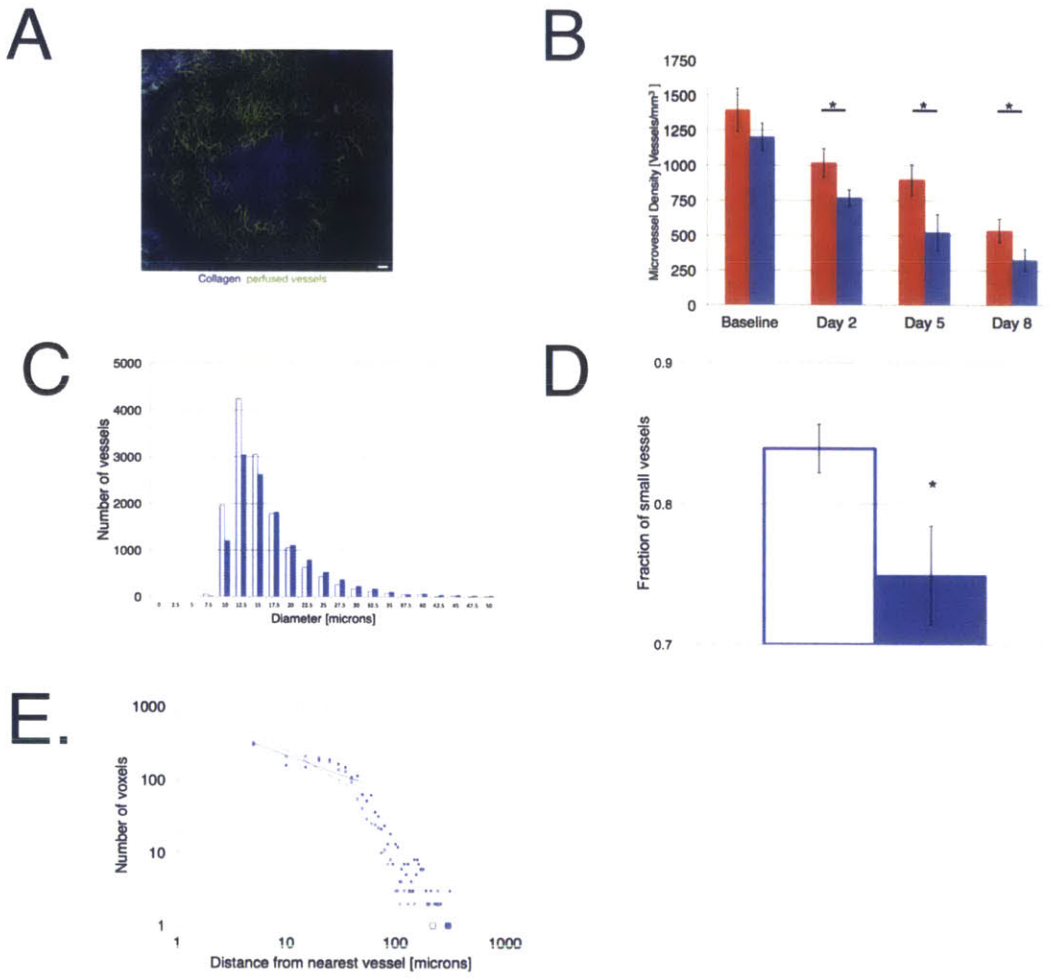


**Figure 3 – DC101 increases the maximum distance to a vessel by pruning small perfused vessels.** Measurement of DC101's effect on vessel network geometry. (**a**) A representative maximum intensity projection of an E0771 tumor's perfused vessels (Scale bar = ??). (**b**) Microvessel density of control- (red) and DC101-treated (blue) tumors (N = 5 mice, * denotes $p<0.05$). (**c**) Histogram of vessel diameters in baseline (white fill) and DC101-treated (blue fill) tumors (N = 5 mice). (**d**) Comparison of the fraction of vessels less than 12.5 microns in diameter (N = 5 mice, p = 0.0?). (**e**) Histogram plot of distance of voxels to the nearest vessels in baseline (white fill) and DC101-treated (blue fill) tumors (N = 5 mice).

**Figure 4-4 DC101 does not improve the delivery of oxygen from individual vessels**

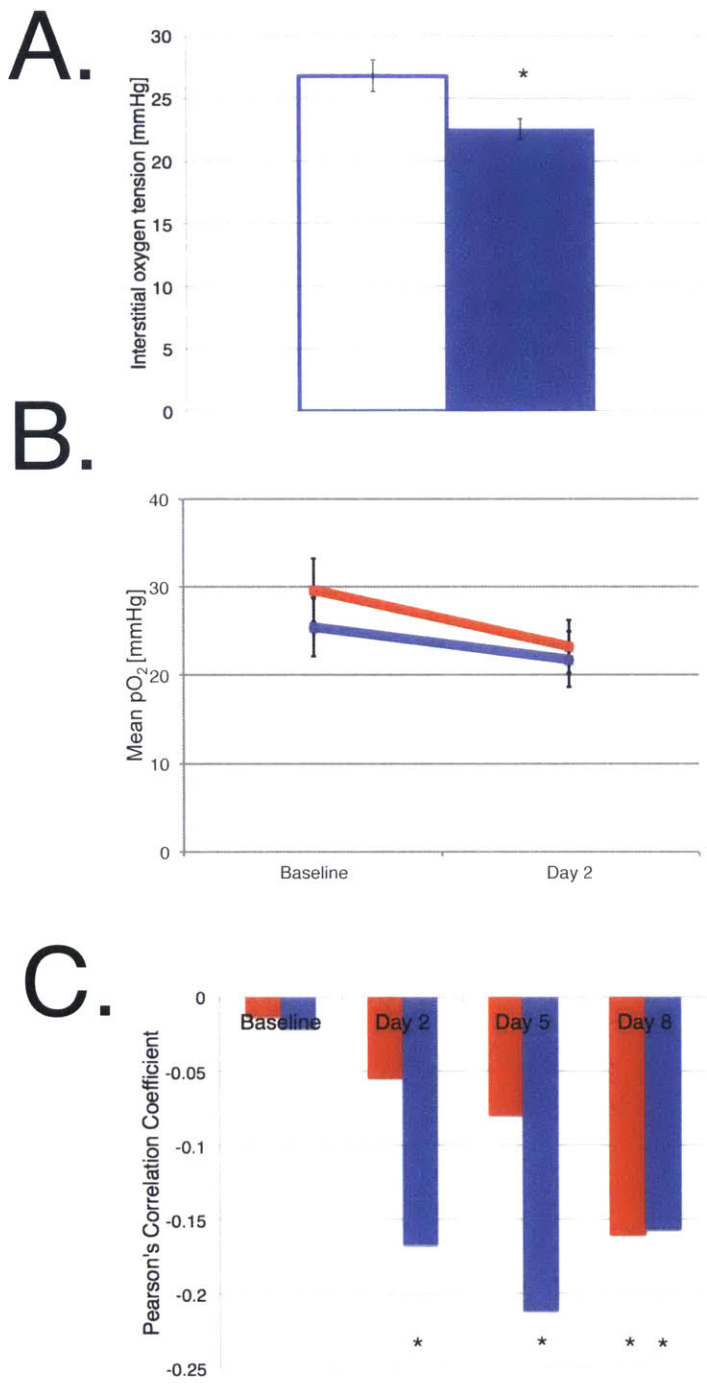


**Figure 4 – DC101 does not improve the delivery of oxygen from individual vessels.** (**a**) One treatment with DC101 does not maintain interstitial oxygenation (N = 5 mice, n = 178-306 vessels, p = 0.0037). (**b**) DC101 does not maintain tumor tissue oxygenation (N =

5 mice, $p = 0.0>?$). (**c**) DC101 imposes an inverse correlation on vessel diameter and interstitial oxygenation (N = 5 mice, n = ???-???, * denotes $p < 0.05$).

**Figure 4-5 Losartan maintains oxygenation of tumors by improving vessel network geometry.**

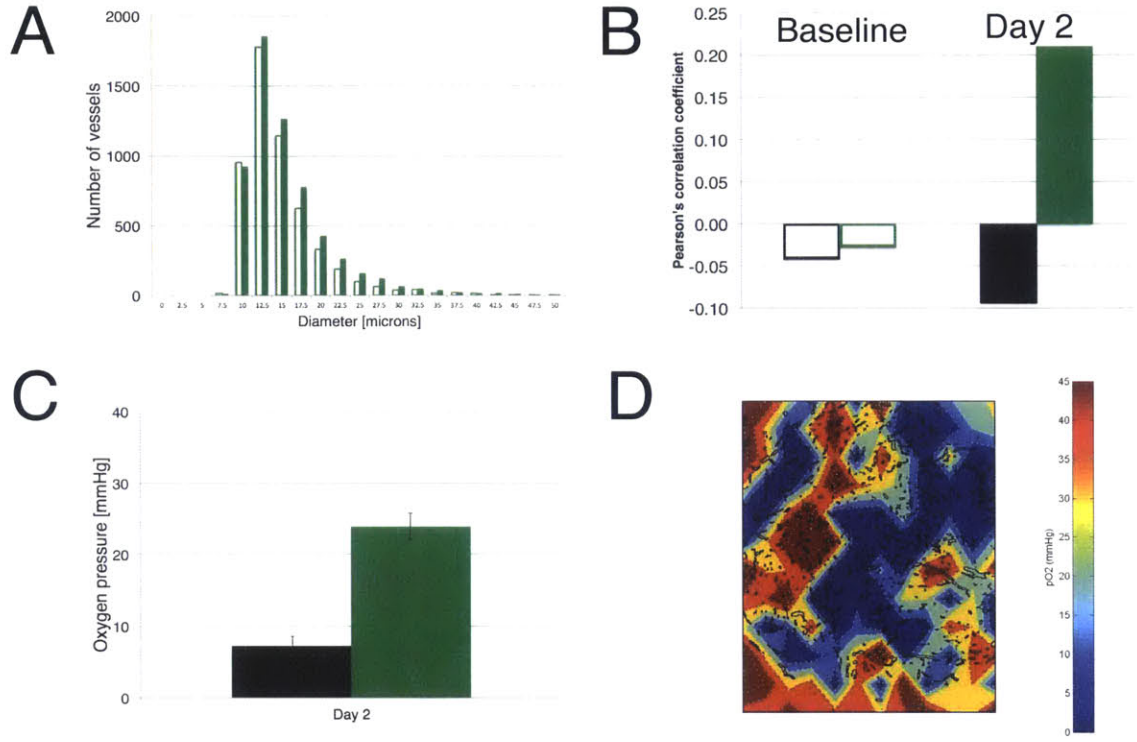


**Figure 5 – Losartan maintains oxygenation of tumors by improving vessel network geometry.** (**a**) Histogram of total perfused vessels in E0771 tumors at baseline (green, empty) and after three days of losartan treatment (green, filled). (N = mice, n = vessels, * denotes p = 0.0) (**b**) Pearson's correlation coefficient for vessel oxygenation and vessel diameter of tumors at baseline (empty) and day 2 (filled) control- (black) or losartan-treated (green). (N = mice, * denotes p = 0.0) (**c**) Bar graph showing the oxygen tension 50 microns from control- (black) and losartan-treated (green) on day 2 (N = mice, n = vessels, * denotes p = 0.0). (**d**) Representative oxygen map with vessels traced in black of an E0771 tumor treated three days with losartan.

**Figure 4-6 Supplementary Figure S1. The distribution of perfused vessel diameters does not change after three days after control treatment with IgG in E0771 tumors.**

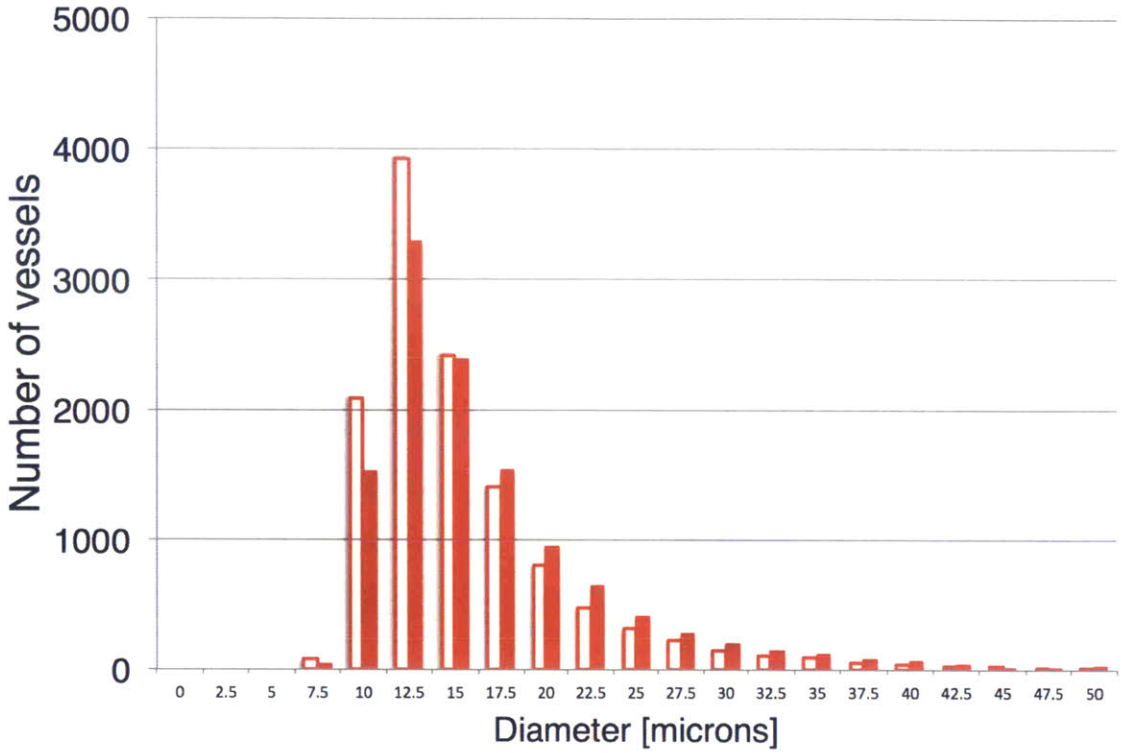


Supplementary Figure S1. The distribution of perfused vessel diameters does not change after three days after control treatment with IgG in E0771 tumors. Histogram bar graphs are shown, which depict the number of perfused vessels of each diameter range. During tumor growth (red fill), vessels become larger with a wider range of diameters compared to pre-treatment (white fill, N=5).

**Figure 4-7 Supplementary Figure S2. The distribution of perfused vessel diameters does not change after three days of control treatment (PBS) in E0771 tumors**

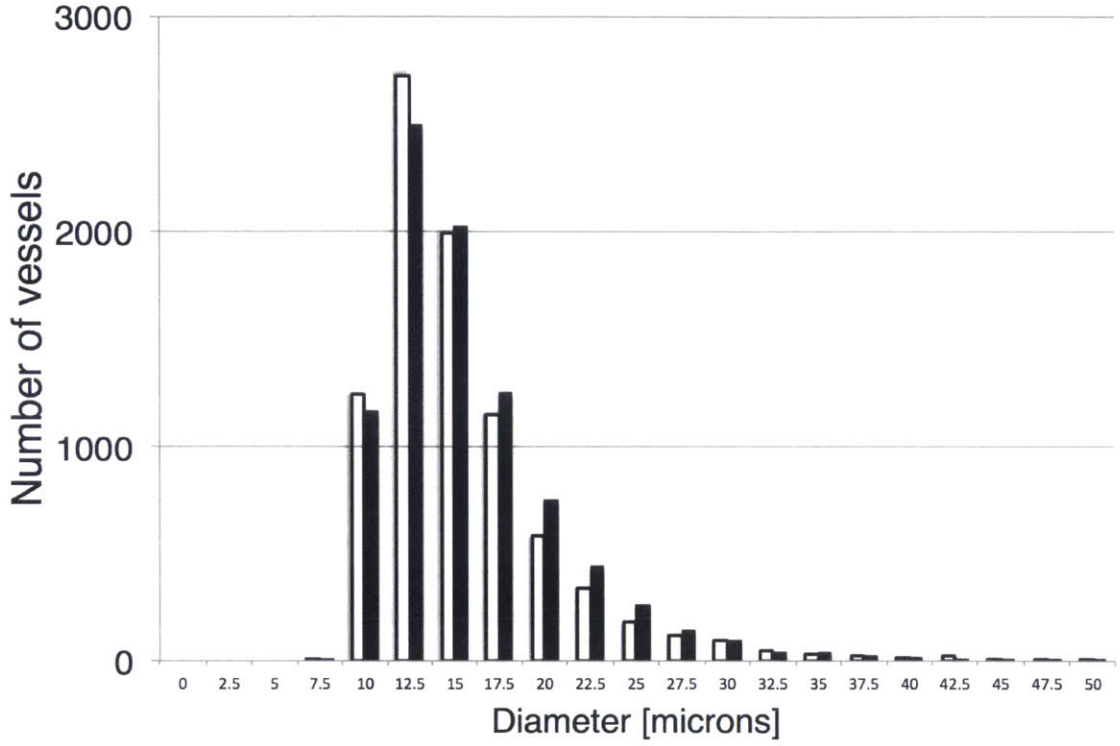


Supplementary Figure S2. The distribution of perfused vessel diameters does not change after three days of control treatment (PBS) in E0771 tumors. Histogram bar graphs are shown, which depict the number of perfused vessels of each diameter range. During tumor growth (black fill), vessels become larger with a wider range of diameters compared to pre-treatment (white fill, N=6).

**Figure 4-8 Supplementary Figure S3. The maximum distance from a vessel decreases in losartan-treated E0771 tumors.**

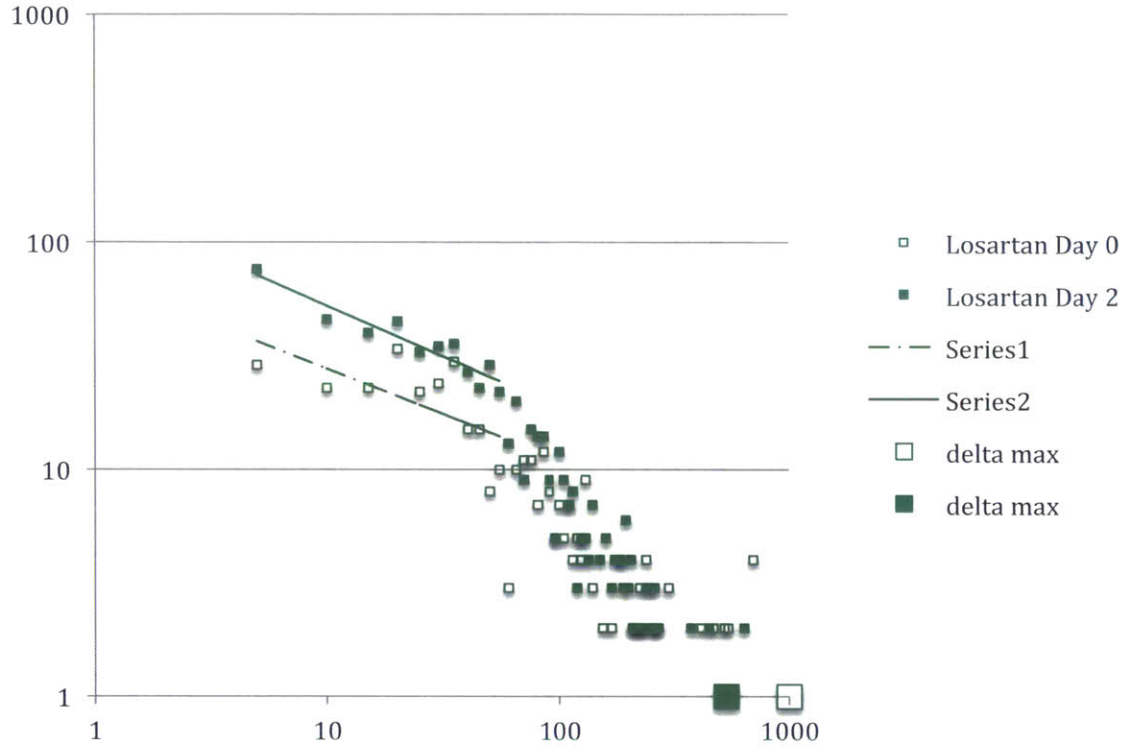


**Supplementary Figure S3. The maximum distance from a vessel decreases in losartan-treated E0771 tumors.** Histograms of the number of voxels present at a given distance from the nearest vessel for E0771 control tumors before (white fill) and after 3 days of losartan treatment (green fill) are shown on a log-log scale (N=4).

**Figure 4-9 Supplementary Figure S4. The maximum distance from a vessel did not change in control-treated (PBS) E0771 tumors.**

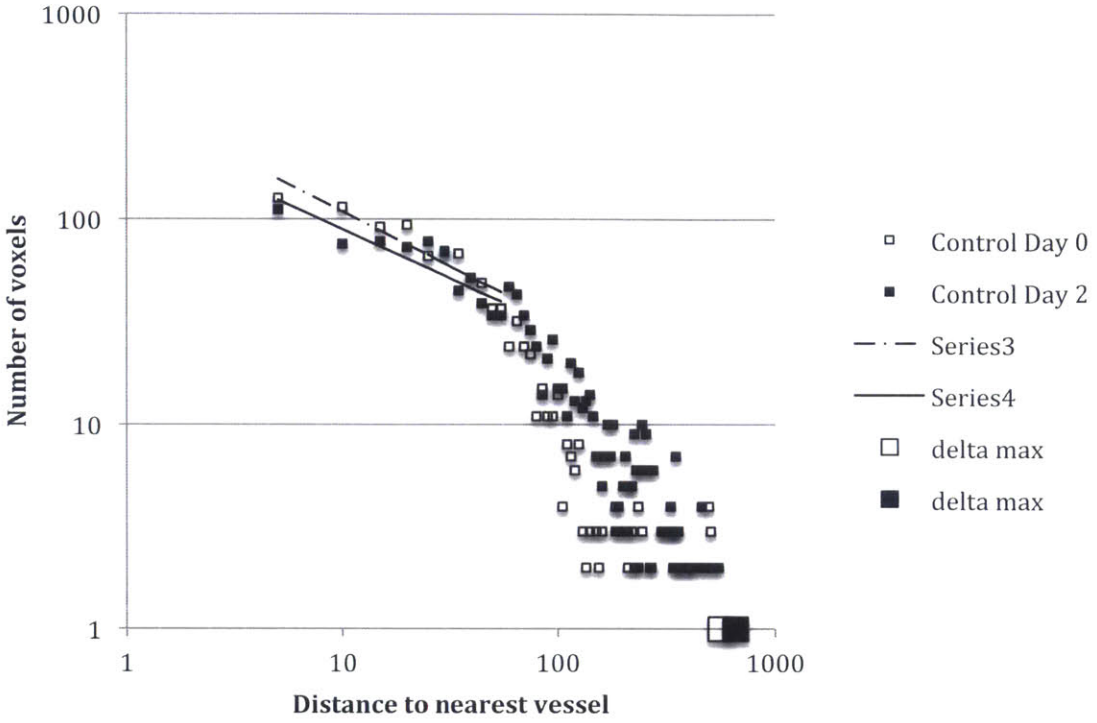


**Supplementary Figure S4. The maximum distance from a vessel did not change in control-treated (PBS) E0771 tumors.** Histogram scatter plot of the number of voxels present at a given distance from the nearest vessel for E0771 control tumors before (white fill) and after 3 daysof PBS treatment (black fill) are shown on a log-log scale (N=6).

## 4.1.6. Methods

Multiphoton Phosphorescence Quenching Microscopy System:

We custom-modified a multiphoton microscope based on the Fluoview 300 laser scanner (Olympus FV300, Optical Analysis, Center Valley, PA) and upright microscopy (Olympus BX61WI Optical Analysis, Center Valley, PA) incorporating a broadband (710 – 1020nm) Ti:Sapphire femtosecond laser (MaiTai HP, Spectraphysics, Mountain View, CA) as the excitation source. The output power of the laser was adjusted by a zero-order half-wave plate (10RP52-2, Newport Corp., Irvine, CA) and Glan-Laser polarizer (10GL08AR.16, Newport Corp., Irvine, CA). For phosphorescence quenching microscopy, we employed a KD*P Pockels cell (Model: 350-50; Conoptics, Inc., Danbury, CT) electro-optic modulator driven by custom-build electronics amplifying triggering pulses from a digital delay generator (DG535, SRS, Sunnyvale, CA) as a temporal gate for excitation pulse selection placed immediately prior to beam expansion into the galvanometer-based scanner. Based on the *in vitro* or biologic system in which $pO_2$ measurements were performed, the excitation pulse for MP-PQM ranged from 1.28 to 15.36 μs. Focusing and collection of light was performed with a 20×, 0.95 NA water immersion objective lens (Olympus XLUMPlanFl, Optical Analysis, Center Valley, PA). Given the short spectral separation

between the long emission of the phosphorescent sensors (~690nm) and the excitation laser wavelengths, a short-pass (<750nm) AR-coated filter was used in the detector path (750SP-2P, Chroma Technology Corp., Rockingham, VT) to limit background counts from the laser. A 690/90 bandpass filter (690/90M, Chroma Technology Corp., Rockingham, VT) and focusing lens were used before the detectors (GaAs photomultiplier tube for *in vivo* measurements: H7421-50, Hamamatsu, Inc., Bridgewater, NJ; or a silicon avalanche photodiode detector for *in vitro* measurements: SPCM-AQR-12-FC, PerkinElmer, Fremont, CA). For time domain photon counting, we used a multichannel scaler (SR430, SRS, Sunnyvale, CA). PQM measurements were performed using a stationary beam with sample scanning performed by an automated mechanized XY stage (H101; Prior

Scientific, Rockland, MA). A custom designed graphical user interface programmed in LabView (National Instruments, Austin, TX) was used for data acquisition and processing with embedded MATLAB fitting algorithms (MathWorks, Natick, MA).

### *Characterization and Calibration of Oxyphor R2 for MP-PQM*

We obtained the soluble phosphorescent oxygen sensor Pd-meso-tetra-(4-carboxyphenyl)porphyrin dendrimer from commercial sources (OxyphorR2, Oxygen Enterprises, Ltd., Philadelphia, PA). We determined the ideal multiphoton excitation wavelength by measuring the single-photon excitation spectrum using a spectrophotometer (Beckham Instruments Inc., Fullerton, CA) with continuous illumination from 400-1000nm and the two-photon excitation spectrum by measuring the photon counts after time-domain pulsed excitation from 800 – 1020nm at constant laser power. We confirmed that phosphorescence saturation did not occur within our selected excitation pulse duration. For calibration of Oxyphor R2, we custom designed a sealed recirculating system employing a fiber oxygenator to equilibrate the circulating fluid with gas mixtures of known oxygen concentration balanced with nitrogen. The oxygen tension in the calibration solution was independently measured using a fiber optic ruthenium-based sensor (FOXY, Ocean Optics, Inc., Dunedin, FL). All tubing in the system was impermeable to oxygen (Tygon PVC, McMaster-Carr Supply Co., Robbinsville, NJ). A solution of 1mg/ml ($3.6 \times 10\text{-}4$ M) OxyphorR2 in PBS at pH 7.4 was equilibrated with known nitrogen gas mixtures of 0, 1, 2, 5, 10% oxygen (0-80mmHg) and various concentrations of bovine serum albumin (BSA) from 0 – 10% using a fiber oxygenator (Hemophan® Membrane Fiber Oxygenator, Harvard Apparatus, Holliston, MA). After equilibration with the applied gas mixture, the solution was passed through an oxygen impermeable spectrophotometer flow cell with 500μm thick walls (45-Q-2, Starna Cells, Inc., Atascadero, CA). MP-PQM calibration measurements were performed within the flow cell at 37°C. To measure the anoxic phosphorescence lifetime ($\tau_0$) measurements, we used a Schlenk-line freeze-pump thaw method to create deoxygenated salutations in 10mm pathlength quartz cuvettes with a vapor pressure of $10^{-5}$ Torr. Using an unconstrained nonlinear optimization in MATLAB, we fit the phosphorescence decays to a two-component Stern-Volmer model due to binding of the oxygen sensor to proteins creating two species with different luminescent lifetimes.

Animal Studies:

All animal experimental protocols were reviewed and approved by the Institutional Animal Care and Use Committee. The dorsal skinfold and mammary fat pad window chamber models were prepared in SCID mice as previously described (22, 23). For the solid tumor experiments, the appropriate tumor type was implanted as a single cell suspension or homogenized tumor tissue from an existing xenograft in the center of the chamber 2-3 days after the initial surgery. The murine mammary adenocarcinomas (MCaIV and EO771), were transplanted from subcutaneous tumors grown in isogenic mice. The human mammary adenocarcinoma (MDA-MB-361HK) was implanted as a single cell suspension of ~$3\times10^{6}$ cells in 30 µl of Hank's Buffered Salt Solution (HBSS). Animals were anesthetized with Ketamine/Xylene(10/1 mg/ml) for surgeries and Isoflurane (1% in medical grade air) for all experiments. To prepare animals for MP-PQM measurements, fifteen minutes prior the animal was anesthetized by Isoflurane (3% for 4 minutes). Immediately following induction a mixture (200µl) of 10mgml Oxyphor R2 with 8mg/ml 2M MW FITC-dextran was injected retro-orbitally. This allows both real-time measurements of $pO_2$ and intravital high-resolution fluorescent angiography. For oxygen tension maps, we manually selected a rectangular region of interest and collected an automated series of mosaic multiphoton microscopy images covering the ROI. Each image contained an axial series up to 400µm deep in the tissue at a 5µm step size. Following collection of the angiography, MP-PQM measurements were performed as a series of 144 stationary points based on a 12×12 grid covering the ROI at four equally spaced depth planes. Total data collection times ranged from two to three hours depending upon the size of the ROI. Anesthesia was maintained at 1% isoflurane in a normoxic (21% FiO2) atmospheric mixture with a circulating water heating pad maintaining the animal's body temperature at 37 °C.

Antiangiogenic VEGF-R2 blockade treatments with DC101 (ImClone Systems Inc., New York, NY) or nonspecific rat IgG were administered intraperitoneally at 40mg/kg as prescribed in previous studies (24). We gave 3 doses of DC101 at three-day intervals (day 0, 3, 6) with MP-PQM performed the day immediately prior to each treatment. Imaging was performed through day 8. Therapeutic initiation was determined through

monitoring of tumor growth by visual inspection of the enface tumor diameter (≥4mm) and angiogenesis of the tumor (vascularized throughout).

Data Analysis:

We used custom code in Matlab to process and analyze the *in vivo* MPM angiography images. Colorized depth projections were created to display the vascular networks in conjunction with the oxygen tension measurements. A semi-automated vascular tracing method previously reported by our group (25, 26) was applied to the mosaic image of the entire ROI. Briefly, this method uses an algorithm that models vascular segments as superellipsoids to obtain three-dimensional trajectories and morphology of the individual segments of the vascular network. The output of the tracing algorithm was correlated with each individual oxygen measurement to quantify distance to nearest vessel and diameter of that vessel. Phosphorescence lifetimes were determined by fitting to a two-component exponential decay model with oxygen tension values calculated using the Stern-Volmer relationship and the quenching constant and anoxic lifetime determined from *in vitro* calibrations. Oxygen tension maps were created in Matlab using custom code to overlay the mesh grid of $pO_2$ values with outlines of the vascular tracing. Mean oxygen tension was calculated from the pool of all the measurements for each individual tumor. We determined tumor oxygen profiles using a sliding averaging procedure. For each tumor type, the distributions are a collection of all tumors imaged at that time-point or within a specific treatment group.

Data are reported as mean ± standard error of the mean (SEM). Significant differences between groups were determined by a multivariate repeated measures ANOVA, which accounted for response to treatment over time (Systat, Systat Software, Inc., Chicago, IL). Comparison between individual timepoints was performed using a two sample Student's t-Test. $P < 0.05$ was considered statistically significant for all comparisons. All correlations were determined using the Pearson product-moment correlation.

## 4.1.7. References


1. W. R. Wilson, M. P. Hay, Targeting hypoxia in cancer therapy. *Nature reviews. Cancer* **11**, 393-410 (2011); published online EpubJun (10.1038/nrc3064).

2. D. M. Gilkes, G. L. Semenza, D. Wirtz, Hypoxia and the extracellular matrix: drivers of tumour metastasis. *Nature reviews. Cancer* **14**, 430-439 (2014); published online EpubJun (10.1038/nrc3726).

3. R. K. Jain, Normalization of tumor vasculature: an emerging concept in antiangiogenic therapy. *Science* **307**, 58-62 (2005); published online EpubJan 7 (307/5706/58 [pii]

10.1126/science.1104819).

4. R. K. Jain, Normalizing Tumor Microenvironment to Treat Cancer: Bench to Bedside to Biomarkers. *Journal of Clinical Oncology* **31**, 2205-2218 (2013); published online EpubMay 13, 2013 (10.1200/jco.2012.46.3653).

5. R. K. Jain, Determinants of tumor blood flow: a review. *Cancer Research* **48**, 2641-2658 (1988); published online EpubMay 15 (

6. P. Carmeliet, R. K. Jain, Molecular mechanisms and clinical applications of angiogenesis. *Nature* **473**, 298-307 (2011); published online EpubMay 19 (nature10144 [pii]

10.1038/nature10144).

7. V. P. Chauhan, Y. Boucher, C. R. Ferrone, S. Roberge, J. D. Martin, T. Stylianopoulos, N. Bardeesy, R. A. DePinho, T. P. Padera, L. L. Munn, R. K. Jain, Compression of pancreatic tumor blood vessels by hyaluronan is caused by solid stress and not interstitial fluid pressure. *Cancer cell* **26**, 14-15 (2014); published online EpubJul 14 (10.1016/j.ccr.2014.06.003).

8. V. P. Chauhan, J. D. Martin, H. Liu, D. A. Lacorre, S. R. Jain, S. V. Kozin, T. Stylianopoulos, A. S. Mousa, X. Han, P. Adstamongkonkul, Z. Popovic, P. Huang, M. G. Bawendi, Y. Boucher, R. K. Jain, Angiotensin inhibition enhances drug delivery and

potentiates chemotherapy by decompressing tumour blood vessels. *Nature Communications* **4**, 2516 (2013); published online Epub10/1/2013 (10.1038/ncomms3516).

9. T. P. Padera, B. R. Stoll, J. B. Tooredman, D. Capen, E. di Tomaso, R. K. Jain, Pathology: cancer cells compress intratumour vessels. *Nature* **427**, 695 (2004); published online EpubFeb 19 (10.1038/427695a427695a [pii]).

10. T. Stylianopoulos, J. D. Martin, V. P. Chauhan, S. R. Jain, B. Diop-Frimpong, N. Bardeesy, B. L. Smith, C. R. Ferrone, F. J. Hornicek, Y. Boucher, L. L. Munn, R. K. Jain, Causes, consequences, and remedies for growth-induced solid stress in murine and human tumors. *Proceedings of the National Academy of Sciences of the United States of America* **109**, 15101-15108 (2012); published online EpubSpetember 18, 2012 (10.1073/pnas.1213353109).

11. V. P. Chauhan, T. Stylianopoulos, J. D. Martin, Z. Popovic, O. Chen, W. S. Kamoun, M. G. Bawendi, D. Fukumura, R. K. Jain, Normalization of tumour blood vessels improves the delivery of nanomedicines in a size-dependent manner. *Nature Nanotechnology* **7**, 383-388 (2012)10.1038/NNANO.2012.45).

12. Y. Huang, J. Yuan, E. Righi, W. S. Kamoun, M. Ancukiewicz, J. Nezivar, M. Santosuosso, J. D. Martin, M. R. Martin, F. Vianello, P. Leblanc, L. L. Munn, P. Huang, D. G. Duda, D. Fukumura, R. K. Jain, M. C. Poznansky, Vascular normalizing doses of antiangiogenic treatment reprogram the immunosuppressive tumor microenvironment and enhance immunotherapy. *Proceedings of the National Academy of Sciences of the United States of America* **109**, 17561-17566 (2012); published online EpubOct 23 (10.1073/pnas.1215397109).

13. E. B. Brown, R. B. Campbell, Y. Tsuzuki, L. Xu, P. Carmeliet, D. Fukumura, R. K. Jain, In vivo measurement of gene expression, angiogenesis and physiological function in tumors using multiphoton laser scanning microscopy. *Nature Medicine* **7**, 864-868 (2001); published online EpubJul (10.1038/8999789997 [pii]).

14. R. K. Jain, Molecular regulation of vessel maturation. *Nature Medicine* **9**, 685-693 (2003); published online EpubJun (10.1038/nm0603-685nm0603-685 [pii]).

15. J. W. Baish, T. Stylianopoulos, R. M. Lanning, W. S. Kamoun, D. Fukumura, L. L. Munn, R. K. Jain, Scaling rules for diffusive drug delivery in tumor and normal tissues.

*Proceedings of the National Academy of Sciences of the United States of America* **108**, 1799-1803 (2011); published online EpubFeb 1 (1018154108 [pii]10.1073/pnas.1018154108).

16. G. Helmlinger, F. Yuan, M. Dellian, R. K. Jain, Interstitial pH and pO2 gradients in solid tumors in vivo: high-resolution measurements reveal a lack of correlation. *Nature Medicine* **3**, 177-182 (1997); published online EpubFeb (

17. B. Diop-Frimpong, V. P. Chauhan, S. Krane, Y. Boucher, R. K. Jain, Losartan inhibits collagen I synthesis and improves the distribution and efficacy of nanotherapeutics in tumors. *Proceedings of the National Academy of Sciences of the United States of America* **108**, 2909-2914 (2011); published online EpubFeb 15 (1018892108 [pii]

10.1073/pnas.1018892108).

18. McGraw, C.M.K., Gamal; Callis, James B., ***Comparison of time and frequency domain methods for luminescence lifetime measurements***. Journal of Physical Chemistry C, 2008. **112**(21): p. 8079-8084.

19. Kruk et al., Journal of Luminescence, 2003.

20. Lakowicz, J.R. *Principles of fluorescence spectroscopy*, (Kluwer Academic/Plenum, New York, 1999).

21. Vovenko et al., Pflugers Arch, 1999.

22. Leunig, M., *et al.* Angiogenesis, microvascular architecture, microhemodynamics, and interstitial fluid pressure during early growth of human adenocarcinoma LS174T in SCID mice. *Cancer Res* **52**, 6553-6560 (1992).

23. Goldman, R.D. & Spector, D.L. *Live cell imaging : a laboratory manual*, (Cold Spring Harbor Laboratory Press, Cold Spring Harbor, N.Y., 2005).

24. Tong, R.T., *et al.* Vascular normalization by vascular endothelial growth factor receptor 2 blockade induces a pressure gradient across the vasculature and improves drug penetration in tumors. *Cancer Res* **64**, 3731-3736 (2004).

25. Tyrrell, J.A., *et al.* Robust 3-D modeling of vasculature imagery using superellipsoids. *IEEE Trans Med Imaging* **26**, 223-237 (2007).

26. Tyrrell, J.A., *et al.* A 2-D/3-D model-based method to quantify the complexity of microvasculature imaged by in vivo multiphoton microscopy. *Microvasc Res* **70**, 165-178 (2005).

# *Chapter 5 Conclusion and future work*

Solid tumors are difficult to cure in part because their microenvironments have low oxygen levels – a condition known as hypoxia – which fuel disease progression by inducing genetic instability, angiogenesis, immunosuppression, inflammation, resistance to cell death, and altered metabolism, among other mechanisms. Additionally, hypoxia causes resistance to therapies that require oxygen to be effective, such as radiation and certain chemotherapies. Finally, because the presence of hypoxia indicates that delivery from the blood vessels is impaired, systemic therapies such as chemotherapy do not reach the entire tumor in sufficient quantities. Thus, developing translatable techniques to increase oxygen tension in tumors will have positive effects on patient outcomes.

There are two factors to modulate in order to affect oxygen delivery to tumor tissue: oxygen supply via blood vessels and oxygen consumption by cells. In my doctoral research, I focused on improving supply to improve the outcome of cancer therapy. Supply, or blood perfusion, is measured as the ratio of the volumetric flow rate of blood to the volume of the tissue being supplied. There are two abnormalities of intratumoral blood vessels that limit supply. The first is vessel compression, which decreases the density of functional vessels. A reduction in the density of vessels with constant tumor tissue volume increases the volume of tissue that each remaining functional blood vessel must supply, thereby reducing perfusion. The second is excessive vessel leakiness, which allows plasma to escape from the blood vessels to cause hemoconcentration and an intravascular pressure drop that together slow blood flow. This reduction in blood flow translates to a reduction in the volumetric flow rate, thereby reducing perfusion. Understanding the physical causes of these two abnormalities has lead to strategies to counter them. There are already clinically proven strategies that repair vessel leakiness to improve oxygen delivery and patient outcomes, so I focused my research on understanding and overcoming vessel compression.

In Chapter 2 of this dissertation, I describe the development of a technique to estimate solid stress in tumors. This technique allowed us to make the first estimates of solid stress in tumors based on measurements of deformation of freshly excised tumors. We made these deformation measurements in numerous types of tumors in patients and mice to confirm that elevated solid stress is a feature of all solid tumors. We then identified structural components within tumors that contribute to solid stress. While

cancer cells were known to compress vessels, we found that depleting them reduced solid stress, as did depleting cancer-associated fibroblasts, collagen I, and hyaluronan. Finally, we demonstrated that depletion of these components in turn decompresses vessels.

Improvements can be made to this technique to give insight into the spatial distribution of solid stresses in tumors. Rather than cutting 80% of the way through an intact tumor diameter to release stress and produce a measurable deformation, other ways of cutting can be performed. Though I demonstrated the difficulty in measuring deformations after cutting tumors into hemispheres, it could be possible to embed the tumor in a gel before cutting it, so that the line of the cut is preserved as the tissue is deformed. Then, the deformation could be measured precisely with a form of microscopy capable of optical sectioning. This would allow two-dimensional mapping of the deformation. If the material properties are measured on a similar length scale, such as by utilizing atomic force microscopy, accurate two-dimensional maps of the stress distribution could be observed. This would allow the confirmation of some predictions in this dissertation, such as how large the region of circumferential tension is at the margin of the tumor. Furthermore, a technique such as this could allow spatial correlation of matrix levels, vessel morphology, vessel function, and solid stress. This would provide insight into whether macro- or microscopic stress distributions are more important for vessel compression. These results would have important implications for the development of future strategies to reverse vessel compression.

Additionally, there likely are other contributors to solid stress that remain identified. For example, how do integrins affect cells' ability to generate, store, and transmit stress? Similarly, how do integrins affect matrix components' ability to store and transmit stress? Can the electrostatic self-repulsion of hyaluronan chains be modulated without depleting hyaluronan itself, potentially by changing the ionic strength of tumor tissues, to decrease solid stress? What is the mechanical cross-talk between tumors and the surrounding normal tissue, and does this affect perfusion in the normal tissue? For example, does a tumor growing in a brain, which is confined by the skull, apply stress to the normal brain and cause it to deform?

In Chapter 3, I describe our efforts to therapeutically reduce solid stress to decompress vessels. First, we found that administering losartan, an FDA-approved therapy indicated for hypertension, to tumor-bearing mice decreased the production and maintenance of

fibroblast populations, collagen, and hyaluronan by blocking angiotensin II receptor I in cancer-associated fibroblasts. Additionally, we found that blocking angiotensin II receptor I was preferable to angiotensin converting enzyme inhibitors, which block both angiotensin II receptor I and II, because stimulation of angiotensin II receptor II reduces desmoplasia. Thus, angiotensin receptor blockers (ARBs) such as losartan are superior to angiotensin converting enzyme inhibitors (ACE-Is) for reducing solid stress. We found that hyaluronan and collagen collaborate to compress vessels. Without sufficient collagen content, hyaluronan does not contribute to vessel compression. Reversing solid stress in this manner decompresses vessels, restores perfusion, and increases delivery of chemotherapy and oxygen. Thus, losartan potentiates chemotherapy, as it provided synergistic gains in primary tumor growth delay, metastatic burden, and overall survival. These results provide an explanation for retrospective analyses, which uncovered a benefit of losartan in cancer patients receiving chemotherapy. Now, colleagues at Massachusetts General Hospital are testing this treatment strategy in patients with pancreatic cancer in a phase II clinical trial (NCT01821729).

While losartan is promising because of its safety, efficacy in preclinical cancer models, and clinical efficacy shown in retrospective clinical analyses, its benefit still needs to be verified in a randomized phase III clinical trial. Other strategies that likely target solid stress, such as sonic hedgehog pathway inhibition, enzymatic hyaluronan depletion, and inhibition of collagen cross-linking have faced obstacles in clinical trials. One potential problem with losartan is its anti-hypertensive effect. Losartan can be dangerous in hypotensive patients or if patients' blood pressure falls too much. Thus, encapsulating losartan or another angiotensin receptor blocker to reduce its effect on the cardiovascular system could reduce side effects and increase the maximum tolerated dose. Additionally, the presence and causes of vessel compression in metastases remain unverified, so it is unclear if losartan will potentiate chemotherapy in overt metastases. Because of the importance of treating metastases with systemic therapy, reversing vessel compression in metastases should be a high priority.

In Chapter 4, I describe the development of a novel technique to map measurements of interstitial tumor oxygenation to perfused blood vessels, allowing for quantitative evaluation of the effects of reversing vessel compression and vessel leakiness on single vessels and the geometry of the vessel network. This technique required applying phosphorescence-quenching microscopy to multi-photon microscopy. We validated this technique *in vivo* in a number of normal and malignant tissues. In treating desmoplastic

breast tumors with losartan or an anti-Vascular Endothelial Growth Factor (VEGF) therapy, which repairs excessive vessel leakiness, we determined the effects of each therapy on single vessel function and vessel network geometry. Surprisingly, we found that VEGF blockade failed to normalize the delivery of oxygen by single vessels as efficiently as proposed. Instead, VEGF blockade affected vessel network geometry in a manner detrimental for oxygen delivery. Losartan was able to delay the onset of a hypoxic state in tumors by improving both single vessel delivery and vessel network geometry.

This work demonstrates how reversing vessel compression and excessive vessel leakiness differentially affect the geometric distribution and function of tumor vessels. Future work will optimize these two strategies towards improving oxygen and chemotherapy delivery to tumors. Furthermore, the recommendations for combining these two approaches needs to be confirmed experimentally and clinically.

In conclusion, the research contained in this dissertation demonstrates the importance of understanding and modulating tissue mechanics in order to improve the treatment of tumors. Furthermore, the methods described in this dissertation enable further study of the effects of tissue mechanics on tumor vessel function. Strategies that modulate tissue mechanics to improve oxygen and drug delivery to tumors need to be validated in the clinic and optimized further in the laboratory.